

**THÈSE DE DOCTORAT
DE SORBONNE UNIVERSITÉ**

Spécialité : Physique

École doctorale n°564: Physique en Île-de-France

réalisée

au Laboratoire Kastler Brossel

sous la direction de **Quentin GLORIEUX**

présentée par

Quentin FONTAINE

pour obtenir le grade de :

DOCTEUR DE SORBONNE UNIVERSITÉ

Sujet de la thèse :

Paraxial fluid of light in hot atomic vapors

soutenue le 31/01/2019

devant le jury composé de :

| | |
|---------------------|--------------------|
| M. Luis OROZCO | Rapporteur |
| M. Iacopo CARUSOTTO | Rapporteur |
| Mme Agnès MAÎTRE | Examinatrice |
| Mme Claire MICHEL | Examinatrice |
| Mme Hélène PERRIN | Examinatrice |
| M. Quentin GLORIEUX | Directeur de thèse |
| M. Alberto BRAMATI | Co-encadrant |

Contents

| | |
|------------------------------------------------------------------------------|-----------|
| Introduction | 1 |
| 1 Atomic vapor | 5 |
| 1.1 Atomic structure | 6 |
| 1.1.1 Fine structure – LS coupling | 6 |
| 1.1.2 Hyperfine structure – IJ coupling | 7 |
| 1.1.3 Line strength: reduction of the dipole operator | 8 |
| 1.2 Two-level atoms | 10 |
| 1.2.1 Is the two-level model relevant ? | 10 |
| 1.2.2 Maxwell-Bloch equation for a closed two-level atom | 12 |
| 1.2.3 Atomic polarization and susceptibility | 14 |
| 1.3 Open three-level atomic system | 18 |
| 1.3.1 Extension to three levels | 18 |
| 1.3.2 Transit and influx rates | 19 |
| 1.3.3 Optical Bloch equations in the interaction picture | 22 |
| 1.3.4 Steady-state solution of the Optical-Bloch equations | 24 |
| 1.3.5 Dielectric susceptibility χ for the 3-level system | 25 |
| 1.3.6 Linear and non-linear response | 26 |
| 1.3.7 General case: open 3-level system with two coupling fields | 27 |
| 1.3.8 Ballistic transport of atoms | 29 |
| 2 Photon fluid in the 2D+1 propagating geometry | 35 |
| 2.1 Nonlinear Schrödinger equation in optics | 36 |
| 2.1.1 Propagation equation in a non-linear medium | 36 |
| 2.1.2 Paraxial approximation for the slowly-varying field envelope | 37 |
| 2.1.3 Comparison with the Gross-Pitaevskii equation | 38 |
| 2.2 Hydrodynamic analogy | 40 |
| 2.2.1 Madelung transform | 40 |
| 2.2.2 Speed of sound | 41 |
| 2.3 Bogoliubov dispersion in a lossless local medium | 42 |
| 2.3.1 Derivation from the Euler’s equations | 42 |
| 2.3.2 Dispersion relation | 43 |
| 2.3.3 Landau criterion for superfluidity | 44 |
| 2.3.4 Derivation from the NLSE | 45 |

| | | |
|----------|---------------------------------------------------------------------------|------------|
| 2.4 | Bogoliubov dispersion in a lossy nonlocal medium | 46 |
| 2.4.1 | Lossy nonlinear medium ($\alpha \neq 0$) | 46 |
| 2.4.2 | Lossy nonlinear medium with effective nonlocal interactions | 47 |
| 3 | Atomic medium characterization | 51 |
| 3.1 | Experimental tools | 52 |
| 3.1.1 | Rubidium cells and oven design | 52 |
| 3.1.2 | Laser sources | 53 |
| 3.2 | Methods I – Absolute vapor temperature measurement | 57 |
| 3.2.1 | Saturated absorption spectroscopy | 57 |
| 3.2.2 | Vapor temperature and atomic density | 58 |
| 3.3 | Methods II – Nonlinear refractive index measurement | 60 |
| 3.3.1 | Thin medium approximation | 61 |
| 3.3.2 | Far-field measurement | 61 |
| 3.4 | Methods III – Scanning phase interferometry | 70 |
| 4 | Dispersion of small amplitude density waves on a photon fluid | 75 |
| 4.1 | Phase velocity measurement | 76 |
| 4.1.1 | Theoretical description | 76 |
| 4.1.2 | Experimental setup and data processing | 85 |
| 4.1.3 | Experimental results and numerical simulations | 89 |
| 4.2 | Group velocity measurement | 94 |
| 4.2.1 | Introduction | 94 |
| 4.2.2 | Theoretical description | 97 |
| 4.2.3 | Numerical simulations | 99 |
| 4.2.4 | Experimental setup and data processing | 101 |
| 4.2.5 | Experimental results | 103 |
| 5 | Optically induced potential in a fluid of light | 111 |
| 5.1 | Modified dielectric response in a N-type atomic system | 112 |
| 5.1.1 | Transit and influx rates | 114 |
| 5.1.2 | Optical-Bloch equations and steady-state solution | 116 |
| 5.1.3 | Linear variation of the refractive index at the defect position | 117 |
| 5.1.4 | Total variation of the refractive index at the defect position | 120 |
| 5.1.5 | Saturation of δn | 125 |
| 5.1.6 | Other routes ? | 127 |
| 5.2 | Optical defect shaping with a Spatial Light Modulator | 128 |
| 5.2.1 | Experimental requirements | 128 |
| 5.2.2 | Absorption-compensated Bessel Beam | 131 |
| 5.2.3 | Droplet beam | 142 |
| 6 | Outlook - Probing superfluidity | 147 |
| 6.1 | Introduction and historical perspective | 148 |
| 6.2 | Flow of light around an all-optical defect | 149 |
| 6.2.1 | Theory and simulations | 149 |
| 6.2.2 | Probing the superfluid phase transition | 151 |
| 6.2.3 | Comments on the results of Michel <i>et al.</i> | 153 |

| | |
|-------------------------------------------------|------------|
| <i>CONTENTS</i> | 3 |
| 6.3 Preliminary results | 154 |
| 6.3.1 Experimental setup and settings | 155 |
| 6.3.2 Real-space scattering pattern | 157 |
| 6.3.3 Far-field diffraction pattern | 158 |
| 6.4 Future works | 161 |
| Summary and future works | 163 |
| Bibliography | 169 |

Introduction

General context

Photons, the quanta of the electromagnetic field, do not interact with each other in vacuum. In dielectric materials however, the situation is different, as photons are likely to couple with the electric charges inside the medium and, thus, to polarize it locally. As polarized matter radiates light, a polarization field appears in response to the incoming electromagnetic one. This response is nonlinear in most materials in the sense that their polarizabilities depend, in a nonlinear manner, on the strength of the incoming light field. In practice nevertheless, only lasers are sufficiently intense to modify in such a way the optical properties of a material. That is why the beginning of the research in nonlinear optics is often considered to be the discovery of second-harmonic generation by Franken and co-workers [1] (1961), shortly after the first experimental demonstration of working laser by Maiman in 1960 [2]. Since then, higher optical intensities are usable and a vast array of nonlinear effects have been explored, with wide-ranging applications from optical frequency conversion [3] to light storage [4] and quantum information processing [5].

Under specific conditions, the effective photon-photon interaction arising from the nonlinear polarizability of certain materials (such as photorefractive crystals, thermo-optic liquids or warm alkaline vapors for instance) makes light behave as a fluid. Indeed, the paraxial propagation of a laser field in a Kerr medium – whose refractive index depends on the input light intensity – is governed by the nonlinear Schrödinger equation. The latter shares strong similarities with the Gross-Pitaevskii equation, describing the dynamics of quantum fluids such as atomic Bose-Einstein condensates (BECs), and can, thus, be reformulated into a set of hydrodynamic equations. In this hydrodynamic analogy, the laser field can be regarded as fluid of light whose density and velocity are respectively defined by the laser intensity and its phase gradient. The first branding of a coherent light field as a photon fluid dates back to the early nineties, where the time-evolution of the electromagnetic field in a laser cavity was reformulated into a Ginzburg-Landau equation [6,7]. In that latter case, the photon-photon interaction was mediated through the nonlinear refractive index of the cavity gain medium. In the following decade, a seminal attempt to observe superfluid-like behaviours in these cavity systems [8] has been followed by a series of theoretical articles by Chiao *et al.* [9,10]. Surprisingly, no other experiments were reported thereafter, possibly because large nonlinearities and high-Q factor cavities were hardly available at the time.

Interestingly, modern research on quantum fluids of light has shifted towards the study of exciton-polaritons in micro-cavities, thanks to progress in semi-conductor nano-structures manufacturing. In these systems, the photon entering the micro-cavity strongly mixes with electron/hole pairs (the excitons) in the bulk material. This leads to the creation of massive interacting bosonic quasi-particles, known as exciton-polaritons. The optical nonlinearity arises here from the Coulomb interaction between the excitons. The spatial confinement, provided by the cavity, moreover assigns a non-zero effective mass to photons. Remarkably, the space-time evolution of the polaritons wave-function follows a similar dynamics to that of interacting atomic BECs, but includes additional detrimental non-equilibrium features arising from its intrinsic dissipative nature. After the observation of polariton BECs [11–13] the hydrodynamical aspects of polariton fluids gained a lot of interest because of the easy experimental access they were offering to many-body physics. For instance, a series of works on the superfluid aspects of these photon fluids has led to the experimental observation of dissipationless flows around a defect [14,15]. The nucleation of quantized vortex/anti-vortex pairs at the breakdown of superfluidity [16], as well as the generation of dark solitons past an obstacle in the supersonic regime [17], have also been reported. All the previous cited articles have been published by our group at LKB and co-workers in between 2009 and 2011.

However, exciton-polariton systems suffer from fundamental limitations. First, they require continuous pumping due to dissipation and losses (light fatally leaks out of the micro-cavity) which thus makes the dynamics of polariton fluids intrinsically driven-dissipative. Moreover, the effective photon-photon interaction strength is fully governed by the exciton-exciton one, which is only marginally tunable. In order to overcome both these limitations, an alternative approach based on cavityless systems can be used. As mentioned previously, the paraxial propagation of a laser field inside a bulk nonlinear material can be described as a fluid of light evolving along the propagation direction as a normal fluid will do over time. These systems are commonly referred to as *propagating* or *paraxial photon fluids*. After the observation by Swartzlander *et al.* of quantized vortex pairs created by the instability of dark soliton stripes in nonlinear liquids [18], the hydrodynamics features of paraxial fluids of light have been extensively investigated theoretically. An exhaustive list of the works published in this field can be found in the review by Carusotto and Ciuti [19]. Especially strong attention was revived toward solitonic structures [20–23]. Surprisingly, few experimental studies have specifically investigated the hydrodynamic features of light propagating in bulk nonlinear mediums and most of them have been performed in the Fleischer’s group from 2007 to 2012. For instance, the generation, the propagation as well as the interaction of optical dispersive shock-waves has first been studied in photorefractive crystals by Jia *et al.* [24] and Wan *et al.* [25] in 2007. Wan and co-workers have also reported the spontaneous nucleation of quantized vortices in the wake of an obstacle in a 2-dimensional geometry [26] and the tunneling of density waves through a small potential barrier in the 1-dimensional case [27]. Their studies have laid the groundwork for studying superfluid effects in paraxial photon fluids. Recently, there has been a renewed interest in this field, with the observation of quantized vortices past an obstacle in thermo-optics liquids [28] and the optomechanical demonstration of frictionless flows of light in photorefractive crystals by Michel *et al.* [29].

Motivations

This thesis aims at studying the hydrodynamical properties of paraxial photon fluids in hot rubidium vapors. In this system, the nonlinear interaction between photons is provided by the nonlinear polarization of the atomic ensemble when the light frequency is tuned close to an atomic resonance. Hot rubidium vapors offer certain compelling advantages compared to other platforms used so far to generate paraxial fluid of light (that is, photorefractive crystals and thermo-optics liquids principally). First, the nonlinear interaction between photon is easily tunable over several orders of magnitude in this system by changing the vapor density (which increases exponentially with the temperature) and/or the laser frequency. Moreover, the vapor optical response is only weakly nonlocal, in contrast to thermo-optic liquids where strong nonlocalities, arising from heat diffusion inside the material, have been reported [28]. Such nonlocalities make the observation of quantum phenomena difficult if not impossible. We thus believe that alkaline vapors could be the first platform to lay the groundwork for studying quantum effects in propagating photon fluids.

Despite the fact that many nonlinear optics experiments have been performed using warm rubidium vapors (and, more generally, alkaline vapors), only few attention has been devoted to studying the hydrodynamical aspect of the nonlinear propagation of laser beams inside these systems. In addition, most of the experimental works on propagating photon fluids reported so far focus mainly on studying strongly nonlinear effects, such as spatial solitons or dispersive shock-waves. The amplitude of such nonlinear phenomena is large enough to locally change the properties of the photon fluid. Conversely, only few studies consider the linear aspect of the dynamics, that is, how small amplitude density waves travel onto the fluid of light. Throughout this manuscript, I will explore phenomena lying on this borderline between nonlinear hydrodynamics and standard nonlinear optics. The main purpose of this thesis is thus to further bridge the gap between this two disciplines, by drawing new parallels between nonlinear optics and Bogoliubov formalism principally.

Thesis Summary

This thesis manuscript consists of three parts. The first one (chapters 2 and 3) is a theoretical introduction to hot rubidium vapors and paraxial photon fluids. The second part (chapter 4) presents the tools and methods used to create and characterize photon fluids in our platform. The third part (chapters 4, 5 and 6) is mainly dedicating to presenting the experimental results I obtained during my thesis.

Chapter 1 – The optical response of a warm rubidium vapor under a near resonance laser-excitation is described using a two level model first and – at a later stage – a more sophisticated 3-level scheme. Effects arising from the atomic motion (Doppler broadening, transport induced nonlocality) are taken into account in this second description.

Chapter 2 – The theoretical ground work for studying propagating fluids of light is laid. The analogy between the propagation of a laser beam in a Kerr medium and the evolution of a fluid of light is discussed in detail. A particular intention is devoted to studying the dynamics of small amplitude density modulations travelling onto the paraxial photon fluid. In this perspective, the dispersion relation of these density waves is derived. The effects of absorption and nonlocality on this dispersion are investigated.

Chapter 3 – The tools and methods used to generate and characterise propagating photon fluids in hot rubidium vapors are introduced. An important part of this chapter is dedicated to presenting the method used to measure the vapor nonlinear refractive index. The latter is based on measuring the self-phase accumulated by a Gaussian beam during its propagation inside the vapor cell. We show that counting the ring appearing in its far-field intensity distribution is enough to access the nonlinear refractive index.

Chapter 4 – A measurement of the dispersion relation of small amplitude density waves is reported. This is achieved by measuring the group velocity of a small amplitude wave-packet travelling onto the photon fluid. The dispersion relation exhibits a linear trend at low excitation wave-vector, whose slope defines the velocity of sound in the paraxial photon fluid. The way the sound velocity depends on the fluid density is studied and perfectly matches theory without any fitting parameter. According to the Landau criterion for superfluidity, demonstrating the existence of such a sonic regime in the dispersion relation is a key step toward the observation of superfluid flow of light.

Chapter 5 – In order to probe the superfluidity of light, the way the fluid flows around a localized obstacle (*ie*, a local change of refractive index) should be investigated. Chapter 5 is dedicated to studying how such an obstacle can be optically generated in rubidium vapors. In the first section, the 2-laser optical scheme designed to that end is theoretically described, using the dressed-state formalism. In the second section, we show that Bessel beams are suitable to generate spatially localized, collimated obstacles. Using a spatial light modulator, we demonstrate that the on-axis intensity of such beam can be tailored so as to compensate absorption locally.

Chapter 6 – Preliminary results obtained by bringing all the previous ingredients together are presented. Images of the near- and far-field scattering patterns generated by making the fluid flow toward the all-optical obstacle are shown. The amount of light scattered by the defect is measured in Fourier space as function of the photon fluid density and velocity.

Chapter 1

Atomic vapor

Photon-photon interactions in paraxial photon fluids arise from the light-matter coupling in nonlinear optical materials. The strength of the nonlinear interaction between photon, as well as the thickness of the nonlinear material, are key parameters in experiments which need to be made as large as possible. Hot alkaline vapors constitute a sound choice because they provide strong optical nonlinearities under a near-resonance laser excitation. Moreover, spectroscopic cells filled with high quality alkaline vapors are easy to handle and also to design according to our specific needs (isotopic concentration, cell length and shape, etc). We chose more specifically to work with rubidium vapors as an expertise in dealing with this atom has already been developed in the team for several years. The purpose of this chapter is to introduce the theoretical framework describing the optical response of a rubidium vapor under a near resonance laser excitation. To this end, I first model the rubidium level structure with a two-level description, that mainly helps introducing the basic concepts and notations. This simplistic model is improved afterward, by taking into account the optical pumping between the rubidium ground states. The effects of the high vapor temperatures on the optical response are also investigated.

1.1 Atomic structure

Rubidium belongs to the alkali metal group of the periodic table and possesses therefore one valence electron on its outermost shell. Two rubidium isotopes are present on Earth: rubidium 85 (^{85}Rb , 72%) and rubidium 87 (^{87}Rb , 28%), which is slightly radioactive, with a half-life time of 49 billion years (safe enough). Natural-abundance mixtures and isotopically pure vapors were used in the lab (more than 99% purity). In the experiments presented in this manuscript, we optically addressed the rubidium D -lines exclusively, either or both the D_1 ($5^2S_{1/2} \rightarrow 5^2P_{1/2}$) and the D_2 ($5^2S_{1/2} \rightarrow 5^2P_{3/2}$) component. The optical properties of the rubidium D -lines have been gathered in review by D.A. Steck [30,31] for rubidium 85 and rubidium 87. In this first section, I will introduce the reader to the fine and hyperfine structures of rubidium D_1 and D_2 lines, that basically determine the optical response of the atomic vapor under a near-resonance laser excitation.

1.1.1 Fine structure – LS coupling

The doublet structure of the rubidium D -line arises from the coupling between the angular orbital momentum \mathbf{L} of the valence electron and its spin angular momentum \mathbf{S} . The total electron angular momentum \mathbf{J} is then defined by: $\mathbf{J} = \mathbf{L} + \mathbf{S}$; the associated quantum number J lies in the range $|L - S| \leq J \leq L + S$. In the ground state of rubidium, $L = 0$ and $S = 1/2$ so $J = 1/2$; in the first excited state, $L = 1$ and $S = 1/2$ so $J = 1/2$ or $3/2$. The fine coupling leads thus to the splitting of the first rubidium excited state into two fine states ($5^2P_{1/2}$ and $5^2P_{3/2}$) and gives, accordingly, a doublet structure to the D -line.

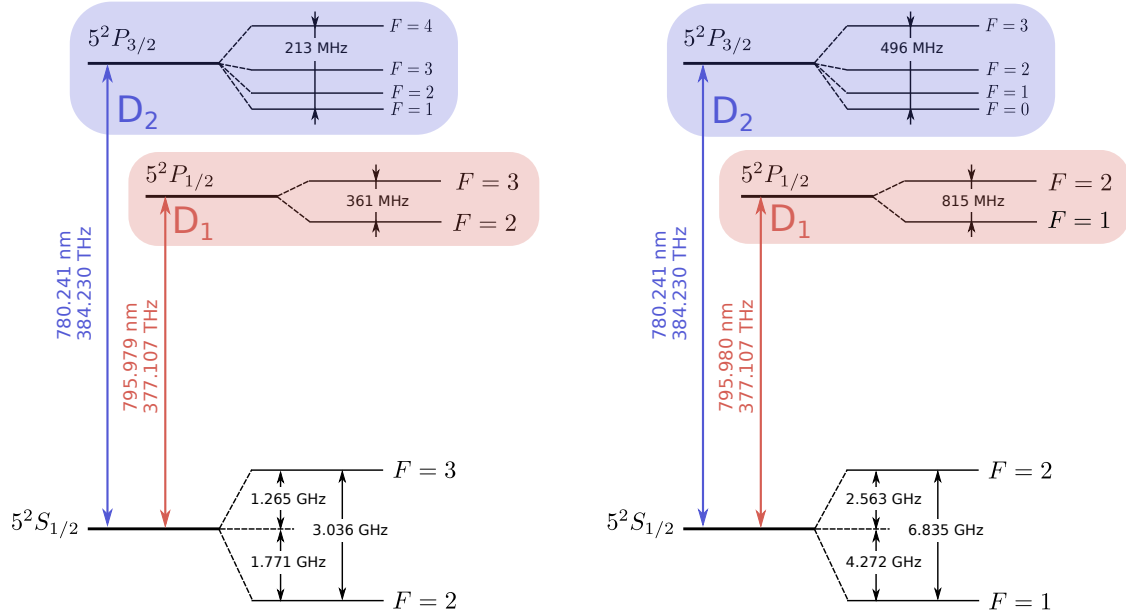


Figure 1.1: ^{85}Rb (left) and ^{87}Rb (right) D -line hyperfine structure.

1.1.2 Hyperfine structure – IJ coupling

We can go one step further by introducing the atomic hyperfine structure, which arises from the coupling between the total electron angular momentum, \mathbf{J} , and the nuclear spin angular momentum, \mathbf{I} . As before, the quantum number F , associated to the atomic angular momentum $\mathbf{F} = \mathbf{J} + \mathbf{I}$, lies in between $|J - I|$ and $J + I$. The nuclear spin differs from one isotope to the other: $I = 5/2$ for ^{85}Rb and $3/2$ for ^{87}Rb . In the ground state, the total electron angular momentum is $1/2$ and F can therefore take two different values: $F = 2$ or $F = 3$ for ^{85}Rb and $F = 1$ or $F = 2$ for ^{87}Rb . The ground state of both isotopes separates thus into two hyperfine states. Moreover, it is straightforward to show that each of the excited states $5^2P_{1/2}$ and $5^2P_{3/2}$ splits into two and four hyperfine states respectively. Let's for instance consider the case of ^{85}Rb :

- For $5^2P_{1/2}$ (D_1 line), F can take any integer values between $I - J = 2$ and $I + J = 3$. The fine state $5^2P_{1/2}$ splits thus into 2 hyperfine states labeled by $F = 2$ and $F = 3$.
- For $5^2P_{3/2}$ (D_2 line), F can take any integer values from $I - J = 1$ to $I + J = 4$ and $5^2P_{3/2}$ splits therefore into 4 hyperfine states labeled by $F = 1, 2, 3, 4$ respectively.

When no external magnetic field is applied, each of the hyperfine ground and excited states are degenerate, as they contain $2F + 1$ magnetic sublevels each, labelled by the total angular momentum projection m_F . The schematic of the D -line hyperfine level structure for both ^{85}Rb and ^{87}Rb is depicted on figure 1.1. The transition frequencies are reported, as well as the frequency difference between (i) the hyperfine ground states and (ii) the furthest apart excited states for in each of the D -lines.

| | | | | | |
|------------------|-------------|----------------|-----------------|-----------------|---------------|
| D_2 line | | D_1 line | | | |
| ^{85}Rb | $F_g \ F_e$ | 1 | 2 | 3 | 4 |
| | 2 | $\frac{1}{3}$ | $\frac{35}{81}$ | $\frac{28}{81}$ | 0 |
| | 3 | 0 | $\frac{10}{81}$ | $\frac{35}{81}$ | 1 |
| D_2 line | | D_1 line | | | |
| ^{87}Rb | $F_g \ F_e$ | 0 | 1 | 2 | 3 |
| | 1 | $\frac{1}{9}$ | $\frac{5}{18}$ | $\frac{5}{18}$ | 0 |
| | 2 | 0 | $\frac{1}{18}$ | $\frac{5}{18}$ | $\frac{7}{9}$ |
| D_2 line | | D_1 line | | | |
| ^{87}Rb | $F_g \ F_e$ | 1 | 2 | | |
| | 1 | $\frac{1}{9}$ | $\frac{5}{18}$ | | |
| | 2 | $\frac{1}{18}$ | $\frac{5}{18}$ | | |

Figure 1.2: Line strengths C_F^2 of the D -lines for ^{85}Rb and ^{87}Rb [32]

1.1.3 Line strength: reduction of the dipole operator

The optical response of the vapor under a monochromatic laser excitation is a key feature we need to characterize in order to accurately describe our experiments. This response is linked to the polarizability (or the dielectric susceptibility) of the material, which strongly depends on the dipole strength of the transition we optically address. In order to evaluate the dipole strength associated to the transition between the ground and excited states $|F_g, m_{F_g}\rangle$ and $|F_e, m_{F_e}\rangle$, we must calculate the matrix element:

$$\langle F_g, m_{F_g} | \hat{\mathbf{d}} | F_e, m_{F_e} \rangle = \langle F_g, m_{F_g} | e \hat{\mathbf{r}} | F_e, m_{F_e} \rangle, \quad (1.1)$$

where $\hat{\mathbf{d}}$ and $\hat{\mathbf{r}}$ are the dipole and position operators. In doing so, we should first factor out the angular dependence and write the matrix element as a product of Wigner 3- j and 6- j symbols times a reduced matrix element. This procedure is called "reduction of the dipole operator" [33] and reads as follows:

$$\begin{aligned} \langle F_g, m_{F_g} | e \hat{\mathbf{r}}_q | F_e, m_{F_e} \rangle &= (-1)^{F_e-1+m_{F_g}} (-1)^{F_e+J_g+1+I} (-1)^{J_e+L_g+1+S} \langle L_g || e \hat{\mathbf{r}} || L_e \rangle \\ &\times \sqrt{2F_g+1} \sqrt{(2F_e+1)(2J_g+1)} \sqrt{(2J_e+1)(2L_g+1)} \\ &\times \begin{pmatrix} F_e & 1 & F_g \\ m_{F_e} & q & -m_{F_g} \end{pmatrix} \begin{Bmatrix} J_g & J_e & 1 \\ F_e & F_g & I \end{Bmatrix} \begin{Bmatrix} L_g & L_e & 1 \\ J_e & J_g & S \end{Bmatrix}, \end{aligned} \quad (1.2)$$

where q labels the components of $\hat{\mathbf{r}}$ in the spherical basis; according to its usual definition, q quantifies the integer change in the angular momentum projection during the transition. The reduced dipole matrix element $d = \langle L_g || \hat{\mathbf{r}} || L_e \rangle$ involves only the quantum number L and is therefore identical for both D lines. The round and curly brackets matrices in (1.2) stand for the Wigner 3- j and 6- j symbols respectively. For linearly polarized light, $q = 0$ and the 3- j symbol is non-zero only when $m_{F_e} = m_{F_g}$. We can for instance express it as a function of the transition wavelength λ and decay rate Γ of the D_1 line. The decay rate associated to the fine-structure transition $J_g \rightarrow J_e$ reads as follows:

$$\Gamma = \frac{\omega^3}{3\pi\epsilon_0\hbar c^3} \frac{2J_g+1}{2J_e+1} |\langle J_g || e \hat{\mathbf{r}} || J_e \rangle|^2, \quad (1.3)$$

where the reduced matrix element $\langle J_g || e \hat{\mathbf{r}} || J_e \rangle$ is related to the reduced dipole factor d by:

$$\langle J_g || e \hat{\mathbf{r}} || J_e \rangle = (-1)^{J_e+L_g+1+S} \sqrt{(2J_e+1)(2L_g+1)} \begin{Bmatrix} L_g & L_e & 1 \\ J_e & J_g & S \end{Bmatrix} \times d. \quad (1.4)$$

For the D_1 line (where $J_g = J_e = 1/2$) the relation above reduces to: $\langle J_g || e \hat{\mathbf{r}} || J_e \rangle = d/\sqrt{3}$. Using (1.3) and rearranging:

$$d = \langle L_g || e \hat{\mathbf{r}} || L_e \rangle = \sqrt{\frac{9\epsilon_0\hbar\Gamma\lambda^3}{8\pi^2}}. \quad (1.5)$$

A similar analysis leads to the same result for the D_2 line. Using the tabulated values [30] for the D -lines wavelengths and decay rates yields $d = 5.182 e a_0$ and $d = 5.177 e a_0$ for the D_1 and D_2 lines respectively, a_0 being the Bohr radius.

The dipole matrix element in equation (1.2) reads finally: $\langle F_g, m_{F_g} | e\hat{r}_q | F_e, m_{F_e} \rangle = c_{m_F} d$, where c_{m_F} is a geometrical factor that depends on the the initial and final hyperfine states of the transition. Since no magnetic field is applied, every hyperfine state is degenerate $2F_g + 1$ times. The total strength $f_{F_g}^{F_e}$ of the $F_g \rightarrow F_e$ hyperfine transition is thus obtained by averaging over the strength of all the Zeeman transitions $m_{F_g} \rightarrow m_{F_e}$ in the hyperfine manifold. We finally obtained that:

$$f_{F_g}^{F_e} = \frac{\sum_{m_F} c_{m_F}^2 d^2}{2F_g + 1} = \frac{C_F^2 d^2}{2F_g + 1}, \quad (1.6)$$

where $C_F^2 = \sum_{m_F} c_{m_F}^2$. The C_F^2 coefficients have been calculated for linearly polarized light and are reported in the table of figure 1.2 for both ^{85}Rb and ^{87}Rb .

It is worth mentioning however that the formula (1.6) is generally an approximation as it amounts to neglecting optical pumping effects between Zeeman sublevels, such as population aligning and population trapping. In other words, we assume here that every Zeeman transition $m_{F_g} \rightarrow m_{F_e}$ is cycling, which is obviously wrong as the excited state $|F_e, m_{F_e}\rangle$ may also decay toward $|F_g, m_{F_e} \pm 1\rangle$ according to the selection rules.

- In the case of a cycling hyperfine transition for which $F_e < F_g$ (the $F_g = 1 \rightarrow F_e = 0$ transition of ^{87}Rb for instance), the atoms get pumped into one of the dark states $|F_g, m_{F_g} = F_g\rangle$ or $|F_g, m_{F_g} = -F_g\rangle$ (population trapping, fig. 1.3(a)) and remain there.
- When F_e and F_g are integers and fulfilled the condition $F_e = F_g$, the Zeeman sublevel on the excited state right edge $|F_e, m_{F_e} = F_e\rangle$ (resp. left edge $|F_e, m_{F_e} = -F_e\rangle$) may only decay toward the sublevels $|F_g, m_{F_g} = F_g\rangle$ or $|F_g, m_{F_g} = F_g - 1\rangle$ (resp. toward $|F_g, m_{F_g} = -F_g\rangle$ or $|F_g, m_{F_g} = -F_g + 1\rangle$). This asymmetry in the decay process forces the atoms to accumulate in the sublevel $m_{F_g} = 0$ (population aligning, fig. 1.3(b)).

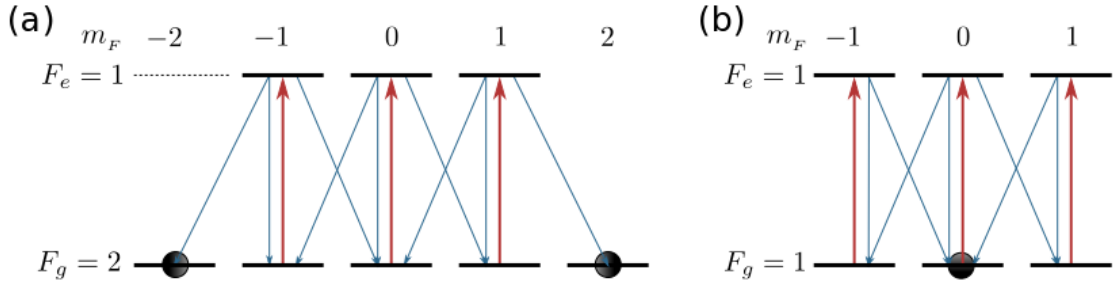


Figure 1.3: Optical pumping between Zeeman sublevels. The excitation laser is linearly polarized and couples ground and excited sublevels sharing the same m_F (red arrows). The blue arrows represent all possible decay channels from F_e to F_g . (a) Sketch of the population trapping process: atoms end up in the $m_{F_g} = \pm F_g$ dark states which are not coupled by the excitation laser with any of the excited Zeeman sublevels. (b) Sketch of the population aligning process: atoms are more likely to decay toward the $m_{F_g} = 0$.

The Zeeman degeneracy can affect the atomic population in the steady-state and change, consequently, the optical response of the rubidium vapor [34]. However, taking the whole hyperfine structure plus the Zeeman degeneracy into account to describe the polarisation of the vapor under a near-resonance laser excitation is far to be easy and not necessary in a first instance to get a good insight about the physical process at play. Let's then continue with equation (1.6), bearing in mind the discussion above.

1.2 Two-level atoms

There is no two-level atom and rubidium is not one of them.

William D. Phillips

As Bill Phillips reminds us, the level structure of the rubidium D -lines is everything but simple and it seems somewhat oversimplified to model it with a two-level system. However, even-though the two-level atom model remains simplistic compared to the real complexity of alkali atomic structures, I still want to introduce it in this section for mainly two reasons. Firstly, this model can effectively describe the rubidium vapor under certain conditions (I will come back to this point in detail in the next section) and, secondly, it enables to present one by one, in a simplified context, all the theoretical tools we will need to cover more complicated situations. I will in particular introduce the dielectric susceptibility χ of the medium and study how it depends on the laser intensity, which is one of the key feature for photon fluid experiments.

1.2.1 Is the two-level model relevant ?

Before getting into the details of the calculations, let's try to assess the relevance of the two-level model in describing rubidium atoms. In order to do so, we have first and foremost to understand which atomic levels among those forming the fine and hyperfine structures of the D -lines are involved in this two-level description.

i Hyperfine splitting

As you may have noticed looking at figure 1.1, there is more than 15 nm difference between the wavelengths of the D_1 and D_2 transition lines. Therefore, when we optically address one of the D -line, the contribution of the other one on the optical response of the rubidium vapor is completely negligible. On figure 1.1, you can also see that the hyperfine ground state splitting δ_0 is almost 10 times larger than the characteristic excited state hyperfine splitting δ_{HF} . Let's focus for example on the D_1 line of ^{85}Rb for which $\frac{\delta_0}{2\pi} \simeq 3.036$ GHz, $\frac{\delta_{\text{HF}}}{2\pi} \simeq 213$ MHz and $\delta_0/\delta_{\text{HF}} \simeq 14.3 \gg 1$. If the laser frequency ω is red-detuned with respect to the $F_g = 3 \rightarrow F_e$ transition frequency ω_{D_1} , the laser detuning Δ , defined by:

$$\Delta = \omega - \omega_{D_1}, \quad (1.7)$$

is negative. In addition, if $\delta_0 > |\Delta| \gg \delta_{\text{HF}}$, the laser couples much more efficiently $F_g = 3$ than $F_g = 2$ to the hyperfine excited states $F_e = 2$ and $F_e = 3$ of the D_1 line. Moreover, as $|\Delta| \gg \delta_{\text{HF}}$, the laser field drives the D_1 line off-resonantly: light/matter interaction processes are dominated by Rayleigh scattering events involving the fine state $5^2P_{1/2}$ as a whole, since the laser detuning is too large to probe its hyperfine level structure in detail.

As things stand at the moment, if the conditions $\Delta < 0$ and $\delta_0 > |\Delta| \gg \delta_{\text{HF}}$ are fulfilled, it seems actually reasonable to model the D_1 line of ^{85}Rb by a two-level atomic system where the ground state $|g\rangle$ is the hyperfine level $F_g = 3$ of $5^2S_{1/2}$ and the excited state $|e\rangle$ the fine level $5^2P_{1/2}$. In practice, the previous conditions on the laser detuning are satisfied.

- In fluid of light experiments, the nonlinear interaction between photons has to be repulsive, which imposes the laser frequency ω to be red-detuned with respect to the resonance frequency (*ie* Δ to be negative). As of now, you must take my word for it. I will come back to this point in paragraph 1.2.3 i.
- If the laser comes closer to resonance, absorption increases and transmission through the vapor highly decreases, according to the Beer-Lambert law. This effect is enhanced if Doppler broadening is taken into account, as we will see in the next paragraph. In experiments, we always keep a transmission above 70% (see paragraph 1.2.3 iii).

ii Doppler broadening

In hot vapors, atoms are constantly moving and do not contribute equally to the medium optical response. If thermal motion causes an atom to move toward the incoming photons, or in other words, if the scalar product $\mathbf{k} \cdot \mathbf{v}$ is negative (\mathbf{k} and \mathbf{v} being respectively the laser wave-vector and the atom velocity), the laser frequency ω_D in the moving frame of this atom will be blue-shifted with respect to ω because of Doppler effect:

$$\omega_D = \omega - \mathbf{k} \cdot \mathbf{v} = \omega - k_z v_z. \quad (1.8)$$

The z-axis defines here the laser optical axis and v_z stands for the component of \mathbf{v} along z . Different atom velocities result therefore in different Doppler shifts, the cumulative effect of which is the line broadening. This resulting line profile is known as a Doppler profile. The susceptibility χ , that characterizes the vapor optical response, must then be averaged over the atomic velocity distribution along z , namely, the 1D Maxwell distribution:

$$\mathcal{P}_{1D}(v) = \sqrt{\frac{m}{2\pi k_B T}} \exp\left(-\frac{m v_z^2}{2 k_B T}\right), \quad (1.9)$$

where m is the rubidium mass, k_B the Boltzmann constant and T the vapor temperature. Using the relation (1.8), \mathcal{P} can be expressed a function of ω and ω_D as follows:

$$\mathcal{P}_{1D}(\omega_D) = \sqrt{\frac{m}{2\pi k_B T}} \exp\left[-\left(\frac{\omega - \omega_D}{\Delta\omega_D}\right)^2\right]. \quad (1.10)$$

The width $\Delta\omega_D$ of this Gaussian distribution is equal to $k \sqrt{2k_B T/m}$. When $T = 400$ K, the Doppler linewidth $\Gamma_D = \Delta\omega_D/2\pi$ is about 350 MHz for the D_1 line of ^{85}Rb . This is much larger than the natural linewidth $\Gamma \simeq 2\pi \times 5.7$ MHz of the D_1 line. Even if the laser is not at resonance with zero velocity atoms, fast moving ones can thus still absorb light, because of Doppler effect. In order to minimize absorption, the laser detuning should be large compared to $\Delta\omega_D$. Moreover, you may have noticed that Γ_D is of the same order of magnitude as δ_{HF} . Doppler broadening will thus smooth the hyperfine structure of the excited state in the absorption profile and, more generally, in the vapor dielectric response. The two-level description of the rubidium D -lines seems then to be even more appropriate to model the optical response of the atomic vapor.

iii Conclusion

Let's summarize. As long as the laser detuning is negative and satisfied $\delta_0 > |\Delta| \gg \delta_{\text{HF}}$ (which also implies that $|\Delta| \gg \Delta\omega_D$ since δ_{HF} and $\Delta\omega_D$ are of the same order of magnitude at $T = 400$ K by the way) the two-level model describes each of the D -lines quite accurately. However, it is worth mentioning that effect such as ground state optical pumping are not taken into account in this simple description of the rubidium level structure. If it is true that the laser couples more efficiently one ground state than the other to the excited level, the latter can still decay with equal probability toward both ground states, as the transition is not cycling. This will lead to a population transfer between ground states that can greatly impact the internal dynamics of rubidium atoms (see section 1.3). But for now, let's further investigate the features of the two-level model by deriving the optical Bloch equations.

1.2.2 Maxwell-Bloch equation for a closed two-level atom

Let us consider the interaction of a monochromatic electric field $\mathbf{E}(t)$ with a system of N two-level atoms per unit volume. In what follows, $|g\rangle$ and $|e\rangle$ stand respectively for the ground and the excited state in this two-level description, while ω_{eg} denotes the resonant transition frequency. We assume that the upper level $|e\rangle$ decays because of spontaneous emission toward the ground state $|g\rangle$ at a rate Γ , and therefore that the lifetime of the $|e\rangle$ is given by $\tau = 1/\Gamma$. This system is called closed since any population that leaves the upper level necessarily enters the lower one.

The interaction between the laser field and the two-level atom is described by a Lindblad master equation, commonly known as the **optical Bloch equation** [35, 36]:

$$\frac{d\hat{\rho}}{dt} = -\frac{i}{\hbar} [\hat{H}, \hat{\rho}] + \sum_{\nu \neq 0} \left(L_\nu \hat{\rho} L_\nu^\dagger - \frac{1}{2} \{L_\nu L_\nu^\dagger, \hat{\rho}\} \right), \quad (1.11)$$

where $\hat{\rho}$ and \hat{H} are respectively the density matrix operator and the system Hamiltonian. Both are Hermitian. The Lindblad operators L_ν are quantum jump operators, describing a random evolution of the system which suddenly changes under the environment influence (at the time scale of the evolution).

The Hamiltonian \hat{H} splits into a non-perturbative diagonal part \hat{H}_0 and a perturbative one \hat{W} that describes the light/matter interaction. The unperturbed Hamiltonian is given by:

$$\hat{H}_0 = \sum_i E_i |i\rangle \langle i| = E_g |g\rangle \langle g| + E_e |e\rangle \langle e|, \quad (1.12)$$

where E_i is the energy associated to the i -th level. As energy is defined up to a constant, we choose to set E_g to zero. Hence:

$$\hat{H}_0 = 0 \times |g\rangle \langle g| + \hbar \omega_{eg} |e\rangle \langle e| = -\hbar \Delta |e\rangle \langle e| + \tilde{H}_0, \quad (1.13)$$

where the laser detuning is still defined by $\Delta = \omega - \omega_{eg}$ and $\tilde{H}_0 = 0 \times |g\rangle \langle g| + \hbar \omega |e\rangle \langle e|$. The role plays by \tilde{H}_0 is explained in the next paragraph. For now, just remember how \hat{H}_0 has been rewritten in order to make explicitly appear Δ in the left hand side of (1.13). Let's now focus on the off-diagonal part \hat{W} of the Hamiltonian \hat{H} .

i Dipole and rotating wave approximation

Under the so-called **dipole approximation**, the spatial variation of the electric field at the atomic scale can be neglected. We can thus think of the atom as an electric dipole that interacts with the laser electric field through $\hat{W} = -\hat{\mathbf{d}} \cdot \mathbf{E}(t)$. This interaction Hamiltonian describes how the quantum dipole operator $\hat{\mathbf{d}}$ tends to align on the classical field $\mathbf{E}(t)$ to minimize the atom plus field overall energy. The dipole operator reads as follows:

$$\hat{\mathbf{d}} = \mathbf{d}^* |e\rangle \langle g| + \mathbf{d} |g\rangle \langle e|. \quad (1.14)$$

Therefore, as $\mathbf{E}(t) = \mathcal{E}_0 \cos(\omega t) \boldsymbol{\xi}$ ($\boldsymbol{\xi}$ being the laser field polarization unit vector):

$$\begin{aligned} \hat{W}(t) &= -\frac{1}{2} \left[\left(\mathbf{d}^* |e\rangle \langle g| + \mathbf{d} |g\rangle \langle e| \right) \right] \cdot \left[\mathcal{E}_0 \left(e^{i\omega t} + e^{-i\omega t} \right) \boldsymbol{\xi} \right] \\ &= -\frac{\hbar}{2} \left(\Omega^* |e\rangle \langle g| + \Omega |g\rangle \langle e| \right) \times \left(e^{i\omega t} + e^{-i\omega t} \right). \end{aligned} \quad (1.15)$$

The Rabi frequency $\Omega = \mathcal{E}_0 \mu_{ge} / \hbar$ measures the strength of the light-matter interaction. For linearly polarized light, the dipole moment $\mu_{ge} = \langle g | \hat{\mathbf{d}} \cdot \boldsymbol{\xi} | e \rangle$ is given by: $\mu_{ge} = \sum_{F_e} f_{F_g}^{F_e}$ (F_e runs over the angular momentum of all the hyperfine levels composing the state $|e\rangle$). The coefficients $f_{F_g}^{F_e}$ are defined in (1.6). Embarrassingly, the interaction Hamiltonian in equation (1.15) contains an explicit time dependence. The usual way for getting rid of it is to place ourselves in the interaction representation with respect to \tilde{H}_0 , defined in (1.13). Let \tilde{U} stand for the interaction picture unitary evolution operator:

$$\tilde{U}(t) = \exp \left(-i\tilde{H}_0 / \hbar \right) = |g\rangle \langle g| + |e\rangle \langle e| e^{-i\omega t}. \quad (1.16)$$

The new Hamiltonian is: $\hat{H} = \tilde{U}^\dagger \hat{H} \tilde{U} = \hat{H}_0 + \tilde{U}^\dagger \hat{W}(t) \tilde{U}$ (because \tilde{U} commutes with \hat{H}_0). Applying this unitary transformation is like switching from a static frame to a rotating one at ω in the complex plane (in which $e^{-i\omega t}$ "rotates" around the origin). The rotating frame "unwinds" part of the evolution of the quantum state, which has at the end of the day a simpler time dependence. The coupling operator in the interaction picture reads:

$$\hat{W}_I(t) = \tilde{U}^\dagger \hat{W}(t) \tilde{U} = -\frac{\hbar}{2} \left(\Omega^* e^{i\omega t} |e\rangle \langle g| + \Omega e^{-i\omega t} |g\rangle \langle e| \right) \times \left(e^{i\omega t} + e^{-i\omega t} \right) \quad (1.17)$$

$$\simeq -\frac{\hbar}{2} \left(\Omega^* |e\rangle \langle g| + \Omega |g\rangle \langle e| \right). \quad (1.18)$$

In equation (1.18), we get rid of the fast oscillating terms at $\pm 2\omega$, that intuitively average to zero in the Bloch equation (1.46). This approximation, the so-called **Rotating Wave Approximation** (RWA), is used in a wide variety of contexts, from quantum optics [37] to atomic physics [38]. In the interaction picture and using the RWA, the time dependence of \hat{W} cancels. By introducing $\hat{\rho}_I = \tilde{U}^\dagger \hat{\rho} \tilde{U}$, equation (1.11) becomes:

$$\frac{d\hat{\rho}_I}{dt} = -\frac{i}{\hbar} \left[\hat{H}_I, \hat{\rho}_I \right] + \sum_{\nu \neq 0} \left(\tilde{L}_\nu \hat{\rho}_I \tilde{L}_\nu^\dagger - \frac{1}{2} \{ \tilde{L}_\nu \tilde{L}_\nu^\dagger, \hat{\rho}_I \} \right), \quad (1.19)$$

with $\hat{H}_I = 0 \times |g\rangle \langle g| - \hbar \Delta |e\rangle \langle e| + \hat{W}_I$. A straightforward calculation leads finally to the following set of Bloch equations for the slowly varying density matrix elements $\rho_{ij}(t)$ (I will drop out the I index in the following):

$$\begin{aligned}
\frac{d\rho_{gg}}{dt} &= \Gamma \rho_{ee} + \frac{i}{2} (\Omega^* \rho_{eg} - \Omega \rho_{ge}) \\
\frac{d\rho_{ee}}{dt} &= -\Gamma \rho_{ee} - \frac{i}{2} (\Omega^* \rho_{eg} - \Omega \rho_{ge}) \\
\frac{d\rho_{eg}}{dt} &= -\tilde{\gamma} \rho_{eg} + \frac{i\Omega}{2} (\rho_{gg} - \rho_{ee})
\end{aligned} \tag{1.20}$$

where $\tilde{\gamma} = \gamma - i\Delta$. The real part of $\tilde{\gamma}$ is the dephasing rate of the atomic dipole moment: the coherence ρ_{eg} is naturally damped over time, at a rate γ . This is usually caused by fluctuations or inhomogeneities in the energy splitting between the two levels $|g\rangle$ and $|e\rangle$, due to random fluctuations of the external electromagnetic fields or to Rb-Rb collisions. Generally, one only takes into account collision-induced decoherence by adding a collision dephasing decay rate γ_{col} to γ so that $\gamma = \Gamma/2 + \gamma_{\text{col}}$. In equation (1.20), ρ_{gg} and ρ_{ee} represent the population of atoms in the ground and in the excited state respectively. The total atomic population is conserved and thus $\rho_{gg} + \rho_{ee} = 1$. One equation among (1.20) is not required to solve the system, which can be rewritten as follows:

$$\dot{\rho}_{ee} - \dot{\rho}_{gg} = -\Gamma (\rho_{ee} - \rho_{gg} + 1) - i (\Omega^* \rho_{eg} - \Omega \rho_{ge}) \tag{1.21}$$

$$\dot{\rho}_{eg} = -\tilde{\gamma} \rho_{eg} + \frac{i\Omega}{2} (\rho_{gg} - \rho_{ee}) \tag{1.22}$$

ii Steady-state solution

The steady-state solution of the optical Bloch equations is obtained by setting the time derivatives to zero in (1.21) and (1.22). One can then derive two time-independent coupled equations which are solved algebraically as follows:

$$\rho_{ee} - \rho_{gg} = -\frac{\gamma^2 + \Delta^2}{\Delta^2 + \gamma^2 + \gamma\Omega^2/\Gamma} \tag{1.23}$$

$$\rho_{eg} = -\frac{\Omega}{2} \frac{\Delta - i\gamma}{\Delta^2 + \gamma^2 + \gamma\Omega^2/\Gamma} \tag{1.24}$$

1.2.3 Atomic polarization and susceptibility

The dielectric response of the atomic ensemble to the laser field excitation is described by the atomic polarization $\mathbf{P}(t)$ (*ie* the dipole moment per unit volume). The applied electric field intuitively shifts electron cloud and atomic nucleus in opposite directions and thus polarizes the atom along the laser field polarisation vector $\boldsymbol{\xi}$. The atomic polarization $\mathbf{P}(t)$ is related to the excitation field $\mathbf{E}(t)$ through the following formula:

$$\mathbf{P}(t) = \epsilon_0 \chi [\mathcal{E}_0] \mathbf{E}(t), \tag{1.25}$$

where $\chi [\mathcal{E}_0]$ defines the atomic susceptibility (or the atomic polarizability), which basically measures the ability of an atom to be polarized under the excitation field $\mathbf{E}(t)$.

The atomic polarization can also be derived as function of the off-diagonal element ρ_{eg} of the density matrix $\hat{\rho}$ (*ie*, the coherence between ground and excited states) as follows [32]: $P(t) = 2N\mu_{ge} \rho_{eg}$, where N is the atomic density. By identifying the foregoing expression with equation (1.25), one finally finds that:

$$\chi = \frac{2N}{\epsilon_0 \mathcal{E}_0} \mu_{ge} \rho_{eg} = \frac{\alpha_0(0)}{\omega_{eg}/c} \frac{i - \Delta/\gamma}{1 + \left(\frac{\Delta}{\gamma}\right)^2 + \left(\frac{\mathcal{E}_0}{\mathcal{E}_s}\right)^2}. \quad (1.26)$$

The linear line-center absorption coefficient:

$$\alpha_0(0) = \frac{\omega_{eg}}{c} \frac{N}{\epsilon_0 \hbar} \frac{|\mu_{ge}|^2}{\gamma_{eg}}, \quad (1.27)$$

defines the absorption coefficient experienced by a weak enough (non-saturating) laser field propagating at resonance inside the atomic vapor. The line-center saturation field strength $\mathcal{E}_s = \hbar\sqrt{\gamma}\Gamma/\mu_{eg}$ is the value at which an on-resonance laser field makes the on-resonance absorption coefficient $\alpha_0(0)$ drop to half of its weak-field value (1.27).

The real and imaginary parts of the atomic polarizability χ show a standard dispersive and Lorentzian lineshape, which is not surprising as they respectively give information about the medium refractive index and absorption coefficient. They have been plotted in blue for different values of $\Omega = \mathcal{E}_0 \mu_{ge}/\hbar$ in figures 1.4(a) and (b). As you may have seen, both lines get broader when the Rabi frequency Ω rises up. This effect is known as power broadening. We can also notice, from (1.26) and from figures 1.4(b), that the line center value of $\text{Im}[\chi]$ – and consequently, of the absorption coefficient $\alpha = \frac{\omega_{eg}}{c} \text{Im}[\chi]$ – decreases with respect to its weak-field value as soon as Ω increases. This tendency of absorption to decrease when intense optical fields are applied is known as saturation.

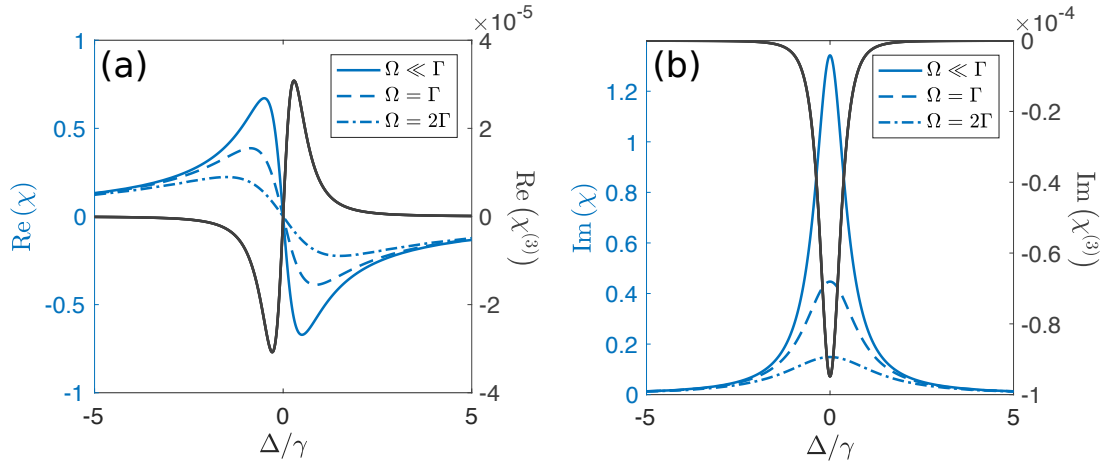


Figure 1.4: Real (a) and imaginary parts (b) of the total (solid, dashed and dotted blue) and third-order (solid black) dielectric susceptibilities. The total susceptibility has been plotted for different Rabi frequencies Ω . Effects of power broadening and saturation on the lineshapes are clearly visible in (a) and (b). The signs of χ and $\chi^{(3)}$ are opposite since the latter represents a saturation of the optical response. Plots obtained for the D_1 line of rubidium 87. Parameters: $T = 400$ K and $N = 2.5 \cdot 10^{13}$ atoms/cm³.

i First- and third-order susceptibilities

As long as $|\mathcal{E}_0/\mathcal{E}_s|^2 \ll 1 + (\Delta/\gamma)^2$, a power series expansion in $\mathcal{E}_0/\mathcal{E}_s$ of equation (1.26) can be performed. By retaining only the zeroth and second order terms:

$$\chi \simeq \frac{\alpha_0(0)}{\omega_{eg}/c} \frac{i - \Delta/\gamma}{1 + (\Delta/\gamma)^2} \left(1 - \left| \frac{\mathcal{E}_0}{\mathcal{E}_s} \right|^2 \frac{1}{1 + (\Delta/\gamma)^2} \right). \quad (1.28)$$

We finally equate the foregoing expression with the standard power series expansion: $\chi = \chi^{(1)} + \frac{3}{4}\chi^{(3)}|\mathcal{E}_0|^2$ in order to obtain analytical expressions for the first- and third-order dielectric susceptibilities as follow:

$$\chi^{(1)} = \frac{\alpha_0(0)}{\omega_{eg}/c} \frac{i - \Delta/\gamma}{1 + (\Delta/\gamma)^2} \quad (1.29)$$

$$\chi^{(3)} = -\frac{4}{3} \frac{1}{|\mathcal{E}_s|^2} \frac{\alpha_0(0)}{\omega_{eg}/c} \frac{i - \Delta/\gamma}{[1 + (\Delta/\gamma)^2]^2} \quad (1.30)$$

The frequency dependence of the real and imaginary parts of $\chi^{(3)}$ is illustrated in figure 1.4 (black lines). The signs of χ and $\chi^{(3)}$ are opposite since $\chi^{(3)}$ represents a saturation of the vapor optical response. The real part of the third-order susceptibility plays a crucial role in photon fluid experiments because it controls the strength of the nonlinear interaction between photons, as we will see later on, in the third chapter. Moreover, the sign of $\text{Re}[\chi^{(3)}]$ defines if this interaction is attractive or repulsive. As we can see in 1.4(a), it changes sign with the laser detuning, going from negative ($\Delta < 0$) to positive values ($\Delta > 0$). By tuning the laser frequency, we are thus able to control the nature and the strength of the nonlinear photon-photon interaction easily. In practice, we always red-detuned the laser frequency from resonance however, in order to generate repulsive interaction between photons.

ii Intensity dependent refractive index: Kerr effect

The dielectric susceptibility χ is related to the dielectric permittivity ϵ_r by:

$$\epsilon_r = \sqrt{1 + \chi} \simeq \sqrt{1 + \text{Re}(\chi)} + \frac{i}{2} \frac{\text{Im}(\chi)}{\sqrt{1 + \text{Re}(\chi)}}. \quad (1.31)$$

The expansion on the right-hand side is valid as long as the condition $|\chi| \ll 1$ is fulfilled. The real part of ϵ_r defines the medium refractive index: $n = \sqrt{1 + \text{Re}(\chi)}$. The absorption coefficient is obtained by multiplying the imaginary part of ϵ_r by the laser wave-vector k_0 in vacuum such that: $\alpha = k \text{Im}(\chi)$ ($k = k_0/n$ is the laser wave-vector inside the medium). In nonlinear optics, the total refractive index is commonly expressed as function of the linear and nonlinear refractive indices n_0 and n_2 (using the fact that $\text{Re}[\chi^{(3)}] \ll \text{Re}[\chi^{(1)}]$):

$$n = \underbrace{\sqrt{1 + \text{Re}(\chi^{(1)})}}_{n_0} + \underbrace{\frac{3}{8} \text{Re}(\chi^{(3)}) |\mathcal{E}_0|^2}_{n_2 I} = n_0 + n_2 \mathcal{I}_0, \quad (1.32)$$

where $\mathcal{I}_0 = \frac{1}{2} \epsilon_0 n_0 c |\mathcal{E}_0|^2$ and consequently $n_2 = \frac{3}{4} \frac{\text{Re}(\chi^{(3)})}{\epsilon_0 n_0 c}$.

The Rubidium vapor behaves as a **third-order Kerr medium** under near-resonance laser excitation since the medium refractive index is intensity dependent. When an intense laser beam propagates in such a medium, it induces a refractive index variation which is larger at its center than at its periphery and accumulates therefore along its propagation a radially dependent nonlinear phase. This self-induced phase modulation acts on the beam as a lens would do, either by focusing (attractive interactions) or spreading (repulsive interactions) the light within the material (depending on the sign of n_2). By measuring this nonlinear phase shift as function of intensity, we can thus access the nonlinear refractive index n_2 , or equivalently, the third-order susceptibility $\chi^{(3)}$ (see section 2.3).

iii Absorption versus non-linearity: how to optimize ?

Depending on what is the intended purpose of his experiment, one should optimize either the nonlinear refractive index n_2 or the nonlinear change of refractive index $\Delta n = n_2 \mathcal{I}$. At the single photon level, observing nonlinear effects requires for instance to optimize the value of n_2 in the limit $\mathcal{I} \ll \mathcal{I}_{\text{sat}}$ (\mathcal{I}_{sat} is the saturation intensity). Reversely, in fluid of light experiments, a macroscopic number of photons is involved. In that case, we can either act on the strength of the nonlinear interaction (namely, on n_2) or on the laser intensity \mathcal{I} to scale up nonlinear effects. We also have to make sure that the condition $\mathcal{I}/\mathcal{I}_{\text{sat}} \ll 1 + (\Delta/\gamma)^2$ is fulfilled in order for the power series expansion (1.55) to be valid.

Experimentally, one might think that the best configuration is to set the laser frequency close to resonance where the nonlinear refractive index n_2 varies significantly. Nevertheless, absorption increases when the laser detuning goes to zero, which results in a reduction of the average field intensity inside the vapor cell, and thus, of the nonlinear change of refractive index Δn . In practice, we allow a minimum transmission of 70% and search for the largest value of n_2 (in absolute value) at this fixed transmission threshold. When $\gamma \ll \Delta$, equations (1.29) and (1.30) yield respectively:

$$\text{Im} [\chi^{(1)}] = \frac{\alpha_0(0)}{\omega_{eg}/c} \left(\frac{\gamma}{\Delta} \right)^2 \propto \frac{N(T)}{\Delta^2} \quad (1.33)$$

$$\text{Re} [\chi^{(3)}] = \frac{1}{|\mathcal{E}_s|^2} \frac{4}{3} \frac{\alpha_0(0)}{\omega_{eg}/c} \left(\frac{\gamma}{\Delta} \right)^3 \propto \frac{N(T)}{\Delta^3} \quad (1.34)$$

where $N(T)$ is the atomic density of the rubidium vapor at the temperature T . If we neglect the nonlinear absorption (scaling as $1/\Delta^4$), the fixed transmission condition requires $\text{Im}[\chi^{(1)}]$ and thus the ratio $N(T)/\Delta^2$ to be constant whatever the detuning; $\chi^{(3)}$ is then proportional to $1/\Delta$ times this constant quantity. In order to maximize the nonlinear refractive index at a given transmission, we should therefore reduce the laser detuning, which consequently leads to lower the vapor temperature (and thus the atomic density N) in order to keep the ratio $N(T)/\Delta^2$ constant. This procedure is obviously limited by our initial assumption, as the detuning should remain much larger than both the excited state hyperfine splitting δ_{HF} and the Doppler broadening $\Delta\omega_D$.

1.3 Open three-level atomic system

The two-level model developed in the previous section provides a good description of each rubidium D -line. In this model, the ground state $|g\rangle$ is defined by the upper hyperfine state of the level $5^2S_{1/2}$ while the excited state $|e\rangle$ is defined by the fine level $5^2P_{1/2}$ (resp. $5^2P_{3/2}$) of the D_1 line (resp. of the D_2 line). As mentioned previously, the two-level description is valid as long as the laser detuning $\Delta = \omega - \omega_{eg}$ satisfies the following conditions: $\Delta < 0$ and $\delta_0 > |\Delta| \gg \delta_{\text{HF}}$, where δ_0 and δ_{HF} are – let us recall it – the hyperfine ground and excited state splitting. Nevertheless, there is nothing preventing the fine states $5^2P_{1/2}$ and $5^2P_{3/2}$ from decaying toward the lower hyperfine state of $5^2S_{1/2}$. In reality, the excited state $|e\rangle$ of the two-level description is therefore coupled to both the upper and lower hyperfine states of $5^2S_{1/2}$. As the laser detuning needs to be negative, we mostly couple the upper hyperfine ground state to the excited state and thus pump preferentially the atom in the lower hyperfine ground state. This population transfer between ground states, known as optical pumping, is not taken into account in the two-level description but will definitively affect the optical response of the atomic vapor. We have therefore to extend the previous description to a 3-level model in which both hyperfine ground states are involved.

1.3.1 Extension to three levels

The 3-level atomic system describing more precisely the rubidium D -lines has been sketched on figures 1.5 (a) and (b). The ground states $|1\rangle$ and $|2\rangle$ stand respectively for the lower and upper hyperfine levels of $5^2S_{1/2}$. The laser detuning Δ is defined with respect to the $|2\rangle \rightarrow |3\rangle$ transition: $\Delta = \omega - \omega_{32}$. If the laser detuning is much larger than the hyperfine excited states splitting δ_{HF} and the Doppler width $\Delta\omega_D$, we can safely forget about the hyperfine structure of the excited levels $5^2P_{1/2}$ and hyperfine transitions allowed by the selection rules between $|2\rangle$ and $|3\rangle$ is addressed by the laser field because of the large laser detuning and Doppler broadening. As in the two level description, the state $|3\rangle$ in the 3-level model is thus a meta excited state hiding the hyperfine complexity of $5^2P_{1/2}$ and $5^2P_{3/2}$.

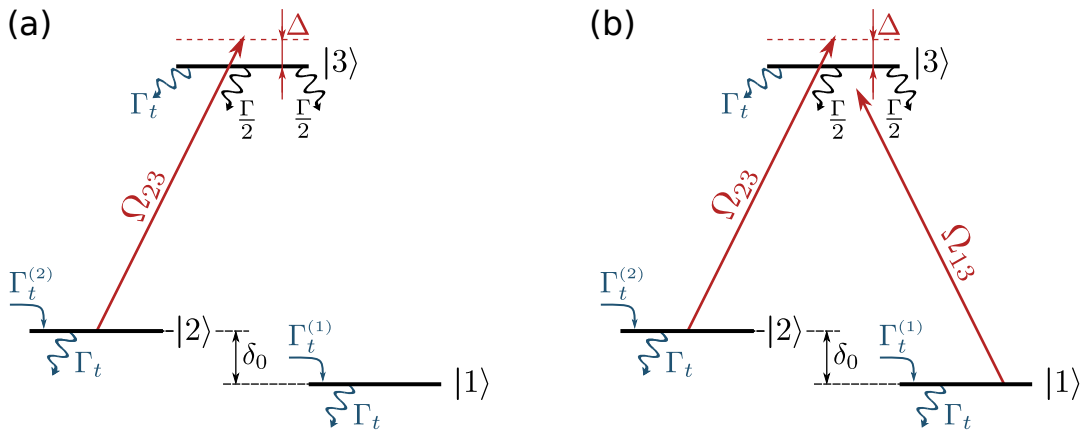


Figure 1.5: Three-level system with one (a) and two (b) coupling beam(s).

In figure 1.5, two different situations are depicted:

- (a) We assume the laser field couples mainly the states $|2\rangle$ and $|3\rangle$. As for the two-level description, this assumption is correct if the laser detuning Δ is negative and fulfills (as usual now) the condition $\delta_0 > |\Delta| \gg \delta_{\text{HF}}$.
- (b) In that case, the laser field couples at the same time the ground states $|1\rangle$ and $|2\rangle$ to the excited state $|3\rangle$. This description is more general because it allows to compute the vapor optical response at every detuning (as long as $|\Delta|$ remains large compared to δ_{HF} and Γ_D), by adding the susceptibilities arising from the coherences between levels $|1\rangle$ and $|3\rangle$ on one hand, levels $|2\rangle$ and $|3\rangle$ on the other. This kind of lambda system is widely used to model strong resonant-driving effects, such as the Electromagnetically Induced Transparency (EIT) [39] or the Autler-Townes splitting [40].

I first focus on the situation sketched in figure 1.5(a), for which the optical Bloch equations in the steady-state are analytically and easily solvable.

1.3.2 Transit and influx rates

If spontaneous emission is the only decay process entering the model, it is not difficult to see that after a sufficiently long amount of time, all the atoms interacting with the laser field are pumped into the uncoupled ground state $|1\rangle$. In the steady-state, the coherence between levels $|2\rangle$ and $|3\rangle$ (and thus the dielectric polarizability χ) vanishes in that case. In order to resolve this issue, we must take into account the finite spatial extension of the laser beam as well as the time of flight of an atom across the beam transverse section.

In hot vapors, atoms are moving and therefore travel across the laser beam during a finite amount of time, which depends on their position \mathbf{r}_0 and velocity \mathbf{v} when they get inside it. They are thus constantly entering and leaving the interaction area, defined by the beam cross-section, at the transit rate Γ_t . Everything happens as if the 3-level system sketched in figure 1.5 was connected to an external atomic reservoir with which it exchanges atoms. This is basically why this model is referred to as "**open 3-level system**".

In any case, whether or not the atomic system is closed, the total population should be conserved *ie* $\sum_i \rho_{ii} = 1$. In other words, the rate at which levels are filled should be equal to the rate at which atoms return to the reservoir. We assume the atoms entering the beam are either in state $|1\rangle$ or in state $|2\rangle$. The filling rates $\Gamma_t^{(1)}$ and $\Gamma_t^{(2)}$ of $|1\rangle$ and $|2\rangle$ are likely to be unbalanced but must, in any event, fulfill the condition: $\Gamma_t^{(1)} + \Gamma_t^{(2)} = \Gamma_t$.

- If we consider that atoms enter the beam only once, they must be initially prepared in a statistical mixture of the states $|1\rangle$ and $|2\rangle$, described by the Boltzmann statistics. At $T = 400$ K, the ground states should be equally populated in average over the atomic ensemble, since the thermal energy (in \hbar units) $k_B T / \hbar \simeq 2\pi \times 50$ THz is much larger than δ_0 . However, both ground states are Zeeman degenerated as no magnetic field is applied. Let $g_i = 2F_i + 1$ be the degeneracy factor of state $|i\rangle$, F_i being the magnitude of the total atomic angular momentum in $|i\rangle$ ($i = 1$ or 2). As F_2 is always bigger than F_1 (for example, $F_1 = 2$ and $F_2 = 3$ in ^{85}Rb), atoms are more likely to enter the beam in state $|2\rangle$. The filling rates are therefore unbalanced and read:

$$\Gamma_t^{(i)} = \frac{g_i}{g_1 + g_2} \Gamma_t = G_i \Gamma_t. \quad (1.35)$$

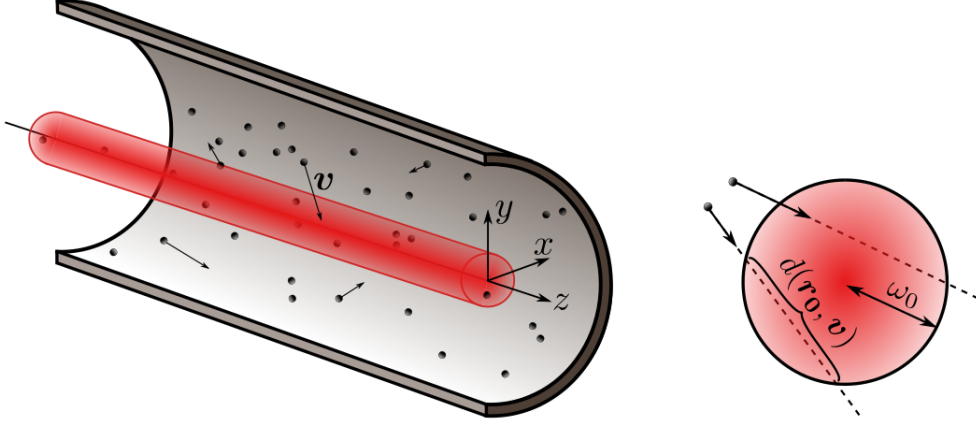


Figure 1.6: Left: sketch of the beam propagation inside the vapor cell. Right: beam cross-section at a given position z on the optical axis. The time an atom takes to flight across the laser beam depends on its position \mathbf{r}_0 and velocity \mathbf{v} when it enters the interaction region.

- We can refine this model by considering the fraction β of atoms that return inside the beam before losing the internal state they have been prepared in before [41,42]. In our collision-free model, atoms eventually interact with the cell walls and may return to the interaction area in the same internal state. Paraffin-coating of the cell walls may additionally conserve the atomic coherences and polarization, since the atom/wall collisions are not phase-interrupting anymore in that case [43]. The laser pumps atoms from state $|2\rangle$ to state $|1\rangle$; the ground state population diffusing outside the beam is therefore likely to be unbalanced. The influx rates are not constant anymore then but depend dynamically on the populations ρ_{11} , ρ_{22} and ρ_{33} :

$$\Gamma_t^{(1)} = \left[(1 - \beta) G_1 + \beta \left(\rho_{11} + \frac{\rho_{33}}{2} \right) \right] \Gamma_t, \quad (1.36)$$

$$\Gamma_t^{(2)} = \left[(1 - \beta) G_2 + \beta \left(\rho_{22} + \frac{\rho_{33}}{2} \right) \right] \Gamma_t. \quad (1.37)$$

The relation $\Gamma_t^{(1)} + \Gamma_t^{(2)} = \Gamma_t$ ensures that the overall atomic population is conserved, as expected. In the stationary-state, equations (1.36) and (1.37) can be understood as follows. When $\beta = 0$, all the atoms have lost the memory of the state they have been prepared in before returning inside the beam; (1.36) and (1.37) reduce to (1.35) in that case. If $\beta = 1$ reversely, the fraction of atoms entering in $|1\rangle$ and $|2\rangle$ is given by the population diffusing outside the beam in those states plus half the population diffusing outside it in the excited state (atoms leaving the beam in $|3\rangle$ will eventually decay toward $|1\rangle$ or $|2\rangle$ with equal probability before getting inside the beam again). The weighting factor β can be computed in practice by solving the diffusion equation that describes the atomic motion outside the beam, assuming a random distribution of the time spent by the atoms outside the interaction region [44].

The influx rates defined in (1.36) and (1.37) will be used when the optical Bloch equations for this open 3-level system are solved numerically. For the sake of simplicity, I will keep considering that $\Gamma_t^{(1)}$ and $\Gamma_t^{(2)}$ are given by equation (1.35) in the calculations below.

Let's now define a bit more precisely the transit rate Γ_t . An atom moving toward the beam along a certain direction will travel a different distance to get across the interaction area depending on the position \mathbf{r}_0 at which it enters. The mean distance \bar{d} is found by averaging all possible paths through the black circle representing the laser cross section in 1.6 [34]:

$$\bar{d} = \frac{2}{\omega_0} \int_{-\frac{\omega_0}{2}}^{\frac{\omega_0}{2}} \sqrt{\omega_0^2 - x^2} dx = \frac{\pi}{4} \omega_0, \quad (1.38)$$

where w_0 stands for the beam width at $1/e^2$. Of course, \bar{d} does not depend on the direction along which the atoms move. The transit rate is finally obtained by averaging the quantity v_\perp/\bar{d} over the 2D Maxwell-Boltzmann velocity distribution:

$$\mathcal{P}_{2D}(\mathbf{v}_\perp) = \frac{1}{\pi u^2} \exp \left[- \left(\frac{v_\perp}{u} \right)^2 \right], \quad (1.39)$$

($u = \sqrt{2k_B T/m}$ is the most probable atomic speed in the transverse plane) which yields:

$$\Gamma_t = \int \frac{v_\perp}{\bar{d}} \mathcal{P}_{2D}(\mathbf{v}_\perp) d\mathbf{v}_\perp = \frac{2\pi}{\bar{d}} \int_0^\infty v_\perp^2 \mathcal{P}_{2D}(v_\perp) dv_\perp = \frac{2}{\sqrt{\pi}} \frac{u}{\omega_0} \quad (1.40)$$

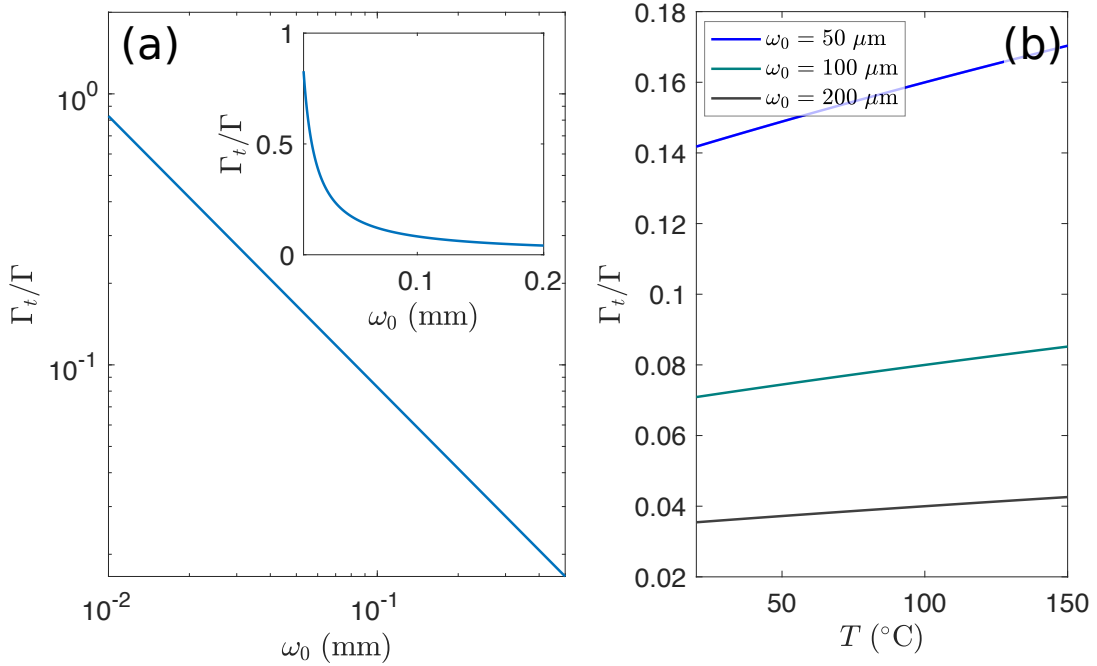


Figure 1.7: (a) Transit rate Γ_t as function of the beam width ($T = 400$ K). The transit rate has been normalized by the radiative decay rate Γ . For small beams ($\omega_0 < 50 \mu\text{m}$), they are of the same order of magnitude. (b) Transit rate as function of the vapor temperature for different beam widths. At room temperature and above, Γ_t only slightly varies with T . Plots obtained for the D_1 line of rubidium 87.

The transit rate Γ_t , normalized by the radiative decay rate Γ , has been plotted as function of the beam width ω_0 and as function of the vapor temperature T on figures 1.7 (a) and (b) respectively. As you may have seen, Γ_t only slightly changes with T at room temperature and above. However, it strongly varies with the width of the laser beam; for $\omega_0 = 25 \mu\text{m}$, Γ_t is almost a third of Γ . When Γ_t and Γ are of the same magnitude, the finite transit time of the atoms across the beam starts making the spectral lines broader. This effect, which is known in the literature as "transit time broadening" [34, 45], can be understood using the Heisenberg's uncertainty principle: $\Delta\tau \Delta\epsilon \simeq 1$. The uncertainty $\Delta\epsilon$ on the energy of an excited state is affected not only by its spontaneous lifetime ($\Delta t \simeq 1/\Gamma$) but also by the transit time ($\Delta t \simeq 1/\Gamma_t$). Thus, a decrease in the transit time will lead to an increase in $\Delta\epsilon$, which will manifest in turn as line broadening. This effect is known to limit the resolution of a variety of spectroscopic applications, such as two-photon [46], and saturated absorption [47] and photon-echo spectroscopy [48].

1.3.3 Optical Bloch equations in the interaction picture

In order to find an expression for the dielectric susceptibility χ of the open 3-level system sketched on figure 1.5, we should go through the same calculation as for the two-level system and derive the optical Bloch equations. I will not reproduce the details of this calculation here but just remind the main steps.

The Hamiltonian \hat{H} of the 3-level system splits into a non-perturbative diagonal part \hat{H}_0 (atomic Hamiltonian), and a perturbative off-diagonal part \hat{W} (atom/field coupling term).

- The atomic counterpart is defined by: $\hat{H}_0 = \sum_{i=1}^3 E_i |i\rangle \langle i|$, where E_i is the energy associated to the i -th level. As energy is defined up to a constant, we choose to set the energy of the lower state to zero (ie $E_1 = 0$). Hence:

$$\begin{aligned} \hat{H}_0 &= \hbar\omega_{21} |2\rangle \langle 2| + \hbar\omega_{31} |3\rangle \langle 3| \\ &= \hbar\delta_0 |2\rangle \langle 2| - \hbar(\Delta - \delta_0) |3\rangle \langle 3| + \underbrace{0 \times |1\rangle \langle 1| + 0 \times |2\rangle \langle 2| + \hbar\omega |3\rangle \langle 3|}_{\hat{H}_0}, \end{aligned} \quad (1.41)$$

Once again, we make explicitly appear the laser detuning $\Delta = \omega - \omega_{32}$ by adding \tilde{H}_0 .

- In the **dipole approximation**, the atom/field interaction Hamiltonian simply reads: $\hat{W} = -\hat{\mathbf{d}} \cdot \mathbf{E}(t)$. Since only the $|2\rangle \rightarrow |3\rangle$ transition is optically addressed in 1.5 (a), the dipole operator can be expressed as follows: $\hat{\mathbf{d}} = \mathbf{d}_{23}^* |3\rangle \langle 2| + \mathbf{d}_{23} |2\rangle \langle 3|$. Therefore, as $\mathbf{E}(t) = \mathcal{E}_0 \cos(\omega t) \boldsymbol{\xi}$ ($\boldsymbol{\xi}$ being the laser polarization vector, as before):

$$\hat{W}_{23}(t) = -\frac{\hbar}{2} \left(\Omega_{23}^* |3\rangle \langle 2| + \Omega_{23} |2\rangle \langle 3| \right) \times \left(e^{i\omega t} + e^{-i\omega t} \right), \quad (1.42)$$

where $\Omega_{23} = \mathcal{E}_0 \mu_{23} / \hbar$ is the Rabi frequency associated to the $|2\rangle \rightarrow |3\rangle$ transition. Let's remind that the dipole moment $\mu_{23} = \langle 2 | \hat{\mathbf{d}} \cdot \boldsymbol{\xi} | 3 \rangle$ is given by: $\mu_{23} = \sum_{F_3} f_{F_2}^{F_3}$. In this formula, F_3 runs over the magnitude of the total atomic angular momentum in all the hyperfine levels of state $|3\rangle$. The coefficient $f_{F_g}^{F_e}$ are defined in (1.6).

Within the **interaction representation** and using the **rotating wave approximation**, the explicit time dependence in (1.42) vanishes. Indeed, if \tilde{U} stands for the interaction picture unitary evolution operator, then:

$$\tilde{U}(t) = \exp \left(-i\tilde{H}_0/\hbar \right) = |1\rangle \langle 1| + |2\rangle \langle 2| + |3\rangle \langle 3| e^{-i\omega t}, \quad (1.43)$$

and the coupling operator in the interaction picture reads:

$$\hat{W}_{23}^I = \tilde{U}^\dagger \hat{W}_{23}(t) \tilde{U} = -\frac{\hbar}{2} \left(\Omega_{23}^* e^{i\omega t} |3\rangle \langle 2| + \Omega_{23} e^{-i\omega t} |2\rangle \langle 3| \right) \times \left(e^{i\omega t} + e^{-i\omega t} \right) \quad (1.44)$$

$$\simeq -\frac{\hbar}{2} \left(\Omega_{23}^* |3\rangle \langle 2| + \Omega_{23} |2\rangle \langle 3| \right). \quad (1.45)$$

The fast oscillating terms at $\pm 2\omega$ in equation (1.44) are neglected as usual using the RWA. The atomic Hamiltonian \hat{H}_0 commutes with $\tilde{U}(t)$; the total Hamiltonian in the interaction picture is thus finally time independent. In this description, the Bloch equation is given by:

$$\frac{d\hat{\rho}_I}{dt} = -\frac{i}{\hbar} [\hat{H}_I, \hat{\rho}_I] + \sum_{\nu \neq 0} \left(\tilde{L}_\nu \hat{\rho}_I \tilde{L}_\nu^\dagger - \frac{1}{2} \{ \tilde{L}_\nu \tilde{L}_\nu^\dagger, \hat{\rho}_I \} \right), \quad (1.46)$$

where $\hat{\rho}_I = \tilde{U}^\dagger \hat{\rho} \tilde{U}$ and $\hat{H}_I = \hbar\delta_0 |2\rangle \langle 2| - \hbar(\Delta - \delta_0) |3\rangle \langle 3| + \hat{W}_{23}^I$. The Lindblad operators \tilde{L}_ν are defined in subsection 1.2.2. A straightforward but tedious calculation leads finally to the following set of Bloch equations for the slowly varying density matrix elements $\rho_{ij}(t)$ (I drop out the I index in the following):

$$\begin{aligned} \frac{d\rho_{11}}{dt} &= -\Gamma_t \rho_{11} + \frac{\Gamma}{2} \rho_{33} + \Gamma_t^{(1)} \\ \frac{d\rho_{22}}{dt} &= -\Gamma_t \rho_{22} + \frac{\Gamma}{2} \rho_{33} + \frac{i}{2} (\Omega_{23}^* \rho_{32} - \Omega_{23} \rho_{23}) + \Gamma_t^{(2)} \\ \frac{d\rho_{33}}{dt} &= -(\Gamma_t + \Gamma) \rho_{33} - \frac{i}{2} (\Omega_{23}^* \rho_{32} - \Omega_{23} \rho_{23}) \\ \frac{d\rho_{32}}{dt} &= -\tilde{\gamma}_{32} \rho_{32} + \frac{i\Omega_{23}}{2} (\rho_{22} - \rho_{33}) \\ \frac{d\rho_{23}}{dt} &= -\tilde{\gamma}_{32}^* \rho_{23} - \frac{i\Omega_{23}^*}{2} (\rho_{22} - \rho_{33}) \end{aligned} \quad (1.47)$$

where $\tilde{\gamma}_{32} = \gamma_{32} - i\Delta$ and $\gamma_{32} = \Gamma/2 + \Gamma_t$. As you can see, the transit rate Γ_t enters now in the optical Bloch equations. Moreover, it appears explicitly in the coherence decay rate γ_{32} , which defines the $|2\rangle \rightarrow |3\rangle$ transition linewidth. The finite transit time of atoms across the laser beam induces therefore a broadening of the transition line, as mentioned before. The Bloch equations (1.47) can be solved together using a 4th-order Runge-Kutta method. The numerical results are shown on figure 1.8 (a) for the D_1 line of ^{87}Rb . The beam width at $1/e^2$ is $\omega_0 = 500 \mu\text{m}$. The laser is 2 GHz red-detuned with respect to the $|2\rangle \rightarrow |3\rangle$ transition and the vapor temperature is set to 415 K. With these values for the parameters, $\Gamma_t/\Gamma \simeq 1.8\%$. The degeneracy weights G_1 and G_2 are respectively equal to $3/8$ and $5/8$; therefore, $\Gamma_t^{(1)}/\Gamma \simeq 0.7\%$ and $\Gamma_t^{(2)}/\Gamma \simeq 1.1\%$. The computation has been performed using the influx rates defined by equation (1.35) ($\beta = 0$). The populations in states $|1\rangle$, $|2\rangle$ and $|3\rangle$ have been plotted in green, purple and black respectively for two different laser power: $\mathcal{P} = 1 \text{ mW}$ ($\Omega/2\pi \simeq 30 \text{ MHz}$, dashed lines) and $\mathcal{P} = 0.5 \text{ W}$ ($\Omega/2\pi \simeq 0.7 \text{ GHz}$, solid lines).

- At low power, the internal state dynamics is controlled by the influx and transit rates exclusively. As $\Gamma_t^{(2)} > \Gamma_t^{(1)}$, ρ_{22} increases at the expense of ρ_{11} . In the steady-state, the proportion of atoms in $|1\rangle$ and $|2\rangle$ is directly given by the unbalanced degeneracy weights G_1 and G_2 . During the transient regime, the population in the excited state is almost zero. The laser power is too weak to populate $|3\rangle$ as well as to pump atoms from state $|2\rangle$ to state $|1\rangle$. The low power situation has been sketched on figure 1.8 (b). Populations in $|1\rangle$ and $|2\rangle$ has been represented by disks of different radii.

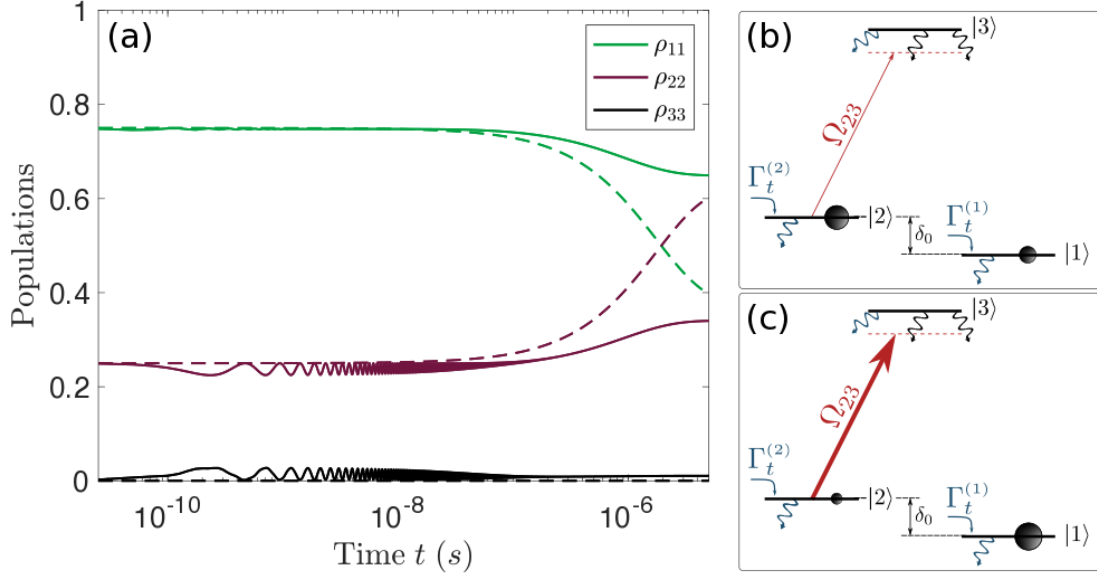


Figure 1.8: (a) Time evolution of the populations in states $|1\rangle$, $|2\rangle$ and $|3\rangle$ for two different laser powers: $\mathcal{P} = 1$ mW (dotted lines) and $\mathcal{P} = 500$ mW (solid lines). At low laser power, this evolution is mainly driven by the filling and transit rates. As $\Gamma_t^{(2)} > \Gamma_t^{(1)}$, ρ_{22} increases while ρ_{11} decreases. In the stationary-state, $\rho_{11}^{\text{eq}} = G_1$ and $\rho_{22}^{\text{eq}} = G_2$. At high laser power, optical pumping from state $|2\rangle$ to state $|1\rangle$ overcomes this filling unbalance. Rabi flopping between states $|2\rangle$ to $|3\rangle$ makes the populations ρ_{22} and ρ_{33} oscillate over time in that case. Both situations are depicted on figures (b) and (c). Parameters in the text.

- At high power, the internal state dynamics is controlled by the laser field and by the influx and transit rates simultaneously. The laser field strongly drives the $|2\rangle \rightarrow |3\rangle$ transition even if the frequency is far red-detuned from resonance. As you can see, Rabi oscillations appear between the populations of states $|2\rangle$ and $|3\rangle$. In the steady-state, even if $\Gamma_t^{(2)} > \Gamma_t^{(1)}$, ρ_{11} remains larger than ρ_{22} . Optical pumping from $|2\rangle$ to $|1\rangle$ overcomes the filling rates unbalance. Nevertheless, $\Gamma_t^{(2)}$ and $\Gamma_t^{(1)}$, together with the transit rate Γ_t , are still playing a crucial role. If the time of flight of atoms across the laser beam was infinite, all the atoms would be pumped in $|1\rangle$ in the stationary-state. The coherence between levels $|2\rangle$ and $|3\rangle$ (and thus the susceptibility), which depends on the population difference $\rho_{33} - \rho_{22}$ (see equation (1.24)), would then drop to zero. The filling and transit rates are thus essential in order for this model to describe experimental observations. The high power case is sketched on 1.8 (c).

1.3.4 Steady-state solution of the Optical-Bloch equations

Looking at figure 1.8, we can observe that the 3-level system quickly converges toward a steady-state in which populations as well as coherences do not evolve over time anymore. By setting the time derivatives to zero in (1.47) and by using the conservation of the total atomic population ($\sum_i \rho_{ii} = 1$), one can recast the Bloch equations into the matrix form:

$$\underbrace{\begin{pmatrix} \Gamma_t + \frac{\Gamma}{2} & \frac{\Gamma}{2} & 0 & 0 \\ \frac{\Gamma}{2} & \Gamma_t + \frac{\Gamma}{2} & -\frac{i\Omega^*}{2} & \frac{i\Omega}{2} \\ \frac{i\Omega}{2} & i\Omega & -\tilde{\gamma} & 0 \\ -\frac{i\Omega^*}{2} & i\Omega^* & 0 & -\tilde{\gamma}^* \end{pmatrix}}_M \underbrace{\begin{pmatrix} \rho_{11} \\ \rho_{22} \\ \rho_{32} \\ \rho_{23} \end{pmatrix}}_\rho = \underbrace{\begin{pmatrix} -\frac{\Gamma}{2} - G_1 \Gamma_t \\ -\frac{\Gamma}{2} - G_2 \Gamma_t \\ \frac{i\Omega}{2} \\ -\frac{i\Omega^*}{2} \end{pmatrix}}_X. \quad (1.48)$$

For the sake of simplicity, we define $\tilde{\gamma} = \tilde{\gamma}_{32}$ and $\Omega = \Omega_{32}$. The steady-state is obtained by inverting equation (1.48) as follows: $\rho_{\text{eq}} = M^{-1} \cdot X$, which yields the following results:

$$\rho_{11}^{\text{eq}} = \frac{G_1}{\mathcal{F}(\Delta, \Omega)} \left[1 + \left(\frac{\Delta}{\gamma} \right)^2 + \frac{1+b}{2b(1+a)} \left(\frac{\Omega}{\gamma} \right)^2 + \frac{G_2}{G_1} \frac{1-b}{2b(1+a)} \left(\frac{\Omega}{\gamma} \right)^2 \right] \quad (1.49)$$

$$\rho_{22}^{\text{eq}} = \frac{G_2}{\mathcal{F}(\Delta, \Omega)} \left[1 + \left(\frac{\Delta}{\gamma} \right)^2 + \frac{b}{2b(1+a)} \left(\frac{\Omega}{\gamma} \right)^2 \right] \quad (1.50)$$

$$\rho_{32}^{\text{eq}} = \frac{G_2}{2} \left(\frac{\Omega}{\gamma} \right) \frac{i - \Delta/\gamma}{\mathcal{F}(\Delta, \Omega)} \quad (1.51)$$

The coefficients a and b basically measure the contribution of the natural and transit time broadening in the linewidth γ : $a = \Gamma/(2\gamma)$ and $b = \Gamma_t/\gamma$. The function \mathcal{F} is defined by:

$$\mathcal{F}(\Delta, \Omega) = 1 + \left(\frac{\Delta}{\gamma} \right)^2 + \frac{1+b}{2b(1+a)} \left(\frac{\Omega}{\gamma} \right)^2. \quad (1.52)$$

1.3.5 Dielectric susceptibility χ for the 3-level system

In the steady-state, the dielectric susceptibility χ of the 3-level system is related to the coherence ρ_{32}^{eq} between the states $|2\rangle$ and $|3\rangle$ (see equation (1.26)):

$$\chi = \frac{2N}{\epsilon_0 \mathcal{E}_0} \mu_{23} \rho_{32}^{\text{eq}} = \frac{\alpha_0(0)}{\omega_{32}/c} \frac{i - \Delta/\gamma}{1 + \left(\frac{\Delta}{\gamma} \right)^2 + \left(\frac{\mathcal{E}_0}{\mathcal{E}_s} \right)^2}. \quad (1.53)$$

As for the two-level system, we define the linear line-center absorption coefficient $\alpha_0(0)$ (that is, the linear absorption coefficient at resonance) by:

$$\alpha_0(0) = G_2 \frac{\omega_{32}}{c} \frac{N}{\epsilon_0 \hbar} \frac{|\mu_{23}|^2}{\gamma}, \quad (1.54)$$

as well as the line-center saturation field strength $\mathcal{E}_s = \sqrt{\frac{2b(1+a)}{1+b}} \hbar \gamma / \mu_{23}$. Equation (1.53) is identical in all respects to equation (1.26). This is an important result as it demonstrates that the optical response of an open 3-level system under a red-detuned laser excitation is comparable to the response of a two-level system. However, as mentioned several times already, the linewidth $\gamma = \Gamma/2 + \Gamma_t$ is broadened by the finite transit time of atoms across the beam in the open 3-level description. This effect is not describe by the over simplistic 2-level model. Moreover, the on-resonance saturation field strength \mathcal{E}_s also depends on the transit rate Γ_t in the present case. The optical response of the rubidium vapor is thus likely to change with the dimensions of the coupling beam.

1.3.6 Linear and non-linear response

In order to derive an expression for the third-order dielectric polarizability, we should first expand equation (1.53) as a power series in $\mathcal{E}_0/\mathcal{E}_s$. This expansion is correct as long as $|\mathcal{E}_0/\mathcal{E}_s|^2 \ll 1 + (\Delta/\gamma)^2$ and read (at the second-order) as follows:

$$\chi \simeq \frac{\alpha_0(0)}{\omega_{32}/c} \frac{i - \Delta/\gamma}{1 + (\Delta/\gamma)^2} \left(1 - \left| \frac{\mathcal{E}_0}{\mathcal{E}_s} \right|^2 \frac{1}{1 + (\Delta/\gamma)^2} \right). \quad (1.55)$$

We now equate the foregoing expression with the usual expansion: $\chi = \chi^{(1)} + \frac{3}{4}\chi^{(3)}|\mathcal{E}_0|^2$ in order to obtain the first- and third-order dielectric susceptibilities :

$$\chi^{(1)} = \frac{\alpha_0(0)}{\omega_{32}/c} \frac{i - \Delta/\gamma}{1 + (\Delta/\gamma)^2}, \quad (1.56)$$

$$\chi^{(3)} = - \frac{1}{|\mathcal{E}_s|^2} \frac{4}{3} \frac{\alpha_0(0)}{\omega_{32}/c} \frac{i - \Delta/\gamma}{[1 + (\Delta/\gamma)^2]^2}. \quad (1.57)$$

Real and imaginary parts of the total (blue solid, dashed and dotted lines) and third-order dielectric polarizabilities (black solid lines) have been plotted on figures 1.9 (a) and (b). As in the two-level case, power broadening and saturation strongly affect the line shape of the total susceptibility at resonance. As expected, the signs of χ and $\chi^{(3)}$ are opposite.

The expansion (1.55) makes sense only if the condition $|\mathcal{E}_0/\mathcal{E}_s|^2 \ll 1 + (\Delta/\gamma_{32})^2$ is fulfilled. In experiments, the laser is typically 3 GHz red-detuned with respect to the resonance. For a beam width of 500 μm , the transit rate is $2\pi \times 91$ kHz ($\Gamma_t/\gamma \simeq 3\%$) at $T = 415$ K. If we address the D_2 line of a isotopically pure ^{87}Rb vapor for example, $\Gamma = 2\pi \times 6.07$ MHz and therefore, $\gamma \simeq 2\pi \times 3.13$ MHz. The dipole moment of the $|2\rangle \rightarrow |3\rangle$ transition is given in that case by: $\mu_{23} = \sum_{F_e} f_{F_g}^{F_e} = \sqrt{1/18 + 5/18 + 7/9} \times \frac{d}{\sqrt{g_2}} \simeq 2.44 \times e a_0$ (see formula (1.6) and the table of figure 1.2). The saturation intensity $\mathcal{I}_s = \frac{1}{2} \epsilon_0 c |\mathcal{E}_s|^2$ is then of 1.5 W/m². With the foregoing values for the parameters, we find an off-resonance saturation intensity $\mathcal{I}_s(\Delta) = \mathcal{I}_s [1 + (\Delta/\gamma)^2]$ around 1.6×10^6 W/m². This value basically sets an upper limit on the laser intensity beyond which the expansion (1.55) starts to be invalid. It is worth mentioning that this result strongly depends on the beam width obviously. Working with smaller beams will indeed increase the off-resonance saturation intensity $\mathcal{I}_s(\Delta)$. It will first increase the line-center saturation intensity, scaling as $\Gamma_t^4 \propto 1/\omega_0^4$ when ω_0 goes to zero. This effect is easily understandable. When the width decreases, the rate at which fresh atoms enter the beam rises up accordingly. In other words, the average time of flight of atoms across the beam becomes shorter and shorter. The laser field should then be more intense in order to drive more efficiently the transition line over this shorter atom/field interaction time $1/\Gamma_t$. A second effect appear when decreasing the beam width, as it will also increase the linewidth γ of the $|2\rangle \rightarrow |3\rangle$ transition. The atomic ensemble will thus get more resonant with the laser excitation at fixed detuning, leading to a reduction in $\mathcal{I}_s(\Delta)$. This effect is appreciable when the natural transition linewidth $\Gamma/2$ and the transit rate Γ_t are comparable, that is, when $\omega_0 < 4u/\sqrt{\pi}\Gamma \simeq 4 \mu\text{m}$ at 400 K, which is much smaller than the beam widths we standardly use experimentally. The off-resonance saturation intensity and power $\mathcal{P}_s(\Delta)$ have been plotted on figure 1.9 (c) for different laser detunings.

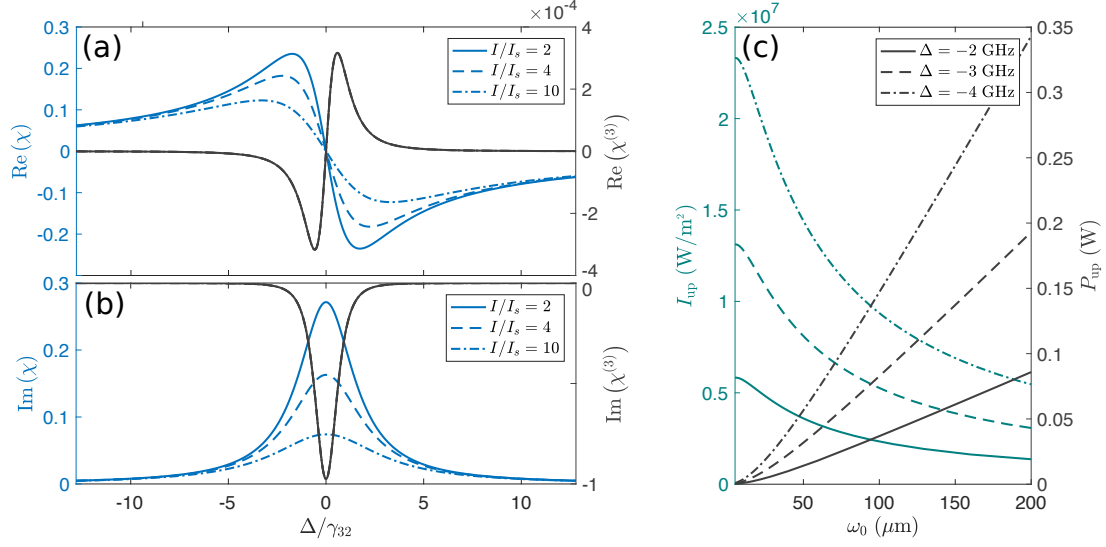


Figure 1.9: Real (a) and imaginary parts (b) of the total (solid, dashed and dotted blue) and third-order (solid black) dielectric susceptibilities. $\text{Re}[\chi]$ and $\text{Im}[\chi]$ are plotted for different values of the saturation parameter I/I_s . Increasing I/I_s makes the line broader, as can be seen on fig.(b) (power broadening), and decreases the absorption (saturation). (c) Off-resonance intensity (cyan) and power (black) as function of the beam width ω_0 for different laser detunings. (a)-(b): $\omega_0 = 500 \mu\text{m}$. (a)-(c): $T = 415 \text{ K}$. Computation made for the D_2 line of an isotopically pure rubidium 87 vapor.

1.3.7 General case: open 3-level system with two coupling fields

So far, the laser field was only driving the $|2\rangle \rightarrow |3\rangle$ transition. Let's now assume it also drives the $|1\rangle \rightarrow |3\rangle$ transition, as sketched on figure 1.5(b). In that case, the steady-state solution of the optical Bloch equations is found by solving the following matrix equation:

$$\begin{pmatrix} -\Gamma_t - \frac{\Gamma}{2} & -\frac{\Gamma}{2} & 0 & 0 & \frac{i\Omega_{13}^*}{2} & -\frac{i\Omega_{13}}{2} & 0 & 0 \\ -\frac{\Gamma}{2} & \Gamma_t + \frac{\Gamma}{2} & 0 & 0 & 0 & 0 & \frac{i\Omega_{23}^*}{2} & -\frac{i\Omega_{23}}{2} \\ 0 & 0 & -\tilde{\gamma}_{21} & 0 & \frac{i\Omega_{23}^*}{2} & 0 & 0 & -\frac{i\Omega_{13}}{2} \\ 0 & 0 & 0 & -\tilde{\gamma}_{21}^* & 0 & -\frac{i\Omega_{23}}{2} & \frac{i\Omega_{13}^*}{2} & 0 \\ i\Omega_{13} & \frac{i\Omega_{13}}{2} & \frac{i\Omega_{23}}{2} & 0 & -\tilde{\gamma}_{31} & 0 & 0 & 0 \\ -i\Omega_{13}^* & -\frac{i\Omega_{13}^*}{2} & 0 & -\frac{i\Omega_{23}^*}{2} & 0 & -\tilde{\gamma}_{31}^* & 0 & 0 \\ \frac{i\Omega_{23}}{2} & i\Omega_{23} & 0 & \frac{i\Omega_{13}}{2} & 0 & 0 & -\tilde{\gamma}_{32} & 0 \\ -\frac{i\Omega_{23}^*}{2} & -i\Omega_{23}^* & -\frac{i\Omega_{13}^*}{2} & 0 & 0 & 0 & 0 & -\tilde{\gamma}_{32}^* \end{pmatrix} \begin{pmatrix} \rho_{11} \\ \rho_{22} \\ \rho_{21} \\ \rho_{12} \\ \rho_{31} \\ \rho_{13} \\ \rho_{32} \\ \rho_{23} \end{pmatrix} = \begin{pmatrix} -\frac{\Gamma}{2} - G_1\Gamma_t \\ -\frac{\Gamma}{2} - G_2\Gamma_t \\ 0 \\ 0 \\ \frac{i\Omega_{13}}{2} \\ -\frac{i\Omega_{13}^*}{2} \\ \frac{i\Omega_{23}}{2} \\ -\frac{i\Omega_{23}^*}{2} \end{pmatrix} \quad (1.58)$$

where $\tilde{\gamma}_{21} = \gamma_{21} + i\delta_0$, $\tilde{\gamma}_{31} = \gamma_{31} - i(\Delta - \delta_0)$ and $\tilde{\gamma}_{32} = \gamma_{32} - i\Delta$. The decoherence rates are defined by: $\gamma_{21} = \Gamma_t$, $\gamma_{31} = \Gamma/2 + \Gamma_t$ and $\gamma_{32} = \Gamma/2 + \Gamma_t$. The linewidths of the $|1\rangle \rightarrow |3\rangle$ and $|2\rangle \rightarrow |3\rangle$ transitions are equal since the probabilities for the excited state to decay toward the upper and lower ground state are the same in our model. This assumption is not perfectly fulfilled because some of the hyperfine transitions between ground and excited states are cycling (the $F_g = 3 \rightarrow F_e = 4$ hyperfine transition in ^{85}Rb for example).

The stationary-state density matrix elements are obtained by inverting equation (1.58). Nevertheless, populations and coherences cannot be easily expressed analytically anymore. We cannot either use density matrix perturbation techniques, as both Rabi frequencies Ω_{13} and Ω_{23} have the same magnitude. They are actually equal in this case, as $\mu_{13} = \mu_{23}$. However, since $\delta_{\text{HF}} \ll \delta_0$, we can think about breaking down this problem into pieces and see the situation sketched in fig. 1.5 (b) as a composition of two open 3-level systems with one coupling field, driving either the $|1\rangle \rightarrow |3\rangle$ or the $|2\rangle \rightarrow |3\rangle$ transition. An approximate steady-state solution can then be found using the set of equations (1.49), (1.50) and (1.51). Within this approximation, the population in state $|1\rangle$ is given for instance by:

$$\rho_{11} \simeq \rho_{11}^{1 \rightarrow 3} + \rho_{11}^{2 \rightarrow 3} - G_1, \quad (1.59)$$

where $\rho_{11}^{i \rightarrow 3}$ stands for the steady-state population of level $|1\rangle$ when the laser only addresses the $|i\rangle \rightarrow |3\rangle$ transition. Therefore, $\rho_{11}^{2 \rightarrow 3}$ is given by equation (1.49) and $\rho_{11}^{1 \rightarrow 3}$ is obtained by (i) interchanging the indices "1" and "2" and (ii) by replacing Δ by $\Delta - \delta_0$ in equation (1.50). The degeneracy weight G_1 should be subtracted in order to take the filling of the ground state $|1\rangle$ into account only once. The steady-state population in $|2\rangle$ can be approximate in a similar way: $\rho_{22} \simeq \rho_{22}^{1 \rightarrow 3} + \rho_{22}^{2 \rightarrow 3} - G_2$. We can also derive an approximate expression for the coherences ρ_{31} and ρ_{32} using (1.51) (after replacing "1" by "2" and Δ by $\Delta - \delta_0$ for ρ_{31}). The ground states coherence ρ_{21} can then simply be expressed as: $\rho_{21} = \frac{i\Omega}{2\gamma_{21}} (\rho_{31} - \rho_{32}^*)$.

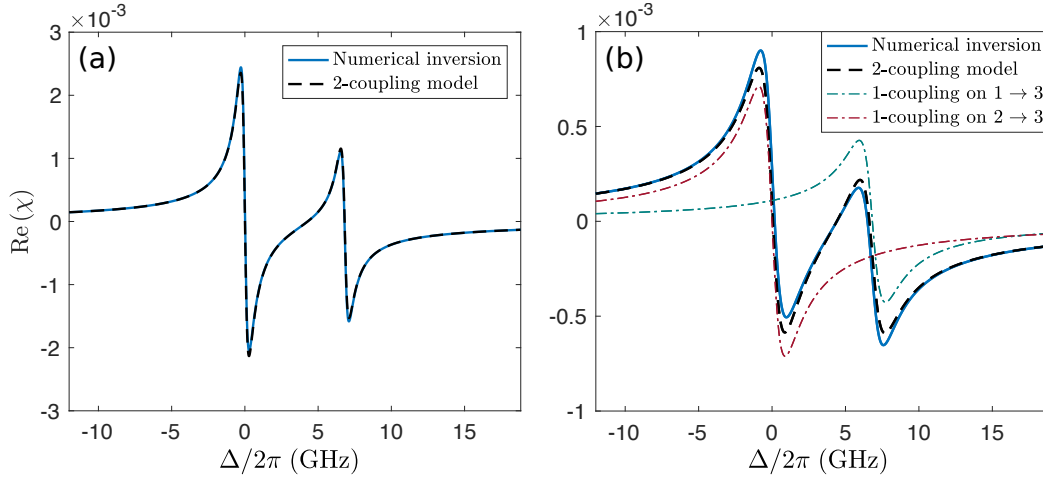


Figure 1.10: Comparison between the total susceptibilities computed from the 2-coupling 3-level model (black dashed line) and the numerical inversion of (1.58) (blue solid line). (a) Low power (10 mW). (b) High power (100 mW). The discrepancy between the black dashed and the blue solid lines starts being visible around $\Delta = 0$ and $\Delta = \delta_0 \simeq 6.8$ GHz. If we consider that the field only addresses the $|2\rangle \rightarrow |3\rangle$ transition, we underestimate the value of $\text{Re}[\chi]$ when the laser is highly red-detuned. The contribution of $|1\rangle \rightarrow |3\rangle$ to $\text{Re}[\chi]$ is about 25% when $\Delta = -2\pi \times 6$ GHz for instance. Parameters in the text.

The real part of the dielectric susceptibility $\text{Re}[\chi]$, obtained either by numerical inversion (blue solid line) or within the approximation above (black dashed lines), has been plotted on figure 1.10 as function of Δ , for $\mathcal{P} = 10$ mW (fig.(a), $\Omega/2\pi \simeq 0.1$ GHz) and $\mathcal{P} = 100$ mW (fig.(b), $\Omega/2\pi \simeq 0.3$ GHz). The laser drives the D_1 line of ^{87}Rb and its width is $500 \mu\text{m}$.

- As long as the coupling field is low enough to safely neglect optical pumping between ground states, the agreement between the numerical inversion of equation (1.58) and the theory is excellent, as can be seen on figure 1.10(a).
- When optical pumping comes into play, the model fails to reproduce exactly the numerical results close to resonances (*ie*, when $\Delta = 0$ and $\Delta = \delta_0 \simeq 2\pi \times 6.8$ GHz). However, for highly red-detuned laser frequencies (typically, when $\Delta/2\pi < -3$ GHz), the model describes perfectly well the vapor optical response. As you may have seen, the contribution of the $|1\rangle \rightarrow |3\rangle$ transition line on the red-detuned optical response (cyan dashed line) is not negligible; the relative error made on $\text{Re}[\chi]$ by considering only one coupling field when $\Delta/2\pi = -6$ GHz is almost 25% for instance.

The two coupling fields model is thus able to correctly predict the dielectric susceptibility at those detunings even for strong driving, which is not the case of the one coupling field and the simplistic two-level descriptions.

1.3.8 Ballistic transport of atoms

Contrary to what might sometimes be believed, hot alkaline vapors are dilute systems. As long as the temperature of the atomic ensemble does not exceed 150 °C, the atomic motion is mainly ballistic and Rb-Rb collisions can be neglected as a first approximation. This ballistic transport affects the atom internal state because it forces the atom/field interaction to happen on a finite time, as described above. In this section, I will introduce other effects resulting from atomic motion –namely, Doppler broadening and transport-induced nonlocal dielectric response – and describe how these effects impact the line shape.

i Doppler broadening

The atomic motion along the optical axis shifts the laser frequency in the translating frame of a moving atom. This Doppler shift affects the transition linewidth (Doppler broadening) by making fast atoms be resonant with a slightly detuned laser beam. In this subsection, I will generalize equations (1.56) and (1.57) by taking Doppler broadening into account. The calculation mainly follows the derivation made in [32].

Let's first define the line shape factors $f_\gamma^{(1)}$ and $f_\gamma^{(3)}$ as follow:

$$f_\gamma^{(1)} = \frac{1}{\gamma} \frac{i - \Delta/\gamma}{1 + (\Delta/\gamma)^2} \quad \text{and} \quad f_\gamma^{(3)} = \frac{1}{\gamma} \frac{i - \Delta/\gamma}{[1 + (\Delta/\gamma)^2]^2}, \quad (1.60)$$

where $\gamma = \gamma_{31} = \gamma_{32} = \Gamma/2 + \Gamma_t$. The linear Doppler broadened susceptibility is obtained by convolving $\chi^{(1)}(\Delta_j)$ with the 1D Maxwell Boltzmann velocity distribution \mathcal{P}_{1D} (1.9):

$$\chi_D^{(1)}(\Delta_j) = \frac{\alpha_0(0)}{\omega_{3j}/c} \gamma \underbrace{\int_{-\infty}^{\infty} f_\gamma^{(1)}(\Delta_j - kv) \mathcal{P}_{1D}(v) dv}_{s(\Delta_j)}, \quad (1.61)$$

where the detuning Δ_j is equal either to Δ or to $\Delta - \delta_0$ if the laser addresses the $|2\rangle \rightarrow |3\rangle$ or the $|1\rangle \rightarrow |3\rangle$ transition.

The magnitude of the susceptibility $\chi_D^{(1)}$ appears simply as a prefactor in equation (1.61). For the sake of convenience, we define the complex function s which is proportional to $\chi_D^{(1)}$ but does not depend on the atomic transition considered. Let's also define $a_j = \Delta_j/ku$ and $b = \gamma/ku$ ($u = \sqrt{2k_B T/m}$ is the most probable speed) and make the change of variable $v \rightarrow x = v/u$ in the integral s . By separating the real and imaginary parts of $f_\gamma^{(1)}$ and by using the convolution theorem, the Fourier transform of the function s reads finally: $S(\tilde{a}_j) = (F_b^R(\tilde{a}_j) + F_b^I(\tilde{a}_j)) P(\tilde{a}_j)$ where:

$$F_b^R(\tilde{a}_j) = - \int_{-\infty}^{\infty} \frac{1}{b} \frac{t/b}{1 + (t/b)^2} e^{-i\tilde{a}_j t} dt = i \pi \operatorname{sgn}(\tilde{a}) e^{-b|\tilde{a}_j|}, \quad (1.62)$$

$$F_b^I(\tilde{a}_j) = \int_{-\infty}^{\infty} \frac{1}{b} \frac{1}{1 + (t/b)^2} e^{-i\tilde{a} t} dt = i \pi e^{-b|\tilde{a}|}, \quad (1.63)$$

$$P(\tilde{a}_j) = \int_{-\infty}^{\infty} g_u(t) e^{-i\tilde{a}_j t} dt = e^{-(\tilde{a}/2)^2}. \quad (1.64)$$

By taking the inverse Fourier transform of S and by rearranging, we finally find that:

$$\begin{aligned} \chi_D^{(1)}(\Delta_j) &= \frac{\alpha_0(0)}{\omega_{3j}/c} b \{ \operatorname{Re} [F(a_j + ib)] + i \operatorname{Im} [F(a_j + ib)] \}, \\ &= \frac{\alpha_0(0)}{\omega_{3j}/c} \left(\frac{\gamma}{ku} \right) \left\{ \operatorname{Re} \left[F \left(\frac{\Delta_j}{ku} + i \frac{\gamma}{ku} \right) \right] + i \operatorname{Im} \left[F \left(\frac{\Delta_j}{ku} + i \frac{\gamma}{ku} \right) \right] \right\}, \end{aligned} \quad (1.65)$$

where F stands for the plasma dispersion function: $F(z) = i \sqrt{\pi} e^{-z^2} \operatorname{Erfc}(-iz)$ and Erfc for the complex complementary error function. The absorption coefficient $\alpha = k \operatorname{Im}(\chi_D^{(1)})$ has a Voigt-type profile arising from the convolution of the Lorentzian absorption profile of an atom at rest and the Gaussian distribution \mathcal{P}_{1D} . By following the exact same steps, we can also derive an expression for the real part of the Doppler broadened third-order dielectric susceptibility. Introducing $z_j = a_j + ib$ and using the relation $F(-z^*) = -F(z)^*$:

$$\begin{aligned} \operatorname{Re} [\chi_D^{(3)}(\Delta_j)] &= -i \frac{1}{|\mathcal{E}_s|^2} \frac{4}{3} \frac{\alpha_0(0)}{\omega_{32}/c} \frac{b^3}{2a} [z_j F(z_j) + z_j^* F(-z_j^*)], \\ &= \frac{1}{|\mathcal{E}_s|^2} \frac{4}{3} \frac{\alpha_0(0)}{\omega_{32}/c} \left(\frac{\gamma}{ku} \right)^2 \left(\frac{\gamma}{\Delta_j} \right) \operatorname{Im} \left[\left(\frac{\Delta_j}{ku} + i \frac{\gamma}{ku} \right) F \left(\frac{\Delta_j}{ku} + i \frac{\gamma}{ku} \right) \right] \end{aligned} \quad (1.66)$$

For the sake of completeness, let me finally derive an expression for the total Doppler broadened dielectric susceptibility χ_D :

$$\chi_D(\Delta_j) = \frac{\alpha_0(0)}{\omega_{3j}/c} \left(\frac{\gamma}{ku} \right) \left\{ \operatorname{Re} [F(a_j + ib_{\mathcal{I}})] + i \frac{\operatorname{Im} [F(a_j + ib_{\mathcal{I}})]}{\sqrt{1 + \mathcal{I}/\mathcal{I}_s}} \right\}, \quad (1.67)$$

where $b_{\mathcal{I}} = b \sqrt{1 + \mathcal{I}/\mathcal{I}_s}$. We recover the formula derived following the Lamb's model in [49], where the effects of gain saturation by strong driving fields in a dilute two-level atomic medium is investigated. The same equation has also been reported in [50]. In the latter, the authors claim that the atomic motion is not only accountable for Doppler broadening but also for a ballistic transport induced nonlocal dielectric response. The next section describes this effect in our configuration.

ii Ballistic transport of excited atoms: nonlocal dielectric response

So far, I have implicitly assumed that the dielectric response of the atomic vapor was local, or, in other words, that it only depends on the field strength or intensity at a given point in space. This assumption is fulfilled as long as no intensity redistribution process makes the susceptibility at \mathbf{r}_0 depend on the surrounding field strength at $\mathbf{r}_0 + \delta\mathbf{r}$. In hot vapors, intensity redistribution do occur through ballistic transport of excited atoms. Even if the laser field is far detuned from resonance, fast moving atoms can still absorb photons because of Doppler effect. Those photons, after being absorbed at \mathbf{r}_0 , can therefore be re-emitted at an other location in space, at $\mathbf{r}_0 + \mathbf{v}\tau$, where $\tau = 1/\Gamma$ is the lifetime of the excited state. This picture is very simplistic but still gives an insight into the physics at play in the transport-induced nonlocal dielectric response of hot vapors.

As mentioned in [49], the degree of nonlocality and the nature of the redistribution process (ballistic, diffusive, ...) both depend on the characteristic length scales associated with the transport of excited atoms. The first length scale is the mean free path *ie* the average distance travelled by an atom before a Rb-Rb collision: $l_c = 1/(\sqrt{2} N \sigma_{i \rightarrow j})$, where $\sigma_{i \rightarrow j}$ is the scattering cross section between two atoms, one in state $|i\rangle$ and the other in state $|j\rangle$. The collisional cross-section between atoms in the ground state is $\sigma_{g \rightarrow g} = 2.5 \times 10^{-17} \text{ m}^2$. For collisions between an atom in the ground state and an other one in the excited state, the cross-section is much larger since the collision process occurs via a long range dipole-dipole interaction [51] and: $\sqrt{T} \sigma_{g \rightarrow e} = 1.8 \times 10^{-14} \text{ K}^{\frac{1}{2}} \text{ m}^2$. At $T = 400 \text{ K}$, $l_c^{g \rightarrow g} \simeq 11 \text{ mm}$ and $l_c^{g \rightarrow e} \simeq 32 \text{ } \mu\text{m}$; both are much larger than the ballistic transport length scale, defined by $l_b = u\tau \simeq 7.6 \text{ } \mu\text{m}$ at 400 K. The transport of excited atoms is mainly ballistic at 400 K and the nonlocal response of the material should then depend on u and τ .

The rate equation for the excited state population is given by the third equation in (1.47). One can rewrite this equation as function of the total absorption coefficient α as follow:

$$\frac{d\rho_{33}}{dt} = -(\Gamma + \Gamma_t) \rho_{33} + \text{Im}(\Omega_{23}^* \rho_{32}), \quad (1.68)$$

$$\begin{aligned} &= -(\Gamma + \Gamma_t) \rho_{33} + \frac{1}{2} \frac{\epsilon_0}{\hbar} |\mathcal{E}|^2 \text{Im}(\chi_{32}), \\ &= -(\Gamma + \Gamma_t) \rho_{33} + \frac{\mathcal{I} \alpha(\mathcal{I})}{\hbar \omega}, \end{aligned} \quad (1.69)$$

using the relations: $\chi_{32} = \frac{2\mu_{23}}{\epsilon_0 \mathcal{E}} \rho_{32}$ and $\alpha = \frac{\omega}{n_0 c} \text{Im}(\chi_{32})$. Equation (1.69) has been derived using the 3-level description sketched in figure 1.5 (a) but is actually much more general since it only involves the total decay rate $\bar{\gamma} = \Gamma + \Gamma_t$ of the excited state and the local rate of excitation $\mathcal{I} \alpha(\mathcal{I}) / \hbar \omega$. The same equation describes for instance the evolution of the excited state population when both the $|1\rangle \rightarrow |3\rangle$ and the $|2\rangle \rightarrow |3\rangle$ transitions are simultaneously driven by the laser field. In that case, $\alpha = k \text{Im}(\chi_{31} + \chi_{32})$. Working within the **paraxial approximation**, I thus suppose that ρ_{33} only substantially varies in the transverse plane, where $\mathbf{r} = x\hat{\mathbf{x}} + y\hat{\mathbf{y}}$ and $\mathbf{v} = v_x\hat{\mathbf{x}} + v_y\hat{\mathbf{y}}$. One can then rewrite eq.(1.69) using the differential formula $\frac{d}{dt} = \frac{\partial}{\partial t} + \mathbf{v} \cdot \nabla_{\perp}$ (where ∇_{\perp} is the gradient operator in the $(\hat{\mathbf{x}}, \hat{\mathbf{y}})$ plane):

$$\frac{\partial \rho_{33}}{\partial t} + \mathbf{v} \cdot \nabla_{\perp} \rho_{33} + \underbrace{(\Gamma + \Gamma_t)}_{\bar{\gamma}} \rho_{33} = \frac{\mathcal{I} \alpha_D(\mathcal{I})}{\hbar \omega}. \quad (1.70)$$

This equation can be solved with the Green function formalism. Let's $G_{\bar{\gamma}}^b$ be the solution of:

$$\frac{\partial \rho_{33}}{\partial t} + \mathbf{v} \cdot \nabla_{\perp} \rho_{33} + \bar{\gamma} \rho_{33} = \delta(t) \delta(\mathbf{r}) \mathcal{P}_{2D}(v), \quad (1.71)$$

where \mathcal{P}_{2D} stands for the 2D Maxwell-Boltzmann velocity distribution, as usual. Averaging the Green function $G_{\bar{\gamma}}^b$ over \mathcal{P}_{2D} yields:

$$\bar{G}_{\bar{\gamma}}^b(\mathbf{r}, t) = \frac{1}{\pi u^2} e^{-\gamma t} \left[\int_{\mathbb{R}^2} \delta(\mathbf{r} - \mathbf{v} t) e^{-(v/u)^2} d\mathbf{v} \right] = \frac{1}{\pi u^2} \frac{e^{-\bar{\gamma} t}}{t^2} e^{-\left(\frac{|\mathbf{r}|}{ut}\right)^2}. \quad (1.72)$$

One can then obtain the spatial distribution of the excited state population by convolving the averaged Green function $\bar{G}_{\bar{\gamma}}^b$ with the local rate of excitation $\mathcal{I} \alpha_D(\mathcal{I}) / \hbar \omega$ of (1.69):

$$\rho_{33}(\mathbf{r}, t) = \frac{1}{\hbar \omega} \int_{-\infty}^t dt' \int_{\mathbb{R}^2} d\mathbf{r}' \bar{G}_{\bar{\gamma}}^b(\mathbf{r} - \mathbf{r}', t - t') \{ \mathcal{I}(\mathbf{r}', t') \alpha [\mathcal{I}(\mathbf{r}', t')] \} \quad (1.73)$$

Let's assume the rate of excitation is constant over time and localized in space at \mathbf{r}_0 such that $\mathcal{I}(\mathbf{r}_0, t) = \delta(\mathbf{r}_0) \mathcal{I}_0$. By making successively the substitutions $t \rightarrow t + t_0$ and $t \rightarrow \xi = \frac{r}{u} \frac{1}{t}$ (where $r = |\mathbf{r} - \mathbf{r}_0|$), one can finally derive an expression for the spatial distribution of the excited state population in the steady-state:

$$\rho_{33}(\mathbf{r}) = \frac{\mathcal{I}_0 \alpha(\mathcal{I}_0)}{\hbar \omega} \frac{1}{\pi u r} \int_0^{\infty} e^{-\bar{\gamma} r / u \xi} e^{-\xi^2} d\xi, \quad (1.74)$$

as well as the steady-state Green function and its spatial Fourier transform:

$$\begin{cases} \bar{G}_{\bar{\gamma}}^b(\mathbf{r} - \mathbf{r}_0) = \frac{1}{\pi u r} \int_0^{\infty} e^{-\bar{\gamma} r / u \xi} e^{-\xi^2} d\xi, \\ \mathcal{F}[\bar{G}_{\bar{\gamma}}^b](k) = \frac{\sqrt{\pi}}{\bar{\gamma}} \frac{e^{1/(k l_b)^2}}{k l_b} \text{Erfc}[1/(k l_b)]. \end{cases} \quad (1.75)$$

The Green function $\bar{G}_{\bar{\gamma}}^b$ is well normalized as $\bar{\gamma} \int G_{\bar{\gamma}}^b(\mathbf{r}) d\mathbf{r} = 1$.

$\bar{G}_{\bar{\gamma}}^b$ and $\mathcal{F}[\bar{G}_{\bar{\gamma}}^b]$ have been plotted on figure 1.11 (a) as function of the scaled coordinates r/l_b and $k l_b$ respectively. As mentioned in [50], the ballistic response (blue curve) falls off much more rapidly than the diffusive one (red curve) in real space. Diffusion is thus much more efficient at spreading the intensity in the transverse plane than ballistic transport. In order to complete the description of the transport-induced nonlocality, let's derive an expression for the nonlocal dielectric susceptibility which also takes Doppler broadening into account. When the laser intensity varies spatially in the transverse plane, we can use the Green function $\bar{G}_{\bar{\gamma}}^b$ to write the steady-state dielectric response as follow:

$$\text{Re}[\chi_D(\mathbf{r})] = \chi_0 \left(\text{Re}[F(a + ib)] + \bar{\gamma} \int_{\mathbb{R}^2} G_{\bar{\gamma}}^b(\mathbf{r} - \mathbf{r}_0) \times \{ \text{Re}[F(a + ib_{\mathcal{I}}(\mathbf{r}_0))] - \text{Re}[F(a + ib)] \} d\mathbf{r}_0 \right), \quad (1.76)$$

$$\text{Im}[\chi_D(\mathbf{r})] = \chi_0 \left(\text{Im}[F(a + ib)] + \bar{\gamma} \int_{\mathbb{R}^2} G_{\bar{\gamma}}^b(\mathbf{r} - \mathbf{r}_0) \times \left\{ \frac{\text{Im}[F(a + ib_{\mathcal{I}}(\mathbf{r}_0))]}{\sqrt{1 + \mathcal{I}(\mathbf{r}_0)/\mathcal{I}_s}} - \text{Im}[F(a + ib)] \right\} d\mathbf{r}_0 \right), \quad (1.77)$$

where $\bar{\gamma} = \Gamma/2 + \Gamma_t$ (which is the decoherence decay rate) and $\chi_0 = \frac{\alpha_0(0)}{\omega_{32}/c} \frac{\bar{\gamma}}{k u}$.

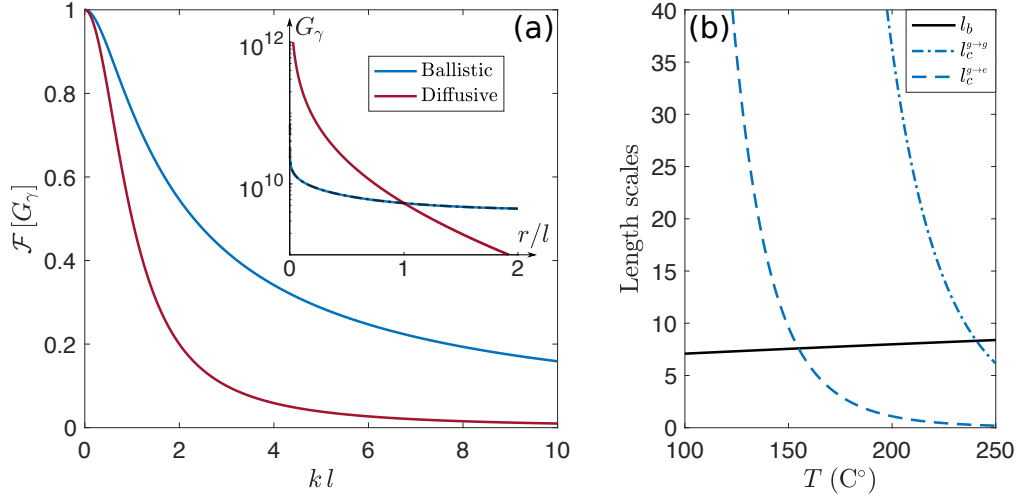


Figure 1.11: (a) Ballistic (blue) and diffusive (red) response functions in k-space. Inset: real space response functions, rescaled to be equal at $r = l$. (b) Transport length scales as function of the vapor temperature T . The ballistic transport length scale l_b (black line) remains lower than the free mean path l_c^{g+e} for $T < 155$ C°. The transport of excited atoms is therefore mainly ballistic at $T = 130$ C°. Figure reproduced from [50].

For high vapor temperatures (when $T > 450$ K), the transport of excited atoms is diffusive: the free mean path l_c^{g+e} becomes smaller than l_b , as can be seen on 1.11 (b). In that case, the evolution of the excited state population is given by the following diffusion equation:

$$\frac{\partial \rho_{33}}{\partial t} - \mathcal{D} \nabla_{\perp}^2 \rho_{33} + \bar{\gamma} \rho_{33} = \frac{\mathcal{I} \alpha_D(\mathcal{I})}{\hbar \omega}, \quad (1.78)$$

where \mathcal{D} is the diffusion constant. Following the exact same steps as before, we can derive an expression for the steady-state diffusive Green function $G_{\bar{\gamma}}^d$ (and its Fourier transform):

$$\begin{cases} \bar{G}_{\bar{\gamma}}^d(\mathbf{r} - \mathbf{r}_0) = \frac{1}{4\pi\mathcal{D}} \int_0^\infty \frac{1}{t} e^{-\bar{\gamma}t} e^{-r^2/(4\mathcal{D}t)} dt = \frac{1}{2\pi\mathcal{D}} \mathcal{K}_0\left(\frac{r}{\sqrt{\mathcal{D}\tau}}\right), \\ \mathcal{F}[\bar{G}_{\bar{\gamma}}^d](k) = 1/(1 + \mathcal{D}\tau k^2), \end{cases} \quad (1.79)$$

where \mathcal{K}_0 is the zeroth-order modified Bessel function of the second kind. The same type of response function has been used to describe the nonlocal dielectric response of thermooptic materials for example [28]. In order to compare the response functions for ballistic and diffusive transport, $\bar{G}_{\bar{\gamma}}^d$ and $\mathcal{F}[\bar{G}_{\bar{\gamma}}^d]$ have also been plotted as function of r/l_d and $k l_d$ on figure 1.11 (a) (we simply assume here that $\sqrt{\mathcal{D}\tau} = l_c^{g+e}$).

The nonlocal dielectric response of materials under a laser excitation should be considered in order to correctly describe the dynamics of a photon fluid. In [52] for instance, the effects of nonlocality on the dispersion of density waves propagating on a fluid of light is reported. The nonlocality plays also an important role in stabilizing nonlinear phenomena such as transverse solitary waves [53] or the nonlinear propagation of more complex laser fields, such as vortex (Laguerre) and dipole (Hermite) beams [50, 54].

Chapter 2

Photon fluid in the 2D+1 propagating geometry

In the previous chapter, I have described in detail the response of a rubidium vapor under a near-resonance laser excitation. However, we have up to now put aside the question of how such a laser field propagates through the vapor cell. This chapter is dedicated to discussing the analogy between this nonlinear propagation and the evolution of a paraxial photon fluid. I first introduce the concept of a fluid of light in the propagating geometry by deriving the nonlinear Schrödinger equation. In this equation, the electric field of the laser beam can be regarded as a fluid flowing in the plane perpendicular to the propagation axis, which plays the role of a time axis in this hydrodynamical description of nonlinear optics. The study of the propagation of small amplitude density waves travelling onto the photon fluid provides crucial insights into this many body system. This chapter presents thus also the theoretical framework required to describe the photon fluids elementary excitations, by introducing, in particular, the Bogoliubov transform and the so-called Bogoliubov dispersion relation.

2.1 Nonlinear Schrödinger equation in optics

A fluid of light refers to a weakly interacting gas of photons which is formed by a laser beam propagating through an optical nonlinear medium. The mean-field dynamics of this many body Bose gas follows a Nonlinear Schrödinger Equation (NLSE) [55, 56]. In this section, I derive the NLSE using both the slowly varying envelope and the paraxial approximations. The laser field $\mathbf{E}(\mathbf{r}, t)$ is monochromatic and linearly polarized and propagates along z in a Kerr nonlinear medium. Those materials exhibit an intensity-dependent refractive index, which comes from a non-zero third-order dielectric susceptibility $\chi^{(3)}$. In chapter 1, we have seen how to obtain such an intensity-dependent optical response in hot rubidium vapors, by tuning the frequency of a laser field close to an atomic resonance. The following derivation is general however, since it only requires a non-zero $\chi^{(3)}$ and remains correct for other sorts of Kerr medium, such as thermo-optic liquids [52] and photorefractive crystals [29].

2.1.1 Propagation equation in a non-linear medium

Starting from the Maxwell equations, we can show that the electric field $\mathbf{E}(\mathbf{r}, t)$ evolves according to the well-known nonlinear wave equation:

$$\nabla^2 \mathbf{E} - \frac{1}{c^2} \frac{\partial^2 \mathbf{E}}{\partial t^2} = \frac{1}{\epsilon_0 c^2} \frac{\partial^2 \mathbf{P}}{\partial t^2}, \quad (2.1)$$

where c and ϵ_0 are the speed of light and the dielectric permittivity in vacuum, respectively. The polarization \mathbf{P} describes the dielectric response of the material to the field excitation. This response is not necessarily linear and tends generally to saturate with the applied field. In nonlinear optics, the polarization is therefore usually expressed as a power series in the field strength (when \mathbf{E} is sufficiently weak):

$$\mathbf{P}(\mathbf{r}, t) = \epsilon_0 \chi[\mathbf{E}(\mathbf{r}, t)] \mathbf{E}(\mathbf{r}, t) \quad (2.2)$$

$$= \underbrace{\epsilon_0 \chi^{(1)} \cdot \mathbf{E}(\mathbf{r}, t)}_{\mathbf{P}^{(1)}(\mathbf{r}, t)} + \underbrace{\epsilon_0 \chi^{(2)} : \mathbf{E}(\mathbf{r}, t)^2}_{\mathbf{P}^{(2)}(\mathbf{r}, t)} + \underbrace{\epsilon_0 \chi^{(3)} : \mathbf{E}(\mathbf{r}, t)^3}_{\mathbf{P}^{(3)}(\mathbf{r}, t)} + \dots \quad (2.3)$$

The $(n+1)$ th-rank tensor $\chi^{(n)}$ describes the n th-order susceptibility of the optical medium. The dielectric response of the material is fully characterized by the set $\{\chi^{(1)}, \chi^{(2)}, \chi^{(3)}, \dots\}$ of all the susceptibilities. The n th-order polarization $\mathbf{P}^{(n)}$ is linked to the electric field \mathbf{E} by the following tensor product:

$$P_j^{(n)}(\mathbf{r}, t) = \epsilon_0 \sum_{i_1 \dots i_n} \int_{-\infty}^{\infty} \chi_{j i_1 \dots i_n}^{(n)}(\mathbf{r} - \mathbf{r}_1, \dots, \mathbf{r} - \mathbf{r}_n; t - t_1, \dots, t - t_n) \times \\ E_{i_1}(\mathbf{r}_1, t_1) \dots E_{i_n}(\mathbf{r}_n, t_n) d\mathbf{r}_1 \dots d\mathbf{r}_n dt_1 \dots dt_n \quad (2.4)$$

The indices $i_1 \dots i_n$ run over the three Cartesian components of the electric field \mathbf{E} .

In practice, equation (2.4) can be highly simplified by considering:

- the physical properties of the optical medium (such as the material symmetries);
- the assumptions made regarding the laser field (polarization, monochromaticity).

Rubidium vapors (and more broadly alkaline vapors) are for instance **centro-symmetric** optical mediums. All the even-order nonlinear susceptibilities ($\chi^{(2)}$, $\chi^{(4)}$, $\chi^{(6)}$, ...) must therefore vanish. Rubidium vapors are also **isotropic** materials for which the polarization is aligned with the applied field \mathbf{E} . As the laser field is linearly polarized (let's say, along x), the polarization \mathbf{P} must only have one non-zero component (along x). The tensor nature of the nonlinear interaction can thus be left out. Moreover, if the dielectric response of the material is **local**, we get rid of the integration over spatial coordinates. As we have seen in the first chapter however, ballistic transport of atoms makes the dielectric response of hot rubidium vapors intrinsically nonlocal. For the sake of simplicity, I will keep assuming the medium is local here; the effects of nonlocality – on the dynamics of the photon fluid elementary excitations, for instance – are discussed in section 2.4.2. The expression of the n th-order polarization vector is drastically simplified as a result of the above discussion:

$$P^{(n)}(\mathbf{r}, t) = \epsilon_0 \int_{-\infty}^{\infty} \chi^{(n)}(t-t_1, \dots, t-t_n) \times E(\mathbf{r}, t_1) \dots E(\mathbf{r}, t_n) dt_1 \dots dt_n. \quad (2.5)$$

Rubidium vapors are **dispersive** optical mediums; the nonlinear response will therefore depend on the laser frequency ω and the integration over temporal coordinates remains. By neglecting polarization degrees of freedom, the monochromatic laser field simply reads: $E(\mathbf{r}, t) = \frac{1}{2} [\mathcal{E}(\mathbf{r}) e^{i\omega t} + \mathcal{E}^*(\mathbf{r}) e^{-i\omega t}]$, where \mathcal{E} is the complex envelope of the electric field. Replacing $E(\mathbf{r}, t)$ in (2.5) by the foregoing expression and using equations (2.1) and (2.3) yield the following stationary equation for \mathcal{E} :

$$\nabla^2 \mathcal{E}(\mathbf{r}) + \frac{\omega^2}{c^2} [1 + \chi^{(1)}(\omega)] \mathcal{E}(\mathbf{r}) = -\frac{3}{4} \frac{\omega^2}{c^2} \chi^{(3)}(\omega) |\mathcal{E}(\mathbf{r})|^2 \mathcal{E}(\mathbf{r}). \quad (2.6)$$

In equation (2.6), only the first- and third-order polarizations are taken into account while higher order contributions ($P^{(5)}$, $P^{(7)}$, ...) are neglected. Moreover, we only keep in $P^{(3)}$ the terms oscillating at $+\omega$, since we only concern about nonlinear wave-mixing processes conserving the input laser frequency. That is why the factor 3 appears on the left hand side of equation (2.6), as $\binom{3}{2} = 3$ is the number of four-wave mixing mechanisms producing a 3rd-order polarization oscillating at $+\omega$ [55]. So as to rewrite equation (2.6) more aesthetically, one usually defines the linear dielectric permittivity of the material $\epsilon_r(\omega) = 1 + \chi^{(1)}(\omega)$:

$$\nabla^2 \mathcal{E}(\mathbf{r}) + k_0^2 \epsilon_r(\omega) \mathcal{E}(\mathbf{r}) = -\frac{3}{4} \frac{\omega^2}{c^2} \chi^{(3)}(\omega) |\mathcal{E}(\mathbf{r})|^2 \mathcal{E}(\mathbf{r}). \quad (2.7)$$

where $k_0 = \omega/c$ stands for the laser wave-vector in vacuum. Let's also introduce the linear refractive index $n_0(\omega) = \sqrt{\text{Re}[\epsilon_r(\omega)]}$ and absorption coefficient $\alpha(\omega) = k_0 \text{Im}[\epsilon_r(\omega)]/n_0$.

2.1.2 Paraxial approximation for the slowly-varying field envelope

Equation (2.7) describes the evolution of the envelope of a monochromatic and linearly polarized laser field inside a Kerr-type medium. This equation is general as no assumption has been made on the envelope so far. In practice however, the wave propagation is often limited to within a small angle from the optical axis, defined by the z -direction let's say, along which the beam propagates. In that case, the field amplitude $\mathcal{E}(\mathbf{r}_\perp, z)$ slowly varies in the transverse plane (that is, on the plane perpendicular to the z -axis) and the so-called **paraxial approximation** can be performed. The field envelope reads thus as follows:

$$\mathcal{E}(\mathbf{r}_\perp, z) = \mathcal{E}_0(\mathbf{r}_\perp, z) e^{ik(\omega)z}, \quad (2.8)$$

where $\mathcal{E}_0(\mathbf{r}_\perp, z)$ is a **slowly-varying** function of z , or, in other words, a function varying on a length scale much larger than the optical wavelength λ . The paraxial approximation is valid as long as $|\nabla_\perp^2 \mathcal{E}_0|/k^2 \sim |\partial_z \mathcal{E}_0|/k \ll 1$, where $k(\omega) = n_0 k_0$ is the laser wave-vector in the nonlinear medium. When this condition is fulfilled, the second-order derivative $\partial_z^2 \mathcal{E}_0$ can be neglected in the equation describing the evolution of the slow-varying envelope \mathcal{E}_0 , which finally takes the form of a nonlinear Schrödinger equation (NLSE):

$$i \partial_z \mathcal{E}_0(\mathbf{r}_\perp, z) = \left[-\frac{1}{2k} \nabla_\perp^2 - \frac{i\alpha}{2} - \frac{3}{8} \frac{k}{n_0^2} \chi^{(3)}(\omega) |\mathcal{E}_0(\mathbf{r}_\perp, z)|^2 \right] \mathcal{E}_0(\mathbf{r}_\perp, z), \quad (2.9)$$

where ∇_\perp is the gradient with respect to the transverse spatial coordinates, $\mathbf{r}_\perp = (x, y)$. For the sake of completeness, we can also take into account the effect of a local modulation of the linear refractive index, δn , on the propagation of the slowly-varying field envelope. Such a modulation can either act as a repulsive obstacle for the light beam (if δn is negative) or as a wave-guide (if δn is positive). In our system, it can be optically generated by locally driving another rubidium transition, using a second laser field tuned close to resonance. This situation is extensively investigated in chapter 5. Including δn in the equation 2.9 is straightforward [56] and finally yields:

$$i \partial_z \mathcal{E}_0(\mathbf{r}_\perp, z) = \left[-\frac{1}{2k} \nabla_\perp^2 - \frac{i\alpha}{2} - k \frac{\delta n(\mathbf{r}_\perp, z)}{n_0} - \frac{3}{8} \frac{k}{n_0^2} \chi^{(3)}(\omega) |\mathcal{E}_0(\mathbf{r}_\perp, z)|^2 \right] \mathcal{E}_0(\mathbf{r}_\perp, z). \quad (2.10)$$

2.1.3 Comparison with the Gross-Pitaevskii equation

If linear absorption is negligible ($\alpha \simeq 0$), that is, if the system is conservative, the NLSE is mathematically analogous to the Gross-Pitaevskii equation (GPE). This equation describes for instance the space-time evolution of the macroscopic wave-function $\Psi(\mathbf{r}, t)$ of a dilute atomic Bose-Einstein condensate (BEC) in the Hartree-Fock approximation:

$$i \hbar \partial_t \Psi(\mathbf{r}, t) = \left[-\frac{\hbar^2}{2m} \nabla^2 + \mathcal{V}(\mathbf{r}) + g |\Psi(\mathbf{r}, t)|^2 \right] \Psi(\mathbf{r}, t), \quad (2.11)$$

where \hbar is the reduced Planck constant, m the boson mass, \mathcal{V} an external potential and $g = 4\pi\hbar^2 a_s/m$ the coupling constant, proportional to the s-wave scattering length a_s [57].

i Space-time mapping

As you may have noticed, equations (2.9) and (2.11) are indeed pretty similar. However, while the GPE describes the evolution of the wave-function Ψ over the real time, the NLSE describes how the electric field envelope \mathcal{E}_0 propagates in space, along the optical axis. Therefore, the z -direction plays the role of an effective time τ in the NLSE so that every transverse plane along the optical axis can be regarded as a snapshot of the nonlinear "time evolution" of the laser beam inside the medium. This seemingly elementary space-time mapping $z \leftrightarrow \tau = zn_0/c$ has profound consequences when one tries to build from (2.9) a fully quantum field theory [56, 58]. Once the z -direction has been mapped into a time axis, the only difference remaining between the NLSE and the GPE lies in their dimensionality. While the GPE describes the time evolution of the condensate wave-function in the three dimensions of space (3D+1 geometry), the "time evolution" of \mathcal{E}_0 intrinsically involves only two spatial dimensions defining the transverse plane (2D+1 geometry).

ii Effective mass and coupling constant

In order to complete the analogy between NLSE and GPE, let's derive an expression for the mass and the coupling constant which characterize the weakly interacting photon gas formed by the laser field inside the Kerr medium. We first define the normalized envelope:

$$\bar{\mathcal{E}}_0(\mathbf{r}_\perp, z) = \mathcal{E}_0(\mathbf{r}_\perp, z) / \left[\int_{\mathcal{S}} |\mathcal{E}_0(\mathbf{r}_\perp, z)|^2 d\mathbf{r}_\perp \right]^{\frac{1}{2}}, \quad (2.12)$$

where \mathcal{S} stands for the surface of the medium cross-section. The amplitude square of $\bar{\mathcal{E}}_0$ is the electric field density. By definition, its integral over \mathcal{S} is one. The integral in equation (2.12) is a conserved quantity, as it is proportional to the laser field input power \mathcal{P}_0 whatever the position z on the optical axis (as long as linear absorption is zero). Therefore, \mathcal{E}_0 can be replaced by $\bar{\mathcal{E}}_0$ in (2.9) and using the space-time mapping yields:

$$i\hbar \partial_\tau \bar{\mathcal{E}}_0(\mathbf{r}_\perp, \tau) = \left[-\frac{\hbar^2}{2(\hbar k/c)} \nabla_\perp^2 - \hbar\omega \delta n(\mathbf{r}_\perp, z) - \hbar\omega n_2 \mathcal{P}_0 |\bar{\mathcal{E}}_0(\mathbf{r}_\perp, z)|^2 \right] \bar{\mathcal{E}}_0(\mathbf{r}_\perp, z). \quad (2.13)$$

The nonlinear refractive index n_2 is defined by: $n_2 = 2\tilde{n}_2/(c\epsilon_0 n_0)$ with $\tilde{n}_2 = 3\chi^{(3)}/(8n_0)$. One can then readily identify the effective mass \bar{m} and coupling constant \bar{g} in (2.13):

$$\bar{m} = \hbar k/c \quad \text{and} \quad \bar{g} = -\hbar\omega n_2 \mathcal{P}_0, \quad (2.14)$$

where $2\mathcal{P}_0/(c\epsilon_0 n_0) = \int_{\mathcal{S}} |\mathcal{E}_0(\mathbf{r}_\perp, z)|^2 d\mathbf{r}_\perp$. A focusing (resp. defocusing) Kerr nonlinearity, for which $n_2 > 0$ (resp. $n_2 < 0$), can therefore be regarded in this analogy as an attractive (resp. repulsive) photon-photon interaction, mediated by the atomic ensemble in our case. The nonlinear refractive index n_2 plays thus a crucial role in photon fluid physics since it controls the strength and nature (either attractive or repulsive) of the effective interaction between photons. Throughout my thesis, I only dealt with defocusing nonlinearities, which make the photon gas stable against modulational instabilities [59, 60]. Let's finally mention that the index modulation δn in (2.9) acts as an external potential on the paraxial photons:

$$\bar{V}(\mathbf{r}_\perp) = -\hbar\omega \delta n(\mathbf{r}_\perp, z) \quad (2.15)$$

which is either attractive ($\delta n > 0$) or repulsive ($\delta n < 0$) depending on the sign of $\delta n(\mathbf{r}_\perp, z)$. We can then think about trapping the photon gas in the (x, y) plane, in order to observe the optical analog of breathers in 2-dimensional BECs [61] for example, or about studying the dynamics of the interacting photon gas in disordered potentials.

It might be interesting to compare the typical values of the coupling constant obtained in 2-dimensional BECs and in interacting photon gas. To that end, we define $N\tilde{g} = 2\bar{m}\bar{g}/\hbar^2$ which is an adimensional quantity introduced usually in 2D BECs to evaluate the strength of the nonlinear interactions. In that case, N stands for the number of bosons inside the BEC. Regarding interacting photon gas, what makes sense is not the number of photons inside the Kerr medium but rather the **flux of photons**, $\Phi = \mathcal{P}_0/\hbar\omega$, through the cell entrance plane ($\hbar\omega$ being the energy of a single photon). When $n_2 = -5 \times 10^{-11} \text{ m}^2/\text{W}$ and $\mathcal{P}_0 = 500 \text{ mW}$ – which are typical experimental values – $N\tilde{g}$ is equal to 3.2×10^3 . In 2D atomic BECs, $N\tilde{g}$ is of the same order of magnitude. It reaches 4×10^3 in [61] for instance. Tuning the value of the product $N\tilde{g}$ in 2D atomic BEC experiments requires to change the intensity I of the laser beams confining the 2D condensate in the desired direction (since \tilde{g} scales as $I^{1/4}$ [61]).

In photon gas experiments, we have control over both the flux of photons Φ , by tuning the laser power \mathcal{P}_0 , and over the nonlinear index of refraction n_2 , by tuning the laser frequency ω in rubidium vapors for instance. It seems therefore that photon gas in propagating geometry are versatile and highly tunable systems to investigate the optical counterpart of nonlinear many-body phenomena arising in 2-dimensional BECs. Nevertheless, it is worth mentioning that the nonlinear "time evolution" of the photon gas in this analogy is intrinsically limited by the length L of the Kerr medium. This may potentially prevent us from observing nonlinear phenomena which establish on time-scales longer than Ln_0/c .

iii Kinetic, interaction and potential energy

It might be useful to introduce the kinetic, the interaction and the potential energies of the interacting photon gas, which are respectively defined as follows:

$$E_{\text{kin}}[\bar{\mathcal{E}}_0] = \frac{\hbar^2}{4m} \int_S |\nabla_{\perp} \bar{\mathcal{E}}_0|^2 d\mathbf{r}_{\perp} \quad (2.16)$$

$$E_{\text{int}}[\bar{\mathcal{E}}_0] = \frac{\bar{g}}{4} \int_S |\bar{\mathcal{E}}_0(\mathbf{r}_{\perp})|^4 d\mathbf{r}_{\perp} \quad (2.17)$$

$$E_{\text{pot}}[\bar{\mathcal{E}}_0] = \frac{1}{2} \int_S \bar{V}(\mathbf{r}_{\perp}) |\bar{\mathcal{E}}_0|^2 d\mathbf{r}_{\perp} \quad (2.18)$$

When the system is conservative (no loss, $\alpha = 0$), the total energy $E_{\text{tot}} = E_{\text{kin}} + E_{\text{int}} + E_{\text{pot}}$ is conserved during the evolution. One retrieves the left hand side of equation (2.13) by computing the functional derivative $\delta E_{\text{tot}}/\delta \bar{\mathcal{E}}_0$, as expected. In this manuscript, I almost exclusively study situations for which $E_{\text{int}} \gg E_{\text{kin}}$. This latter condition defines the so-called **Thomas-Fermi** or **hydrodynamic regime** [62], in which the envelope of the electric field behaves as a 2-dimensional photon fluid in the transverse plane.

2.2 Hydrodynamic analogy

The analogy between NLSE and GPE indicates that it is somehow possible to describe a laser beam propagating in a Kerr medium as a fluid of light flowing in the transverse plane. In this section, I will explicitly transpose the NLSE into a set of hydrodynamic equations, using the Madelung transform [63]. In addition to being highly aesthetic, the hydrodynamic formulation of the NLSE provides an easy understanding about the optical counterparts of a broad range of classical fluid phenomena, such as, for instance, the transition from laminar to turbulent flow [64], undular bores [65] or Rayleigh-Taylor instabilities [66].

2.2.1 Madelung transform

The **Madelung transform** enables one to express the electric field envelope \mathcal{E}_0 as function of its non-normalized density ρ and phase Φ as follows:

$$\mathcal{E}_0(\mathbf{r}_{\perp}, z) = \sqrt{\rho(\mathbf{r}_{\perp}, z)} e^{i\Phi(\mathbf{r}_{\perp}, z)} \quad (2.19)$$

The density $\rho = |\mathcal{E}_0|^2$ is proportional to the laser intensity \mathcal{I}_0 . Using (2.19), equation (2.9) yields the following set of hydrodynamic equations for ρ and Φ :

$$\frac{\partial \rho}{\partial \tau} + \nabla_{\perp} \cdot (\rho \mathbf{v}) + \tilde{\alpha} \rho = 0 \quad (2.20)$$

$$\frac{c}{n_0 k} \frac{\partial \Phi}{\partial \tau} + \frac{1}{2} v^2 - \frac{c^2}{n_0^2} \left(\frac{n_2}{n_0} \rho + \frac{1}{2k^2} \frac{\nabla_{\perp}^2 \sqrt{\rho}}{\sqrt{\rho}} \right) = 0 \quad (2.21)$$

where $\tilde{\alpha} = \alpha c / n_0$. The effective time is still defined by $\tau = z n_0 / c$ and the nonlinear index of refraction by $\tilde{n}_2 = 3 \chi^{(3)} / (8 n_0)$. As you may have noticed, equations (2.20) and (2.21) look respectively like the continuity and Euler equations, describing how an incompressible fluid of density $\rho(\mathbf{r}_{\perp}, \tau)$ locally flows in the plane (x, y) at a velocity $\mathbf{v}(\mathbf{r}_{\perp}, \tau) = \frac{c}{n_0 k} \nabla_{\perp} \Phi$.

- The continuity equation (2.20) refers to the non-conservation of the mass so to speak, because of linear losses. The fluid density decays exponentially during propagation, as expected from the Beer-Lambert law: $\rho(\mathbf{r}_{\perp}, \tau) = \rho(\mathbf{r}_{\perp}, 0) \exp(-\tilde{\alpha} \tau)$.
- The second term inside the bracket on the right hand-side of the Euler equation (2.21) is the so-called quantum pressure [62] and does not have any counterpart in real fluids. It opposes any stretching or contraction of the fluid over distance smaller than the healing length ξ , defined in subsection 2.3.2. As long as the density is slowly varying in the transverse plane, the quantum pressure can be neglected; reversely, it starts dominating the dynamics in regions of rapidly changing density.

Seen from the hydrodynamic analogy perspective, the propagation geometry appears to be a simple and straightforward implementation of a photon fluid. The initial fluid density and its flow velocity can be easily tuned controlling the transverse intensity distribution and the spatial phase profile of the incident laser beam at the medium entrance plane (using a Spatial Light Modulator (SLM) for instance).

2.2.2 Speed of sound

In liquids, the sound consists of compression waves whose speed – the sound velocity c_s – depends on the fluid compressibility and density. According to the Newton-Laplace formula, $c_s = \sqrt{\mathcal{K}/\rho}$ [67], \mathcal{K} being the bulk modulus of the fluid. This quantity measures how resistant to compression the liquid is. It is basically defined as the ratio of the infinitesimal pressure increase to the resulting relative decrease of the volume. In other words, if P stands for the pressure inside the fluid, the bulk modulus \mathcal{K} reads: $\mathcal{K} = \rho \partial P / \partial \rho$. In paraxial photon fluids, the repulsive interactions between photons create a local bulk pressure $P = n_2 c^2 \rho^2 / (2 n_0^2)$. This pressure is related – through the Newton-Laplace formula – to the **speed of sound**:

$$c_s^2 = \frac{\partial P}{\partial \rho} = \left(\frac{c}{n_0} \right)^2 \frac{\Delta n}{n_0} \quad (2.22)$$

$\Delta n = \tilde{n}_2 \rho = n_2 \mathcal{I}_0$ being the nonlinear change of refractive index and \mathcal{I}_0 the laser intensity. The fact that there is a well defined sound velocity in propagating photon fluids necessarily implies that density modulations in those system behave as sound-like collective excitations, under certain conditions. Phonons in crystals also propagate at a given speed of sound c_{ph} , independently of their wavelength Λ , as long as the latter is larger than the microscopic details of the lattice. In other words, the group velocity $v_g(k) = \partial \omega_{\text{ph}} / \partial k$ does not depend on the phonons wave-vector $k = 2\pi/\Lambda$ at long wavelengths: $v_g(k) \simeq c_{\text{ph}}$. This results in a

linear dependence of the phonons frequency $\omega_{ph}(k)$ on the wave-vector k : $\omega_{ph}(k) \simeq c_{ph} k$. The same kind of linear dispersion relation at low wave-vectors is expected for density waves in propagating photon fluids. In the next section, I will precisely derive a formula for this dispersion relation – the so-called **Bogoliubov dispersion relation** – which indeed scales linearly at low values of the wave-vector.

2.3 Bogoliubov dispersion in a lossless local medium

In most cases, even if the Madelung formulation of the NLSE is highly aesthetic and gives a physical insight into the hydrodynamical nature of the dynamics, the coupled system of equations (2.20) and (2.21) cannot be solved analytically. It is then of particular interest to study how small density modulations propagate on top of an uniform background fluid. In that case, the continuity and the Euler equations can be linearized. Using the so-called Bogoliubov transform, I will show that density waves in propagating photon fluids obey the well known Bogoliubov dispersion relation. The first clear experimental observation of this dispersion in fluids of light is reported in the next chapter.

2.3.1 Derivation from the Euler's equations

In the following section, equations (2.20) and (2.21) will be directly expressed as function of the propagation distance z (while bearing in mind the mapping $z \leftrightarrow \tau$):

$$\frac{\partial \rho}{\partial z} + \frac{1}{k} \nabla_{\perp} \cdot (\rho \nabla_{\perp} \Phi) + \alpha \rho = 0 \quad (2.23)$$

$$\frac{\partial \Phi}{\partial z} + \frac{1}{2k} (\nabla_{\perp} \Phi)^2 - k \frac{n_2}{n_0} \rho - \frac{1}{2k} \frac{\nabla_{\perp}^2 \sqrt{\rho}}{\sqrt{\rho}} = 0 \quad (2.24)$$

When small amplitude density waves propagate over an uniform background fluid at rest, the density and phase of the overall system can be expressed as follows:

$$\rho(\mathbf{r}_{\perp}, z) = \rho_0(z) + \delta \rho(\mathbf{r}_{\perp}, z) \quad (2.25)$$

$$\Phi(\mathbf{r}_{\perp}, z) = \Phi_0(z) + \delta \Phi(\mathbf{r}_{\perp}, z) \quad (2.26)$$

where $\delta \rho \ll \rho_0$ and $\delta \Phi \ll \Phi_0$ respectively. At the zeroth-order, equations (2.23) and (2.24) simply reads: $\frac{d\rho_0}{dz} - \alpha \rho_0$ (i) and $\frac{d\Phi_0}{dz} = k_0 n_2 \rho_0$ (ii) (k_0 is the laser wave-vector in vacuum). The first equation (i) accounts for the exponential decay of the background density because of linear losses: $\rho_0(z) = \rho_0(0) e^{-\alpha z}$. The second equation (ii) describes the evolution of the phase accumulated by the background field envelope along propagation. In a Kerr medium, the refractive index depends on the laser intensity. We thus expect the phase accumulated by the background fluid at a distance z from the entrance plane to be equal to $k_0 \Delta n z$, where $\Delta n = n_2 \rho$ is the nonlinear change of refractive index. As Δn depends here on the propagation distance because of linear losses, the self-induced zeroth-order phase shift Φ_0 is then finally given by: $\Phi_0(z) = k_0 \langle \Delta n(z') \rangle_z z$, where $\langle \Delta n(z') \rangle_z = \frac{1}{z} \int_0^z \Delta n(z') dz'$ is the average of $\Delta n(z)$ over z . You might be surprised by the fact that there is no contribution in Φ_0 accounting for the linear phase accumulated by the laser beam along propagation. Equation (2.8) provides an explanation for this: by introducing the slow-varying envelope, we choose to describe the physics from the translating frame at c/n_0 so to speak, in which no linear phase is accumulated, by definition.

At the first perturbation order in $\delta\rho$ and $\delta\Phi$, equations (2.23) and (2.24) read:

$$\frac{\partial\delta\rho}{\partial z} + \frac{\rho_0}{k} \nabla_{\perp}^2 \delta\Phi + \alpha\delta\rho = 0 \quad (2.27)$$

$$\frac{\partial\delta\Phi}{\partial z} - k \frac{n_2}{n_0} \delta\rho - \frac{1}{4k} \frac{\nabla_{\perp}^2 \delta\rho}{\rho_0} = 0 \quad (2.28)$$

Drawing on the second-quantization protocol of the Bose field operator one usually carries out in dilute BECs [68], we rewrite $\delta\rho$ and $\delta\Phi$ as follows:

$$\delta\rho(\mathbf{r}_{\perp}, z) = \sqrt{\rho_0} \int \frac{d\mathbf{k}_{\perp}}{(2\pi)^2} \left[a(\mathbf{k}_{\perp}) f_+(\mathbf{k}_{\perp}, z) e^{-i\mathbf{k}_{\perp} \cdot \mathbf{r}_{\perp}} + \bar{a}(\mathbf{k}_{\perp}) f_+^*(\mathbf{k}_{\perp}, z) e^{i\mathbf{k}_{\perp} \cdot \mathbf{r}_{\perp}} \right] \quad (2.29)$$

$$\delta\Phi(\mathbf{r}_{\perp}, z) = \frac{1}{2i\sqrt{\rho_0}} \int \frac{d\mathbf{k}_{\perp}}{(2\pi)^2} \left[a(\mathbf{k}_{\perp}) f_-(\mathbf{k}_{\perp}, z) e^{-i\mathbf{k}_{\perp} \cdot \mathbf{r}_{\perp}} - \bar{a}(\mathbf{k}_{\perp}) f_-^*(\mathbf{k}_{\perp}, z) e^{i\mathbf{k}_{\perp} \cdot \mathbf{r}_{\perp}} \right] \quad (2.30)$$

By reinstating the foregoing expressions of $\delta\rho$ and $\delta\Phi$ in (2.27) and (2.28), one finally obtains a Bogoliubov-de Gennes matrix equation on the Fourier amplitudes f_+ and f_- :

$$i \frac{\partial}{\partial z} \begin{pmatrix} f_+ \\ f_- \end{pmatrix} = - \left[i \frac{\alpha}{2} + \mathcal{H}_{\mathbf{k}_{\perp}} \right] \begin{pmatrix} f_+ \\ f_- \end{pmatrix}, \text{ where } \mathcal{H}_{\mathbf{k}_{\perp}} = \begin{pmatrix} 0 & -\frac{k_{\perp}^2}{2k} \\ -\frac{k_{\perp}^2}{2k} + 2k_0 \Delta n & 0 \end{pmatrix} \quad (2.31)$$

2.3.2 Dispersion relation

We first assume that $\alpha = 0$. In this ideal lossless situation, the matrix $\mathcal{H}_{\mathbf{k}_{\perp}}$ is homogeneous. The Fourier components f_{\pm} of the density and phase fluctuations are therefore plane waves, whose amplitude and longitudinal wave-vector depend on k_{\perp} : $f_{\pm}(\mathbf{k}_{\perp}, z) = f_{\pm}(\mathbf{k}_{\perp}) e^{i\Omega_B(\mathbf{k}_{\perp})z}$. Equation (2.31) reduces finally to an eigenvalue equation whose solutions, the branches of the **Bogoliubov dispersion relation** $\Omega_B(\mathbf{k}_{\perp})$, are found by diagonalizing the matrix $\mathcal{H}_{\mathbf{k}_{\perp}}$:

$$\Omega_B(\mathbf{k}_{\perp}) - \mathbf{k}_{\perp} \cdot \mathbf{v} = \pm \sqrt{-\frac{n_2}{n_0} \rho_0 k_{\perp}^2 + \frac{k_{\perp}^4}{4k^2}}. \quad (2.32)$$

For defocusing Kerr nonlinearity ($n_2 < 0$), $\Omega_B(k_{\perp})$ is a real function of k_{\perp} , which stands for the transverse wave-vector of the plane wave density modulation. The dispersion relation links usually the wave frequency to the wave-vector. In propagating photon fluids however, $\Omega_B(k_{\perp})$ is an inverse length, since the system evolves along z and not over time as usual. Similarly, the sound velocity c_s , the background transverse speed \mathbf{v} or the density wave group velocity \mathbf{v}_g are measured in adimensional units, as they have the physical meaning of propagation angles with respect to the z -axis. Nevertheless, $\Omega_B(k_{\perp})$ can be regarded as a frequency through the $z \leftrightarrow \tau$ mapping. The relation (2.32) describes then the response frequency of the fluid of light to a small density fluctuation $\delta\rho$ whose wave-vector is \mathbf{k}_{\perp} . The term $\mathbf{k}_{\perp} \cdot \mathbf{v}$ describes the shift in this response frequency because of the Doppler effect, when the background fluid is not at rest anymore.

When the wavelength of the modulation $\Lambda = 2\pi/k_{\perp}$ is larger than the **healing length**:

$$\xi \approx \frac{1}{k_{\xi}} = \frac{1}{k} \sqrt{\frac{n_0}{|\Delta n|}}, \quad (2.33)$$

the Bogoliubov dispersion relation is linear and density excitations propagate as collective sound waves. This regime is entirely characterized by the speed of sound: $c_s = \sqrt{-\Delta n/n_0}$ which scales as the square root of the fluid density. Conversely, when Λ is smaller than ξ , the dispersion relation becomes quadratic. Excitations have then a particle-like behaviour: they propagate in the transverse plane as "massive" free particles. Nonlinear interactions only affect in that case the effective time $\tau = L n/c$ (L being the length of the medium) over which those particles propagate – and therefore the dynamical phase accumulated – by modifying the refractive index $n = n_0 + n_2 \mathcal{I}_0$. The Bogoliubov dispersion relation has been plotted in black solid on figure 2.1 for a background fluid at rest (that is, for $\mathbf{v} = \mathbf{0}$). The transverse wave-vector has been scaled by k_ξ and Ω_B by the inverse of the so-called **nonlinear length**, defined by $z_{\text{NL}} = 1/k_0|\Delta n|$ [69]. The red lines and the blue parabola represent the asymptotic sound- and particle-like regimes respectively.

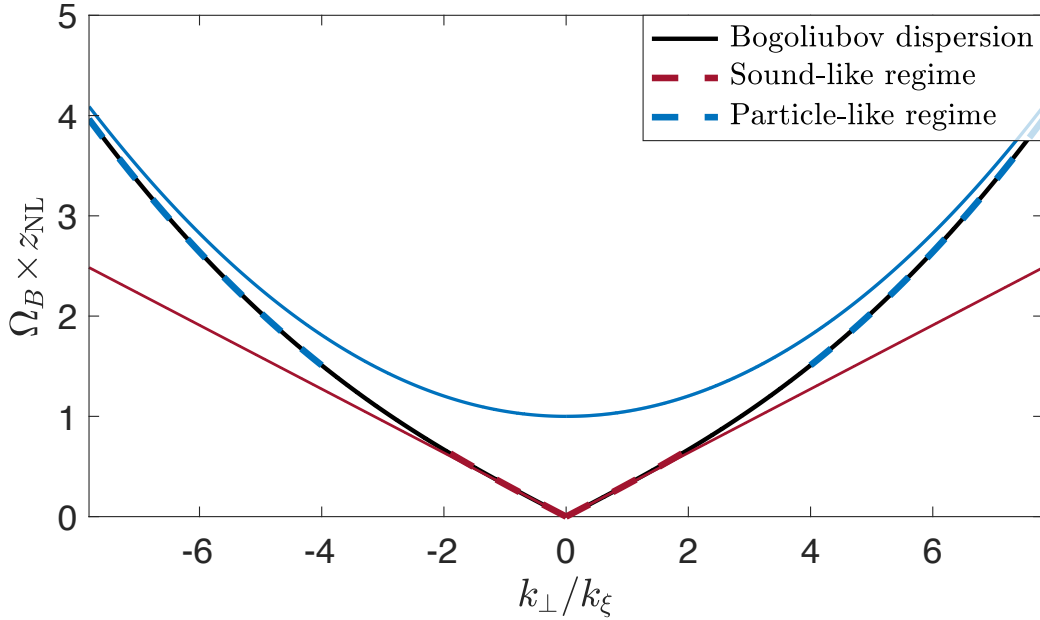


Figure 2.1: Bogoliubov dispersion relation (black solid line) obtained for a fluid at rest. The asymptotic sound- and particle-like regimes have been plotted in red and blue solid. The transverse wave-vector has been scaled by $k_\xi = 2\pi/\xi$ and Ω_B by $1/z_{\text{NL}} = 1/k_0|\Delta n|$.

2.3.3 Landau criterion for superfluidity

The **Landau criterion for superfluidity** states that below some critical flow velocity v_c , the background fluid cannot transfer kinetic energy by exciting density waves anymore [70]. Let's look at equation (2.32) to understand what it is all about. Spontaneous emission of elementary excitations (namely energy dissipation), can occur if and only if such a process is energetically favorable. Emitting a density wave at \mathbf{k}_\perp on a background fluid flowing at \mathbf{v} in the transverse plane costs an energy $\Omega_B|_{\mathbf{v} \neq \mathbf{0}}(\mathbf{k}_\perp) = \mathbf{k}_\perp \cdot \mathbf{v} + \Omega_B|_{\mathbf{v}=\mathbf{0}}(\mathbf{k}_\perp)$. In order for dissipation to be energetically favorable, this energy cost $\Omega_B|_{\mathbf{v} \neq \mathbf{0}}(\mathbf{k}_\perp)$ should be negative:

$$\mathbf{k}_\perp \cdot \mathbf{v} + \Omega_B|_{\mathbf{v}=\mathbf{0}}(\mathbf{k}_\perp) < 0. \quad (2.34)$$

This condition is fulfilled only if $\mathbf{k}_\perp \cdot \mathbf{v} < 0$ and if $\Omega_B|_{\mathbf{v}=0}(\mathbf{k}_\perp) < |\mathbf{v}||\mathbf{k}_\perp|$. In other words, equation (2.34) is satisfied when density waves are emitted upstream and the fluid velocity $|\mathbf{v}|$ exceeds the critical speed defined by:

$$v_c = \min_{\mathbf{k}_\perp} \left\{ \frac{\Omega_B|_{\mathbf{v}=0}(\mathbf{k}_\perp)}{|\mathbf{k}_\perp|} \right\}. \quad (2.35)$$

For a particle-like dispersion for which $\Omega_B|_{\mathbf{v}=0}(\mathbf{k}_\perp) \propto k_\perp^2$, this second condition is fulfilled for arbitrary small fluid velocities and density waves are created as soon as an obstacle is dropped into the flow. Nevertheless, for a sound-like dispersion, equation (2.35) states that excitation are emitted only if $v > v_c = c_s$. This is the Landau criterion for superfluidity: the minimum flow velocity requires to excite a wave by scattering on an obstacle is c_s ; below this limit, the kinetic energy of the fluid is too low to excite any density fluctuation. In order to prove that photon fluids in the propagating geometry are likely to be superfluid, we should thus first demonstrate the existence of such a critical velocity v_c experimentally. In chapter 4, we report the first observation of a sound-like regime in the dispersion relation of density waves in paraxial photon fluids, which is enough to ensure the existence of v_c , according to the Landau criterion. It should thus be possible to observe superfluidity of light using our platform. In this perspective, preliminary results will be discussed in chapter 6.

2.3.4 Derivation from the NLSE

For the sake of completeness, it has to be stressed that the Bogoliubov dispersion relation can be derived directly by linearizing the NLSE, assuming $\mathcal{E}_0(\mathbf{r}_\perp, z) = \mathcal{E}_0(z) + \delta\mathcal{E}(\mathbf{r}_\perp, z)$. One can use the Madelung transform once again to express the field envelope as:

$$\mathcal{E}_0(\mathbf{r}_\perp, z) = \sqrt{\rho_0(z) + \delta\rho(\mathbf{r}_\perp, z)} e^{i[\Phi_0(z) + \delta\Phi(\mathbf{r}_\perp, z)]}, \quad (2.36)$$

which leads at the first-order expansion in $\delta\rho$ and $\delta\Phi$ to the following expression for \mathcal{E}_0 :

$$\mathcal{E}_0(\mathbf{r}_\perp, z) = \underbrace{\sqrt{\rho_0(z)} e^{i\Phi_0(z)}}_{\mathcal{E}_0(z)} + \underbrace{\left[\frac{1}{2} \frac{\delta\rho(\mathbf{r}_\perp, z)}{\sqrt{\rho_0(z)}} + i\sqrt{\rho_0(z)} \delta\Phi(\mathbf{r}_\perp, z) \right]}_{\delta\mathcal{E}(\mathbf{r}_\perp, z)} e^{i\Phi_0(z)}. \quad (2.37)$$

By reinstating equations (2.29) and (2.30) in the right-hand side of equation (2.37), one gets:

$$\mathcal{E}_0(\mathbf{r}_\perp, z) = \mathcal{E}_0(z) + e^{i\Phi_0(z)} \int \frac{d\mathbf{k}_\perp}{(2\pi)^2} \left[u(\mathbf{k}_\perp, z) b(\mathbf{k}_\perp) e^{-i\mathbf{k}_\perp \cdot \mathbf{r}_\perp} + \bar{v}(\mathbf{k}_\perp, z) \bar{b}(\mathbf{k}_\perp) e^{i\mathbf{k}_\perp \cdot \mathbf{r}_\perp} \right], \quad (2.38)$$

where $u = \frac{1}{2}(f_+ + f_-)$ and $v = \frac{1}{2}(f_+ - f_-)$ are the so-called Bogoliubov amplitudes which obey the normalization condition $|u|^2 - |v|^2 = \text{Re}(\bar{f}_+ f_-) = 1$, in the lossless case ($\alpha = 0$). In the lossy case (when $\alpha \neq 0$), $|u_{\mathbf{k}_\perp}|^2 - |v_{\mathbf{k}_\perp}|^2 = N(\mathbf{k}_\perp, z)$, where $N(\mathbf{k}_\perp, z)$ is a non-trivial normalization function that depends on α [71]. The same transformation was used in 1958 by Nikolay Bogolyubov so as to find solutions of the BCS theory in homogeneous systems [72]. By replacing in the NLSE equation (2.9) \mathcal{E}_0 by its expression equation (2.38), one easily obtains a coupled system of equations on the Bogoliubov amplitudes u and v :

$$\left\{ -\frac{\partial \Phi_0}{\partial z} u + i \frac{\partial u}{\partial z} \right\} e^{i\Phi_0} = - \left\{ \frac{k_{\perp}^2}{2k_0} + i \frac{\alpha}{2} \right\} u e^{i\Phi_0} - k_0 n_2 \left(2|\mathcal{E}_0|^2 u e^{i\Phi_0} + \mathcal{E}_0^2 v e^{-i\Phi_0} \right) \quad (2.39)$$

$$\left\{ \frac{\partial \Phi_0}{\partial z} v + i \frac{\partial v}{\partial z} \right\} e^{-i\Phi_0} = \left\{ \frac{k_{\perp}^2}{2k_0} - i \frac{\alpha}{2} \right\} v e^{-i\Phi_0} + k_0 n_2 \left(2|\mathcal{E}_0|^2 v e^{-i\Phi_0} + \mathcal{E}_0^{*2} u e^{i\Phi_0} \right) \quad (2.40)$$

which can be simplified using the fact that $\mathcal{E}_0 = \sqrt{\rho_0} e^{i\Phi_0}$ and $\frac{d\Phi_0}{dz} = k_0 n_2 |\mathcal{E}_0|^2$:

$$i \frac{\partial}{\partial z} \begin{pmatrix} u \\ v \end{pmatrix} = - \left[i \frac{\alpha}{2} + \overline{\mathcal{H}}_{\mathbf{k}_{\perp}} \right] \begin{pmatrix} u \\ v \end{pmatrix}, \text{ where } \overline{\mathcal{H}}_{\mathbf{k}_{\perp}} = \begin{pmatrix} \frac{k_{\perp}^2}{2k} + k_0 \Delta n & k_0 \Delta n \\ -k_0 \Delta n & -\frac{k_{\perp}^2}{2k} - k_0 \Delta n \end{pmatrix}. \quad (2.41)$$

One finally retrieves the Bogoliubov dispersion relation (2.32) by diagonalizing $\overline{\mathcal{H}}_{\mathbf{k}_{\perp}}$.

2.4 Bogoliubov dispersion in a lossy nonlocal medium

So far, we have derived the Bogoliubov dispersion relation in the ideal lossless case, even if the derivations in subsections 2.3.1 and 2.3.4 take linear losses into account. In experiments, linear absorption cannot be neglected usually. Moreover, as mentioned in paragraph 1.3.8, photon-photon interactions in warm rubidium vapors are nonlocal because of the ballistic transport of excited atoms. In the next section, the Bogoliubov dispersion relation (2.32) is therefore generalized in order to take both these effects into account.

2.4.1 Lossy nonlinear medium ($\alpha \neq 0$)

We first generalize the Bogoliubov dispersion relation (2.32) for a lossy local Kerr medium. Suppose the absorption coefficient α is non-zero but sufficiently small to make the evolution of the field envelope \mathcal{E}_0 adiabatic along the z -axis. The eigenvectors of $\mathcal{H}_{\mathbf{k}_{\perp}}(z)$ defined in equation (2.31) are then slowly-varying functions of z that strictly follow the variations of the corresponding eigenvalues along z [71]. The adiabatic solutions of equation (2.31) may thus be written as follow: $f_{\pm}(\mathbf{k}_{\perp}, z) = \tilde{f}_{\pm}(\mathbf{k}_{\perp}, z) e^{i\Omega_{\text{eff}}(\mathbf{k}_{\perp})z}$ where:

$$\Omega_{\text{eff}}(\mathbf{k}_{\perp}) = \langle \Omega_B(\mathbf{k}_{\perp}, z') \rangle_z, \quad (2.42)$$

$$\Omega_B(\mathbf{k}_{\perp}, z) = i \frac{\alpha}{2} + \sqrt{-\frac{n_2}{n_0} \rho_0(z) k_{\perp}^2 + \frac{k_{\perp}^4}{4k^2}}, \quad (2.43)$$

$$\tilde{f}_{\pm}(\mathbf{k}_{\perp}, z) \propto \left(\frac{k_{\perp}^2/(2k)}{\Omega_B(\mathbf{k}_{\perp}, z) - i\alpha/2} \right)^{\pm \frac{1}{2}}, \quad (2.44)$$

for a background fluid at rest ($\mathbf{v} = \mathbf{0}$). The density fluctuation amplitude exponentially decays because of the linear absorption. The latter also affects the background density which decreases similarly along the z -axis, according to the Beer-Lambert law. The sound velocity decreases consequently from one plane to the next since it depends on the square root of the fluid density. Everything happens as if sound-waves were moving slower and slower as "time" goes by. One can then define an effective sound velocity by averaging $c_s(z)$ over z : $c_{s,\text{eff}} = \langle \sqrt{-\Delta n(z')/n_0} \rangle_L = c_s(0) z_{\text{eff}}(\alpha)/L$, where $z_{\text{eff}}(\alpha) = 2[1 - \exp(-\alpha L/2)]/\alpha$.

In our experiments, the main effect of absorption is to multiply the sound velocity c_s of the lossless case by the scaling factor $z_{\text{eff}}(\alpha)/L$. It thus mainly changes the slope of the dispersion in the sonic regime without affecting its shape in-depth. In other words, if the input intensity \mathcal{I}_0 is multiplied by $L/z_{\text{eff}}(\alpha)$, the curve of the effective dispersion relation $\Omega_{\text{eff}}(\mathbf{k}_\perp)$ will almost exactly translate on the curve of $\Omega_B|_{\alpha=0}(\mathbf{k}_\perp)$, obtained for $\Delta n = n_2 \mathcal{I}_0$.

2.4.2 Lossy nonlinear medium with effective nonlocal interactions

In the previous paragraph, the dielectric response of the medium was supposed to be local. The nonlinear change of refractive index Δn at a given position \mathbf{r}_\perp in the transverse plane was thus only depending on the laser intensity at that point and not on the intensity nearby. Let's assume from now on that the medium optical response is nonlocal, which is by the way the case in a wide variety of Kerr nonlinear mediums, such as hot alkaline vapors [50] but also thermo-optic liquids [28]. The NLSE (2.9) reads then as follow:

$$i\partial_z \mathcal{E}_0(\mathbf{r}, z) = - \left[\frac{1}{2k} \nabla_\perp^2 + \frac{i\alpha}{2} + k \frac{n_2}{n_0} \int_S G(\mathbf{r} - \mathbf{r}') |\mathcal{E}_0(\mathbf{r}', z)|^2 d\mathbf{r}' \right] \mathcal{E}_0(\mathbf{r}, z), \quad (2.45)$$

where G is the nonlocal response function in real space. Equation (2.31) is still correct in the nonlocal case if the fluid density $\rho = |\mathcal{E}_0|^2$ is replaced by the integral in the right-hand side of equation (2.45), which is the convolution of ρ_0 with G . Let \tilde{G}_γ^b stand for the Fourier transform of the ballistic response function \tilde{G}_γ^b in Rubidium vapors:

$$\tilde{G}_\gamma^b(k_\perp) = \mathcal{F}[\tilde{G}_\gamma^b](\mathbf{k}_\perp) = \frac{\sqrt{\pi}}{\gamma} \frac{e^{1/(k_\perp l_b)^2}}{k_\perp l_b} \text{Erfc}[1/(k_\perp l_b)]. \quad (2.46)$$

This expression has been derived in the first chapter (see paragraph 1.3.8 ii, equation (1.75)). The ballistic transport length scale is defined by $l_b = u \tau$, where $u = \sqrt{2k_B T/m}$ stands for the most probable speed of the atoms in the transverse plane (at the vapor temperature T) and $\Gamma = \Gamma + \Gamma_t$ for the total decay rate of the excited state addressed by the laser field. Using the convolution theorem, the dispersion relation (2.43) can be rewritten as follows:

$$\Omega_B(\mathbf{k}_\perp, z) - \mathbf{k}_\perp \cdot \mathbf{v} = i\frac{\alpha}{2} + \sqrt{-\frac{n_2}{n_0} \rho_0(z) [\gamma \tilde{G}_\gamma^b(k_\perp)]} k_\perp^2 + \frac{k_\perp^4}{4k^2}. \quad (2.47)$$

As previously, the term $\mathbf{k}_\perp \cdot \mathbf{v}$ describes the shift of the density wave frequency because of Doppler effect when it propagates at \mathbf{k}_\perp on top of a moving background. Equation (2.47) is the most general expression for the Bogoliubov dispersion relation, taking into account absorption and nonlocality at the same time. The dispersions obtained in local (green line) and nonlocal (red line) Kerr medium have been plotted as function of k_\perp/ξ on figure 2.2(a) in the lossless case. The dashed black lines represent the sound-like and the particle-like asymptotic regimes in the local case. The ballistic transport length scale l_b is about $7.5 \mu\text{m}$ at $T = 400 \text{ K}$. For clarity, the red curve has been plotted for $l_d = 100 \mu\text{m}$ in order to clearly observe the effects of nonlocality on the dispersion.

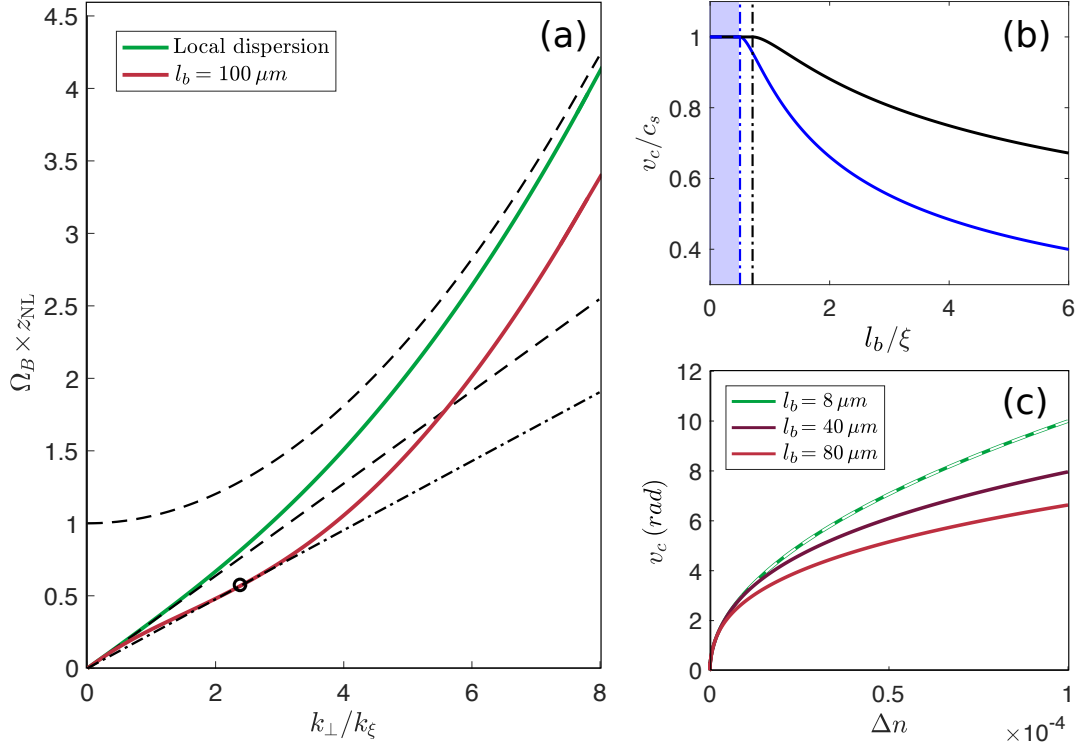


Figure 2.2: (a) Local (green) and nonlocal (red) Bogoliubov dispersion relations obtained in the lossless case. Asymptotic behaviours are plotted in dashed black for the local case. For high enough nonlocalities, an inflexion point appears (circle) and the critical velocity starts being lower than c_s . (b) Variation of v_c/c_s as function of l_b/ξ for ballistic (black line) and diffusive nonlocality (blue line). In the ballistic case, $v_c = c_s$ as long as $l_b < 0.71 \xi$, while, in the diffusive one, $v_c = c_s$ as long as $l_b < \xi/2$ precisely [73]. (c) Critical velocity v_c as function of Δn . The white dashed line plots the behaviour of c_s for comparison.

The Landau criterion for superfluidity (see subsection 2.3.3) states that below a critical flow velocity, the photon fluid cannot dissipate energy anymore by emitting density waves and behaves thus as a superfluid in the transverse plane. In the local case, this critical velocity v_c is equal to the speed of sound c_s . In the nonlocal case however, the situation is different. For strong enough nonlocality, an inflexion point (black circle) appears on the nonlocal dispersion curve. The speed of sound c_s is still well defined as $\Omega_B|_{\mathbf{v}=0}(\mathbf{k}_{\perp}) \simeq c_s k_{\perp}$ when $k_{\perp} \ll k_{\xi}$ (indeed, $\tilde{G}_{\gamma}^b(k_{\perp}) \simeq 1/\gamma + O(k_{\perp}^2)$ in that case). However, it is not anymore equal to the critical speed, which is given by the slope of the tangent to the nonlocal dispersion curve at the inflexion point now (black dashed-dotted line) and therefore, $v_c < c_s$. In order to be superfluid, the photon fluid must flow toward any obstacle with a velocity lower than v_c ; the nonlocality has thus reduced the range of velocities for which superfluid flows of light can be observed. Let's be more quantitative. According to equation (2.35), the critical speed is obtained by calculating the minimum of the phase velocity $v_{\text{ph}}(\mathbf{k}_{\perp}) = \Omega_B|_{\mathbf{v}=0}(\mathbf{k}_{\perp})/|\mathbf{k}_{\perp}|$.

On figure 2.2(b), the critical speed (normalized by the sound velocity c_s) has been plotted as function of l_b/ξ in black solid. Two regimes can be identified:

- (1) For weak enough nonlocalities, that is, when l_b/ξ is lower than 0.71, the minimum of v_{ph} is obtained for $k_\perp = 0$ and is still equal to the speed of sound c_s . The nonlocality slightly affects the shape of the dispersion relation but the "local" Landau criterion for superfluidity remains valid.
- (2) For higher nonlocalities (right side of the black dashed-dotted line), the critical speed starts decreasing slowly when l_b/ξ increases.

On figure 2.2(b), the critical speed obtained by considering a diffusive nonlocality has also been plotted (blue solid line), for comparison. This is, for instance, the kind of nonlocality encountered in thermo-optic liquids, where the heat diffusion inside the material makes the optical response nonlocal [28]. By using a distributed loss model [73], we can show that the Fourier transform of the response function is Lorentzian in that case: $\tilde{G}_\sigma^d(\mathbf{k}_\perp) = 1/(1+\sigma^2 k_\perp^2)$ (σ is the range of the nonlocal interaction). This diffusive response function falls off much more rapidly than the ballistic one in Fourier space (as mentioned in paragraph 1.3.8 ii). Consequently, it is not surprising to observe that the critical speed decreases more slowly for ballistic nonlocality than for diffusive one. Moreover, the threshold value at which v_c starts decreasing is higher in our case than for thermo-optic liquids, for which it lies at $\sigma/\xi = 0.5$ (blue dashed-dotted line). Much larger effects on the dispersion relation are thus expected in fluids of light propagating in these systems than in rubidium vapors.

Let's finally briefly comment the figure 2.2(c), where the critical velocity v_c has been plotted as function of the nonlinear change of refractive index $\Delta n = n_2 \mathcal{I}_0$, for a ballistic nonlocality. As you can see, it perfectly matches the speed of sound (white dashed line) when $l_b = 8 \mu\text{m}$. In this case, when Δn ranges from 0 to 1×10^{-4} , the ratio l_b/ξ varies from 0 to 0.64 and remains below 0.71. In other words, at every value took by Δn on the graph of figure 2.2(c), the critical speed is equal to the speed of sound when $l_b = 8 \mu\text{m}$. This is not anymore true when $l_b = 40 \mu\text{m}$ or $80 \mu\text{m}$, as l_b/ξ varies then up to 3.2 and 6.4, respectively. In both cases, there is thus a critical value of the nonlinear change of refractive index, Δn_c , at which an inflexion point appears in the dispersion. Thereupon, we expect the critical speed to remain lower than the speed of sound when further increasing Δn . This is indeed what we observe.

Chapter 3

Atomic medium characterization

In chapter 2, I have shown how the envelope of an intense laser field, propagating through a Kerr-type medium, can be regarded as a 2D photon fluid flowing into the plane perpendicular to the optical axis. The main motivations of this work is to study experimentally some of the hydrodynamical properties of those photon fluids in hot rubidium vapors. But before showing the results we obtained in that respect, I would like to introduce the experimental tools and methods used to produce and characterise such paraxial fluids of light. I first give some technical details about the glass cells containing the rubidium vapor and about the home-made heating system designed to control its temperature. I then briefly present the laser sources used to generate propagating photon fluids and, more generally, to address the rubidium D -lines. In a second part, the measurements performed to access the vapor temperature T , the atomic density N and the nonlinear refractive index n_2 are presented.

3.1 Experimental tools

3.1.1 Rubidium cells and oven design

The glass cells we use have all been manufactured by *Triad Technology* which provides high purity reference cells for spectroscopic applications. They are cylindrical (1" diameter) and closed on both sides by 1 mm thick anti-reflective coated windows at 780 and 795 nm. The length of the cells ranges from 1 to 7.5 cm depending on the experiment we carry out. In order to heat the rubidium vapor at high temperatures, the cells are disposed inside a copper cylinder (5 mm thick, 10 cm long) which is enveloped by Kapton flexible heaters (wattage: 5 or 10 W/in at 28 V) from *Omega*. The copper cylinder has a good thermal inertia protecting the cell from fast temperature variations. The whole is placed into an aluminum enclosure with flat 1 mm thick anti-reflective coated windows on both sides to maintain optical access to the cell. The temperature is monitored by a sensor set close to the cell tip (thermocouple). Setting up a feedback loop was not required, as the heating system was efficient enough to stabilize the cell temperature at $\pm 1^\circ\text{C}$ during experiments. Let's finally mention that about 6% of laser input power is lost in reflections on the cell and enclosure windows (8 interfaces), when the laser is highly detuned from the rubidium *D*-lines.

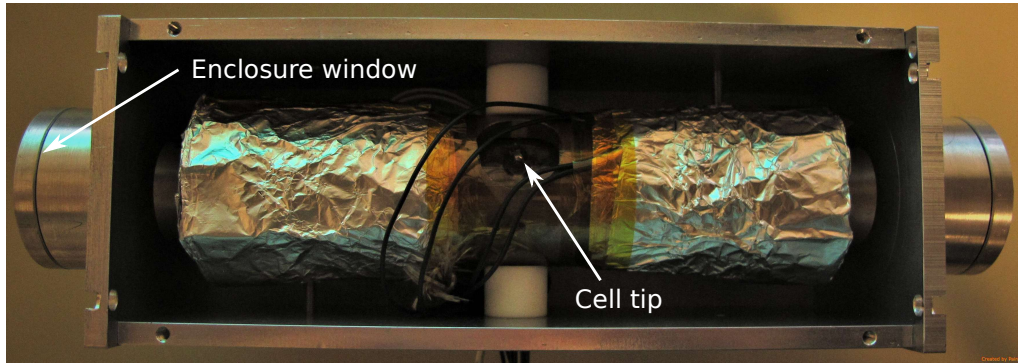


Figure 3.1: Heating system. A 7.5 cm long cell is placed inside 5 mm thick copper cylinder. Flexible heaters are arranged all around and covered with several layers of aluminum foils to reduce losses by thermal radiation and provide a better heating efficiency. The cell tip (visible at the center of the picture) is about 80°C .

The heating system is designed to prevent rubidium from condensing on the cell windows. In the cell, part of rubidium is liquid and the rest is in vapour phase. Despite the fact that condensation is very unlikely to happen at temperatures above the rubidium melting point ($T_m = 39.3^\circ\text{C}$), small droplets can still form locally at the center of the cell windows, where the glass temperature is lower. Things are getting worse then as a kind of avalanche nucleation process leads the rubidium nearby to condense a well. If condensation appear only on one window, increasing slightly the voltage applied across the heater rolled around the window at issue is often sufficient to remove it. If it appears on both windows, we have then to displace the cold point from their centers to the cell tip. As you can see on figure 3.1, a 1.5 cm diameter hole has been drilled in the copper cylinder to let the cell tip be in contact with the air inside the enclosure, which maintains it at a lower temperature. By doing so, the rubidium will preferentially condenses inside of it and not on the windows anymore.

Of course, the temperature recorded with the thermocouple (silver wire on the picture 3.1) is not the absolute temperature of the rubidium vapor T . In order to estimate parameters such as the atomic density N , the atoms average speed u or the transport length scales (and thus to characterize the vapor optical response), the absolute temperature is required. It can be extrapolated in practice by fitting the linear transmission spectrum, which is Doppler broadened by the atomic motion in the cell, as we will see in subsection 3.2.2.

3.1.2 Laser sources

The transverse plane dynamics of nonlinear phenomena is controlled by the nonlinear change of refractive index $\Delta n = n_2 \mathcal{I}_0$. In order for this dynamics to be conservative, linear losses should be low, which is possible only when the laser frequency is detuned far off-resonance. In that case, the nonlinear refractive index n_2 is small as well, because it scales as $1/\Delta^3$ (Δ being the laser detuning), as discussed in the paragraph 1.2.3 iii. Moreover, being in the hydrodynamical regime (defined in section 2.1.3 iii) requires large values of Δn and thus high laser intensities. At the end of the day, generating paraxial photon fluids in rubidium vapors requires powerful CW laser sources which can be easily tuned on a wide range of frequencies (several gigahertz) around the desired atomic resonance. Two kinds of sources satisfying these conditions are used in the lab. The first is a continuous-wave Ti-Sapphire laser and the second an amplified external-cavity diode laser. Both sources provide an output power greater than 2 W and an easy control over the laser frequency, which can be widely tuned around the rubidium D_1 and D_2 line. In this subsection, I will give some technical details about these two sources, starting with the Ti-sapphire laser, which is the one I predominantly used throughout my thesis.

i SolsTiS Ti-sapphire laser

SolsTiS is a tunable narrow linewidth continuous-wave Ti-Sapphire laser from *M Squared*. It consists of a monolithic ring cavity in which a crystal of sapphire, doped with Ti^{3+} ions, has been introduced. This crystal is pumped with a Verdi V10 manufactured by *Coherent*, which is a 10 W frequency-doubled Nd:YVO4 laser. Because of the large gain bandwidth of the crystal, lasing effect can be reached for a broad range of wavelengths, extending from 670 to 990 nm. In order to ensure the single-frequency operation of the SolsTiS cavity, hole burning effects in the gain medium must be removed. This is achieved in SolsTiS by using the so-called bow tie cavity geometry, together with an optical isolator, which forces the ring cavity to operate uni-directionally. This results in a traveling wave that ensures a minimum of spatial-hole burning.

In order to tune the SolsTiS output wavelength, a motorized birefringent filter (BRF) is used. This filter introduces a wavelength dependent loss into the cavity. The wavelength tuning is then performed by simply rotating the BRF, which provides a relatively rapid but coarse frequency adjustment however. If a finer control over the wavelength is needed, the SolsTiS intracavity Fabry-Pérot étalon can be used. The étalon introduces a spectral loss into the cavity that is a much sharper function of frequency than the BRF. Thus, by electronically adjusting the étalon spacing (that is, its tilt angle), the SolsTiS output wavelength may be finely adjusted. In order to ensure the long-term single mode operation of the ring cavity, an electronic servo locking of étalon is provided.

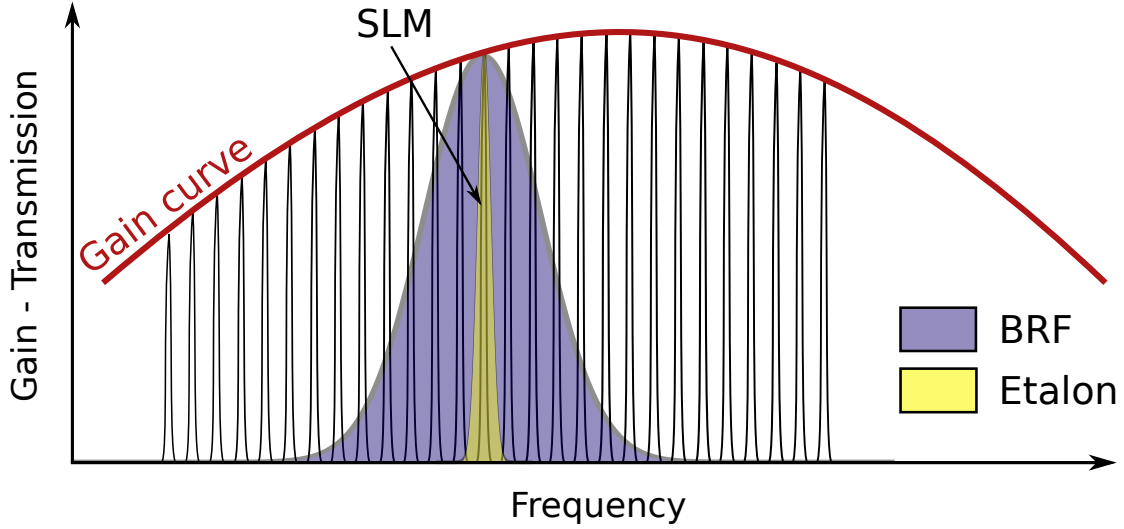


Figure 3.2: Principle of the single-mode operation of the Ti-Sapphire laser. The gain of the crystal is plotted in red as function of frequency. The laser frequency comb (black peaks) represents all the longitudinal modes (LM) sustained by the ring cavity. The Lyot filter (or birefringent filter, BRF) transmits only certain modes. The étalon, whose spacing is electrically stabilized, finally selects a single longitudinal mode (SLM).

The servo locking of the étalon prevents the cavity from jumping from one longitudinal mode to the other. However, this locking does not compensate for the long-term frequency drifts of the cavity itself. In order to solve this issue, the SolsTiS cavity has been locked on a high stability, high finesse reference cavity. This locking reduces the laser linewidth to less than 50 KHz. Slaving the SolsTiS to this internal reference is performed by:

- (1) directing a small fraction of its output power to the reference cavity;
- (2) locking its output frequency to a reference cavity fringe, mounting one of the SolsTiS cavity mirror on a fast piezo-electric transducer (PZT).

With the SolsTiS cavity slaved to the reference cavity, the laser output frequency can then be scanned (or offset) by scanning (or adjusting) the reference cavity length itself with a high degree of precision. Moreover, temperature-induced changes in the reference cavity length are compensated, further enhancing the stability of the reference cavity and, consequently, the stability of the SolsTiS output laser frequency. Nevertheless, it is worth noting that this internal reference is not locked to an absolute reference, such as an atomic absorption line. This might seem a bit surprising at first but as we always highly detuned the laser frequency far off-resonance, the remaining drift in the Solstis frequency – which is about 50 MHz/hr/°C – does not have any influence in practice. Moreover, we continuously monitor the laser frequency in experiments using a lambda-meter (either the WSB-10 from *High Finesse* or the LW10 from *Resolution Spectra*). This enables us to reset (by hand) the laser frequency as soon as it drifts too far from the initial desired value. Let's finally mention that the stability of the internal locking depends strongly on the injection of the Verdi inside the SolsTiS cavity. When the alignment is optimized (at a given frequency), the output power should be maximized (typically, $P_0 \simeq 3.2$ W at 780 nm) as well as the robustness of the SolsTiS internal locking system.

ii Amplified external-cavity diode laser

Amplified external-cavity diode lasers is a compact, low cost and easy-to-handle alternative to Dye or Ti-Sapphire laser ring systems. In this paragraph, I briefly present the different blocks composing this other laser source, that we also used to generate paraxial photon fluids.

Diode laser. Diode lasers are semiconductor p - n junction devices in which lasing conditions are created at the junction by pumping a diode with an electrical current. Forward electrical bias across the laser diode causes the two species of charge carrier – holes and electrons – to be "injected" from opposite sides of the p - n junction into the depletion region. This region, devoid of any charge carriers, forms as a result of the difference in electrical potential between n - and p -type semiconductors. By recombining, electron/hole pairs releases a photon whose energy is defined by the semiconductor band-gap. This process is spontaneous but can also be stimulated by photons passing nearby. In order to enhance stimulated recombination of electron/hole pairs, the gain medium is surrounded by a cavity, as in every other laser system. In the simplest diode laser design, an optical waveguide – trenched in the crystal surface – confines the light to a relatively narrow line. The two ends of the crystal are cleaved to form a Fabry–Pérot resonator. Light reflects back and forth inside the cavity and is amplified by stimulated emission. Finally, if there is more amplification than loss, the diode starts lasing.

The emission frequency of a diode laser can be fine-tuned by adjusting the current across the p - n junction and its temperature. If the laser diode is tuned by adjusting the current at fixed temperature, mode hops – *ie* jumps over large wavelength intervals – will occur after a short continuous dependence of the wavelength on the current. These points of mode instability can be shifted by changing the p - n junction temperature. Most of the time nevertheless, the desired wavelength can not be reached by adjusting only these two parameters.

External-cavity diode laser (ECDL). ECDL systems are tunable laser sources based on double heterostructures diode lasers, whose operation principal is sketched on figure 3.3(a). The light emitted from the front facet of the laser diode is collimated with a lens and hits a reflection grating, aligned in the "Littrow" configuration [74], as illustrated on figure 3.3(b). The first diffraction order is reflected and focused back into the laser diode. As this optical feedback is much higher than the reflection from the diode front facet, the extended cavity, formed by the diode rear facet (highly reflective) and the reflection grating, forces the diode into single-frequency operation. Since the length of this extended cavity resonator is larger than the diode one, ECDLs provide lower phase noise and smaller emission linewidth than free-running laser diodes. Moreover, in this external-cavity configuration, the frequency of the master oscillator (that is, of the laser diode) can be coarsely tuned over several tens of nanometers by simply rotating the reflection grating.

Tapered amplifier (TA). A TA is an optical amplifier that is usually used to increase the power of the laser field generated by the ECDL system. Its operation principle is as follows. The diode output beam is injected into a ridge waveguide, which is only a few microns wide. Thereafter, the light gets into the tapered region of the gain medium, whose width increases towards the output facet of the TA (up to hundred of micrometers). This tapered structure is required to prevent the TA from being damage by large intensities. The whole tapered area is covered with an electrode for supplying the pump current (typically a couple of amperes), which makes the device amplifying, just as in a conventional semiconductor optical amplifier.

The anti-reflection coating on the TA facets prevents any laser emission without seeding and ensures the single-mode operation of the amplifier. Because of its broad gain profile, the TA operates in a wide frequency range (typically, from 775 nm to 800 nm) and delivers a laser power greater than 2.5 W, which is sufficient for our applications.

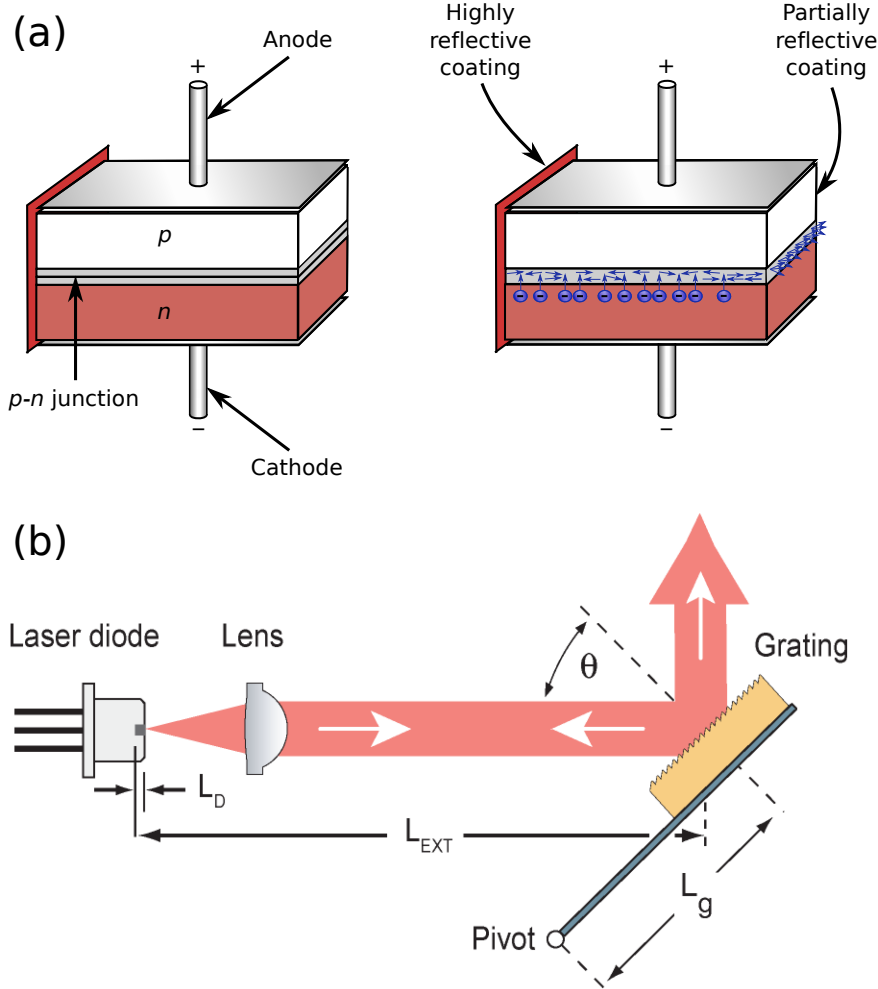


Figure 3.3: (a): Sketch of a double heterostructures diode laser source. A layer of a low band-gap material is sandwiched between two layers of a high band-gap material. Each of the junctions between different band-gap materials is called a heterostructure, hence the name double heterostructure (DH) laser. In that respect, the diode laser described in the text may be referred to as a homojunction laser. The active region of a DH laser, where free electrons and holes exist simultaneously, is limited to within the thin middle layer. Consequently, the amount of electron hole-pairs that contributes to amplification is much higher in DH diode lasers than in homojunction ones. (b) Sketch of the Litrow configuration (from [75]). The diode of figure (a) emits light that is collimated by a lens onto a diffracting grating. The first diffraction order is sent back into the laser diode, which enables us to select a single longitudinal cavity mode. Tuning the angle θ allows to coarsely change the laser frequency.

3.2 Methods I – Absolute vapor temperature measurement

As we have seen in chapter 1, many parameters characterizing the rubidium vapor depend on the absolute temperature T . It controls for instance the atoms velocity which impacts the Doppler width, the filling and transit rates and the transport length scales. It also sets the atomic density. Being able to accurately measure T is thus of paramount importance. I start this section by introducing the Doppler-free saturated absorption spectroscopy. This technique provides an accurate frequency reference used to measure T by fitting the transmission spectrum of a low power beam, as we will see in a second step.

3.2.1 Saturated absorption spectroscopy

i Doppler-limited spectroscopy

Frequencies at which hyperfine transitions occur can all be seen as absolute and universal frequency references. They can be used to calibrate frequency-measuring devices such as lambdameters for instance. At millikelvin temperatures, Doppler broadening is inexistent. In that case, the transmission profile of a weak probe passing through a cold rubidium gas as function of its frequency is a succession of dips. Each dip is related to a hyperfine transition. By identifying them, one is able to:

- (1) define an absolute frequency reference, by associating the minimum of one dip to the corresponding tabulated hyperfine transition frequency.
- (2) scale the frequency axis accurately, by associating the distance between two dips to the difference in the transition frequencies to which they correspond.

The precision of this calibration is limited by the dips linewidth, which is typically of the order of $\Gamma \simeq 2\pi \times 6$ MHz. However, the situation drastically changes at room temperature. The width of the Maxwell-Boltzmann distribution is about $2\pi \times 300$ MHz at $T \simeq 20^\circ\text{C}$, *ie* of the order of the splittings between hyperfine excited states and much larger than Γ . Because of the Doppler broadening, the dips will therefore merge with each other, making the previous identification difficult if not impossible. Moreover, in cases where steps (1) and (2) are still doable (when the laser frequency is tuned over the D_1 line of ^{87}Rb for instance, for which the excited state splitting $\delta_{HF} \simeq 2\pi \times 815$ MHz is larger than the Doppler width) the resolution on the frequency reference is then limited by the Doppler linewidth.

ii Doppler-free spectroscopy

In order to overcome the issue of Doppler broadening without cooling down the atomic vapor to millikelvin temperatures, one usually resorts to saturated absorption spectroscopy [76] which is based on a simple pump-probe experiment. A laser beam is sent through the vapor to saturate the atomic transitions (pump) and reflects back onto a mirror. The counter-propagating reflected beam (probe) is separated from the incoming one by a beam splitter. As pump and probe address opposite velocity classes (since they counter-propagate inside the rubidium cell), only atoms having a zero velocity projection on the optical axis are resonant simultaneously with both lasers. In that case, the absorption of the probe beam is reduced by the saturation induced by the pump. Transmission peaks appear then in the transmission spectrum when the laser frequency matches one of the transition frequencies between ground and hyperfine excited states. Those peaks are clearly visible in the spectra

plotted on insets (a) and (c) of figure 3.4, obtained by scanning the laser frequency ω over the rubidium D_2 line. Four large dips are also clearly discernible.

- The 1st and 4th (from left to right) result from the overlap of the Doppler-broadened absorption lines associated to transitions from the ground states $F_g = 2$ and $F_g = 1$ to the hyperfine states within the fine level $5^2P_{3/2}$ of rubidium 87 (see figure 3.4(a)). The spacing between these two dips is therefore equal to the ground state hyperfine splitting in rubidium 87 ($\delta_0 \simeq 6.8$ GHz).
- The 2nd and 3rd result from the overlap of the Doppler-broadened absorption lines associated to transitions from the ground states $F_g = 3$ and $F_g = 2$ to the hyperfine states within the fine level $5^2P_{3/2}$ of rubidium 85. The spacing between the dips is thus the ground state hyperfine splitting in rubidium 85 ($\delta_0 \simeq 3.0$ GHz).

In the D_2 line, three transitions are allowed between each ground state and the hyperfine excited state manifold. Three saturated absorption peaks are thus expected in each of the large dips of the transmission profiles. As you may have noticed, the saturated absorption spectra show however a more complex structure: crossover resonance peaks appear exactly in between each pair of transition peaks. By identifying each feature in these spectra and by calculating the frequency spacing between two of them, one can then calibrate the frequency axis with a much better accuracy than using Doppler-limited spectroscopy. The resolution is now given by the width of the transmission peak, which is of the order of the decoherence rate $\Gamma/2$ (or Γ for cycling transitions), when no other phenomenon than spontaneous emission contributes to the linewidth (such as Rb-Rb collisions for example). In figure 3.4, I choose the position of the $F_g = 3 \rightarrow F_e = 4$ transition peak (2) of ^{85}Rb as origin for the x -axis. It is 1.13 GHz blue-detuned with respect to the $F_g = 2 \rightarrow F_e = 3$ transition peak (1) of ^{87}Rb , used to scale the frequency axis.

3.2.2 Vapor temperature and atomic density

As mentioned in 3.1.1, measuring the absorption of a low power probe beam propagating through a rubidium cell is an accurate way of accessing the vapor absolute temperature T . The absorption of a monochromatic laser field propagating along the z -direction across a uniform density atomic vapour is given by the Beer-Lambert law [32]:

$$\mathcal{I}(\mathbf{r}, z) = \mathcal{I}_0(\mathbf{r}) \exp \left\{ - \int_0^z \alpha [T, \mathcal{I}(\mathbf{r}, z')] z' dz' \right\} \simeq \mathcal{I}_0(\mathbf{r}) \exp [-\alpha_0(T) z] \quad (3.1)$$

where $\mathcal{I}(\mathbf{r}, z)$ is the laser intensity after a propagation over z in the medium, $\alpha_0 = k \text{Im} [\chi^{(1)}]$ the linear absorption coefficient and $\mathcal{I}_0(\mathbf{r})$ the laser intensity in the cell entrance plane. Equation (3.1) holds only if the intensity of the incoming field is sufficiently weak to ensure that α is independent of \mathcal{I} . In that case, the absorption profile can be easily fitted (T being the only fitting parameter). A discussion on how weak the light has to be for this assumption to be valid is given in [32]. In practice, the input light intensity has to be way smaller than the on-resonance saturation intensity. The medium transmission is then defined by: $\mathcal{T} = \exp [-\alpha_0(T) L]$ (L being the length of the cell). In the 3-level system described in 2.3, a good approximation of the dielectric susceptibility $\chi^{(1)}$ is obtained by summing the linear susceptibilities associated to the $|1\rangle \rightarrow |3\rangle$ and the $|2\rangle \rightarrow |3\rangle$ transitions: $\chi^{(1)} \simeq \chi_{1 \rightarrow 3}^{(1)} + \chi_{2 \rightarrow 3}^{(1)}$ (because $\mathcal{I} \ll \mathcal{I}_s$). The expression of $\chi_{1 \rightarrow 3}^{(1)}$ and $\chi_{2 \rightarrow 3}^{(1)}$ taking into account Doppler broadening has been derived in section 2.3. Therefore, the theoretical Doppler broadened transmission of the medium is known and can be used to fit the experimental transmission spectra.

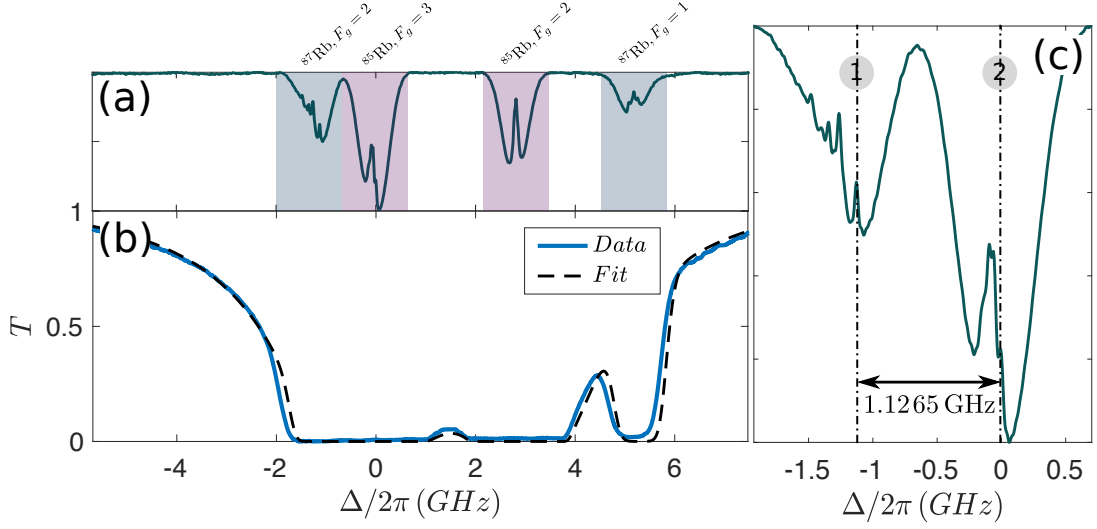


Figure 3.4: (a) and (c): Saturated absorption spectra obtained using an **isotopic mixture** of rubidium atoms (natural proportions), heated up at 50°C to increase the atomic density and the signal over noise ratio. As mentioned in the text, the $F_g = 3 \rightarrow F_e = 4$ transition peak (2) has been chosen as origin for the x -axis; the frequency scale has been calibrated using the frequency spacing between peaks (2) and (1), the latter corresponding to the $F_g = 2 \rightarrow F_e = 3$ transition. (b) Transmission spectrum of an isotopically pure ^{85}Rb vapor heated up at 134°C. The experimental profile (blue line) has been fitted to extract the absolute vapor temperature (dashed line). The cell is 7.5 cm long.

The experimental transmission profile is obtained by sending on a photo-diode a low power Gaussian beam which has propagated through the rubidium cell. The laser frequency is scanned over 15 GHz across the rubidium D_2 line. At high temperatures, the transmission profile looks like the blue solid curve on figure 3.4(b). As you may have noticed, the ^{85}Rb vapor is not truly isotopically pure. The last transmission dip on the right is created by a small fraction (less than 1%) of ^{87}Rb atoms, at resonance with the laser field when it gets across the $F_g = 1 \rightarrow F_e$ transition of ^{87}Rb . Similarly, the transmission dip on the right gets broadened by the $F_g = 2 \rightarrow F_e$ transition of ^{87}Rb . We have therefore to extend the theoretical model to the case of an isotopic mixture of rubidium atoms in order to correctly fit the transmission spectrum. We also need an accurate frequency reference, provided by the saturated absorption spectrum of figures 3.4 (a) and (c). The best fit curve is shown in black dashed on inset (b). From this fit, we extract both the vapor temperature and the ^{87}Rb fraction, which is about 0.4 % in this cell. Once T is known, parameters such as the atomic density N , can be evaluated.

The vapor pressure (for $298\text{K} < T < 550\text{ K}$) is given by the following formula [77]:

$$\begin{cases} \log_{10}(\mathcal{P}_v) = 2.881 + 4.857 - \frac{4215}{T} & (\text{solid phase}) \\ \log_{10}(\mathcal{P}_v) = 2.881 + 4.312 - \frac{4040}{T} & (\text{liquid phase}) \end{cases} \quad (3.2)$$

where \mathcal{P}_v stands for the vapor pressure (in Torr). The atomic density N is then obtained straightaway using the ideal gas law:

$$N = 133.323 \times \frac{\mathcal{P}_v(T)}{k_B T} \quad (3.3)$$

The factor 133.323 converts the vapour pressure from Torr to Pascal. Since both isotopes are present in the cell, the number densities need to be calculated separately according to their abundance. The vapor pressure \mathcal{P}_v and the atomic density N (for an isotopically pure rubidium vapor) are plotted on the figure below.

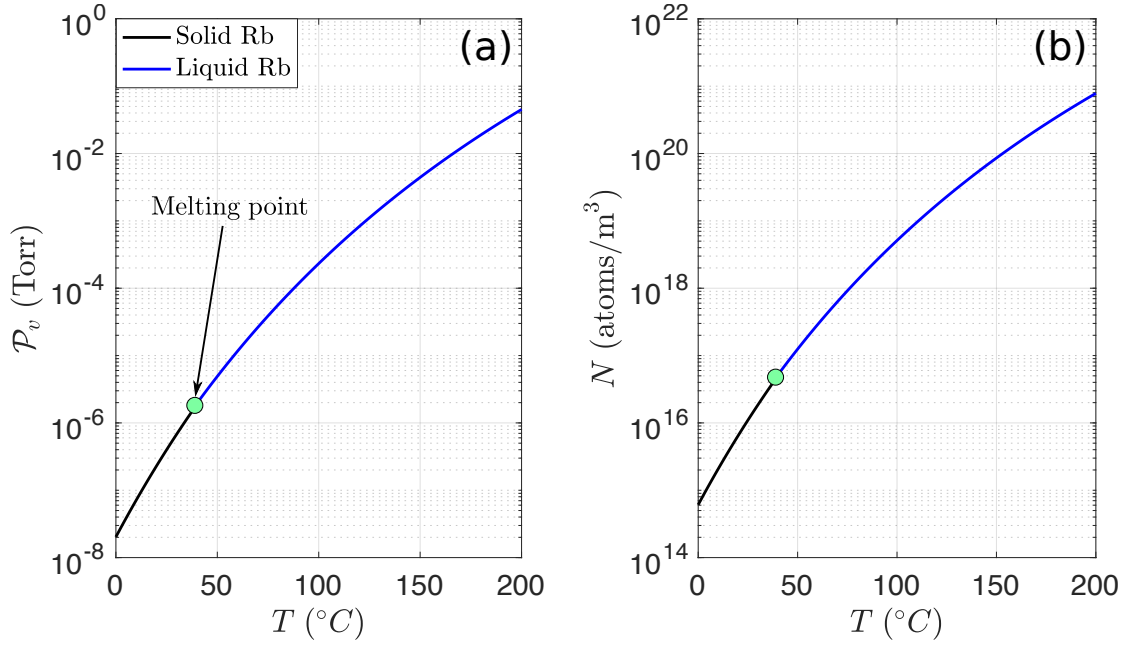


Figure 3.5: Vapor pressure (a) and atomic density (b) as function of the temperature T . The melting point of rubidium is 39.31°C. The density is in atoms/m³.

3.3 Methods II – Nonlinear refractive index measurement

In propagating fluids of light, the strength of the photon-photon interaction is proportional to the third-order susceptibility $\chi^{(3)}$ or, equivalently, to the nonlinear refractive index n_2 . This quantity plays therefore an important role in studying the photon fluid physics and finding a convenient and precise method to measure it has been one of our main concerns during my thesis. This issue is far from being fully solved and the technique I will present is conjointly being improved by the next generation of PhD students and other teams from the fluid of light community [78, 79]. Surprisingly, only a few methods exist to measure the nonlinear refractive index n_2 and all require the medium to be sufficiently thin in order to neglect the change in the beam shape along its propagation. The so-called z -scan technique is surely the most well-known among them [80, 81]. In this subsection, I first elaborate on this thin medium approximation and the constraints it imposes on the beam width mainly. I then present in details the method we currently use in the lab to accurately measure n_2 .

3.3.1 Thin medium approximation

When an intense Gaussian beam propagates inside a third-order Kerr medium, it induces a spatially dependent refractive index variation within the material, larger at its center than on its periphery, since $n = n_0 + n_2 \mathcal{I}(\mathbf{r}, z)$. If $n_2 < 0$ (resp. $n_2 > 0$), the medium acts therefore as a negative (resp. positive) lens and makes the laser beam diverge (resp. focus). The **thin medium approximation** (TMA) consists in assuming self-effects do not affect the shape and width of the Gaussian intensity profile. In order to be more quantitative, let's introduce the medium effective focal length defining the propagation length above which the TMA breaks down. Within the TMA, the intensity profile in the vicinity of the beam center reads: $\mathcal{I}(\mathbf{r}, z) \simeq \mathcal{I}_0 (1 - 2r^2/\omega_0^2)$. In order for this expansion to be correct, the beam should also be collimated over the length of the Kerr medium, which amounts to neglecting the z -dependence in its width. The nonlinear self-induced phase accumulated by the beam over its propagation is therefore given by: $\Phi_{\text{NL}}(\mathbf{r}, z) \simeq k \frac{n_2}{n_0} \mathcal{I}_0 (1 - 2r^2/\omega_0^2) z$. By identifying this expression at $z = L$ (i.e., in the cell output plane) with the phase profile of a Fresnel lens [82]: $\Phi_{\text{FL}}(\mathbf{r}) = 2\pi \times r^2/2f\lambda$ (f being the focal length), one can define the medium effective focal length f_{eff} as follows:

$$f_{\text{eff}} = \frac{1}{2} \frac{z_r}{k (n_2/n_0) \mathcal{I}_0 L} = \frac{1}{2} \frac{z_r}{\Phi_{\text{NL}}(\mathbf{0}, L)}, \quad (3.4)$$

where $z_r = \pi\omega_0^2/\lambda$ is the Rayleigh length. We assume here the on-axis intensity \mathcal{I}_0 does not depend on z (which is true for lossless mediums only). In lossy ones, it decays exponentially over z and \mathcal{I}_0 should then be replaced by: $\langle \mathcal{I}_0(z') \rangle_L = \mathcal{I}_0(0) [1 - \exp(-\alpha L)] / \alpha L$ in (3.4). In any case, f_{eff} goes to infinity when n_2 tends to zero: the nonlinearity is so weak that it does not induce any lensing effect anymore. Reversely, when n_2 increases, f_{eff} decreases. In other words, the length scale over which self-effects start modifying the beam intensity profile decreases, as expected. The TMA finally reduces to the set of assumptions below:

$$(i) L \ll z_r \text{ and } (ii) L \ll f_{\text{eff}} \quad (3.5)$$

The first assumption (i) basically translates the fact that the beam should be collimated over a distance greater than the cell length, so as to neglect diffraction. The second one (ii) defines then an upper limit on the average self-phase accumulated at the beam center along propagation: $\Phi_{\text{lim}} = z_r/(2L)$, above which the TMA breaks down. For a 7.5 cm long cell and a beam width of $500 \mu\text{m}$ for instance, the self-phase should be much smaller than $\Phi_{\text{lim}} \simeq 2\pi$ for the TMA to apply. Because Φ_{lim} scales with the beam cross-section, the best is to increase ω_0 to push it up. That is why ω_0 is usually about 2 mm when we measure n_2 in experiments. Now that foundations have been laid, I will present the measurement method itself.

3.3.2 Far-field measurement

When a Gaussian beam passes through a Kerr medium, a concentric ring intensity pattern forms in the far field. This phenomenon has aroused wide interest in the nonlinear optics community since Callen and al. [83] observed the far-field annular intensity distribution of a He-Ne laser beam passing through a nonlinear liquid CS_2 . Similar phenomena have been observed in liquid crystals by Durbin and al. [84]. Recently, theoretical progress have been made in understanding the linear relationship existing between the number of rings in far-field and the on-axis nonlinear phase accumulated by the laser over its propagation inside

a non-saturable Kerr medium [85]. Such a relation has been experimentally observed in a colloidal solution of oil and gold nanoparticles [86]. It provides an easy way to measure the nonlinear refractive index n_2 of the material. This technique starts being used in the fluid of light community [78,87] and have recently been extended to the case of anisotropic nonlinear refractive indices in [79]. The following paragraph is a review on the theoretical tools developed to describe the formation of this self-induced ring-shaped pattern in far-field. A recent unpublished work by Nicolas Pavloff [88] is also discussed.

i Theoretical description of the self-defocusing case

Let's consider that a Gaussian beam propagates along the z -axis through a self-defocusing ($n_2 < 0$) Kerr medium of thickness L . Let's also suppose that the beam waist lies exactly at the medium entrance plane ($z = 0$). Therefore, the radius $R(z)$ of the beam wavefront curvature is positive inside the medium (*ie* for $z > 0$). Both diffraction and self-defocusing make the beam diverge in that case. Conversely, when the waist is set at the output plane, they compete with each other, as the beam convergence will in some ways counterbalance self-defocusing inside the nonlinear medium. This competition can dramatically modify the far-field ring pattern [85]. In practice however, as long as the condition $L \ll z_r$ is fulfilled, setting the waist at the input or the output plane does not change significantly the result. The complex envelope of the laser electric field at the medium entrance plane reads:

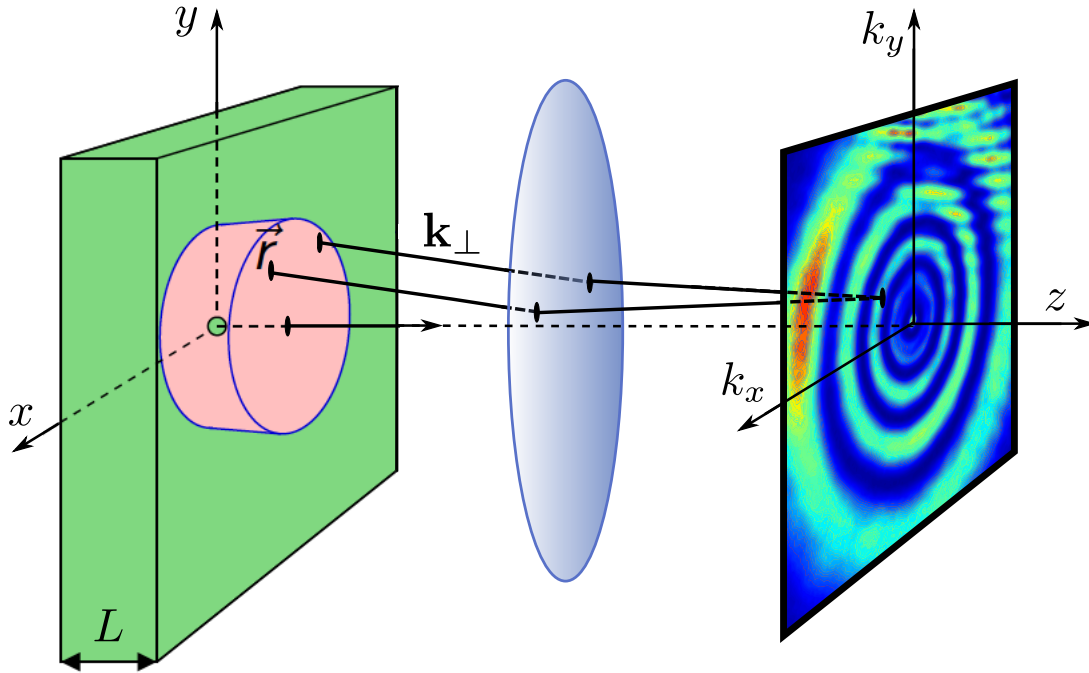


Figure 3.6: Sketched of the experimental setup. A Gaussian beam propagates through a Kerr medium (green slab). A lens at the exit plane focuses it. The far-field (Fourier space) is magnified and imaged on a camera. An example of the ring-shaped pattern we observe is shown on the right. Figure inspired from the N.Pavloff's talk at QFLM (2018) [88]

$$\mathcal{E}(\mathbf{r}, 0) = \mathcal{E}_0 \exp\left(-\frac{r^2}{w_0^2}\right) \quad (3.6)$$

By propagating through the nonlinear medium, it accumulates an additional phase shift:

$$\Delta\Phi(\mathbf{r}) = \langle \Phi_{\text{NL}}(\mathbf{r}, z') \rangle_L = \frac{k}{n_0} \int_0^L \Delta n(\mathbf{r}, z') dz', \quad (3.7)$$

where $\Delta n(\mathbf{r}, z) = n_2 \mathcal{I}(\mathbf{r}, z)$ is the nonlinear change of refractive index. Within the TMA, the Gaussian intensity profile of the laser beam is almost not modified along propagation. The electric field envelope at the exit plane can thus be expressed as:

$$\mathcal{E}(\mathbf{r}, L) = \mathcal{E}_0 \exp\left(-\frac{\alpha L}{2}\right) \exp\left(-\frac{r^2}{w_0^2}\right) \exp(-i\Phi(\mathbf{r})), \quad (3.8)$$

where α is, as usual, the linear absorption coefficient (nonlinear absorption is negligible). The phase shift $\Phi(\mathbf{r})$ is defined by:

$$\Phi(\mathbf{r}) = kL + \frac{kr^2}{2R(L)} + \Delta\Phi(\mathbf{r}) \simeq kL + \langle \Phi_{\text{NL}}(\mathbf{0}, z') \rangle_L \exp\left(-2r^2/w_0^2\right). \quad (3.9)$$

The Gaussian phase shift $kr^2/2R(L)$, arising from the wavefront curvature, is neglected as we assume the beam is collimated along the cell ($L \ll z_r$). The far-field intensity pattern is obtained either by letting the beam evolve in free space (the intensity distribution can be expressed using the Fraunhofer approximation of the Fresnel-Kirchhoff diffraction formula in that case) or by imaging the focal plane of a converging lens. We prefer this second option in practice as it saves space on the optical table. The intensity distribution in k-space is then given by the following equation:

$$\mathcal{I}(\mathbf{k}_\perp) = (2\pi)^2 \mathcal{I}_0(L) \left| \int_0^\infty J_0(k_\perp r) \exp\left(-\frac{r^2}{\omega_0^2} - i\Phi(r)\right) r dr \right|^2. \quad (3.10)$$

J_0 standing for the zero-order Bessel function of the first kind and $\mathcal{I}_0(L) = \mathcal{I}_0 \exp(-\alpha L)$. Equation (3.10) can not be more simplified and does not provide any insight into the physical process underlying the rings pattern formation in far-field. Let's try to push further our understanding by studying the 1D case first, which is more intuitive.

(a) 1D case – Stationary phase approximation

I now suppose that the Gaussian beam is infinitely elongated in the y -direction, as sketched on figure 3.7(a). The k-space electric field envelope is then given by:

$$\mathcal{E}_{\text{1D}}(k_x) = \mathcal{E}_0(L) \int_{-\infty}^{\infty} \exp\left(-\frac{x^2}{\omega_0^2}\right) \exp[i(k_x x + \Phi(x))] dx \quad (3.11)$$

where $\mathcal{E}_0(L) = \mathcal{E}_0 \exp(-\alpha L/2 - ikL)$. Let's define $\Psi_{k_x}(x) = k_x x - \Phi(x)$. This quantity is plotted as function of x/ω_0 on figure 3.7 (b) for a given value of k_x . The slope of the black dashed line is $k_x \omega_0$. As you may have noticed, Ψ has two extrema x_1 and x_2 , both lying in the $x > 0$ half-plane when k_x is positive. When k_x decreases, the slope of the dashed line also do so and x_1 progressively tends to zero while x_2 goes to infinity. Using the **stationary phase approximation**, we can rewrite the k-space electric field envelope (3.11) as follows:

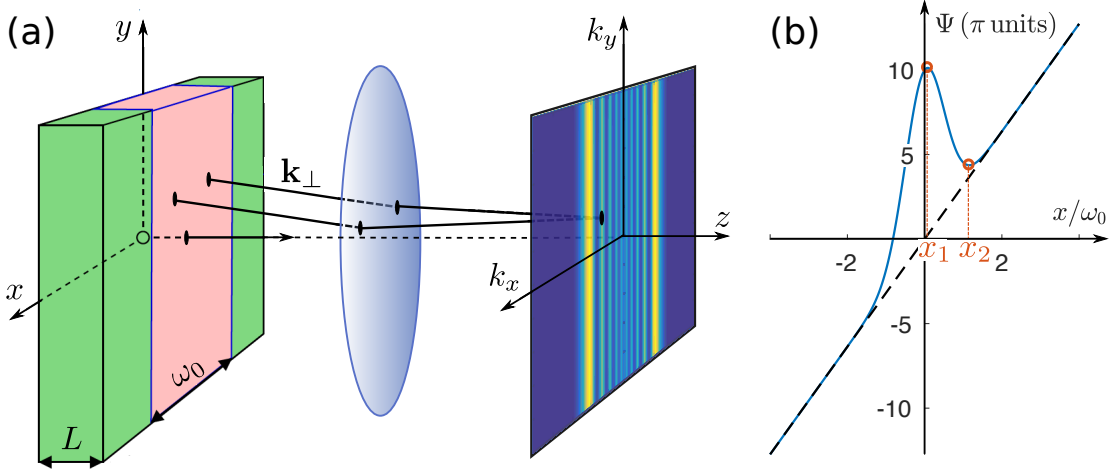


Figure 3.7: (a) Sketch of the 1D case. The beam is spatially elongated along the y -axis. A cylindrical lens in the exit plane focuses it in the x -direction. (b) Variation of Ψ_{k_x} as function of x/ω_0 for a given value of k_x . In k -space, the electric field at k_x is obtained by summing the fields coming from the vicinity of the points having x_1 or x_2 as abscissa in the cell exit plane. Figure inspired from the Nicolas Pavloff's talk at QFLM (2018) [88]

$$\mathcal{E}_{1D}(k_x) \simeq \sqrt{2\pi} e^{-ikL} \sum_{\alpha=1,2} \frac{\mathcal{E}(x_\alpha, 0)}{\sqrt{|\Psi''_{k_x}(x_\alpha)|}} \exp[-i(\Psi_{k_x}(x_\alpha) + \pi\sigma_\alpha/4)], \quad (3.12)$$

Ψ''_{k_x} being the second derivative of Ψ_{k_x} and σ_α the sign of Ψ''_{k_x} at x_α . This approach is valid only if Ψ_{k_x} has extrema, which is ensured solely when the slope of the black dashed line on 3.7(b) is smaller than the maximum of Φ' , that is, when: $k_x \omega_0 < 2 |\langle \Phi_{NL}(0, z') \rangle_L| e^{-1/2}$. The intensity distribution at k_x in Fourier space seems therefore to result from a two-wave interference process. According to the Fermat's principle, the light rays coming from a point of abscissa x in the cell exit plane propagate in straight lines along a direction defined by the wave-vector $\mathbf{k} = k_x \mathbf{e}_x + k_z \mathbf{e}_z$. The longitudinal component of \mathbf{k} , k_z , is given by: $k_z = \sqrt{k_0^2 - k_x^2}$ (k_0 being the in-air laser wave-vector). The transverse component, k_x , is related to the derivative of Φ through: $k_x(x) = +\Phi'(x)$. The light rays whose transverse wave-vector are equal to k_x come therefore from the points in the cell exit plane for which $\Psi'_{k_x}(x) = 0$. The preceding equation admits exactly two solutions, which are x_1 and x_2 . In the Fourier space, the envelope of the electric field at k_x is thus obtained by summing the fields coming from the vicinity of the points x_1 and x_2 at the medium exit plane, which is what equation (3.12) suggests indeed. We can push a bit further assuming the amplitudes of the interfering waves are equal. By doing so, the intensity envelope of the interference pattern will obviously be improperly described but not the oscillating trend, which only depends on the phase terms $\Psi_{k_x}(x_1) - \pi/4$ and $\Psi_{k_x}(x_2) + \pi/4$. We thus obtained:

$$\mathcal{I}_{1D}(k_x) \simeq C [1 + \sin(\Delta\Psi_{k_x})], \quad (3.13)$$

where $\Delta\Psi_{k_x} = \Psi_{k_x}(x_1) - \Psi_{k_x}(x_2)$ and C is a constant. Looking at 3.7(b), you can convince yourself that $\Psi_{k_x}(x_2)$ goes to zero and $\Psi_{k_x}(x_1)$ to $|\langle \Phi_{NL}(0, z') \rangle_L|$ when k_x tends toward zero.

The phase difference $\Delta\Psi_{k_x}$ is therefore equal to $|\langle\Phi_{\text{NL}}(0, z')\rangle_L|$ when $k_x = 0$. At low input intensity \mathcal{I}_0 , the rubidium vapor behaves as a linear medium and the intensity profile in k -space is uniform according to equation (3.13) (Gaussian in experiments). When \mathcal{I}_0 increases, $|\langle\Phi_{\text{NL}}(0, z')\rangle_L|$ rises accordingly, and the on-axis intensity in Fourier space, $\mathcal{I}_{1\text{D}}(0)$, reaches a first maximum for $|\langle\Phi_{\text{NL}}(0, z')\rangle_L| = \pi/2$ and then a minimum for $|\langle\Phi_{\text{NL}}(0, z')\rangle_L| = 3\pi/2$, etc. By extrapolating, the average on-axis nonlinear phase shift is equal to $2n\pi + \pi/2$ when the k -space intensity distribution exhibits $2n$ maximums plus a bright fringe at the center (that is, at $k_x = 0$) and to $(2n-1)\pi + \pi/2$ when it has $2n$ maximums plus a dark fringe at the center this time. Counting the "rings" in far-field (that is, in the 1D case, the pairs of maximums having the same transverse wave-vector in absolute value) provides therefore a way of measuring $|\langle\Phi_{\text{NL}}(0, z')\rangle_L|$ (and also n_2 , if \mathcal{I}_0 and α are known). Within the TMA, the ring-counting procedure in 1D can finally be formulated as follows:

- when the far-field diffraction pattern is composed of n rings plus a bright central spot (constructive interference at $k_x = 0$), the nonlinear phase shift is $2n\pi + \pi/2$;
- when the far-field diffraction pattern is composed of n rings plus a dark central spot (destructive interference at $k_x = 0$), the nonlinear phase shift is $(2n-1)\pi + \pi/2$;

(a) General 2D case

The stationary phase approximation can be generalized to the 2D case. The electric field envelope in k -space can indeed be approximated by the following formula [89]:

$$\mathcal{E}_{2\text{D}}(\mathbf{k}_\perp) \simeq 2\pi e^{-ikL} \sum_{\alpha} \frac{\mathcal{E}(\mathbf{r}_\alpha, 0)}{\sqrt{|\det[\mathcal{H}_{\mathbf{k}_\perp}(\mathbf{r}_\alpha)]|}} \exp[-i(\Psi_{\mathbf{k}_\perp}(\mathbf{r}_\alpha) + \pi\sigma[\mathcal{H}_{\mathbf{k}_\perp}(\mathbf{r}_\alpha)]/4)], \quad (3.14)$$

where $\mathbf{k}_\perp = k_x \mathbf{e}_x + k_y \mathbf{e}_y$ is the transverse wave-vector and \mathbf{r}_α the α -th position in the medium output plane at which the gradient of $\Psi_{\mathbf{k}_\perp}(\mathbf{r}) = \mathbf{k}_\perp \cdot \mathbf{r} - \Phi(\mathbf{r})$ is zero. We have also introduced the Hessian matrix $\mathcal{H}_{\mathbf{k}_\perp}$ associated to the function $\Psi_{\mathbf{k}_\perp}$:

$$\mathcal{H}_{\mathbf{k}_\perp}(\mathbf{r}_\alpha) = \begin{pmatrix} \partial_{xx}\Psi_{\mathbf{k}_\perp} & \partial_{xy}\Psi_{\mathbf{k}_\perp} \\ \partial_{yx}\Psi_{\mathbf{k}_\perp} & \partial_{yy}\Psi_{\mathbf{k}_\perp} \end{pmatrix} \Big|_{\mathbf{r}=\mathbf{r}_\alpha} \quad (3.15)$$

and the signature σ of $\mathcal{H}_{\mathbf{k}_\perp}$ (which is the number of positive minus the number of negative eigenvalues of $\mathcal{H}_{\mathbf{k}_\perp}$). The phase $\Psi_{\mathbf{k}_\perp}$ has been plotted as function of the scaled coordinates x/ω_0 and y/ω_0 on figure 3.8 for $\mathbf{k}_\perp = k_x \mathbf{e}_x$. It can be shown that whatever the initial values of k_x and k_y , one can always define new basis vectors \mathbf{e}_X and \mathbf{e}_Y such that $\mathbf{k}_\perp = k_X \mathbf{e}_X$. Let's consider, for the sake of simplicity, that $\mathbf{k}_\perp = k_x \mathbf{e}_x$. This is what is done on figure 3.8. As long as $k_x \omega_0 < 2|\langle\Phi_{\text{NL}}(0, z')\rangle_L| e^{-1/2}$, $\Psi_{\mathbf{k}_\perp}$ exhibits only one maximum at \mathbf{r}_1 and one saddle point at \mathbf{r}_2 , as can be seen on figure 3.8. As in the 1D case, the intensity distribution at \mathbf{k}_\perp in Fourier space results therefore from the interference of the waves coming from the vicinity of \mathbf{r}_1 and \mathbf{r}_2 in the cell output plane. Moreover, it is straightforward to show that $\partial_{xy}\Psi_{\mathbf{k}_\perp}|_{\mathbf{r}_\alpha} = \partial_{yx}\Psi_{\mathbf{k}_\perp}|_{\mathbf{r}_\alpha} = 0$ and consequently that $\sigma[\mathcal{H}_{\mathbf{k}_\perp}(\mathbf{r}_1)] = -2$ while $\sigma[\mathcal{H}_{\mathbf{k}_\perp}(\mathbf{r}_2)] = 0$. There is thus a constant dephasing of $\pi/2$ between the two waves interfering in far-field, exactly like in the 1D case once more. This can be intuitively understood by looking at the signs of the second-order derivatives at \mathbf{r}_1 and \mathbf{r}_2 . In the vicinity of \mathbf{r}_1 , $\partial_x^2\Psi_{\mathbf{k}_\perp}$ and $\partial_y^2\Psi_{\mathbf{k}_\perp}$ are negative which suggests that the light coming from there will tend to spread over the (x, y) plane during the in-air propagation. Close to the saddle point, $\partial_x^2\Psi_{\mathbf{k}_\perp}$ is positive while

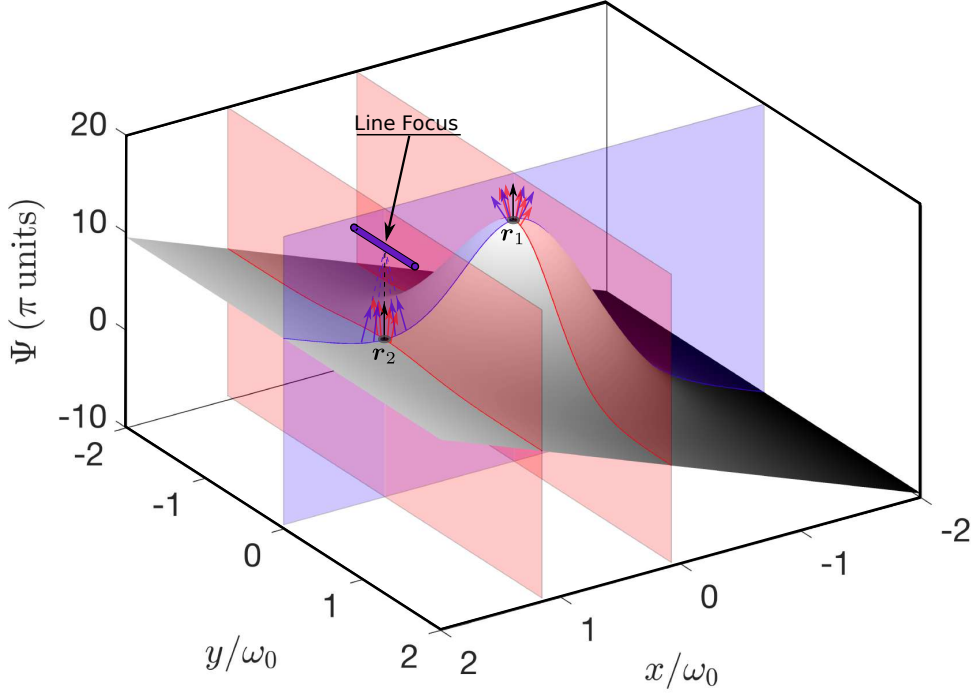


Figure 3.8: Variation of $\Psi_{\mathbf{k}_\perp}$ in the transverse plane for $\mathbf{k}_\perp = k_x \mathbf{e}_x$. The total electric field at \mathbf{k}_\perp in Fourier space is obtained by summing the fields coming from the vicinity of the local maximum (at \mathbf{r}_1) and the saddle point (at \mathbf{r}_2). The light emitted at \mathbf{r}_2 accumulates an additional $\pi/2$ phase shift since it passes through a line focus.

$\partial_y^2 \Psi_{\mathbf{k}_\perp}$ is negative. The light coming from the vicinity of \mathbf{r}_2 will thus simultaneously focus along the x -axis and spread over the y -direction during propagation. In geometrical optics, it is well known that light accumulates an additional phase – the so-called Gouy phase – when it passes through a focus. This phase shift is equal to $\pi/2$ if light propagates from $-\infty$ to $+\infty$ through a line focus and to π when it propagates from $-\infty$ to $+\infty$ through a point-like one. The Gouy phase shift of any focused light arises from its transverse spatial confinement which introduces, through the uncertainty principle, a spread in its transverse momenta and hence a shift in the expectation value of its longitudinal wave-vector [90]. In the present case, the focus is a line (because \mathbf{r}_2 is a saddle-point). The light coming from \mathbf{r}_2 accumulates thus an additional $\pi/2$ phase shift with respect to the light coming from \mathbf{r}_1 , as mentioned above. The same reasoning can be applied in 1D in order to explain the $\pi/2$ dephasing in far-field between the waves emitted at x_1 and x_2 in the cell exit plane.

We can finally, as in 1D, approximate the \mathbf{k} -space intensity distribution in the following way: $\mathcal{I}_{2D}(\mathbf{k}_\perp) \simeq C [1 + \sin(\Delta\Psi_{\mathbf{k}_\perp})]$. It is easy to see that $\Delta\Psi_{\mathbf{k}_\perp} = |\langle \Phi_{NL}(0, z') \rangle_L|$ when $\mathbf{k}_\perp = \mathbf{0}$. Consequently, the ring-counting procedure in 2D is the same as in 1D. Within the TMA, it can be formulated as follows:

- when the far-field diffraction pattern is composed of n rings plus a bright central spot (constructive interference at $\mathbf{k}_\perp = \mathbf{0}$), the nonlinear phase shift is $2n\pi + \pi/2$;
- when the far-field diffraction pattern is composed of n rings plus a dark central spot (destructive interference at $\mathbf{k}_\perp = \mathbf{0}$), the nonlinear phase shift is $(2n - 1)\pi + \pi/2$;

REMARK. It is worth mentioning that the counting procedure above is not the one usually discussed in the literature. It is commonly accepted that $|\langle \Phi_{\text{NL}}(0, z') \rangle_L|$ is equal to $2n\pi$ when n rings plus a bright central spot are visible in far-field and to $(2n - 1)\pi$ for n rings plus a dark central spot [78,79]. The $\pi/2$ Gouy phase shift predicted by the theory seems to be omitted in these works where the relationship between the number of rings and the on-axis self-phase modulation has been inferred using numerical simulations.

ii Numerical simulation

Studying numerically the dynamics of the ring pattern formation requires to solve both the linear (LSE) and the nonlinear (NLSE) Schrödinger equations, introduced in chapter 2. In order to do so, we used the second-order split step method, which provides both good accuracy and high performance speed. I will only discuss here simulations in the 1D case (which are easier to perform), since the 2D situation is analogous.

We first look at the ring pattern formation in 1D by solving the z -evolution of the electric field envelope (i) inside the nonlinear medium with the NLSE and (ii) outside, using either the LSE to describe in detail the field evolution after the lens or a 1D FFT to directly access its far-field intensity distribution (that is faster). On figure 3.9(a), the field intensity has been plotted as function of z . The nonlinear medium is 2.5 cm long here. A converging lens (white double-headed arrow, $f = 5$ cm) has been set at the medium output plane, at $z = 0$. At that point, the laser beam starts focusing. As you may have noticed, interferences do not only occur in the focal plane (white dashed line). We must thus be extremely careful when we image the Fourier space on the camera, as a small mistake on the imaged plane position can lead to misestimate the number of rings. An other possibility to get rid of this issue is to let the beam propagates freely after the cell, as mentioned before. It suffices then to image a plane far away from the medium exit plane.

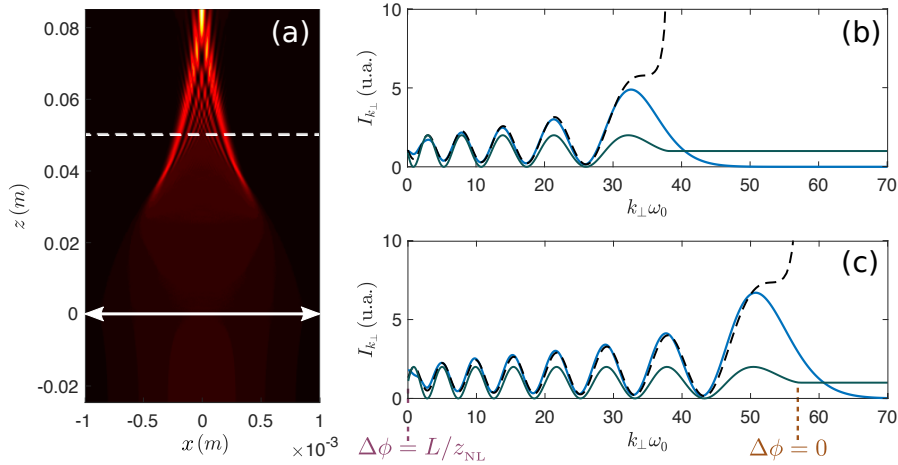


Figure 3.9: (a) Evolution of the intensity distribution along z . A lens ($f = 5$ cm) focuses the beam at the nonlinear medium exit plane. Because of self-defocusing, the beam waist is not located in the focal plane (dotted line) anymore. (b-c) Comparison between simulations (blue solid lines) and the predictions of equation (3.12) (black dashed lines) and (3.13) (green solid lines). Parameters: $\omega_0 = 1$ mm, $n_2 = 4 \cdot 10^{-11}$ m²/W, $\mathcal{I}_0 = 10^7$ W/m² and $\alpha = 0$.

Finally, we compare on figures 3.9 the far-field intensity profiles resulting from the numerical simulations with the theoretical predictions of equations (3.12) and (3.13), for on-axis nonlinear phase shifts of 10π (b) and 15π (c). The intensity profile obtained with equation (3.12) (black dashed line) exactly matches the results of the numerical simulations (blue solid line), when the stationary phase approach is valid, *ie*, as long as $k_x \omega_0 < 2 |\langle \Phi_{\text{NL}}(0, z') \rangle_L| e^{-1/2}$. More surprisingly, the approximate solution (3.13) (green solid line) properly reproduces the oscillating trend of the far field interference pattern; to count the number of rings, it is thus enough to count the maxima of $\sin(\Delta\Psi)$ when $\Delta\Psi$ varies from zero to $\langle \Phi_{\text{NL}}(0, z') \rangle_L$.

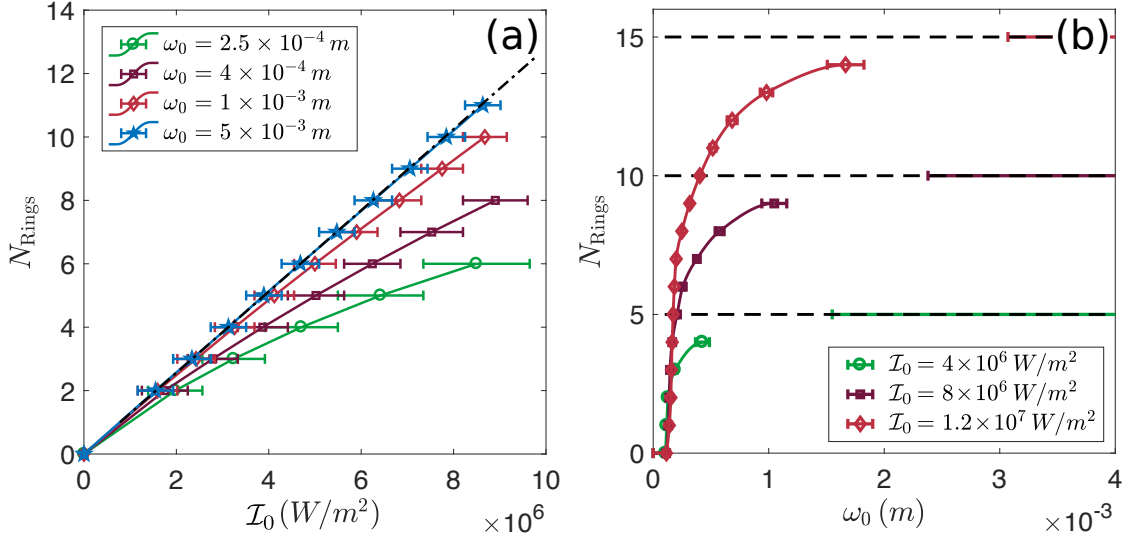


Figure 3.10: Number of rings in far-field as function (a) of the input on-axis intensity \mathcal{I}_0 and (b) of the beam width ω_0 . Parameters: $L = 2.5$ cm, $n_2 = 4 \times 10^{-11}$ m²/W and $\alpha = 0$.

So far, the impact of the beam width on the ring pattern formation has been neglected, as I always assumed the TMA was valid. Let's now study the effect of self-defocusing on the far-field diffraction pattern. The data points on figure 3.10(a) are the number of visible rings in far-field, for various beam widths ω_0 . The horizontal bars stand for the range of intensities over which the number of rings, N_{Rings} , remains the same. The on-axis nonlinear phase shift $|\langle \Phi_{\text{NL}}(0, z') \rangle_L| (= k_0 n_2 \mathcal{I}_0 L$ in the lossless case) has also been plotted (black dashed line) in 2π units. For a 2.5 cm long cell and a beam width of $\omega_0 = 5$ mm (blue stars), the TMA is valid as $|\langle \Phi_{\text{NL}}(0, z') \rangle_L| \ll \Phi_{\text{lim}} \simeq 320 \times 2\pi$, whatever the value of the input intensity \mathcal{I}_0 . As you may have seen, the number of rings increases linearly with \mathcal{I}_0 in that case. However, when ω_0 decreases, the value of the input intensity at which new rings appears increases, shifting the data points rightward. This shift moreover increases with \mathcal{I}_0 , as if the number of rings was saturating at high input intensities. This behaviour is expected when the TMA breaks down. In that case, we notice a spreading of the beam intensity in the transverse plane because of self-defocusing. This effect is enhanced when the beam width decreases, as the medium effective focal length f_{eff} scales as ω_0^2 . The beam spreading results in a diminution of the on-axis intensity during propagation. The relationship between \mathcal{I}_0 and $|\langle \Phi_{\text{NL}}(0, z') \rangle_L|$ (and therefore, between \mathcal{I}_0 and the number of rings in far-field) is thus not linear anymore.

In figure 3.10(b), the number of rings in far-field has been plotted as function of ω_0 this time, for different input intensities. It increases with ω_0 until it saturates. The width at which the number of rings starts being constant indicates the minimum beam width required to fulfill the thin medium conditions and correctly measure n_2 using the ring-counting method.

iii Experimental results

In the experiments, we almost exclusively use the ring-counting technique to measure the nonlinear refractive index n_2 of the rubidium vapor. The data we got using this technique are exploited further on to support the main results of my work in the following chapters. Ring-counting curves will therefore sporadically appear in the remaining of this manuscript. I thus present here only few experimental data. On figure 3.11(a), an example of a ring-counting curve is shown. The on-axis nonlinear phase shift $\langle \Phi_{\text{NL}}(0, z') \rangle_L$ has been plotted as function of the input intensity using the counting procedure of i(b) (blue points) and the counting procedure described in [78,79] (red points). Blues points are shifted up from the red ones by $\pi/2$. The uncertainty comes from our inability to accurately evaluate at which intensity the central spot is the brightest or the darkest. On figure (b), the far-field patterns associated to each points are shown. These data have been obtained with an isotopically pure ^{85}Rb vapor. The cell was 7.5 cm long and the temperature about 125 °C. The beam width was set to 825 μm . In order for the TMA to be valid, $|\langle \Phi_{\text{NL}}(0, z') \rangle_L|$ has to be smaller than $\Phi_{\text{lim}} = 8 \times 2\pi$. This condition is not fulfilled at high intensity. Therefore, we expect the number of rings in far-field (and thus $|\langle \Phi_{\text{NL}}(0, z') \rangle_L|$) to saturates with \mathcal{I}_0 because of self-defocusing, as shown on figure 3.10(a).

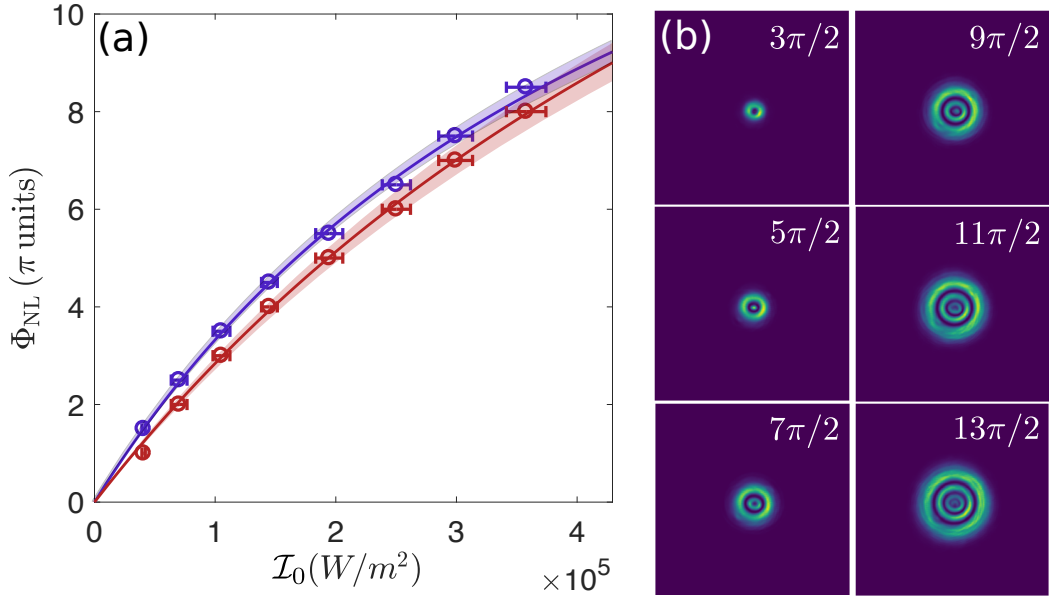


Figure 3.11: (a): On-axis nonlinear phase shift as function of the input intensity, measured using the counting method of paragraph 3.3.2 i(b) (blue points) and the one adopted in [78,79] (red points). The data are fitted in both case using equation (3.16) to extract n_2 . (b): Far-field patterns associated to the data points on the left. Parameters: $L = 7.5$ cm, $T \simeq 125$ °C and $\Delta \simeq 2\pi \times 3.1$ GHz from the $F_g = 3 \rightarrow F'$ transition of ^{85}Rb .

Saturation. Rubidium vapors are saturable nonlinear mediums. At high enough intensity, higher order susceptibilities ($\chi^{(5)}, \chi^{(7)}, \dots$) start contributing to the nonlinear response and make the nonlinear change of refractive index saturating. That may also explain the trend observed on figure 3.11. In order to take the effects of self-defocusing as well as of the atomic saturation into account, we fit the data using the following model [78]:

$$|\langle \Phi_{\text{NL}}(0, z') \rangle_L| = \frac{k_0 n_2 \mathcal{I}_0 L}{1 + \mathcal{I}_0 / \mathcal{I}_{\text{sat}}} \quad (3.16)$$

where n_2 and the saturation intensity \mathcal{I}_{sat} are fitting parameters.

Comparison between the two ring-counting procedures. By doing so, we find that $n_2 = 2.1 \pm 0.1 \times 10^{-10} \text{ m}^2/\text{W}$ and $\mathcal{I}_{\text{sat}} \simeq 5.0 \times 10^5 \text{ W/m}^2$ using the counting procedure detailed in section 3.3.2 i(b) (blue points) and $n_2 = 1.7 \pm 0.1 \times 10^{-10} \text{ m}^2/\text{W}$ and $\mathcal{I}_{\text{sat}} \simeq 8.3 \times 10^5 \text{ W/m}^2$ using the one of [78, 79] (red points). The relative variation of the fitted value of the nonlinear refractive index obtained with the two counting methods is 20%. In this experiment, the laser was 3 GHz red-detuned from the $F_g = 3 \rightarrow F'$ transition of ^{85}Rb . The theoretical value of the off-resonance saturation intensity $\mathcal{I}_s(\Delta)$ is (with the parameters above) about $8 \times 10^5 \text{ W/m}^2$. As you can see, this value matches almost exactly the fitted value of the saturation intensity obtained using the counting procedure of [78, 79]. This is in fact quite surprising because $1/\mathcal{I}_{\text{sat}} = 1/\mathcal{I}_s(\Delta) + 1/\mathcal{I}_{\text{eff}}$, where \mathcal{I}_{eff} is an effective saturation intensity describing the effective contribution of self-defocusing in the saturation of $|\langle \Phi_{\text{NL}}(0, z') \rangle_L|$. In the present case, self-defocusing plays a role for sure, as the TMA is not perfectly fulfilled. We thus expect a value of \mathcal{I}_{sat} lower than $\mathcal{I}_s(\Delta)$. In this sense, the value of \mathcal{I}_{sat} provided by our ring-counting method seems therefore more reasonable.

Moreover, if we attribute an on-axis nonlinear phase shift of π to the far-field diffraction pattern composed of one ring plus a dark central spot, as in [78, 79], the related point (that is, the circle of lowest intensity) does not lie on the fitted curve (red line). This observation is actually quite systematic, as if the first ring in far field was obtained for a slightly too high input intensity if we use the counting procedure described in [78, 79]. By shifting up the red points by $\pi/2$, this issue seems to be solved, as the point of lowest intensity lies then on the blue fitted curve. These two remarks make us think that the $\pi/2$ Gouy phase shift should definitely be taken into account in the ring-counting method.

3.4 Methods III – Scanning phase interferometry

In photon fluid experiments, measuring the phase of the fluid at the medium output plane provides useful information. It allows, for instance, to access the flow velocity distribution of the fluid after propagation, or also to highlight and study the formation and the dynamics of phase singularities (quantized vortices, solitons, etc). Such a measurement can also be used to retrieve the spatial variations of the nonlinear change of refractive index (and thus, to extract n_2) [91]. This possibility is further investigated by Murad Abuzarli, PhD student in the group. This short section is devoted to presenting the phase shifting interferometry, that is used in our experiments to retrieve the spatial phase distribution of the light at the medium exit plane. This phase reconstruction procedure is a generalization of the standard four-frame interferometric technique, described in [92].

The experimental setup built in order to performed phase shifting interferometry is sketched on figure 3.12 below. A laser beam comes out from the optical fiber and is magnified to the desired size before entering a Mach-Zehnder interferometer. A polarized beam splitter (PBS) splits the incoming light beam into two parts, the reference and the fluid (which propagates through the cell). The half-wave plate ($\lambda/2$) positioned in between the telescope and the PBS enables us to control the amount of light sent in each arm. Reference and fluid recombine in the 50/50 beam splitter (BS). The length of the reference arm is modulated by setting one mirror on a piezo-actuated translation stage (referred to as PEM). The high tension $U(t)$ applied across the piezo-actuator is depicted in the inset on the right. A function generator produces a 0.2 Hz triangular signal amplified by a high voltage generator. Its amplitude δU is increased gradually until the reference phase is exactly scanned over 2π . In order to maximize the contrast of the interference pattern, one can tune the reference intensity by turning the half wave plate on its path. The cell exit plane is finally imaged on the camera using a second 4- f telescope (depicted with a bi-convex lens for clarity).

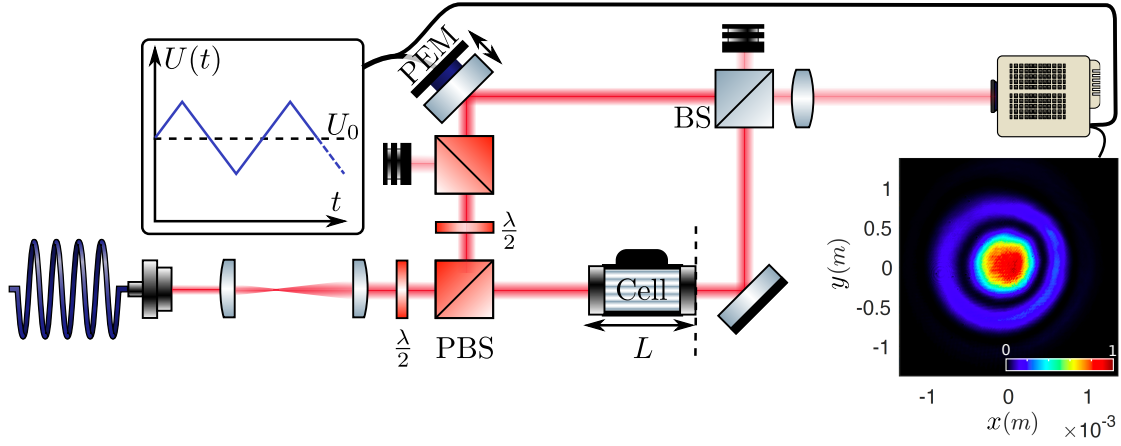


Figure 3.12: Experimental setup. A Mach-Zehnder interferometer is used so as to measure the beam transverse phase profile in the cell exit plane. Left inset: high voltage triangular signal making the PEM scan the phase of the reference beam. Right inset: example of an interferogram obtained when the angle between the reference and the fluid is zero.

The intensity of the two-beam interference pattern at the exit plane can be described by:

$$\mathcal{I}_n(\mathbf{r}) = \mathcal{I}(\mathbf{r}, L) \{1 + V(\mathbf{r}) [\cos(\Phi(\mathbf{r}) - \theta_n)]\}, \quad (3.17)$$

where $\mathcal{I}(\mathbf{r}, L)$ is the beam intensity at the medium output plane, $V(\mathbf{r})$ the fringe visibility and $\theta_n = \frac{2\pi}{N}(n-1)$ (n being an integer in $\{1, \dots, N\}$) an arbitrary reference phase which is scanned over 2π under the PEM translation. Each of the $\mathcal{I}_n(\mathbf{r})$ portrays an interferogram (see for instance the inset of fig. 3.12); the complete set of N interferograms is used to reconstruct $\Phi(\mathbf{r})$. By using the angle difference identity, one can rewrite (3.17) as follows:

$$\mathcal{I}_n(\mathbf{r}) = I(\mathbf{r}, L) \{1 + V(\mathbf{r}) \cos[\Phi(\mathbf{r})] \cos(\theta_n) + V(\mathbf{r}) \sin[\Phi(\mathbf{r})] \sin(\theta_n)\} \quad (3.18)$$

By multiplying the previous equation by (i) $\sin(\theta_n)$ and (ii) $\cos(\theta_n)$ before summing over n :

$$\sum_{n=1}^N \mathcal{I}_n(\mathbf{r}) \cos(\theta_n) = \mathcal{I}(\mathbf{r}, L) \sum_{n=1}^N \{ \cos(\theta_n) + V(\mathbf{r}) \cos[\Phi(\mathbf{r})] \cos^2(\theta_n) + \dots \\ V(\mathbf{r}) \sin[\Phi(\mathbf{r})] \sin(\theta_n) \cos \theta_n \} \quad (3.19)$$

$$\sum_{n=1}^N \mathcal{I}_n(\mathbf{r}) \sin(\theta_n) = \mathcal{I}(\mathbf{r}, L) \sum_{n=1}^N \{ \sin(\theta_n) + V(\mathbf{r}) \sin[\Phi(\mathbf{r})] \sin^2(\theta_n) + \dots \\ V(\mathbf{r}) \cos[\Phi(\mathbf{r})] \cos(\theta_n) \sin \theta_n \} \quad (3.20)$$

The first terms and the mixed terms on the right hand side of equations (3.19) and (3.22) cancel because of the orthogonality of the trigonometric functions. We thus obtain that:

$$\sum_{n=1}^N I_n(\mathbf{r}) \cos(\theta_n) = \frac{N}{2} I(\mathbf{r}, L) V(\mathbf{r}) \cos[\Phi(\mathbf{r})] \quad (3.21)$$

$$\sum_{n=1}^N I_n(\mathbf{r}) \sin(\theta_n) = \frac{N}{2} I(\mathbf{r}, L) V(\mathbf{r}) \sin[\Phi(\mathbf{r})] \quad (3.22)$$

which provides an simple algorithm to process the N interferograms and calculate $\Phi(\mathbf{r})$:

$$\tan[\Phi(\mathbf{r})] = \left(\sum_{n=1}^N I_n(\mathbf{r}) \sin(\theta_n) \right) / \left(\sum_{n=1}^N I_n(\mathbf{r}) \cos(\theta_n) \right) \quad (3.23)$$

In our experiments, the trigger of the camera acquisition is set on the high voltage signal. The camera acquires a sequence of 40 images equally spaced in time on a rising ramp only (to reduce hysteresis effects). An example of an interferogram is shown on figure 3.13(a). The photon fluid is formed by a Gaussian beam whose width is $850 \mu\text{m}$. It accumulates an additional phase shift $\Delta\Phi = |\langle \Phi_{\text{NL}}(0, z') \rangle_L|$ by propagating through a 2.5 cm long ^{85}Rb cell. The angle between the reference and the fluid is zero, explaining the concentric ring-shaped pattern observed on figure 3.13(a). The corresponding spatial phase modulation retrieved from equation (3.23) is shown on figure 3.13(b). Reconstructing in such a way the nonlinear phase shift $\Delta\Phi$ is — knowing the vapor transmission — a way of measuring n_2 accurately [91]. It is worth mentioning that reconstructing the phase profile of the fluid at the cell exit plane using the phase shifting interferometry only requires to evaluate numerically equation 3.23, unlike phase retrieval methods using a single interferogram (that are based on FFT filtering). The scanning phase interferometry is consequently extremely robust and has no issue in reconstructing phase maps full of singularities.

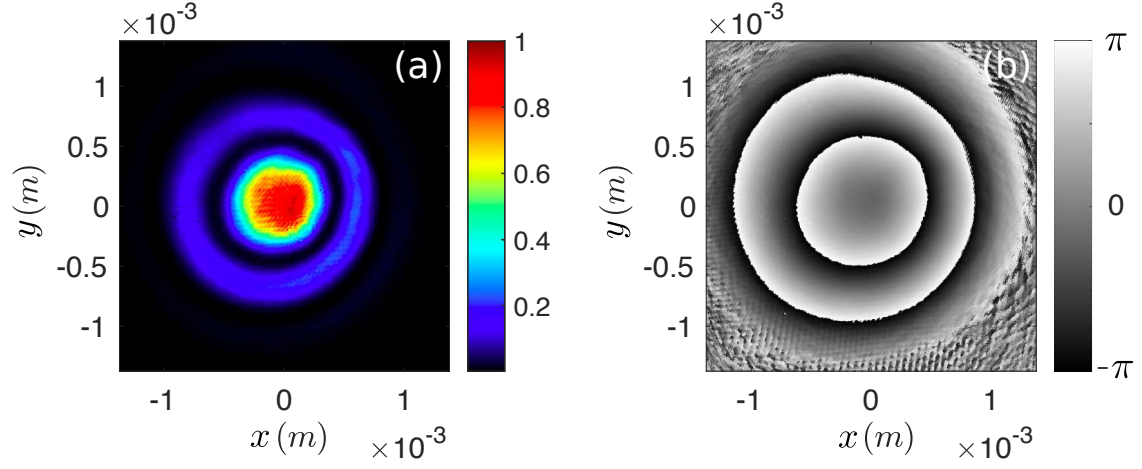


Figure 3.13: (a) Example of an interferogram obtained with the setup sketched in figure 3.12. The fluid of light is formed by a Gaussian beam whose width is $850 \mu\text{m}$. By propagating through a 2.5 cm long vapor cell, this beam accumulates a nonlinear phase shift $\Delta\Phi$ that is greater at its center than on its periphery. When the angle between the reference and the fluid is zero, a concentric ring-shaped pattern appears on the camera. (b) Reconstruction of the fluid phase at the cell exit plane using the phase shifting interferometry.

Chapter 4

Dispersion of small amplitude density waves on a photon fluid

As mentioned in chapter 2, measuring how small amplitude density waves propagating onto a photon fluid disperse represents an essential step toward the observation of more striking phenomena with this system, such as superfluidity. Although this dispersion has been well characterized in atomic BEC experiments [93–96], direct measurements in paraxial photon fluids was attempted [52] but remain elusive. I will start this fourth chapter by introducing the method used so far to measure the dispersion relation in those systems, which consists in measuring the phase velocity of density waves travelling onto the photon fluid. I will also adapt the theoretical framework developed by Pierre-Élie Larré in [71] to correctly analyse the experimental observations we made using this technique. In a second time, I will present the method we have developed so as to more reliably retrieve the dispersion of density waves in paraxial photon fluids. Our approach relies on the measurement of their group velocity. The results of this section have been published in two consecutive papers: "Observation of the Bogoliubov Dispersion in a Fluid of Light", *Phys.Rev.Lett.* 121, 183604 (2018) [87] and: "Interferences between Bogoliubov excitations and their impact on the evidence of superfluidity in a paraxial fluid of light", *arXiv:2005.14328* (2020) [97].

4.1 Phase velocity measurement

The method used by Vocke *et al.* [52] to measure the dispersion relation of small amplitude density waves in paraxial photon fluids relies on a pump/probe experiment that has been initially proposed by Iacopo Carusotto in [56]. It basically consists in measuring the phase velocity of a plane wave modulation travelling with the transverse wave-vector \mathbf{k}_\perp onto a fluid of light. The latter is obtained by sending a wide laser beam (the pump) through the self-defocusing Kerr medium. The small amplitude plane wave modulation is created by making interfere this pump beam with a wide and weak probe field, which propagates at a small angle θ_i with respect to the optical axis. The resulting interference pattern can be regarded as a density wave travelling onto the photon fluid at \mathbf{k}_\perp , as soon as the beams enter the nonlinear medium. From now on, I will suppose that the interference fringes are parallel to the y -direction and thus that $\mathbf{k}_\perp = k_0 \sin(\theta_i) \mathbf{e}_x$. In what follows, I first introduce the theoretical framework to describe this experimental configuration.

4.1.1 Theoretical description

The phase velocity $v_{\text{ph}}(\mathbf{k}_\perp)$ of a plane wave propagating on top of a photon fluid is given by:

$$v_{\text{ph}}(\mathbf{k}_\perp) = \Omega_B(k_\perp)/k_\perp, \quad (4.1)$$

where $\Omega_B(k_\perp)$ is the Bogoliubov dispersion introduced in chapter 2. As the speed of sound, c_s , scales as the square root of the fluid density ρ_0 (that is, as the square root of the pump intensity \mathcal{I}_0), the phase velocity should increase with ρ_0 . Therefore, the interference pattern forming the plane wave should be shifted along the x -direction at the medium output plane when the fluid density increases. By measuring in this plane, for different wave-vectors \mathbf{k}_\perp , the spatial shift $\Delta S(k_\perp)$ between the interference fringes at low and high fluid densities, one should be able to retrieve the dispersion relation. The shift $\Delta S(k_\perp)$ plays a crucial role in what follows. In order to further familiarize yourselves with this quantity, let me present a geometrical argument explaining qualitatively its origin.

i Geometric approach

In a linear medium of refractive index n_0 , the longitudinal wave-vector k_z of the probe beam is defined by $k_z = \sqrt{k^2 - k_\perp^2}$. In the paraxial approximation ($k_\perp \ll k_z$), this formula yields: $k_z \simeq k - k_\perp^2/2k = k + \delta k_z$, where $\delta k_z = -k_\perp^2/2k$. In a self-defocusing ($\Delta n < 0$) Kerr medium, $\delta k_z = -\Omega_B(k_\perp)$. Indeed, the Bogoliubov dispersion $\Omega_B(\mathbf{k}_\perp)$ describes the variation of the longitudinal wave-vector of the probe field $\delta \mathcal{E}$ when it enters the Kerr medium supported by the pump field \mathcal{E} , with the transverse wave-vector \mathbf{k}_\perp .

Figure 4.1(a) shows the wave-vectors of the pump and the probe. The black arrow represents the pump wave-vector, that is equal to $k\mathbf{e}_z$. Its head defines the origin of the $(k_\perp, \delta k_z)$ plane. The red and blue arrows are the probe wave-vectors in the linear and nonlinear mediums. In the linear one, $\delta k_z = -k_\perp^2/2k$. This is the equation of the black dotted parabola on which the head of the red arrow lies. In the nonlinear medium, $\delta k_z = -\Omega_B(k_\perp)$. The tip of the blue arrow lies thus on the negative branch of the Bogoliubov dispersion relation (blue curve). As you can see, the axial component of the probe wave-vector has been squeezed by moving from the linear to the nonlinear case. This has an impact on the interference pattern between the pump and the probe beams.

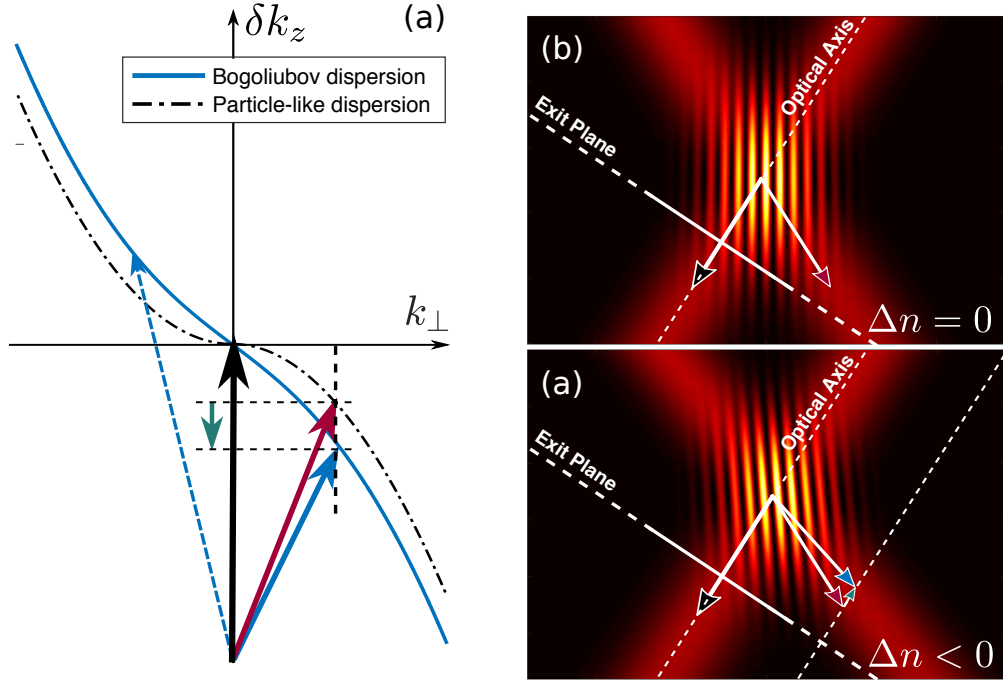


Figure 4.1: Qualitative explanation of the shift in the interference pattern as a result of the shortening of the probe axial wave-vector in the nonlinear scenario. Figure (a) shows the pump wave-vector (black arrow) as well as the probe one, in a linear (red arrow) and a nonlinear (blue arrow) medium. The photon fluid is at rest, which means that the pump evolves along the optical axis. Therefore, its wave-vector does not have any transverse component. The probe enters the medium with a non-zero transverse wave-vector. In the linear scenario figure (b), the magnitudes of the wave-vectors of pump and probe are equal. The two beams, propagating downward, create an interference pattern that is parallel to the vertical axis. In the nonlinear scenario sketched on figure (c), the magnitude of the probe wave-vector is smaller than the pump one, which thus tilts the interference fringes. By imaging a plane perpendicular to the optical axis (dotted line), one observes a shift of the interference pattern when switching from the linear to the nonlinear situation.

On figures 4.1(b) and (c) two beams are propagating from top to bottom, inside a linear and a nonlinear self-defocusing medium respectively. For the sake of clarity, the angle between them has been exaggerated. The pump propagates along the optical axis (black dashed line). Its wave-vector has been reported on both panels (black head arrow). The probe propagates from left to right, as indicated by the red and blue head arrows, representing its wave-vector in the linear and nonlinear cases respectively. The shortening of the axial component of the probe wave-vector is shown by the small green head arrow on figure 4.1(c). It induces a tilt of the interference fringes (that are vertical in the linear case), which in turn translates into a shift ΔS of the interference pattern in a plane perpendicular to the optical axis.

According to the definition of the shift, ΔS can be expressed as follows:

$$\Delta S(k_\perp) = \frac{\Delta\Phi(k_\perp)}{k_\perp} = \frac{\Delta\Phi_{\text{nl}}(k_\perp) - \Delta\Phi_1(k_\perp)}{k_\perp}, \quad (4.2)$$

where $\Delta\Phi_1$ and $\Delta\Phi_{\text{nl}}$ are the differences between the phases accumulated by the probe and the pump beams, propagating inside a linear (l) and a nonlinear (nl) medium respectively. Let $\Phi_{0,l}(L)$ and $\Phi_{0,\text{nl}}(L)$ stand for the phase of the pump at the exit plane of a linear and a nonlinear medium of length L . Similarly, let $\Phi_1(k_\perp, L)$ and $\Phi_{\text{nl}}(k_\perp, L)$ be the phase of the probe in the same conditions. The phase shifts $\Delta\Phi_1$ and $\Delta\Phi_{\text{nl}}$ can then be expressed as: $\Delta\Phi_1(k_\perp) = \Phi_1(k_\perp, L) - \Phi_{0,l}(L)$ and $\Delta\Phi_{\text{nl}}(k_\perp) = \Phi_{\text{nl}}(k_\perp, L) - \Phi_{0,\text{nl}}(L)$.

Some of the quantities defined previously are easy to express as function of the parameters. For instance: $\Phi_{0,l}(L) = k_0 n_0 L$, where n_0 is the linear refractive index of the medium, and: $\Phi_1(k_\perp, L) \simeq k_0 n_0 L [1 + \sin^2(\theta_r)/2]$, θ_r being the angle of refraction of the probe beam at the medium input facet. It is defined by the Snell law: $\sin(\theta_i) = n_0 \sin(\theta_r)$. It is interesting to notice that the transverse component k_\perp of the probe \mathbf{k} -vector is unchanged when the probe goes through the air/medium interface. Indeed, using the Snell law, it appears that the in-air transverse wave-vector $k_\perp^{(i)} = k_0 \sin(\theta_i)$ is equal to $k_\perp^{(r)} = k_0 n_0 \sin(\theta_r)$. Therefore,

$$\Delta\Phi_1(k_\perp) = \frac{1}{2} k_0 n_0 L \sin^2(\theta_r) = \frac{k_\perp^2}{2k} L. \quad (4.3)$$

A simple way to understand the relation (4.3) is to move into the frame translating at c/n_0 along the optical axis. This is by the way what we do, in chapter 2, when we introduce the slow-varying envelope \mathcal{E}_0 of the electric field amplitude \mathcal{E} : $\mathcal{E}_0(\mathbf{r}_\perp, z) = \mathcal{E}(\mathbf{r}_\perp, z) \exp(-ikz)$. This formula can be regarded, in some ways, as a change of observation frame. Indeed, using \mathcal{E}_0 instead of \mathcal{E} is like describing the physics from the frame translating at the speed c/n_0 along z . In this frame, pump photons are at rest and probe photons behave as free-particles of \mathbf{k} -vector k_\perp and energy $\hbar\Omega = \hbar c k_\perp^2 / (2n_0 k)$ (remembering the $z \leftrightarrow t$ mapping). Those particles exist during $t = n_0 L / c$ and accumulate the phase $\Omega t = k_\perp^2 L / (2k)$ during their lifetime. It seems then natural to suppose that the same applies in the nonlinear case, namely, that $\Delta\Phi_{\text{nl}}(k_\perp) = \Omega_B(k_\perp) L$. This assumption has been made in [52] and leads to the following expression for the shift:

$$\Delta S(k_\perp) = \frac{k_\perp}{2k} \left[\sqrt{1 + \frac{|\Delta n|}{n_0} \left(\frac{2k}{k_\perp} \right)^2} - 1 \right] L. \quad (4.4)$$

This formula matches with the geometrical argument discussed above. By moving from the linear to the nonlinear situation, the probe wave-vector is squeezed along the optical axis by $\delta k = \Omega_B(k_\perp) - k_\perp^2 / 2k$. The phase shift $\Delta\Phi$ is therefore given by $\Delta\Phi = \delta k L$ and, by using (4.2), we recover (4.4) (in absolute value). Equation (4.4) predicts that the shift reaches an asymptotic value, $c_s L$, when $k_\perp \ll k_\xi$, or in other words, the linear increase of $\Delta\Phi$ with k_\perp when $k_\perp \ll k_\xi$. Conversely, $\Delta\Phi$ should tend toward $k_0 \Delta n L$ when $k_\perp \gg k_\xi$. I remind you that $k_\xi = k \sqrt{\Delta n / n_0}$ is the inverse of the healing length ξ .

This last point seems quite natural. Indeed, in the particle-like regime, plane-wave density modulations follow a quadratic dispersion as $\Omega_B(k_\perp) \approx k_0 \Delta n + k_\perp^2 / (2k)$. The offset stems basically from the value the dispersion takes at the end of the sound-like regime, that is, when $k_\perp = k_\xi$. Because plane wave modulations propagating onto a low and a high density background fluid behave both as massive particles as long as $k_\perp \gg k_\xi$, the phase difference accumulated between them only comes from this offset and $\Delta\Phi \approx k_0 \Delta n L$, as stated by the formula above. However, the non-zero value of the shift for $k_\perp \ll k_\xi$ is not easy to understand. We have fought long and hard to observe it experimentally – without any success – before questioning the validity of equation (4.4).

When pump and probe get inside the nonlinear medium, they spontaneously generate an idler beam, having the same frequency ω , which propagates at the conjugate k-vector $-k_\perp$. This third order nonlinear wave mixing process is known as degenerate four wave mixing. Since the three beams involved in this mechanism have the same frequency, they will not fulfill phase matching conditions, except when pump and probe are copropagating, that is, when $k_\perp = 0$. The generation of the idler field in experiments is therefore due to the sudden change in the nonlinearity at the medium input plane. But contrarily to what is said in [52], the idler beam is not suppressed shortly thereafter. Energy exchanges between probe and idler beams (by means of the pump) continuously take place all along their propagation in the nonlinear medium (probe and idler are plane waves and are thus spatially overlapping). In order to derive a reliable formula linking ΔS to Ω_B , we need to properly describe the evolution of the probe field inside the nonlinear medium and thus to take the coupling between the probe and the idler beams into account. We can as of now state that this more exhaustive approach will not change the behaviour of the shift when $k_\perp \gg k_\xi$, since in that case degenerate for wave mixing processes are not phase matched at all and thus completely inefficient in generating the idler field. At large k_\perp , the impact of the idler on the propagation of the probe can therefore be neglected and the formula (4.4) applies, as mentioned in [98]. However, we will see that this correction has drastic effect at low k_\perp .

ii Full description using Bogoliubov theory

In the framework of Bogoliubov's theory, the small plane-wave modulation spontaneously excites a superposition of two Bogoliubov modes when it gets inside the nonlinear medium. Those modes are counter-propagating, in the transverse plane, at $\pm v_{ph} = \pm \Omega_B(k_\perp) / k_\perp$. In what follows, I will sometimes erroneously name these counter-propagating modes "probe" and "idler". However, I must emphasize that probe and idler fields are technically generated at the the nonlinear medium exit plane in this description. I will come back to this point in a moment. For now, let's derive, within the Bogoliubov's formalism, an exact expression for $\Delta\Phi_{nl}$ and ΔS , taking linear absorption into account (*ie* $\alpha \neq 0$). The in-air slowly varying electric field envelope, right before the medium input plane, reads as follows:

$$\mathcal{E}_0(\mathbf{r}_\perp, z) = \mathcal{E}_0(z) + e^{i\Phi_0(z)} \int \frac{d\mathbf{k}_\perp}{(2\pi)^2} a(\mathbf{k}_\perp, z) e^{-i\mathbf{k}_\perp \mathbf{r}_\perp}. \quad (4.5)$$

Let's set the phase of the pump at $z = 0^-$ to zero. Let's also assume that the field energy is conserved through the air/medium interface (perfect window anti-reflection coating). The Fourier amplitudes $a(\mathbf{k}_\perp, 0^-)$ and $a^*(-\mathbf{k}_\perp, 0^-)$ are then related to the Bogoliubov operators $b(\mathbf{k}_\perp)$ and $b^*(-\mathbf{k}_\perp)$ by:

$$\begin{pmatrix} a_{\mathbf{k}_\perp}(0^-) \\ a_{-\mathbf{k}_\perp}^*(0^-) \end{pmatrix} = \sqrt{n_0} M_{\mathbf{k}_\perp}(0) \begin{pmatrix} b_{\mathbf{k}_\perp} \\ b_{-\mathbf{k}_\perp}^* \end{pmatrix} \text{ whith } M_{\mathbf{k}_\perp}(z) = \begin{pmatrix} u_{\mathbf{k}_\perp}(z) & v_{\mathbf{k}_\perp}^*(z) \\ v_{\mathbf{k}_\perp}(z) & u_{\mathbf{k}_\perp}^*(z) \end{pmatrix}, \quad (4.6)$$

where $u_{\mathbf{k}_\perp}(z) = \tilde{u}_{\mathbf{k}_\perp}(z) e^{i\Omega_{\text{eff}} z}$ and $v_{\mathbf{k}_\perp}(z) = \tilde{v}_{\mathbf{k}_\perp}(z) e^{i\Omega_{\text{eff}} z}$ (Ω_{eff} is defined in subsection 2.4.1). One can derive a relation similar to (4.6) at the second air/medium interface, when $z = L$. Combining both and setting $|u_{\mathbf{k}_\perp}|^2 - |v_{\mathbf{k}_\perp}|^2 = N(\mathbf{k}_\perp, z)$, we finally get a relation between the input and output Fourier components of the electric field envelope:

$$\begin{pmatrix} a_{\mathbf{k}_\perp}(L^+) \\ a_{-\mathbf{k}_\perp}^*(L^+) \end{pmatrix} = \left[\sqrt{n_0} M_{\mathbf{k}_\perp}(L) \right] \cdot \left[\frac{M_{\mathbf{k}_\perp}^{-1}(0)}{\sqrt{n_0}} \right] \begin{pmatrix} a_{\mathbf{k}_\perp}(0^-) \\ a_{-\mathbf{k}_\perp}^*(0^-) \end{pmatrix} \quad (4.7)$$

$$= \frac{1}{N(\mathbf{k}_\perp, 0^+)} \begin{pmatrix} U_{\mathbf{k}_\perp} & V_{\mathbf{k}_\perp}^* \\ V_{\mathbf{k}_\perp} & U_{\mathbf{k}_\perp}^* \end{pmatrix} \begin{pmatrix} a_{\mathbf{k}_\perp}(0^-) \\ a_{-\mathbf{k}_\perp}^*(0^-) \end{pmatrix}. \quad (4.8)$$

The normalization constant $N(\mathbf{k}_\perp, 0^+)$ is equal to one. Indeed, in the thin medium limit (*ie* when $L \rightarrow 0$) the effect of linear absorption on the propagation of the beams is negligible and the normalization condition reduces to the one of the lossless case $|u_{\mathbf{k}_\perp}|^2 - |v_{\mathbf{k}_\perp}|^2 = 1$. Right before the nonlinear medium entrance plane ($z = 0^-$), the idler beam has still not been generated. Therefore, the amplitude $a_{-\mathbf{k}_\perp}^*(0^-)$ is zero, which amounts to saying that the idler is seeded by vacuum. The input-output relation (4.8) can easily be understood. The probe spontaneously generates two counter-propagating Bogoliubov modes at $\pm \mathbf{k}_\perp$ when it enters the medium. Bogoliubov modes are eigenstates of the nonlinear dynamics; they consequently accumulate the phase $\pm \Omega_{\text{eff}} L$ before reaching the medium output plane. At that point, each of the two counter-propagating Bogoliubov excitations spontaneously turns into a superposition of probe and idler fields. The idler beam is thus only generated at the medium output plane, as mentioned at the beginning of this derivation. Its k-space amplitude is given by $a_{-\mathbf{k}_\perp}^*(L^+) = V_{\mathbf{k}_\perp} a_{\mathbf{k}_\perp}(0^-)$, where the function $V_{\mathbf{k}_\perp}$ is defined by:

$$V_{\mathbf{k}_\perp} = \tilde{u}_{\mathbf{k}_\perp}^*(0) \tilde{v}_{\mathbf{k}_\perp}(L) e^{i\Omega_{\text{eff}} L} - \tilde{v}_{\mathbf{k}_\perp}^*(0) \tilde{u}_{\mathbf{k}_\perp}(L) e^{-i\Omega_{\text{eff}}^* L}. \quad (4.9)$$

The input-output relation (4.8) for the probe field reduces to: $a_{\mathbf{k}_\perp}(L^+) = U_{\mathbf{k}_\perp} a_{\mathbf{k}_\perp}(0^-)$, with:

$$U_{\mathbf{k}_\perp} = \tilde{u}_{\mathbf{k}_\perp}(L) \tilde{u}_{\mathbf{k}_\perp}^*(0) e^{i\Omega_{\text{eff}} L} - \tilde{v}_{\mathbf{k}_\perp}^*(L) \tilde{v}_{\mathbf{k}_\perp}(0) e^{-i\Omega_{\text{eff}}^* L}. \quad (4.10)$$

The phase accumulated by the probe while propagating in the medium is thus given by:

$$\Phi_{\text{nl}}(k_\perp, L^+) = \arg(U_{\mathbf{k}_\perp}) + \Phi_{0,\text{nl}}(L^+), \quad (4.11)$$

and, finally, $\Delta\Phi_{\text{nl}}(k_\perp) = \arg(U_{\mathbf{k}_\perp})$. When the phase matching conditions are not fulfilled, that is, when $k_\perp \gg k_\xi$, the amplitude of the "idler" beam is much lower than the "probe" one ($v_{\mathbf{k}_\perp} \ll u_{\mathbf{k}_\perp}$). The second term on the right hand side of (4.10) is negligible in that case and $\arg(U_{\mathbf{k}_\perp}) \simeq \Omega_{\text{eff}}(\mathbf{k}_\perp)$. As you may have noticed, equation (4.11) reduces then to the relation we have intuited before in order to derive the formula (4.4) which thus correctly describes how the shift evolves when $k_\perp \gg k_\xi$. But when quasi-phase matching conditions are fulfilled, the argument of U depends in a complicated manner on the the amplitude and phase of the Bogoliubov amplitudes u and v . By using the relations $\tilde{u} = \frac{1}{2}(\tilde{f}_+ + \tilde{f}_-)$ and $\tilde{v} = \frac{1}{2}(\tilde{f}_+ - \tilde{f}_-)$ as well as the expression for the slow-varying Fourier components \tilde{f}_\pm , defined in 2.4.1, one can go through the tedious but straightforward computation of $\Delta\Phi_{\text{nl}}$ in the general case. At the end of the day:

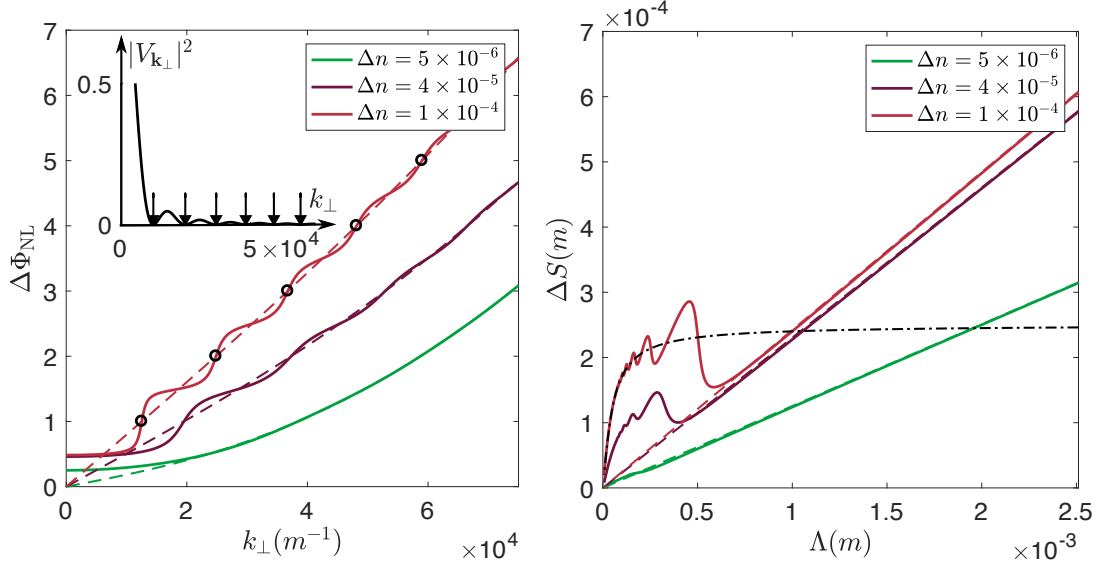


Figure 4.2: Plots of the nonlinear phase shift $\Delta\Phi_{\text{nl}}$ (a) and of the shift ΔS (b) as function of k_{\perp} and $\Lambda = 2\pi/k_{\perp}$ respectively, for various values of the nonlinear refractive index Δn . (a): The nonlinear phase shift follows globally the curve $k_{\perp} \rightarrow \Omega_B(\mathbf{k}_{\perp})L$ (dotted lines) but exhibits a stair-like structure, which is more and more pronounced as $\Delta n = n_2 \mathcal{I}_0$ increases. Moreover, $\Delta\Phi_{\text{nl}}$ tends toward a non-zero constant when k_{\perp} goes to zero (see formula (4.14)). (b): This translates into a linear increase of the shift ΔS for large modulation wavelengths. The oscillations on the right come for the stair-like structure of $\Delta\Phi_{\text{nl}}$. The black dashed-dotted line shows, for comparison, the shift obtained from equation (4.4) when $\Delta n = 10^{-4}$. It predicts a saturation of ΔS at large $\Lambda = 2\pi/k_{\perp}$ which is not observed experimentally. Inset of (a): idler intensity in k-space as function of k_{\perp} for $\Delta n = 10^{-4}$. The positions at which is cancels (black arrows) are reported on the plot of $\Delta\Phi_{\text{nl}}$ obtained at the same Δn (black circles). They correspond to the points at which $\Delta\Phi_{\text{nl}}$ crosses the dispersion relation.

$$\Delta\Phi_{\text{nl}}(k_{\perp}) = \arctan \left[\frac{k_{\perp}^4 + 4k^2 \text{Re}[\Omega_B(\mathbf{k}_{\perp}, 0)] \text{Re}[\Omega_B(\mathbf{k}_{\perp}, L)]}{2k k_{\perp}^2 \{\text{Re}[\Omega_B(\mathbf{k}_{\perp}, 0)] + \text{Re}[\Omega_B(\mathbf{k}_{\perp}, L)]\}} \times \tan \{ \text{Re}[\Omega_{\text{eff}}(\mathbf{k}_{\perp}, L)] L \} \right] \quad (4.12)$$

which, in the lossless case ($\alpha = 0$), reads barely simpler:

$$\Delta\Phi_{\text{nl}}(k_{\perp}) = \arctan \left[\frac{k_{\perp}^4 + 4k^2 [\Omega_B(\mathbf{k}_{\perp})]^2}{4k k_{\perp}^2 \Omega_B(\mathbf{k}_{\perp})} \times \tan \{ \Omega_B(\mathbf{k}_{\perp}) L \} \right]. \quad (4.13)$$

The formulas (4.12) and (4.13) cannot be easily inverted in order to express the Bogoliubov dispersion relation as function of the nonlinear phase shift $\Delta\Phi_{\text{nl}}$, or equivalently, as function of the shift ΔS using the relation (4.2). Measuring $\Delta\Phi_{\text{nl}}$ to retrieve the dispersion relation of small amplitudes density waves seems therefore to be quite unsuitable. However, we can still observe some non-trivial behaviour of the nonlinear phase shift when $k_{\perp} \ll k_{\xi}$. In that case, $\Delta\Phi_{\text{nl}}$ tends toward a non-zero value:

$$\Delta\Phi_{\text{nl}}(k_{\perp} \simeq 0) = \arctan \left\{ 2k_0 \Delta n(0) L \times \frac{2}{\alpha L} \frac{1 - \exp(-\alpha L/2)}{1 + \exp(-\alpha L/2)} \right\}, \quad (4.14)$$

which is rather counter-intuitive from the linear optics perspective, in which we expect it to simply go to zero. Indeed, if we consider naively that the effect of nonlinearity is to shift the value of the refractive index n_0 by $\Delta n = n_2 \mathcal{I}_0$, there is no reason why $\Delta \Phi_{\text{nl}}$ should not go to zero when the pump and the probe are parallel. Figure 4.2(a) shows the trend of the nonlinear phase shift as function of k_{\perp} for different values of Δn and for $\alpha = 0$. The phase shift $\Delta \Phi_{\text{nl}}$ tends toward a non-zero value when k_{\perp} goes to zero. This asymptotic limit quickly saturates when Δn increases, as suggested by equation (4.14). Moreover, the nonlinear phase shift exhibits a stair-like structure, more visible at low k_{\perp} , which follows globally the trend of the curve $k_{\perp} \rightarrow \Omega_B(\mathbf{k}_{\perp})L$ (dotted lines). It becomes more and more marked as Δn increases. The plateaus in this stair-like structure exactly lie at the transverse wave-vectors at which counter-propagating Bogoliubov modes interfere destructively in the exit plane, that is, when k_{\perp} fulfills: $\Omega_B(k_{\perp})L = n\pi + \pi/2$, n being a positive integer. Reversely, the inflection points in between consecutive plateaus precisely mark the locations of the wave-vectors at which Bogoliubov modes constructively interfere in the output plane. These interferences occur when $\Omega_B(k_{\perp})L = n\pi$ (black circles). Figure 4.2(a) shows the evolution of the shift ΔS as function of the modulation wavelength $\Lambda = 2\pi/k_{\perp}$, for the same values of Δn as before. Because of the stair-like structure of $\Delta \Phi_{\text{nl}}$, the shift exhibits strong oscillations when $\Lambda \simeq \xi$. The linear increase of ΔS with the modulation wavelength when $\Lambda \gg \xi$ results from the behaviour of $\Delta \Phi_{\text{NL}}$ when $k_{\perp} \ll k_{\xi}$. The slope of this linear trend is equal to the right hand side of equation (4.14) times $1/2\pi$. For comparison, the shift obtained using the model proposed in [52] has been reported on the same graph (black dashed line), for $\Delta n = 10^{-4}$. As expected, both descriptions match in the particle-like regime (that is, for $\Lambda \ll \xi$) but instead of a linear increase at high Λ , equation (4.4) predicts a saturation of ΔS toward $c_s L$ (which has never been observed with our setup).

iii Quasi-particles interferences

As we have seen in the previous paragraph, the key features in the curves of $\Delta \Phi_{\text{nl}}$ and ΔS shown on figure 4.2 can be explained in terms of interferences between counter-propagating Bogoliubov modes. A way of developing a better understanding about these quasi-particle interferences is to move from a spatial to a temporal description of the dynamics, using the $z \leftrightarrow t$ mapping once again. In doing so, we can think about the Bogoliubov modes as a quasi particle/antiparticle pair that is generated at $\tau = 0$ (where τ is defined by $\tau = zn_0/c$). The particle ("idler") evolves at $-\mathbf{k}_{\perp}$ over the positive time while the antiparticle ("probe") evolves at \mathbf{k}_{\perp} over the negative time (as if it was going back in the past). Indeed, in the frame translating at c/n_0 along the optical axis, probe photons seems to move backward, that is, toward the negative z values, at a velocity $c\Omega_B(k_{\perp})/k$. In the lossless case, particle and antiparticle respectively accumulate a phase $-\Omega_B(\mathbf{k}_{\perp})L$ and $\Omega_B(\mathbf{k}_{\perp})L$ during their lifetime. As they are overlapping in the transverse plane (I assume they are plane-waves), they will totally interfere (constructively or destructively) as soon as $\text{mod}\{2\Omega_B(\mathbf{k}_{\perp})L, \pi\} = 0$, or, in other words, when $\Omega_B(\mathbf{k}_{\perp})L = n\pi/2$ (n being a positive integer).

It is interesting to notice that quasi-particle interferences lead moreover to the cancellation of the idler intensity in the Fourier space. From equation (4.8), one gets (when $\alpha = 0$):

$$\begin{aligned} \frac{\mathcal{I}_{-\mathbf{k}_\perp}(L^+)}{\mathcal{I}_{\mathbf{k}_\perp}(0^-)} &= \left| \frac{a_{-\mathbf{k}_\perp}(L^+)}{a_{\mathbf{k}_\perp}(0^-)} \right|^2 = |V_{\mathbf{k}_\perp}|^2 = |2 \tilde{u}_{\mathbf{k}_\perp} \tilde{v}_{\mathbf{k}_\perp}|^2 \sin^2 [\Omega_B(\mathbf{k}_\perp) L] \\ &= (k_0 \Delta n L)^2 \text{sinc}^2 [\Omega_B(\mathbf{k}_\perp) L], \end{aligned} \quad (4.15)$$

where sinc stands for the cardinal sine function. The idler intensity in Fourier space, $\mathcal{I}_{-\mathbf{k}_\perp}$, is maximum at $k_\perp = 0$, when phase matching conditions are perfectly fulfilled. For $k_\perp \ll k_\xi$, the envelope $|2 \tilde{u} \tilde{v}|^2$ of the k-space intensity profile scales as $1/k_\perp^4$. This is understandable, as the phase matching between pump and probe is getting worse when the probe transverse wave-vector increases. In addition, one can show that: $|U_{\mathbf{k}_\perp}|^2 - |V_{\mathbf{k}_\perp}|^2 = 1$ and, therefore, that probe and idler intensities in k-space are related by: $\mathcal{I}_{\mathbf{k}_\perp}(L^+) = \mathcal{I}_{\mathbf{k}_\perp}(0^-) + \mathcal{I}_{-\mathbf{k}_\perp}(L^+)$. Consequently, any variation in the idler intensity translates into a similar variation in the probe intensity, $\mathcal{I}_{\mathbf{k}_\perp}$. Equation (4.15) also indicates that the idler intensity $\mathcal{I}_{-\mathbf{k}_\perp}$ in k-space cancels at some specific values of k_\perp (located by the black arrows on the inset of figure 4.2(a) for instance), at which $\Omega_B(k_\perp)L = n\pi$. At those wave-vectors, we thus expect an increase in the contrast of the interference fringes at the medium exit plane, as both probe and idler are in phase. This of course depends on the length of the medium.

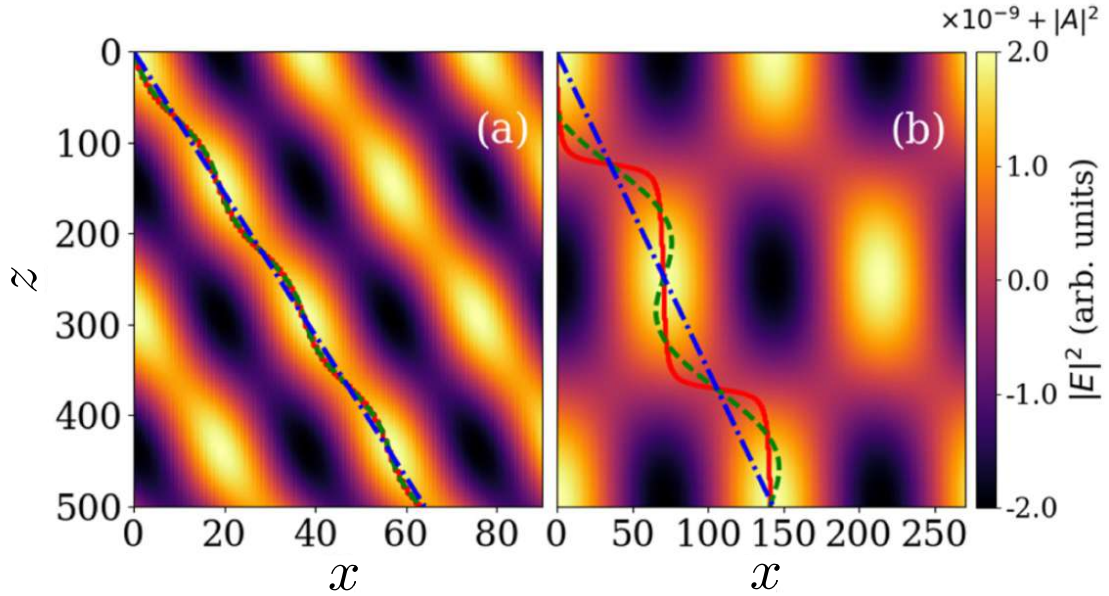


Figure 4.3: Figure taken from D. Ferreira *et al.* [98]. The intensity of the total electric field is shown as function of the transverse position x and the propagation distance z (top view), for $k_\perp \gg k_\xi$ (a) and $k_\perp \ll k_\xi$ (b) respectively. The contrast of the interference patterns is modulated over z . We can complete the description made in [98] by noticing that Bogoliubov modes destructively interfere when $\Omega_B(k_\perp)z = n\pi + \pi/2$, reducing consequently the contrast of the interference fringes. On the contrary, when $\Omega_B(k_\perp)z = n\pi$, Bogoliubov modes constructively interfere and the contrast is maximized.

Solving numerically the nonlinear Schrödinger equation allows to compute the intensity of the total electric field inside the nonlinear medium in any transverse plane along the z -axis. In figure 4.3, we present a cut along the x -axis, for $k_{\perp} \gg k_{\xi}$ (a) and $k_{\perp} \ll k_{\xi}$ (b) respectively. This figure is taken from [98] where the feasibility of measuring the Bogoliubov dispersion Ω_B for propagating photon fluids in nematic liquid crystals is theoretically investigated, using the pump/probe technique described here. On figure 4.3, the background fluid density has been subtracted. The contrast of the interference fringes in (a) and (b) is modulated along the z -axis. When $\Omega_B(k_{\perp})z = n\pi$, Bogoliubov modes constructively interfere and the contrast is increased. Reversely, when $\Omega_B(k_{\perp})z = n\pi + \pi/2$, Bogoliubov modes destructively interfere and the contrast is reduced. Moreover, $\mathcal{I}_{-\mathbf{k}_{\perp}}$ (and thus $\mathcal{I}_{\mathbf{k}_{\perp}}$) increases when the transverse wave-vector decreases, explaining why the variations of the contrast are bigger on figure (b) than on figure (a).

iv Nonlinear optics approach

I would like to conclude this paragraph mentioning that equation (4.15) can also directly be derived using textbook nonlinear optics. Let \mathcal{E}_{pu} , \mathcal{E}_{pr} and \mathcal{E}_i stand for the pump, the probe and the idler electric field envelopes. By neglecting the dependence of the various fields on the transverse spatial coordinates x and y , the equation driving the evolution of the idler inside the nonlinear medium reads as follows (in the paraxial approximation) [55]:

$$i \frac{\partial \mathcal{E}_i}{\partial z} = -k \frac{n_2}{n_0} [\mathcal{E}_{pu}]^2 \mathcal{E}_{pr}^* \exp(i \Delta k z), \quad (4.16)$$

where k_{pu} , k_{pr} and k_i are the pump, the probe and the idler axial wave-vectors respectively. The wave-vector mismatch Δk is equal to $2k_{pu} - k_{pr} - k_i$. Since $k_{pr} = k_i = k_{pu} - \Omega_B(k_{\perp})$ (see for instance figure 4.1(a)), $\Delta k = 2\Omega_B(k_{\perp})$ in the present case. When $\Delta k = 0$, that is, when $k_{\perp} = 0$ (perfect phase matching), the idler maintains a fixed phase relation with respect to the nonlinear polarization $\mathcal{P}_i = \frac{n_2}{n_0} [\mathcal{E}_{pu}]^2 \mathcal{E}_{pr}^* \exp(i \Delta k z)$ and is therefore able to extract energy more efficiently from the incident waves. When $\Delta k \neq 0$, the idler gets out of phase with its driving polarization \mathcal{P}_i and part of its power can flow back into the pump. Let \mathcal{I}_{pr} stand for the probe intensity. The idler intensity \mathcal{I}_i at the medium exit plane is finally obtained by integrating equation (4.16) from 0 to L :

$$\mathcal{I}_i(\Delta k) \simeq \mathcal{I}_{pr} (k_0 \Delta n L)^2 \left| \frac{e^{i \Delta k L} - 1}{\Delta k L} \right|^2 = \mathcal{I}_{pr} (k_0 \Delta n L)^2 \text{sinc}^2 \left[\frac{\Delta k L}{2} \right]. \quad (4.17)$$

Equations (4.17) and (4.15) are strictly analogous. Bogoliubov's theory and nonlinear optics lead unsurprisingly to the same result but it is still interesting however to compare the understanding each of these approaches provides about the same physical phenomenon.

v Discussion

As mentioned previously, measuring the shift ΔS is not necessarily the most suitable way to retrieve the dispersion relation of density waves travelling onto propagating photon fluids. There are at least two reasons for this, that I would like to discuss before ending this section. The first is a technical limitation, that constrains the range of transverse \mathbf{k} -vectors we can explore in practice. The second is more fundamental and concerns our ability to extract the dispersion relation of density waves from the shift, using equations (4.2) and (4.12).

- In order to measure the shift, pump and probe beams have to overlap all along their propagation inside the nonlinear medium. Therefore, probe and idler are also superimposed at the medium exit plane, which is annoying as we only want to observe the interference pattern between pump and probe. Measuring the shift requires then to filter out the $-\mathbf{k}_\perp$ component of the field in k-space, that is, the contribution from the idler beam. In practice, the exit plane is imaged on camera using a $4f$ telescope made of two lenses. The idler beam is therefore simply cut by positioning a mask in the focal plane of the first of these lenses. As the pump undergoes self-defocusing by propagating inside the nonlinear medium, its extension in k-space can be large enough to cover the range of wave-vectors over which the Bogoliubov dispersion relation is sound-like. Moreover, the mask should not cut a part of the pump beam in k-space, at the risk of distorting the real space filtered image, which drastically limits the range of usable transverse wave-vectors at the end of the day.
- As outlined above, the second and more fundamental issue of the shift measurement concerns how the dispersion relation – which is a priori not known – is extracted from the shift using equations (4.2) and (4.12). Once ΔS has been measured for various transverse wave-vectors k_\perp , the relation (4.12) has to be inverted assuming it applies to the unknown dispersion $\Omega(k_\perp)$. In doing so, we are not supposing directly that $\Omega = \Omega_B$, but however that equation (4.12), derived within the Bogoliubov framework, is still valid replacing Ω_B by Ω . Things go consequently round and round in circles. It is absolutely essential to measure the dispersion relation of density waves using a technique that does not require any knowledge about Bogoliubov theory but shows, reversely, that this theory is appropriate to describe the dispersion relation Ω .

In section 4.2, I will introduce a new experimental technique that overcomes these issues. Before that, I would like to present some results we obtained from the shift measurement. In the following subsections, I start by describing the setup and how data are post-processed, before discussing the results and putting them into perspective with numerical simulations. I conclude by briefly commenting the results obtained by Vocke *et al.* in [52].

4.1.2 Experimental setup and data processing

The experimental setup designed to measure the shift has been sketched on figure 4.4. The continuous-wave laser field at 780 nm is provided by a Ti:Sapphire cavity, pumped with a 10 W frequency-doubled Nd:YVO4 laser. The output laser beam is sent onto the optical table through a single-mode polarization-maintaining high power fiber. The power of the outgoing beam is controlled using a half-waveplate ($\frac{\lambda}{2}$) and a polarized beam splitter (PBS). The beam is first magnified and then highly elongated in the x direction using a set of two cylindrical lenses ($f_1 = 500$ mm and $f_2 = 100$ mm). This cylindrical telescope is slightly misaligned in order to loosely focus the beam onto the medium input facet. In that plane, the minor axis width $\omega_{0,y}$ (at $1/e^2$) is around $500 \mu\text{m}$ and the major axis one, $\omega_{0,x}$, is larger than 1 cm. The intensity profile is thus quasi uniform along the x -axis. Squeezing the beam in the other direction is thus mostly a way to increase the intensity (and thus Δn) along this axis. The Rayleigh length associated to $\omega_{0,y}$ is about 1 m which is much longer than the length of the cell ($L = 7.5$ cm). We can thus safely consider the beam as being collimated inside the nonlinear medium (as long as self-defocusing is negligible of course).

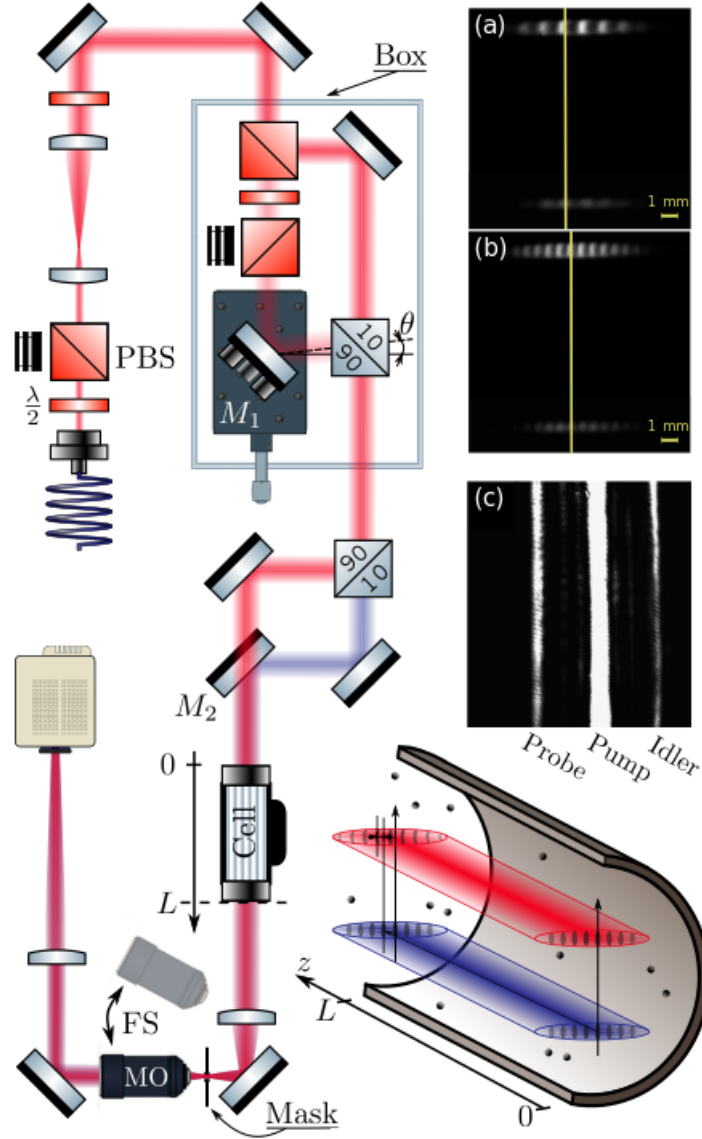


Figure 4.4: Experimental setup. The laser beam goes out from the fiber and is (i) magnified and (ii) elongated along the x -direction, before entering a Mach-Zehnder interferometer. From there, the beam splits into a high and a low power part (referred to as pump and probe). The piezo-electronically actuated mount of the mirror M_1 allows to finely tuned the angle θ_i between them. Pump and probe recombine and form an interference pattern whose fringes are parallel to the y direction. A 90:10 ($R:T$) beam splitter separates once again the beam in two parts after the Mach-Zehnder. The blue part is a low power reference while the red one is highly powerful. They propagate one above the other inside the vapor cell. The cell exit plane is imaged onto the camera with a $4f$ telescope. (a) and (b): output plane at low and large angle θ_i between pump and probe. The shift ΔS between the lower and the upper beam is clearly visible. The upper beam is broader because of self-defocusing. (c) Image of the Fourier space, obtained with a infinity corrected microscope objective (MO). Pump ($k_{\perp} = 0$), probe ($k_{\perp} = k_0 \sin(\theta_i)$) and idler ($k_{\perp} = -k_0 \sin(\theta_i)$), as well as the sidebands they generate, are visible on this image.

After having been shaped, the laser beam enters a Mach-Zehnder interferometer, which is protected against air turbulences by a box made of Plexiglas. At that point, the beam splits into a high power and a low power part (referred to as pump and probe in the section 4.1). The probe reflects on the mirror M_1 that is hold in a piezo-actuated mount which in turn is fixed on a translation-stage. Tuning the voltage across the piezo allows to finely control the angle θ_i between pump and probe and thus the wavelength $\Lambda = 2\pi/k_\perp$ of the density waves. We make sure that the interference fringes that form when the beams recombine are parallel to the y -axis. On the probe arm, an other combination of half waveplate and polarized beam splitter controls the modulation depth (less than 5%). As soon as pump and probe exit the Mach-Zehnder interferometer, a 90:10 ($R:T$) beam splitter splits the recombined laser beam into two parts. The blue part on figure 4.4 is a low power reference for which the medium response is basically linear, while the red one is highly powerful and will thus behave as an interacting photon fluid. Blue and red beams propagates one above the other inside the vapor cell (the D-shaped mirror M_2 only reflects the reference), as sketched on the bottom right inset of figure 4.4. The cell exit plane is imaged onto a CMOS camera, with a $4f$ imaging system made of two lenses of focal length $f_3 = 200$ mm and $f_4 = 300$ mm. By flipping on the beam path a microscope objective (MO), we can image the focal plane of the first lens in this $4f$ system (inset (c) of 4.4) and thus precisely positioned the mask (razor blade) that filters out the idler beam.

In order to accurately measure the shift ΔS , we need to precisely align the reference beam with respect to the high power one. The alignment procedure is as follow:

- (1) We first make sure that both background beams (probe off) roughly propagate with the same transverse wave-vector and are correctly positioned one above the other.
- (2) We then switch the probe beam on. The next step is to align the interference fringes of the lower and upper interference patterns. We start by removing the vapor cell and make sure that bright fringes on the bottom face bright fringes on the top. Of course, by doing so, the optical axis of the lower and upper beams are not parallel anymore. We should then switch to k -space, bring back the backgrounds to the initial position ($k_\perp = 0$) and repeat this procedure iteratively (beam walking). We finally check that for every transverse wave-vector k_\perp the interference fringes remain aligned before putting the cell back on the beams path.

Images obtained in the cell output plane are shown on the insets (a) and (b) of figure 4.4. The contrast of the interference pattern (*ie* the modulation depth) has been increased for the sake of clarity. The shift between the interference fringes is clearly visible for low (a) and high k_\perp (b). As you may have seen, the fringes on the upper interference pattern slightly bend toward the propagation direction of the density modulation (that is, from right to left). As the intensity profile of the upper beam along the vertical axis is Gaussian, the nonlinear phase shift the probe accumulates by propagating over it depends on y . The sound velocity is higher along the upper beam major axis than slightly above or below. Sound-waves will consequently propagate faster along this axis than along the beam edges, which as a result locally bends the fringes. In order to avoid error in the data analysis, we therefore only average the intensity profile over 30 pixels on both sides of the backgrounds major axis (*ie* in between the white dotted line on figure 4.5). This is the maximal range for which fringe bending has negligible effects on the shift we measure.

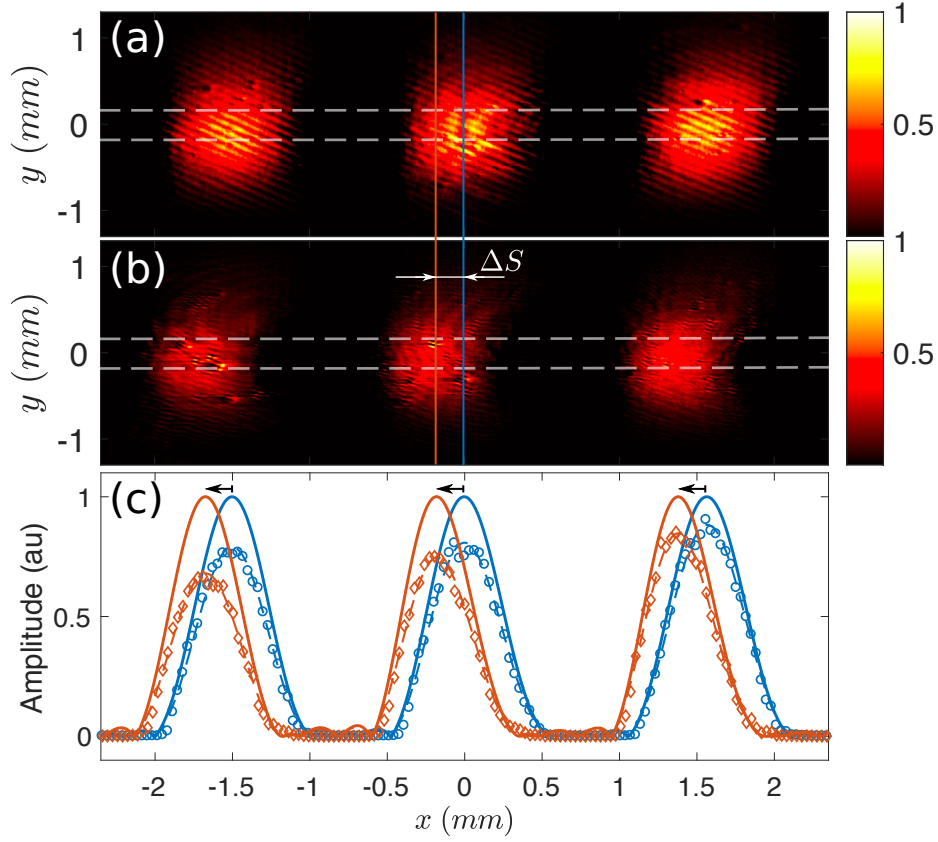


Figure 4.5: Data analysis. The background subtraction reveals the small amplitude density modulations that are propagating onto a low (a) and a high power background fluid (b). The blue and red data points in (c) are obtained by integrating the intensity in between the white dashed lines in (a) and (b) respectively. In order to clean the profiles, we first filter out the high frequencies noise (dashed lines) and then remove the intensity envelopes of the interference fringes (solid lines). The shift ΔS is finally computed by measuring the nearest peak-to-peak distance between the solid lines in average (black arrow).

The data analysis requires several post-processing steps that must be carefully performed. We start first by removing the background intensity distribution to keep only the density modulation on top of it, using the camera software directly. This was not a clever choice, as the background subtraction function of this software is not only performing an image subtraction but sets, in addition, all the negative intensities to zero, as you can see by looking at figure 4.5(c). We then integrate the intensity in between the white dashed lines on the interference patterns of figures 4.5(a) and (b), which are obtained respectively at low and high background fluid powers. The resulting profiles have been plotted on figure 4.5(c) (blue and red points). The high frequency noise is filtered out in Fourier space (dashed lines) and the interference fringes envelopes are removed to obtain the blue and red solid curves, using a Cubic spline interpolation method. The shift is finally computed by averaging the distance between the maximums of the blue and red solid lines (black arrows) over several interference fringes. The experimental results obtained with the setup sketched on figure 4.4 and the data analysis above are presented in the next subsection.

4.1.3 Experimental results and numerical simulations

i Comparison between experimental data and theory

The results we obtained with the shift experiment has been gathered together on figure 4.6. All the beams are propagating through a 7.5 cm cell filled with an isotopically pure vapor of rubidium 85, heated up at 130 °C. The laser frequency is 2.6 GHz red-detuned from the $F_g = 3 \rightarrow F'$ transition of the ^{85}Rb D_2 line. At these temperature and detuning, the vapor transmission is about 60%. Figure (a) shows the shift measured at low background density (grey diamonds) as function of the modulation wavelength Λ . The pump power \mathcal{P}_f is about 120 mW and the reference one around 10 mW. The probe power was small enough for the modulation depth to be less than 5%. The blue line is obtained by fitting the data using equations (4.12) and (4.2). The fit provides the value of the nonlinear refractive index change: $\langle \Delta n(z') \rangle_L = 1.3 \times 10^{-6}$. As you can see on figure 4.6(a), the agreement with theory is excellent

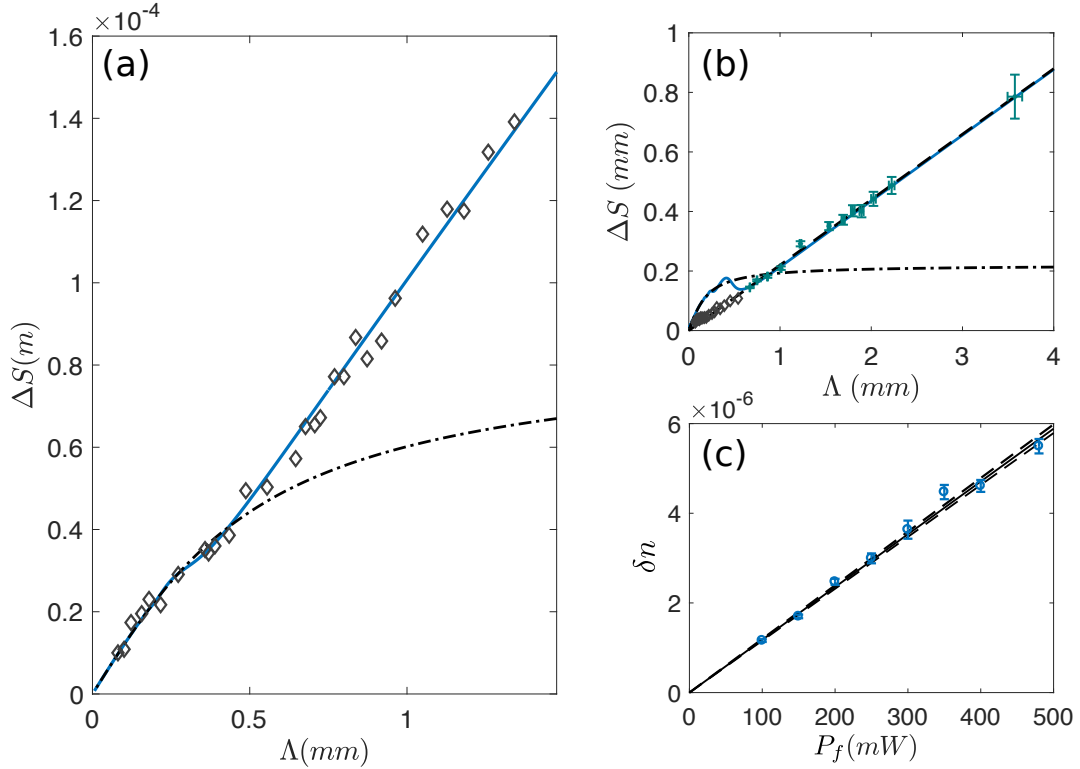


Figure 4.6: Shift experiment. (a): Shift ΔS as function of the modulation wavelength Λ for a fluid power of 120 mW. The experimental data (grey diamonds) are in good agreement with the theory (blue line) for $\langle \Delta n(z') \rangle_L = 1.3 \times 10^{-6}$. For comparison, the shift obtained using equation (4.4) has also been plotted (black dashed-dotted line). The latter predicts a saturation of ΔS at large modulation wavelengths, which is not observed experimentally. (b): Same as before for a fluid power of 480 mW this time. The theoretical curve does not match anymore with the data in the particle-like regime. (c): By fitting the shift with a line in the sound-like regime, the slope a_s of the linear trend can be measure as function of the fluid power \mathcal{P}_f . We then check that δn , defined in equation (4.14), linearly scales with \mathcal{P}_f .

and the shift ΔS increases linearly with the modulation wavelength, when it is larger than the healing length $\xi \simeq 300 \mu\text{m}$. This is an important result as it shows that the shift does not tend toward a finite value at large Λ , unlike what it is claimed in [52]. The shift computed with the model proposed in [52] – equation (4.4) – has also been plotted for comparison on the same graph (black dashed dotted line). The discrepancy between this model and the data is clearly visible in the regime where $\Lambda \gg \xi$. On figure 4.6(b), an example of data measured at higher background densities ($\mathcal{P}_f = 480 \text{ mW}$) is shown as function of Λ . As you can see, ΔS still linearly increases with the modulation wavelength, when it is larger than 0.5 mm .

The linear trend at large Λ is theoretically described by the following equation:

$$\Delta S(\Lambda) \simeq \arctan \left[2 k_0 \Delta n(0) L \times \frac{2}{\alpha L} \frac{1 - \exp(-\alpha L/2)}{1 + \exp(-\alpha L/2)} \right] \frac{\Lambda}{2\pi}, \quad (4.18)$$

derived from the formula (4.14). Knowing the absorption coefficient ($\alpha \simeq 7 \text{ m}^{-1}$), we can fit the linear trend of the shift at large Λ (cyan diamonds), taking the errorbars into account. This provides the value of the nonlinear change of refractive index in the input plane $\Delta n(0)$. We then plot the theoretical shift obtained for this specific value of $\Delta n(0)$ (blue solid line). As you can see, the experimental data at small Λ (grey diamonds) are not in good agreement with the theoretical model at high fluid densities (figure 4.6(b)). I will discuss this point later. Nevertheless, we can still measure how the slope of the linear trend, a_s , evolves with \mathcal{P}_f .

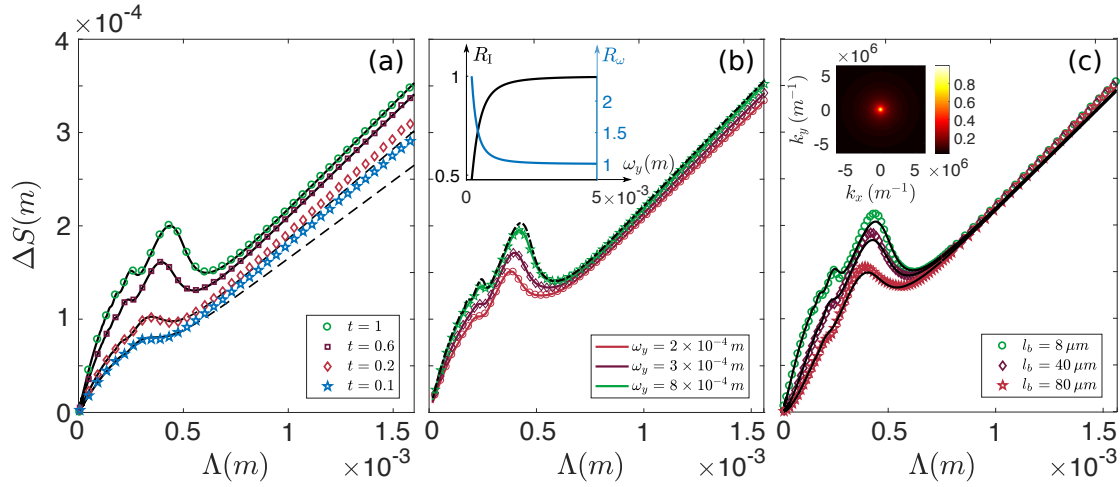


Figure 4.7: (a): Shift ΔS as function of the modulation wavelength Λ , for different vapor transmissions t . Simulations and theory match as long as the variation of the fluid density along z remains adiabatic ($t > 0.5$). Absorption seems to smooth the oscillations of the shift but it only reduces the average nonlinear refractive index change $\langle \Delta n(z') \rangle_L$ actually. (b): ΔS as function of Λ for various background widths w_y . The amplitude of the oscillations decreases with w_y . This behaviour is expected as self-defocusing is more likely to spread out the intensity of the background fluid in the transverse plane (and thus to reduce $\langle \Delta n(z') \rangle_L$) when w_y decreases. (c): ΔS as function of Λ for different nonlocal transport length scales. The oscillations are smoothed by nonlocality. However, for decent values of l_b , this effect is totally negligible. The inset of figure (c) shows the nonlocal response function in k -space. Parameters: $\Delta n(0) = 1.0 \times 10^{-5}$ and $L = 7.5 \text{ cm}$.

We already know that the nonlinear refractive index increases linearly with the fluid density and, consequently, with the pump power. We can thus invert equation (4.18) as follows:

$$\Delta n(0) = \frac{1}{4} \frac{\alpha}{k_0} \frac{1 + \exp(-\alpha L/2)}{1 - \exp(-\alpha L/2)} \tan[2\pi a_s(P_f)], \quad (4.19)$$

and check that it is the case, plotting $\Delta n(0)$ as function of P_f . By doing so, we obtain the blue points on figure 4.6(c). As expected, the relationship between $\Delta n(0)$ and P_f is linear indicating that the slope of the linear trend at large Λ correctly scales with the fluid density.

ii Discrepancy at low modulation wave-vectors

As mentioned previously, the agreement between data and theory at low Λ on figure 4.6(b) is not good. Actually, we never managed to observe experimentally the oscillations of the shift ΔS predicted by the theory at low Λ , when the fluid density is large enough. Moreover, our data does not even match the geometrical relationship between shift and modulation wavelength in the particle-like regime: $\Delta S(\Lambda) = k_0 \Delta n \Lambda / 2\pi$. This issue either comes from an uncontrolled systematic error in performing the experiment or from some physical process that is not taken into account in the theory yet. In order to test this second hypothesis, we numerically solve the NLSE in 2D using a second order split step method. The effect of linear absorption, self-defocusing and nonlocality on the shift are investigated. The results of the numerical simulations are grouped together on figure 4.7. They all have been performed using the same set of parameters. The background intensity, \mathcal{I}_0 , is set to 2.5×10^5 W/m² and the nonlinear index of refraction, n_2 , to 4×10^{-11} m²/W. The nonlinear change of refractive index is thus equal to 1.0×10^{-5} in the lossless case. The background fluid is also infinitely elongated in the x -direction. On figure (a), ΔS has been plotted as function of the modulation wavelength for different cell transmissions $t = \exp(-\alpha L)$. The coloured points stem from numerical simulations whereas the theoretical curves are plotted in black solid. The agreement between simulations and theory is excellent as long as the variation along z of the fluid density because of absorption remains adiabatic [71]. Absorption seems to smooth the shift oscillations, but actually, it only reduces the average change of refractive index $\langle \Delta n(z') \rangle_L$. In other words, if the input intensity is multiplied by $[1 - \exp(-\alpha L)] / \alpha L$, α being for instance the absorption coefficient corresponding to a cell transmission of 10%, the blue stars on figure (a) will almost exactly translate onto the green circles, for which $t = 1$. Absorption is thus not the cause of the discrepancy observed on figure 4.4(b). Figure 4.7(b) shows the effect of the pump width $\omega_{0,y}$ on the shift. We clearly observe a reduction in the amplitude of the shift oscillations when $\omega_{0,y}$ decreases. This is due to the fact that the effective focal length f_{eff} of the nonlinear medium shortens in that case. Self-defocusing is then more likely to spread the background intensity in the transverse plane. This results in a diminution of the intensity along the pump major axis during propagation, which reduces $\langle \Delta n(z') \rangle_L$ once again. The inset of figure 4.7(b) shows the ratios $R_\omega = \omega_{0,y}(0) / \omega_{0,y}(L)$ and $R_{\mathcal{I}} = \mathcal{I}_0(0) / \mathcal{I}_0(L)$ as function of the input width $\omega_{0,y}(0)$. Unsurprisingly, R_ω and R_I tend toward one when $z_{\text{eff}} \gg L$. Reversely, when $\omega_{0,y}(0)$ decreases, R_ω starts decreasing as well and R_I consequently rises up. For $\omega_{0,y}(0) \approx 500$ μm (experimental width), self-defocusing has definitely an effect but it does not smooth out the shift oscillations as on figure 4.4(b).

Figure 4.7(c) shows the effects of nonlocality on the shift. As on figures 4.7(a) and 4.7(b), ΔS has been plotted as function of Λ , for various nonlocal ballistic length scales l_d this time. The coloured points stem from numerical simulations. The formula (4.12) has been generalized using the nonlocal dispersion relation (2.46) to take into account the ballistic transport of excited atoms in our model. The theoretical predictions are plotted in black solid on figure (c) and match perfectly the simulations. As you may have noticed, nonlocality does not affect the value of $\langle \Delta n(z') \rangle_L$, because the way the shift increases at large Λ remains unchanged whatever the value of l_d . The changes induced by nonlocality are therefore more structural. However, nonlocality only significantly modifies the shift for values of the ballistic transport length scale much bigger than the one expected at 130 °C (which is about 7.5 μm , see 1.3.8 ii). Consequently, it cannot either be liable for the discrepancy observed in figure 4.4(b).

So far, we do not have a clear understanding about why the shift is not matching the theory in the particle-like regime for some data sets. We checked experimentally if the issue was coming from the alignment procedure detailed in subsection 4.1.2 by measuring the shift in the exact same way as in experiments without the rubidium cell. In that case, ΔS is zero whatever the angle between pump and probe, as expected. The shift measurement is also extremely sensitive to the phase of the pump and probe beams in the cell entrance plane. Indeed, the pump phase gradient at $z = 0$ defines the initial velocity distribution of the photon fluid in the transverse plane. The latter starts thus flowing as soon as the phase of the pump beam is not uniform in the entrance plane. If the photon fluid flows along the x -axis, the phase velocity of the density waves (and therefore the shift) will certainly be modified by Doppler effect. Such a flow may come from the poor collimation of the background beam in the x -direction for instance. An other possibility is that the rubidium cell was not perfectly aligned on the optical axis, defined by the pump wave-vector. If the input window forms an angle $0 < \beta \ll 1$ with the x -axis, the background beam progressively enters the nonlinear medium from left to right and its left end (at which the intensity falls to \mathcal{I}_0/e^2) propagates over $2\omega_{0,x} \tan(\beta)$ before the right end gets inside the cell. From the medium perspective, it is as if the reference and photon fluid backgrounds had a non-zero transverse wave-vector $\mathbf{k}_{pu} = k_0 \sin(\beta) \mathbf{e}_{x'}$, ie a non-zero transverse speed $\mathbf{v} = \sin(\beta) \mathbf{e}_{x'}$, when they enter the cell (with $\mathbf{e}_{x'} = \cos(\beta) \mathbf{e}_x + \sin(\beta) \mathbf{e}_z$). The probe imprints in that case a density modulation on a moving photon fluid, which can slightly affects the shift.

iii Comments on the results of Vocke *et al.*

The shift measurement has first been performed by Vocke *et al.* in [52], following a proposal by Carusotto [56]. The setup they use is almost identical to the one sketched on figure 4.4. Vocke *et al.* report in [52] a saturation of the shift ΔS at large modulation wavelengths and fit their data using equation (4.4). From this fit, they retrieve the dispersion relation on one hand and measure parameters such as the nonlinear change of refractive index Δn and the diffusive transport length scale σ on the other. The latter defines the range of the nonlocal interaction between photons in the thermo-optic liquid they use as Kerr medium. In [52], Vocke *et al.* claim that interferences between counter-propagating Bogoliubov modes are suppressed by simply cutting in k -space the idler field. Moreover, they use this argument to derive equation (4.4) in their article, on which all their data analysis is based. It is worth mentioning however that this reasoning is wrong as it amounts to saying that the idler and the Bogoliubov mode travelling at $-\mathbf{k}_\perp$ are the same physical object. Indeed, by deriving

carefully the input-output relation (4.8), we show that the idler field results from the mixing in the output plane of both the Bogoliubov modes moving at $+\mathbf{k}_\perp$ and $-\mathbf{k}_\perp$. Cutting the idler in k -space will thus not totally suppress the interference occurring between these modes in the cell exit plane. Consequently, as mentioned in [98], the model derived by Vocke et al. to retrieve the dispersion relation from the shift measurement is incomplete. We therefore tried to fit their data with the model developed in 4.1.1 ii following the work of Larré [71]. Nevertheless, the saturation of the shift ΔS observed by Vocke et al. at large modulation wavelength cannot anymore be explained using this full theoretical description, even by including huge diffusive nonlocality. It should consequently come from an uncontrolled error in performing the experiments. Such a saturation can for instance be observed when the idler beam is not perfectly suppressed in k -space, which is more likely to happen in the large Λ (*ie* low k_\perp) regime. In that case, part of the idler interfere with the pump which counterbalance the shift ΔS along $+\mathbf{e}_x$ by slightly shifting the interference fringes in the opposite direction, that is, along $-\mathbf{e}_x$. This leads to an effective saturation of the shift and might explain the behaviour observed in [52].

4.2 Group velocity measurement

In the previous section, we saw that retrieving the dispersion of density waves travelling onto paraxial photon fluids from the shift measurement relies on a complex numerical inversion. This is mainly due to the fact that pump and probe have to be nearly plane-waves in this approach and, consequently, that probe and idler spatially overlap and exchange energy all along their propagation inside the Kerr medium. But what would happen if the probe beam, instead of being a plane wave, was spatially localized in the nonlinear medium input plane? In other words, how will evolve a small amplitude Gaussian wave-packet propagating at the transverse wave-vector \mathbf{k}_\perp on top of an uniform photon fluid at rest? In what follows, I first theoretically investigate this situation and show that measuring the group velocity of such a wave-packet is a way to access the dispersion relation of density waves, without having, a priori, any knowledge about the Bogoliubov theory. I then present the results we obtained using this new experimental configuration. This section reviews and completes the paper we published in PRL: "Observation of the Bogoliubov Dispersion in a Fluid of Light" [87]. In what follows, I still suppose that the probe wave-vector is parallel to the x -direction.

4.2.1 Introduction

i Travelling of a wave packet onto a photon fluid

Let's imagine that the probe beam is focused in the x -direction but still infinitely elongated along the y -axis. In that case, we can safely forget about the y -direction and address the problem as if it was 1-dimensional (1D+1 geometry). When it enters the nonlinear medium, the probe no longer excites plane wave density fluctuations in that case but rather a spatially localized wave-packet along the x -axis. The aim of this paragraph is to study how the latter travels onto some paraxial photon fluids. The wave-packet generated by the probe beam onto the background fluid can be regarded as a superposition of several plane waves, each with its own transverse wave-vector $k_x = k_0 \sin(\theta_i) + \delta k_x$. The more localized the wave-packet is in real space, the larger is its extension δk_{pr} in k -space. In dispersive mediums, it is known that a wave-packet, while moving at a constant speed (the group velocity v_g), spreads during its propagation. Every plane wave composing this wave-packet travels with its own velocity, which causes this spreading along the x -axis. This is what would happen to the probe if it propagates inside a linear medium. In that case, probe photons behave as free particles in the transverse plane and follow a quadratic particle-like dispersion $\Omega(k_x) = k_x^2/2k_0$ – such as the one plotted on figure 2.1 – when we adopt an effective time description of the dynamics. The phase velocity, which is defined by $v_{ph}(k_x) = \Omega(k_x)/k_x$, depends on k_x and varies thus in the wave-packet from one plane wave to another. This explains why the probe undergoes diffraction in linear mediums using the fluid of light terminology.

In nonlinear materials, the situation is different. The quadratic dispersion Ω is replaced by the Bogoliubov dispersion relation Ω_B . Therefore, in the sonic-regime (that is, for $k_x \ll k_\xi$), the phase velocity does not depend on k_x . Consequently, all the plane waves composing the Gaussian envelope of the probe beam travel at the same speed – the sound velocity c_s – in the transverse plane. This is true as long as $k_\perp + \Delta k_x \ll k_\xi$, where $k_\perp = k_0 \sin(\theta_i)$ stands as usual for the probe transverse wave-vector. The wave-packet forming the probe beam should therefore not spread along the x -direction in this regime.

More surprisingly, the group velocity v_g , which is defined by:

$$v_g(k_\perp) = \frac{d\Omega_B}{dk_\perp}, \quad (4.20)$$

is constant and equal to the sound velocity c_s in that case. By probing the sound-like regime of the Bogoliubov dispersion relation, the probe generates a wave-packet that travels at the same speed along the x -axis, regardless of its angle of incidence θ_i in the entrance plane, as long as $k_\perp = k_0 \sin(\theta_i) \ll k_\xi$. In other words, the position of the wave-packet in the medium output plane remains unchanged while changing θ_i . This nonlinear refraction law, counter-intuitive from the classical optics perspective, comes from the sound-like behaviour of the Bogoliubov dispersion relation at low transverse wave-vectors.

ii Fundamentals of the group velocity measurement

In the previous paragraph, I did not mention the presence of the idler beam, which is still generated at the medium entrance plane, where the effective photon-photon interaction experiences a quench. Two counter-propagating wave-packets are therefore spontaneously created at the cell input facet (at $z = 0$), when the small Gaussian perturbation forming the probe beam onto the photon fluid, that is not an eigenstate of the nonlinear dynamics, enters the medium. They then travel with the speed $\mathbf{v} = \pm v_g(k_\perp) \mathbf{e}_x$ in the transverse plane. Measuring the distance $d(k_\perp)$ between these two wave-packets at the propagation distance z provides thus a direct access to the group velocity v_g . At the cell exit plane, this distance is given by $d(k_\perp) = 2Lv_g(k_\perp)$. We then retrieve the dispersion relation $\Omega(k_\perp)$ by scanning the modulation wave-vector $-ie$ by tuning the angle θ_i between the pump and the probe – and integrating the group velocity from 0 to k_\perp as follows: $\Omega(k_\perp) = \int_0^{k_\perp} v_g(q) dq$.

The fundamentals of this group velocity measurement is sketched on figure 4.8. The pump (red) is a wide and intense Gaussian beam. It generates a quasi-uniform photon fluid at rest when it goes inside the cell. The probe (orange) is elongated in the y -direction in order to only sound the fluid along the x -axis, as previously mentioned. In this direction, the probe width $\omega_{0,x}$ is way smaller than the pump one. When it goes inside the nonlinear medium, the probe beam excites two counter-propagating Bogoliubov wave-packets. In the first case (ie for $k_\perp = 0$), the two density modulations acquire a non-zero transverse speed even if the probe transverse velocity is zero initially. Because of its k -extension, the probe excites a set of plane waves, whose wave-vectors k_x range from $-\delta k_{pr}$ to δk_{pr} , in the sonic regime of the Bogoliubov dispersion relation. Each of these plane waves generates in the cell input facet two counter-propagating Bogoliubov modes travelling at the sound velocity c_s . This process takes place all along the x -axis and results in the creation of two wave-packets, that move rightward and leftward at c_s . As the efficiency of such wave-mixing mechanisms depends on the phase-matching conditions, the high k -vector components of the probe envelope do not efficiently generate Bogoliubov modes, which induces an asymmetry in the wave-packets at large propagation distances. As long as $k_\perp \ll k_\xi$, or, in other words, as long as the probe angle θ_i remains inside the cone of aperture c_s , the probe excites in a similar way a collection of modes in the sonic part of the dispersion that are all going to move at the speed of sound in the transverse plane. In this regime, we do not expect the wave-packets to spread during their propagation and the distance d between them in the exit plane should remain the same ($d = 2c_s L$). Reversely, when $k_\perp \gg k_\xi$, the excitations behave as single-particles and move

along the x -axis at $\pm v_g(k_\perp) \mathbf{e}_x$. The distance between wave-packets centers should therefore increases linearly with the probe wave-vector k_\perp . Indeed, in the particle-like regime (that is, when $k_\perp \gg k_\xi$), the Bogoliubov dispersion is parabolic and $v_g(k_\perp) = k_\perp/k_0$. We recover then the standard refraction law of linear optics.

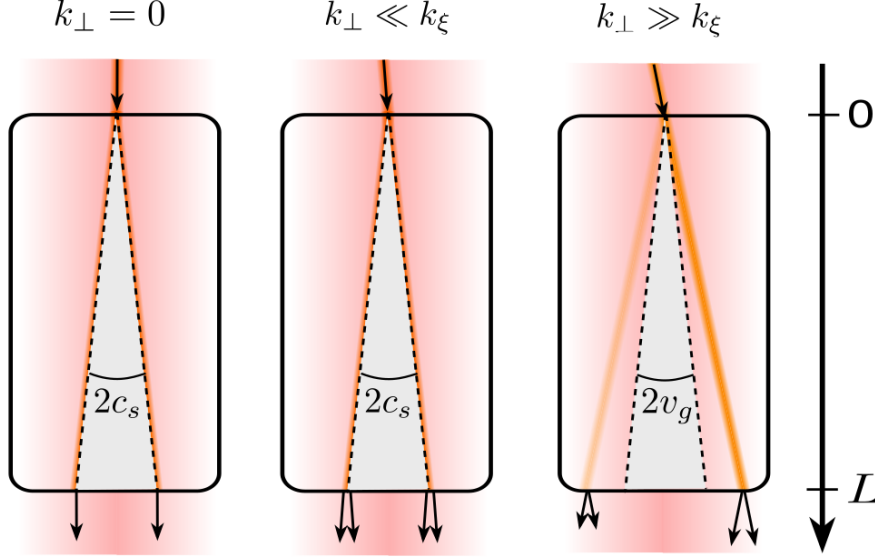


Figure 4.8: Sketch of the group velocity measurement. The pump (red) is a wide and intense Gaussian beam forming the photon fluid at rest (normal incidence). The probe (orange) has a way smaller width than the pump in the x -direction. Both beams have the same frequency. The probe excites two counter-propagating Bogoliubov wave-packets in the input plane. As long as the probe angle θ_i lies inside the cone of aperture c_s (that is, for $k_\perp \ll k_\xi$) the excitations behave as collective phonons and move at $\pm c_s \mathbf{e}_x$ in the transverse plane. Reversely, when $\theta_i > c_s$ ($k_\perp \gg k_\xi$), the excitations behave as single particles propagating at $\pm v_g(k_\perp) \mathbf{e}_x$ along the x -axis. On the right panel, the probe beam intensity is higher than the idler one because phase match conditions are not fulfilled in that case. In situations where the conjugate beam is not visible in the exit plane, we simply measure the distance $d/2$ between the positions of the probe in the input and output planes.

iii Advantages and validity criterion

Measuring the group velocity as function of the probe transverse wave-vector is a suitable way to access the dispersion relation $\Omega(k_\perp)$ of density waves onto paraxial photon fluids. Indeed, this technique does not require any knowledge about the dispersion a priori and relies only on the relationship relating Ω to the group velocity v_g . Normally, Ω should be equal to the Bogoliubov dispersion relation Ω_B . But this is not anymore a requirement as it was for the shift experiment, in the sense that the dispersion Ω can still be retrieved from the group velocity measurement otherwise. This method overcomes therefore the main issue of retrieving the dispersion from the shift ΔS . Moreover, since "probe" and "idler" are spatially separated in the cell exit plane using this new pump/probe configuration, the idler beam does not need to be filtered in Fourier space anymore. The group velocity – and thus the dispersion relation Ω – can then be measured whatever the probe transverse wave-vector, even in the very low- k_\perp regime in which pump, probe and idler overlap in k -space.

We already know, from the shift experiment, that interactions between counter-propagating wave-packets inside the medium can make the relationship between d and v_g more complex. If the probe width, $\omega_{0,x}$, is small enough and the nonlinear change of refractive index, Δn , sufficiently large, we can expect the Bogoliubov wave-packets to overlap (and thus interact) only at the beginning of their propagation inside the nonlinear medium. Once they leave this interaction zone, they propagate independently one with respect to the other (as shown on figure 4.9(a) for instance). In that case, we can suppose that the interaction between the wave-packets only slightly affects their positions in the cell exit plane, and thus, the distance d separating them. In order for this assumption to be correct, we make sure that d is at least twice larger than the probe width in the output plane; the two Gaussian wave-packets are then fully separated after propagation. Moreover, we want the probe to be collimated along the nonlinear medium (which is 7.5 cm long in experiments). This sets thus a lower bound on the probe width $\omega_{0,x}$: $\omega_{0,x} > \sqrt{\lambda z_r / \pi} \approx 150 \mu\text{m}$ (when the Rayleigh length z_r is 10 cm). This constraint on the probe collimation translates directly into a constraint on its k-space extension $\delta k_{pr} \approx 2/\omega_{0,x}$, that should be small compared to k_ξ as we want the probe to sound "locally" (in k-space) the dispersion relation. At low wave-vectors k_\perp , the group velocity is equal to the sound velocity and the constraint on the distance d finally rewrites as follows: $\Delta n > n_0 (\omega_{0,x}/L)^2 \approx 4 \cdot 10^{-6}$. Thus, for a 7.5 cm long vapor cell, a probe width of $150 \mu\text{m}$ and a nonlinear change of refractive index greater than $4 \cdot 10^{-6}$, we can safely consider that $d(k_\perp) = 2v_g(k_\perp)L$ and use the group velocity measurement to access the dispersion.

4.2.2 Theoretical description

The density modulation $\delta\rho$ generated by the probe on top of the background fluid can be theoretically described using the Bogoliubov formalism. The amplitude $\delta\mathcal{E}$ of the probe field, at the medium entrance plane, reads as follows:

$$\delta\mathcal{E}(\mathbf{r}_\perp, 0^-) = \delta\mathcal{E}_0 \exp\left[-(x/\omega_{0,x})^2 - (y/\omega_{0,y})^2\right] e^{-i\mathbf{k}_\perp \cdot \mathbf{r}_\perp}, \quad (4.21)$$

where $\omega_{0,x}$ and $\omega_{0,y}$ stand respectively for the widths of the probe along the x - and y -axes. For the sake of simplicity, we assume $\omega_{0,x}$ and $\omega_{0,y}$ do not depend on z , which amounts to saying that the probe is collimated in both the x and y directions. The in-air amplitude of the total electric field right before the medium input plane can then be expressed as follows:

$$\mathcal{E}(\mathbf{r}_\perp, 0^-) = \mathcal{E}_0(0^-) + e^{i\Phi_0(0^-)} \int \frac{d\delta\mathbf{k}_\perp}{(2\pi)^2} \delta\tilde{\mathcal{E}}(\mathbf{k}_\perp + \delta\mathbf{k}_\perp) e^{-i\delta\mathbf{k}_\perp \cdot \mathbf{r}_\perp}, \quad (4.22)$$

where $\delta\tilde{\mathcal{E}}$ is the Fourier transform of the probe field amplitude $\delta\mathcal{E}$. The density modulation, created by the probe onto the photon fluid, is given by the formula (see subsection 2.3.4): $\delta\rho(\mathbf{r}_\perp, z) = 2\sqrt{\rho_0(z)} \text{Re} [\delta\mathcal{E}(\mathbf{r}_\perp, z) e^{-i\Phi_0(z)}]$. Using the input-output relation (4.8), we find the following expression for this density modulation $\delta\rho$:

$$\begin{aligned} \delta\rho(\mathbf{r}_\perp, z) &= \frac{1}{2} \int \frac{d\delta\mathbf{k}_\perp}{(2\pi)^2} \left[\left(a_{\delta\mathbf{k}_\perp}(L^+) + a_{-\delta\mathbf{k}_\perp}^*(L^+) \right) e^{-i\delta\mathbf{k}_\perp \cdot \mathbf{r}_\perp} + \text{c.c.} \right] \\ &= \frac{1}{2} \int \frac{d\delta\mathbf{k}_\perp}{(2\pi)^2} \left[\left(U_{\delta\mathbf{k}_\perp} + V_{\delta\mathbf{k}_\perp} \right) \delta\tilde{\rho}(\mathbf{k}_\perp + \delta\mathbf{k}_\perp) + \dots \right. \\ &\quad \left. \left(U_{\delta\mathbf{k}_\perp}^* + V_{\delta\mathbf{k}_\perp}^* \right) \delta\tilde{\rho}(-\mathbf{k}_\perp + \delta\mathbf{k}_\perp) \right] e^{-i\delta\mathbf{k}_\perp \cdot \mathbf{r}_\perp}, \end{aligned} \quad (4.23)$$

where $\tilde{\rho}(\mathbf{k}_\perp) = 2\sqrt{\rho_0} \delta\tilde{\mathcal{E}}(\mathbf{k}_\perp)$. The foregoing expression is hard to compute. Let's then go one step further by assuming $\delta\rho$ does not depend much on the y coordinate. This assumption is fulfilled experimentally by sending a elliptical probe beam elongated along the y -direction such that $\omega_{0,x} \ll \omega_{0,y}$. In that case, we can address the problem as if it was 1-dimensional. Let's also neglect the linear losses ($\alpha = 0$) and consider, in a first instance, that the angle of incidence of the probe beam is zero ($k_\perp = 0$). The modulation density reads then:

$$\delta\rho_{k_\perp=0}(x, z) = \int_{-\infty}^{\infty} \frac{dk_x}{2\pi} \cos(\Omega_B(k_x) L) \delta\tilde{\rho}(k_x, 0^-) e^{-ik_x x} \quad (4.24)$$

Equation (4.24) is derived by B.B. Baizakov *et al.* in [99], where the dispersive properties of matter waves propagating onto one- and two-components Bose-Einstein condensates are theoretically investigated. In this paper, the integral on the left hand side of equation (4.24) is computed using the stationary phase approximation (for $x > c_s L$):

$$\delta\rho_{k_\perp=0}(x, L^+) \simeq \frac{\delta\tilde{\rho}(\bar{k}, 0^-)}{\sqrt{2\pi L \left| \frac{d^2 f}{dk_x^2} \right|_{\bar{k}}}} \cos \left[\mathcal{F}_{\bar{k}}(x) L - \frac{\pi}{4} \right] e^{i\Phi_0(L^+)}, \quad (4.25)$$

where $\mathcal{F}_{k_x}(x) = k_x x/L - \Omega_B(k_x)$ and \bar{k} stands for the transverse wave-vector at which the stationary phase condition $d\mathcal{F}/dk_x = 0$ is fulfilled. So far, we did not make any assumption regarding the k -space extension of the probe beam. If it is highly focused onto the medium input plane, it will excite counter-propagating Bogoliubov modes both in the sound-like and in the particle-like regimes of the Bogoliubov dispersion relation. As modes having different wave-vectors propagate at slightly different group-velocities (even deep in the sonic regime), they start interfering after a sufficiently long propagation distance. These interferences are described by the cosine term on the right hand side of (4.25). The resulting oscillations in the transverse intensity distribution make the propagation of small density wave-packets onto photon fluids look like dispersive shocks. It is worth noting that there are significant differences between these two phenomena, the first one being a purely dispersive effect while the second is highly non-perturbative and makes the nonlinearity play a crucial role. Nevertheless, when the k -extension of the probe beam is such that $\delta k_{pr} \ll k_\xi$, interferences between travelling modes start affecting the density profile for propagation distances longer than the length $L = 7.5$ cm of the medium. In that case, the cosine in the right-hand side of equation (4.24) contributes to the integral only when k_x is small, that is, when the Bogoliubov dispersion relation is linear, so that:

$$\begin{aligned} \delta\rho_{k_\perp=0}(x, L^+) &= \int_{-\infty}^{\infty} \frac{dk_x}{4\pi} \delta\tilde{\rho}(k_x, 0^-) \left[e^{-ik_x(x-c_s L)} + e^{-ik_x(x+c_s L)} \right] \\ &\simeq \frac{1}{2} \delta\rho_0 \left[\exp \left\{ \left(-\frac{(x-c_s L)^2}{\omega_{0x}^2} \right) \right\} + \exp \left\{ \left(-\frac{(x+c_s L)^2}{\omega_{0x}^2} \right) \right\} \right], \end{aligned} \quad (4.26)$$

where $\delta\rho_0 = 2\sqrt{\rho_0} \delta E_0$. At the air/medium interface, the Gaussian perturbation induced by the probe beam splits into two wave-packets which propagate in opposite direction at c_s . This result provides therefore an easy way to measure the sound velocity and how it evolves with the photon fluid density ρ_0 . When k_\perp is non-zero but still fulfills the condition $k_\perp \ll k_\xi$,

we expect the preceding result to hold. The centers of the counter-propagating wave-packets should still lie at $d = 2c_s L$ one from the other because the excitation wave-vector remains inside the sound-like regime in that case, where the group velocity v_g is not k -dependant. However, the amplitude of the "probe" envelope (that is, of the envelope of the wave-packet propagating along $+\mathbf{e}_x$) must then be greater than the "idler" one, because phase matching conditions are not perfectly fulfilled. Reversely, when k_\perp starts being much larger than k_ξ , equation (4.23) can be drastically simplified by noticing that $|u_{\mathbf{k}_\perp}| \simeq 1$ and $|v_{\mathbf{k}_\perp}| \simeq (k_\xi/k_\perp)^2$. Therefore, $U_{\mathbf{k}_\perp} + V_{\mathbf{k}_\perp} \simeq \exp[i\Omega_B(k_\perp)L]$ and using the stationary phase method yields:

$$\delta\rho_{k_\perp \gg k_\xi}(x, L^+) = \delta\rho_0 \exp\left\{\left(-\frac{(x - v_g(k_\perp)L)^2}{\omega_{0x}^2}\right)\right\} \cos[k_\perp x + \Omega_B(k_\perp)L]. \quad (4.27)$$

In that case, only the probe beam remains in the output plane. The Gaussian envelope is centered around $v_g(k_\perp)L \simeq \sin(\theta_r)L$, what is expected from the Snell law of linear optics. The only remaining effect of nonlinearity on the particle-like dynamics of the probe in the transverse plane is the Kerr-type phase term $k_0 \Delta n L$ it accumulates during its propagation. Indeed, this phase shift appears in the cosine function when Ω_B is expanded for $k_\perp \gg k_\xi$.

REMARK When α is non-zero, the results above are still correct if the group-velocity $v_g(k_\perp)$ in the lossless case is replaced by its average over the propagation distance $\langle v_g(k_\perp, z) \rangle_z$. The sound velocity c_s in equation (4.26) should then also be replaced by $c_{s,\text{eff}}$, defined in subsection 2.4.1. The density modulation decays exponentially in that case along the z -axis and the right-hand side of (4.26) and (4.27) must therefore be multiplied by $\exp(-\alpha z)$.

4.2.3 Numerical simulations

In order to illustrate more explicitly how the Bogoliubov wave-packets evolve in the medium, I numerically solved the NLSE to compute the intensity of the total electric field in any plane along the z -axis. To that end, I used a second-order split step algorithm for one transverse spatial dimension only (1D+1 geometry), as the probe is supposed to be infinitely elongated in the y -direction. The probe waist is located in the cell input plane ($z = 0$) and its width, $\omega_{0,x}$, is equal to $150 \mu\text{m}$. On the 2D maps shown on figure 4.9, the uniform density ρ_0 of the background fluid is subtracted. The z -evolution of the counter-propagating Bogoliubov wave-packets is shown for $k_\perp \approx 0$ (sonic regime) and for $k_\perp \gg k_\xi$ (particle-like regime) on figures 4.9(a2) and (b2) respectively. In either case, the red arrow indicates the direction of incidence of the incoming probe field. Figure 4.9(a2) illustrates the nonlinear refraction law. Even if the probe has no transverse speed, it gives rise to a pair of counter-propagating wave-packets moving along the x -axis at $\pm c_s$. Of course, the total transverse momentum is conserved and equal to zero in that case, because the amplitudes of the wave-packets travelling upward and downward are the same.

As you may have noticed, the wave-packets spatially overlap during a certain "time" before coming apart (at $z \approx 2 \text{ cm}$ here) on figure 4.9(a2). This can be explained looking at the energy carried by the density modulation. Because the probe has no transverse speed in the entrance plane, it only brings some additional interaction energy into the system. Part of it turns into kinetic energy, which sets the wave-packets in motion. The distance over which this energy transfer occurs turns out to be the distance at which the wave-packets separate.

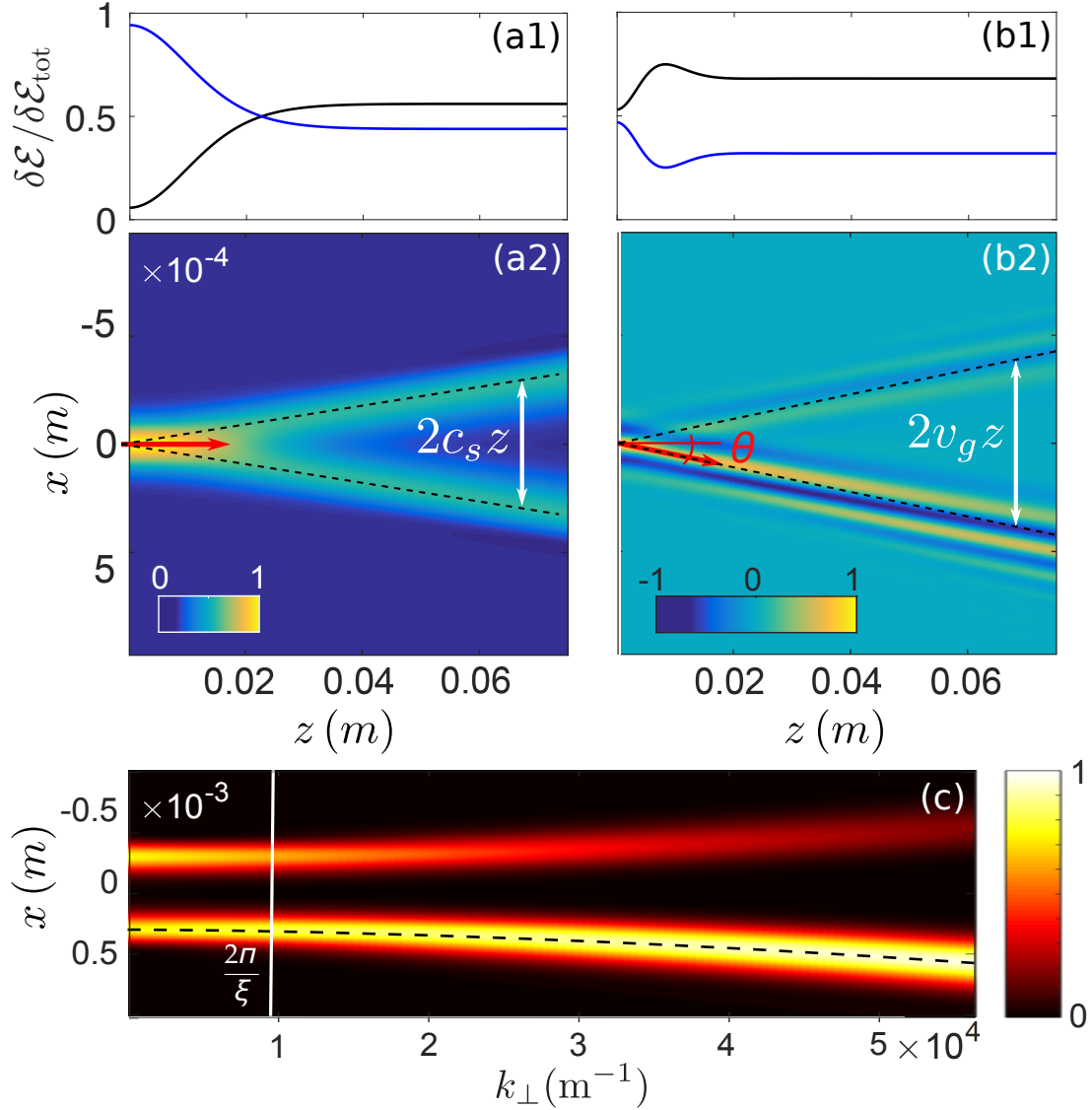


Figure 4.9: 1D numerical simulation. (a2) and (b2): Propagation of a weak Gaussian density modulation onto an uniform background fluid (top view), in the sound-like ($\theta_i \approx 0$ rad) and in the particle-like regime ($\theta_i = 5$ mrad). The background density has been subtracted in both cases. In (a2), the modulation created by the probe onto the photon fluid splits into two counter-propagating wave-packets (even if the probe transverse speed is zero initially). In the output plane, they are separated by $d = 2c_s L$. In (b2), the probe propagates as inside a linear medium. Phase matching between pump and probe gets worse when θ_i increases, explaining why the amplitude of the wave-packet travelling at $k_{\perp} = -k_0 \sin(\theta_i)$ is lower. (a1) and (b1): Interaction energy $\delta\mathcal{F}_{\text{int}}$ (blue line) and kinetic energy $\delta\mathcal{F}_{\text{kin}}$ (black line) of the density modulation as function of z (normalized by its total energy $\delta\mathcal{F}_{\text{tot}} = \delta\mathcal{F}_{\text{int}} + \delta\mathcal{F}_{\text{kin}}$). $\delta\mathcal{F}_{\text{int}}$ and $\delta\mathcal{F}_{\text{kin}}$ reach a stationary regime when the wave-packets on figures (a2) and (b2) are fully separated. (c) Envelope of the intensity profile in the exit plane as function of k_{\perp} . In the sound-like regime (*ie* on the left side of the white line), the distance separating the wave-packets remains constant while it increases linearly with k_{\perp} in the particle-like regime. Parameters: $\lambda = 780$ nm, $\Delta n = 1.3 \cdot 10^{-5}$, $\omega_{\text{pr}}^{(x)} = 150$ μm and $\alpha = 0$ (lossless case).

Let $\delta\mathcal{F}_{\text{int}}$ and $\delta\mathcal{F}_{\text{kin}}$ stand for the interaction and kinetic energies of the density modulation. At any position on the z -axis, $\delta\mathcal{F}_{\text{int}}$ is obtained by subtracting the interaction energy of the background fluid $\mathcal{F}_{\text{int}}[\mathcal{E}_0]$ from the total interaction energy $\mathcal{F}_{\text{int}}[\mathcal{E}]$, where \mathcal{F}_{int} is defined by: $\mathcal{F}_{\text{int}}[\mathcal{E}] = \frac{k}{4} \frac{n_2}{n_0} \int_S |\mathcal{E}(\mathbf{r}_\perp)|^4 d\mathbf{r}_\perp$. Similarly, $\delta\mathcal{F}_{\text{kin}} = \mathcal{F}_{\text{kin}}[\mathcal{E}] - \mathcal{F}_{\text{kin}}[\mathcal{E}_0] = \frac{1}{4k} \int_S |\nabla_\perp \delta\mathcal{E}|^2 d\mathbf{r}_\perp$. Figures 4.9(a1) and (b1) show the z -evolution of $\delta\mathcal{F}_{\text{int}}$ (blue line) and $\delta\mathcal{F}_{\text{kin}}$ (black line), when the probe field enters the medium with the same incidence as on figures (a2) and (b2). Energies are normalized on both graphs by the total free energy $\delta\mathcal{F}_{\text{tot}} = \delta\mathcal{F}_{\text{int}} + \mathcal{F}_{\text{kin}}$ of the density modulation. As you may have seen, $\delta\mathcal{F}_{\text{kin}}$ is almost zero on figure 4.9(a1) when $z = 0$. The small offset results from the non-zero transverse speed of the high k_x -components of the probe field, giving a small but non-zero initial kinetic energy to the density modulation. Then, $\delta\mathcal{F}_{\text{kin}}$ increases while $\delta\mathcal{F}_{\text{int}}$ decreases until both of them reach a stationary regime, which occurs, indeed, when the wave-packets stop overlapping on figure 4.9(b1).

Let's now focus on figures 4.9(b1) and (b2), where the probe field sounds the particle-like regime of the Bogoliubov dispersion relation this time. As you can see on figure 4.9(b2), the wave-packet travelling upward (idler) is barely visible, as the phase matching conditions between pump and probe are not fulfilled anymore. Moreover, interference fringes appear as the fringe spacing $\Lambda = 2\pi/k_\perp$ is smaller than the probe width $\omega_{0,x}$ in that case. By looking at figure 4.9(b1), we see that the kinetic energy brought by the probe is non-zero anymore and, as in the case where $k_\perp \approx 0$, $\delta\mathcal{F}_{\text{int}}$ and \mathcal{F}_{kin} stop varying along z as soon as the wave-packets are spatially separated. Scanning the angle θ_i from 0 (a2) to 5 mrad (b2) allows to plot the envelope of the intensity profile at the medium exit plane (*ie*, at $z = L$) as function of k_\perp . This has been done on figure 4.9(c). As you can see, the distance between the wave-packets in the exit plane does not depend much on k_\perp in the sound-like regime (that is, on the left side of the white solid line). Reversely, it increases when the probe starts reaching the particle-like regime of the dispersion relation. We can also notice the spreading of the wave-packets over the x -axis for high values of k_\perp . The theoretical distance $d/2$ between the input plane position of the probe beam ($x = 0$) and the output plane position of the downward-moving wave-packet has been plotted in black dashed. As you can see, the agreement between theory and simulation is excellent. Figure 4.9(c) exactly illustrates what is the purpose of the experiments: measuring the distance d between the wave-packets at $z = L$ as function of k_\perp . In the following subsection, I present the experimental setup I designed and built to this end.

4.2.4 Experimental setup and data processing

The experimental setup is shown on figure 4.10. As in the shift experiment, the continuous-wave laser beam at 780 nm is produced by a Ti:Sapphire laser source (see subsection 2.1.2) and sent on the optical table using a single-mode polarization-maintaining high power fiber. The outgoing beam is magnified before entering a Mach-Zehnder interferometer, protected from air-turbulences by a box. From there, the beam splits into a high power pump (red) and a low power probe (blue). The pump is expanded twice before being loosely focused into the nonlinear medium using a set of two cylindrical lenses. The resulting beam is elongated in the x -direction; its widths along the x - and y -axes are 3.2 mm and 300 μm respectively. The pump intensity (and thus the background fluid density) is then almost uniform along x . The Rayleigh length $z_{r,y}$ associated to the pump width along y is 37 cm, which is five times longer than the length of the nonlinear medium ($L = 7.5$ cm). Consequently, we can safely suppose that the pump beam is collimated (when self-defocusing is negligible obviously).

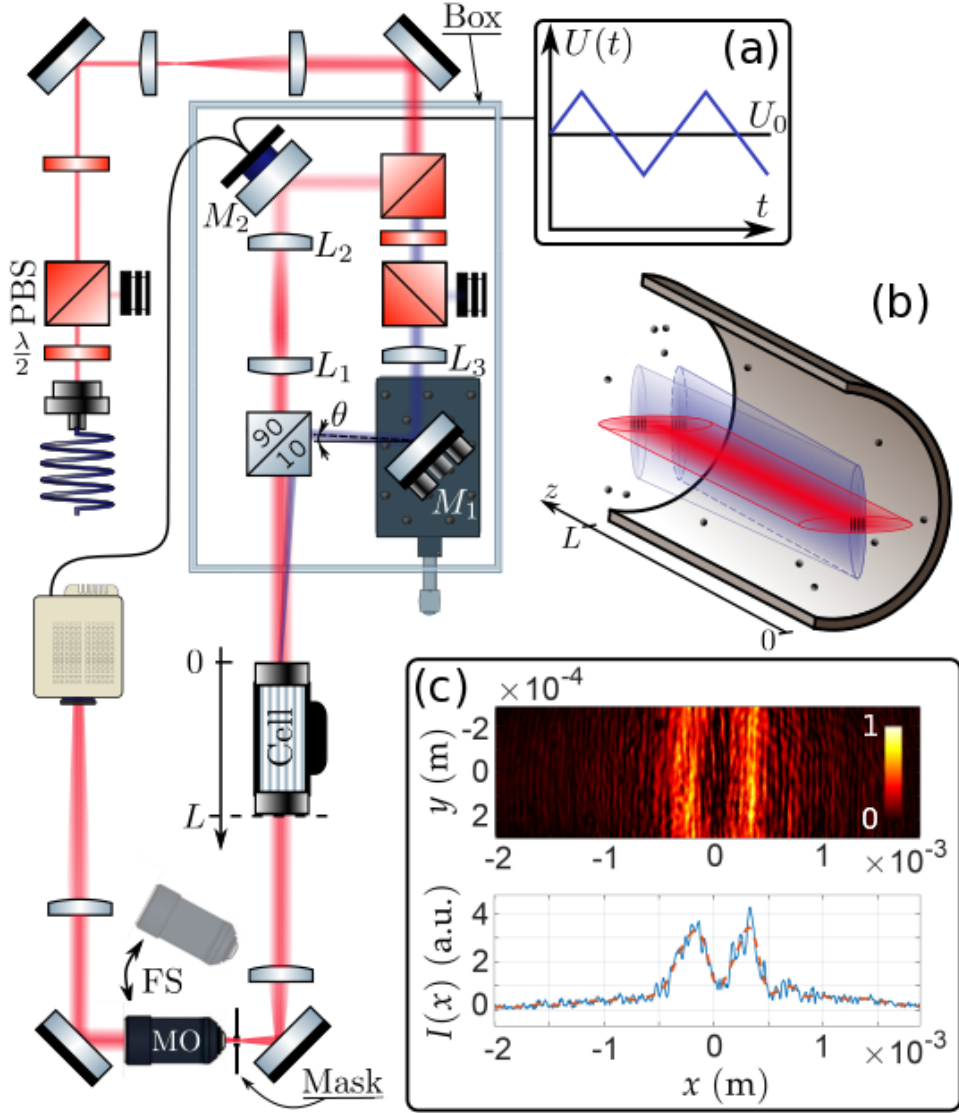


Figure 4.10: Experimental setup. The laser beam goes out from the fiber and is magnified before going inside a Mach-Zehnder interferometer. A PBS splits the beam into two parts, the pump (red) and the probe (blue). The pump is magnified one more time and spatially elongated along y -direction using a set of two cylindrical lenses. The probe is focused along the x -axis onto the cell entrance plane with a cylindrical lens of focal length $f = 1$ m. The probe is therefore elongated in a direction perpendicular to the pump, as sketched on the inset (b). The piezo-electronically actuated mount of the mirror M_1 allows to finely tune the angle θ_i between pump and probe. The cell output plane is imaged onto the camera with a $4f$ telescope. The inset (c) shows an example of a background-subtracted image obtained for $\theta_i \approx 0$ rad and the related integrated profile (blue line). On the latter, two well separated wave-packets are clearly visible.

The probe beam is directly focused with a cylindrical lens onto the medium entrance plane. It is elliptically elongated along y , that is, in a direction perpendicular to the pump beam. This cross-configuration, sketched on figure 4.10(b), allows to only probe the fluid along the x -axis, where the intensity (and thus Δn) has been made higher by focusing the pump. At the probe waist, $\omega_{0,x} = 180 \pm 10 \mu\text{m}$ and $\omega_{0,y} = 1.7 \text{ mm}$. The value of the minor width, $\omega_{0,x}$, is chosen in order for the wave-packets to properly separate at the medium exit plane. For $\omega_{0,x} \simeq 180 \mu\text{m}$, the probe is also collimated along x inside the medium (as $z_{r,x} \simeq 13 \text{ cm}$). Before recombining with the pump, the probe reflects onto the mirror M_1 . The latter is held in a piezo-actuated mount which allows to finely tune the angle θ_i . The depth of the density fluctuation is adjustable too by turning the half wave-plate before the PBS on the probe arm. In experiments, it represents less than 5% of the background fluid density. Pump and probe propagate then inside a 7.5 cm long cell, filled with an isotopically pure vapor of rubidium 85. The cell is heated up to 150°C with the homemade oven described on subsection 2.1.1. The Kerr nonlinearity is obtained by red-detuning the laser frequency from the $F_g = 3 \rightarrow F_e$ transition frequency ($\Delta = -2\pi \times 6 \text{ GHz}$). The vapor transmission is then about 70%.

The cell exit plane is imaged onto a CMOS camera using a $4f$ imaging system made of two lenses of focal length 150 mm and 500 mm respectively. The magnification factor has been measured and is about 3.4. A microscope objective can be flipped onto the beam path so as to image the focal plane of the first lens and measure the probe transverse wave-vector k_\perp . Images of the pump alone (background), of the probe alone and of the k -space (without cell) are captured at every angle θ_i . Moreover, as we only care about the envelope of the wave-packets in the exit plane, the relative phase between pump and probe is scanned over 2π . To that end, we mount the mirror M_2 onto a piezo-actuated translation stage. By ramping up the high voltage applied across the piezo (see inset (a)), we modulate the length of the pump path in the Mach-Zehnder, and consequently the relative phase between the beams. 40 images are captured during a phase ramp. We subtract the background from each of them before integrating the resulting intensity distribution over 100 pixels around the x -axis. We finally retrieve the wave-packets envelope by summing – in absolute value – all the 40 intensity profiles we obtained after integration. The distance d between the wave-packets is measured by performing a 1D two-Gaussian fit of the intensity envelope, as long as the idler beam is visible in the exit plane. Otherwise, d is directly measured from the distance between the input and output positions of the probe beam.

4.2.5 Experimental results

In this subsection, I present the experimental results I obtained with the setup and the data analysis described above. I first show the dispersion relation retrieved from the group velocity measurement in a low-density photon fluid. At high densities, a discrepancy appears between the measured group velocity and the theoretical expectation. I show that nonlocality could have explained it if the values of the nonlocal ballistic transport length scale, l_d , at which notable disturbances on the group velocity arise were not so unrealistic. I finally demonstrate that this discrepancy is the experimental signature of quasi-particle interferences, that is, of interferences between the two counter-propagating Bogoliubov wave-packets.

i Dispersion relation in a low-density photon fluid

The experimental group velocity and dispersion relation are plotted as function of k_\perp on figures 4.11(a) and (b) (blue circles). The pump power is 175 mW, which corresponds to a nonlinear change of refractive index $\Delta n(0)$ of 3.9×10^{-6} in the input plane. On figure 4.11(a), two regimes are clearly distinguishable. The group velocity is constant at low wave-vectors while it linearly increases at larger ones. The transition between these regimes occurs when $k_\perp \simeq 1.8 \times 10^4 \text{ m}^{-1}$. This value is slightly greater than k_ξ , which is about $1.6 \times 10^4 \text{ m}^{-1}$. The theoretical group velocity, obtained for $\Delta n(0) = 3.9 \times 10^{-6}$ and for 70% transmission, has been plotted on black dashed. As you can see, it perfectly predicts the value toward which the measured group velocity tends when k_\perp goes to zero. Nevertheless, the plateau observed experimentally at low k_\perp is much longer than expected. Moreover, an offset between the data and the model is clearly visible at large k_\perp . By taking nonlocality into account, which arises in hot vapors because of the ballistic transport of fast moving excited atoms, we obtain the black solid line on figure 4.11(a). When $T = 150^\circ\text{C}$, the nonlocal ballistic length scale, l_b , is about $8 \mu\text{m}$. It does not sound like much but it is enough to make the nonlocal model better describe the asymptotic trend of the data at large k_\perp . However, nonlocality does not explain why the plateau at low k_\perp is longer than theoretically expected.

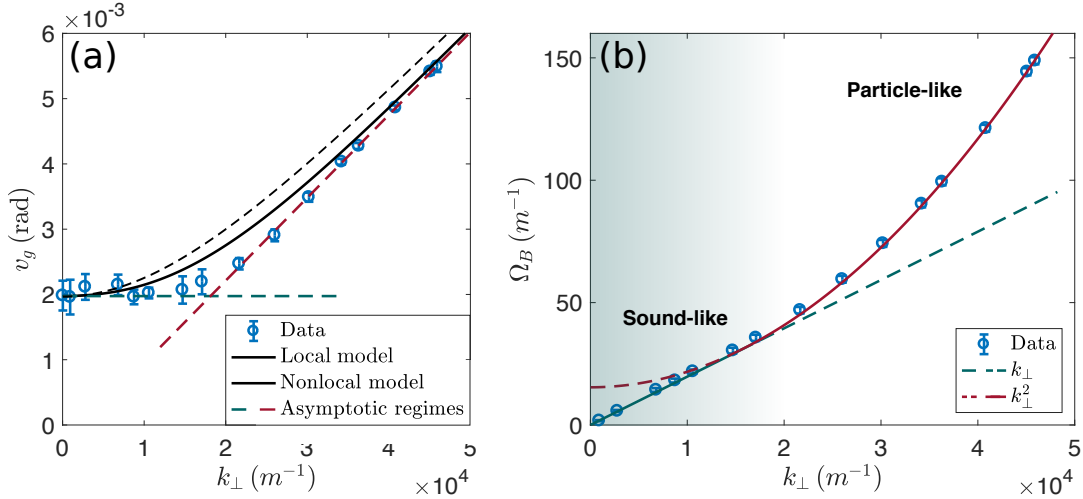


Figure 4.11: (a): Group velocity v_g as function of the transverse wave-vector $k_\perp = k_0 \sin(\theta_i)$. The blue circles represent the experimental data obtained for a fluid power $\mathcal{P}_f = 175 \text{ mW}$. The theoretical model is plotted in black solid. It takes into account the nonlocal response of the vapor, due to the ballistic transport of fast moving excited atoms. For comparison, the group velocity predicted by the local theory is plotted in black dashed on the same graph. The dashed lines highlight the asymptotic behaviours of the group velocity, which remains constant in the sonic regime (cyan) and linearly increase in the particle-like regime (red). (b) shows the dispersion relation obtained after integration of the group velocity in (a). It exhibits a linear increase at low k_\perp characterized by the sound velocity $c_{s,\text{eff}}$.

Integrating the data on figure 4.11(a) yields the dispersion relation plotted on figure 4.11(a). As you can see, it linearly increases for $k_{\perp} < 1.8 \times 10^4 \text{ m}^{-1}$. This is an important result as it proves that small amplitude density waves behave like collective phonons for low enough excitation wave-vectors. This sound-like regime is fully characterized by the speed of sound, $c_{s,\text{eff}} = \langle c_s(z') \rangle_L \simeq 2.0 \text{ mrad}$. Moreover, the linear increase of the dispersion relation at low k_{\perp} guarantees that light propagating through rubidium vapors can be superfluid, as suggested by R.Chio two decades ago [9]. Indeed, according to the Landau criterion for superfluidity, the speed of sound $c_{s,\text{eff}}$ defines a critical speed below which the photon fluid cannot dissipate energy anymore by emitting sound-like excitations (see subsection 2.3.3). In order to further investigate the sound-like regime of the dispersion, we set the probe wave-vector to zero. In that case, the wave-packets in the cell exit plane are separated by $2c_{s,\text{eff}}L$; we can then measure how the sound velocity increases with the background intensity. The data are shown on figure 4.12(a). The red circles and the grey diamonds are the results obtained from two measurements performed successively, at the same laser detuning and vapor temperature. As you may have seen, the theoretical prediction (black line) matches the data pretty well, indicating that $c_{s,\text{eff}}$ scales with the square-root of the background fluid density, as expected. It is worth mentioning that the nonlinear refractive index n_2 is measured independently (using the ring counting technique of subsection 2.3.2), which sets the only parameter in the theoretical model. The results from the ring counting measurement are shown on figure (b).

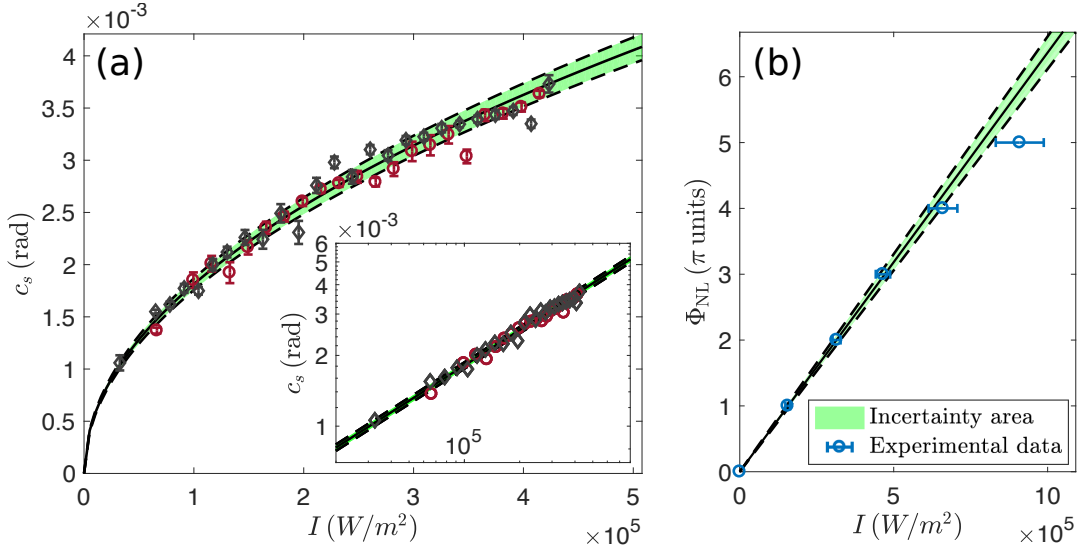


Figure 4.12: (a): Speed of sound c_s as function of the pump intensity I_0 . The red circles and the grey diamonds represent two sets of data taken successively at the same laser detuning and vapor temperature. The sound velocity increases with the square root of I_0 , as expected. The theoretical prediction (black line) matches the data pretty well. No free-parameter is needed because the nonlinear refractive index n_2 has been measured independently, using the ring counting technique of subsection 2.3.2. The uncertainty on c_s (green area) derives from the uncertainty on n_2 . (b): Ring-counting measurement. The self-phase Φ_{NL} accumulated by a Gaussian beam propagating through the cell is measured as function of the beam intensity. The nonlinear refractive index is obtained by fitting the data with a line. We find $n_2 = 3.3 \pm 0.2 \times 10^{-11} \text{ m}^2/\text{W}$.

ii Discrepancy at high fluid densities

The data shown on figures 4.11(a) and (b) have been obtained at low background densities. Aside from the fact that the plateau at low k_{\perp} is longer than expected on figure 4.11(a), the experimental observations match well with the prediction of the Bogoliubov's theory in that case. Nevertheless, the situation is more complicated at high background densities. Figure 4.13(a) shows the group velocities measured as function of k_{\perp} for various fluid powers. The data plotted on figure 4.11(a) have been reported on this graph (circles). As you can see, the data points form a dip when the fluid power \mathcal{P}_f is equal to 350 or 525 mW. Its location ($k_{\text{dip}} \simeq 1.8 \times 10^4 \text{ m}^{-1}$) does not depend much on the background power and roughly match the end of the plateau formed by the data points, at low k_{\perp} , when $\mathcal{P}_f = 175 \text{ mW}$. Moreover, the depth of the dip increases with \mathcal{P}_f while its bottom remains at the same height (2 mrad). As on figure 4.11(a) the theoretical group velocities in local (black dashed line) as well as in nonlocal mediums (black solid line) have been plotted as function of k_{\perp} for $\mathcal{P}_f = 525 \text{ mW}$. As you can see, both models correctly predicts the value of the measured group velocity when k_{\perp} goes to zero. This is why the measured sound velocity still matches the theory on figure 4.12(a). However, neither the local nor nonlocal description is able to explain the dip.

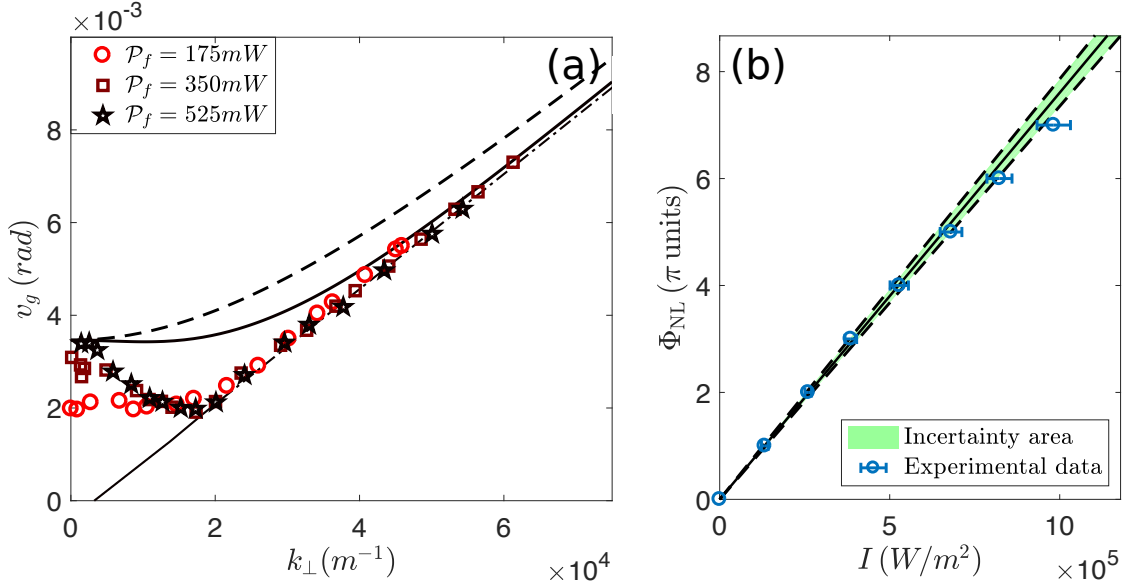


Figure 4.13: (a): v_g as function of k_{\perp} for different fluid powers \mathcal{P}_f . The experimental data shown on figure 4.11 have been reported on this graph (red circles). When \mathcal{P}_f is equal to 350 or 525 mW, the data exhibit a dip, whose location does not seem to depend much on the fluid power (that is, on Δn). The depth of this dip increases with \mathcal{P}_f while its bottom remains at the same height. The black dashed and solid lines are the theoretical predictions in local and nonlocal mediums respectively, for $\mathcal{P}_f = 525 \text{ mW}$. Taking nonlocality into account allows to better describe the asymptotic trend of the experimental data at high k_{\perp} . However, it does not explain why the dip appears. Surprisingly, the theory still match the data when k_{\perp} tends to zero. (b): Ring-counting measurement. The value of n_2 used in (a) to plot the theoretical predictions is measured experimentally using the ring-counting technique of subsection 2.3.2; we find $n_2 = 3.1 \pm 0.2 \times 10^{-11} \text{ m}^2/\text{W}$.

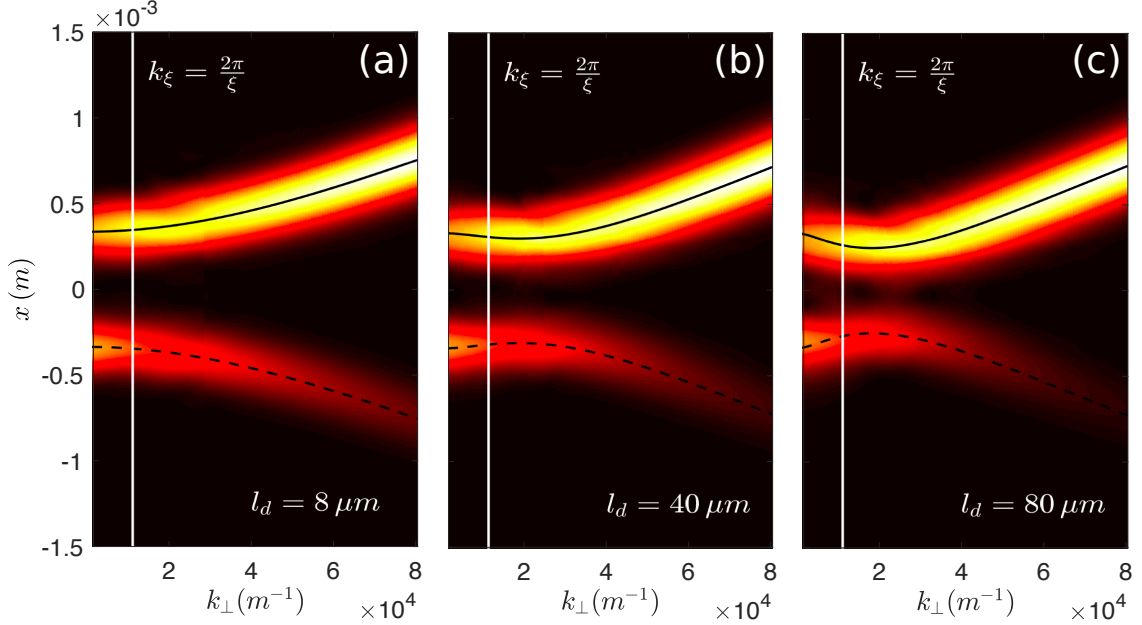


Figure 4.14: Envelope of the intensity profile along x in the output plane as function of k_{\perp} for different ballistic transport length scales l_d . The realistic situation is shown on the left. On figures (b) and (c), the minimum distance between the wave-packet is not anymore obtained at $k_{\perp} = 0$ but for a wave-vector slightly larger than k_{ξ} (white line). This distance decreases when l_d increases. Nonlocality could therefore have explained the dip observed on figure 4.13. However, the values of l_d at which this effect significantly impacts the distance between the wave-packets are very large. The theoretical predictions are plotted in black solid and black dashed. Parameters: $\Delta n = 1.0 \times 10^{-5}$, $L = 7.5$ cm and $\alpha = 0$.

At first, we thought it was due to nonlocality, as it is known to modify the dispersion relation (and the group velocity) in a way that could have explained its appearance on figure 4.13(a). The effects of diffusive nonlocality on the dispersion are investigated in [52] for instance. The envelope of the intensity profile along x in the cell output plane has been plotted as function of k_{\perp} on figure 4.14, for different values of the ballistic transport length scale l_d . Indeed, the distance between the wave-packets (which is proportional to the group velocity) does not continuously increase with k_{\perp} on figures (b) and (c) but rather exhibits a minimum located at a wave-vector slightly bigger than k_{ξ} (white line). This feature starts appearing as soon as nonlocality is strong enough to create an inflexion point in the dispersion relation (see figure 2.2) and is more and more pronounced as l_d increases. However, the values of l_d at which nonlocal effects induce a dip comparable to what is observed on figure 4.13(a) are completely unrealistic. At $T = 150$ °C, the nonlocal ballistic length scale is around $8 \mu\text{m}$. For such a value, nonlocality only generates a plateau at low k_{\perp} , as can be seen on figures 4.13(a) (black line) and 4.14(a), and allows to better describe the asymptotic trend of the data points at high k_{\perp} , as already mentioned in the previous paragraph.

The causes beyond the emergence of the dip at high background densities on figure 4.13(a) lie thus elsewhere. In the next paragraph, we investigate the possibility that the dip may arise from destructive interferences between the counter-propagating Bogoliubov wave-packets.

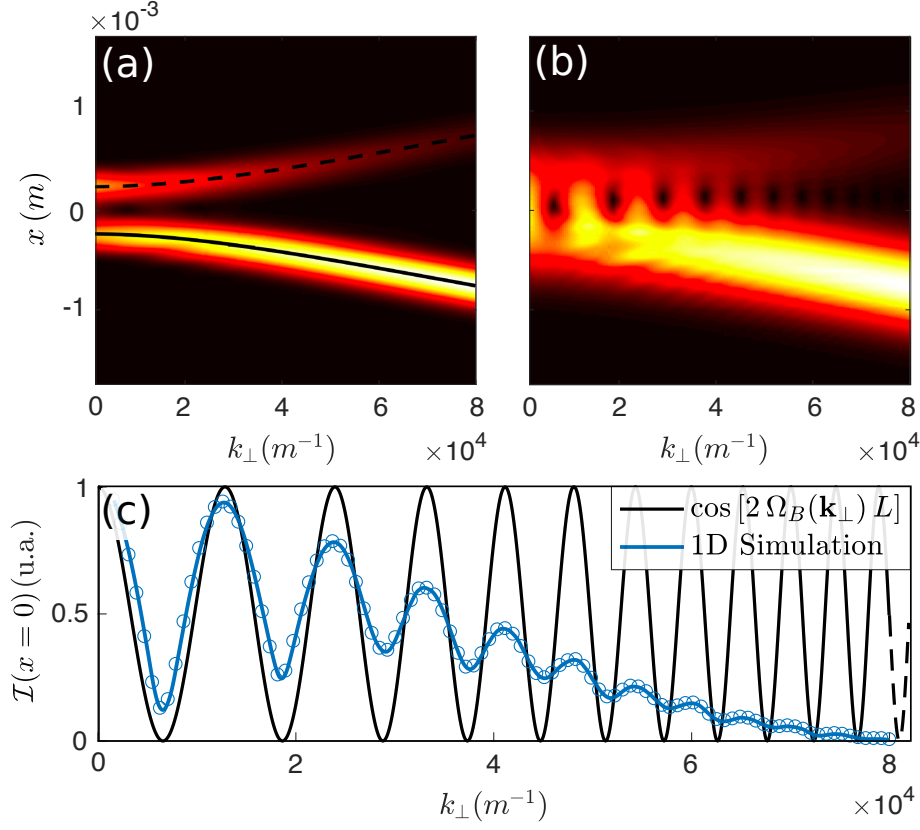


Figure 4.15: Envelope of the intensity profile along x in the output plane as function of k_{\perp} , for a probe width $w_{0,x}$ of $150 \mu m$ (a) and $450 \mu m$ (b) respectively. In figure (a), the envelopes of the wave-packets are fully separated in the cell exit plane. This is not anymore the case on figure (b). Interference between the upward- and downward-moving wave-packets occurs in that case. Depending on the probe wave-vector, the envelope of the density modulation exhibits two distinct peaks (destructive interference) or just one (constructive interference). Figure (c) shows the intensity at $x = 0$ in the exit plane as function of k_{\perp} for $w_{0,x} = 450 \mu m$. It oscillates in a similar way as $\cos[2\Omega_B(k_{\perp})L]$ (black solid line), that describes the beating between two counter-propagating Bogoliubov modes at k_{\perp} . The amplitude of the oscillations is damped because the overlap between the wave-packets decreases with k_{\perp} . Parameters: $\Delta n = 1.0 \times 10^{-5}$, $L = 7.5$ cm and $\alpha = 0$.

iii Quasi-particle interferences: experimental evidence

So far, we have supposed that the wave-packets were spatially separated in the cell exit plane, or, in other words, that the criterion of paragraph 4.2.1 iii was fulfilled. If this is not the case anymore, we expect interferences between counter-propagating wave-packets to occur. This is indeed what we observe on figure 4.15(b), where the width of the probe beam $\omega_{0,x}$ at the entrance plane is $450 \mu\text{m}$, three times larger than on figure (a). On these two figures, the envelope of the intensity profile along x in the output plane is plotted as function of k_\perp . While the wave-packets on figure (a) are fully separated after propagation (whatever k_\perp), they overlap at low wave-vectors on figure (b) and interfere therefore one with each other. Figure (c) shows a cut of the 2D map (b) along the horizontal axis ($x = 0$). As you can see, the intensity $\mathcal{I}(x = 0)$ (blue line) oscillates in a similar way as the function $\cos[2\Omega_B(k_\perp)L]$ (black line), describing the beating between two counter-propagating Bogoliubov modes at $\pm k_\perp$ in the transverse plane. The overlap between the two wave-packets decreases with k_\perp , explaining thus why the oscillations of the blue curve are damped along the horizontal axis. When interferences are destructive, the wave-packets are well separated and the 1D two-Gaussian fit, used to extract the output spacing between them, gives the expected value for d . Reversely, when interferences are constructive, the intensity in between the wave-packets strongly increases, which can induce an error in the estimation of d by the fitting procedure.

So as to check if quasi-particle interferences are observable in experiments, I have plotted on figure 4.16 the experimental envelope of the intensity profile (measured in the cell exit plane) as function of k_\perp . The 2D intensity distributions shown on the maps (a), (c), (d) and (e) are obtained by interpolating the experimental data, using a spline interpolation method. Let's first compare the maps (a) and (b). The latter shows the results we obtain by solving numerically the NLSE in 2D for the same parameters as in (a): $\mathcal{P}_f = 350 \text{ mW}$, $\omega_{0,x} = 180 \mu\text{m}$ and $\omega_{0,y} = 300 \mu\text{m}$. We also take absorption into account in simulation. As you can see, the maps (a) and (b) look pretty similar. A destructive interference between the counter-propagating wave-packets occurs at $k_\perp \simeq 1.6 \times 10^4 \text{ m}^{-1}$ on both figures. This exactly matches the dip location on figure 4.13(a). Moreover, the positions of the wave-packets provided by the two-Gaussian fit on map (b) (black dashed lines) deviate from the theoretical predictions (black solid lines) when k_\perp gets closer to $1.6 \times 10^4 \text{ m}^{-1}$. More precisely, the distance between the wave-packets is under-estimated by the fitting procedure when a destructive interference occurs at low k_\perp . This is mainly why a dip appears in the data shown on figure 4.13(a).

We can go further by comparing the wave-vectors at which interferences occur in simulation and in experiments. The stripe at the bottom of figure (b) shows the Laplacian $\nabla^2 \mathcal{I}(x, k_\perp)$ of the intensity distribution plotted above it, from -0.2 to 0.2 mm . The peaks lying along this stripe locate the destructive interferences while the dips locate the constructive ones. On figure (d), the 2D map (a) as well as the stripe of figure (b) have been plotted together. As you can see, the wave-vectors at which interferences occur in the simulation almost correspond to the wave-vectors at which they are observed in experiments. We can compare in a similar manner the results of the simulation with the experimental data obtained for $\mathcal{P}_f = 175 \text{ mW}$ (c) and $\mathcal{P}_f = 525 \text{ mW}$ (e) respectively. On figure (c), the simulations predict exactly the wave-vectors at which interferences occur experimentally. The agreement is less convincing on figure (e) but the simulations still predict pretty well the locations of the first destructive and the first constructive interferences.

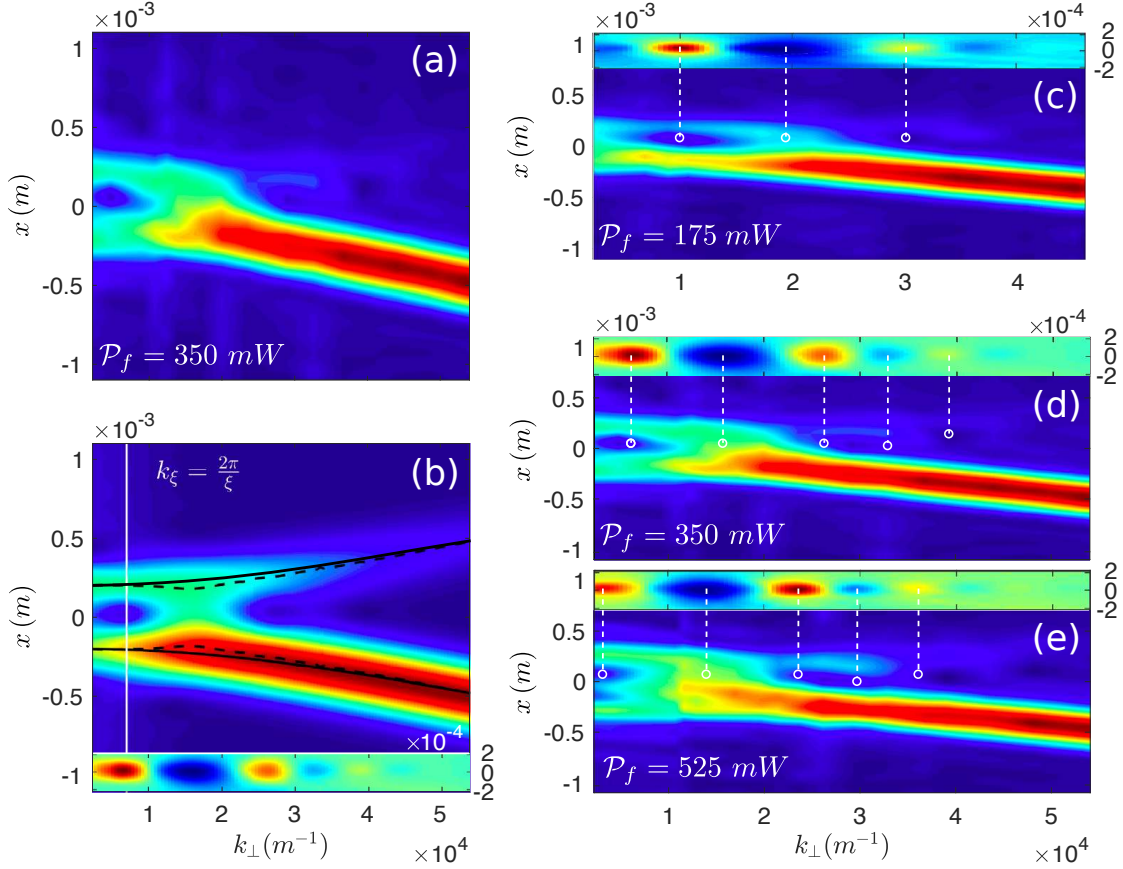


Figure 4.16: Quasi-particle interferences. On figure (a), the envelope of the intensity profile in the cell exit plane is shown as function of k_{\perp} , for a fluid power of 350 mW. (b) We compare these experimental data to simulation, solving the NLSE in 2D for the same beam widths and powers as in experiments. The theoretical positions of the wave-packets centers are plotted in black solid on figure (b). The black dashed lines are the positions provided by the two-Gaussian fit. The latter slightly under-estimates the spacing between the wave-packets when the destructive interference occurs. This is why a dip appears in the data of figure 4.13. The stripe at the bottom of figure (b) shows the Laplacian $\nabla^2 \mathcal{I}(x, k_{\perp})$ of the intensity distribution plotted above (from -0.2 to 0.2 mm). The peaks and the dips on this stripe respectively locate the constructive and destructive interferences visible on the 2D map (b). On figures (c), (d) and (e), the wave-vectors at which interferences occur in simulation and in experiments are compared for $\mathcal{P}_f = 175$ mW (c), $\mathcal{P}_f = 350$ mW (d) and $\mathcal{P}_f = 525$ mW (e). The 2D maps are experimental data while the strips on each figure represent the variation of $\nabla^2 \mathcal{I}(x, k_{\perp})$ from -0.2 to 0.2 mm, obtained by simulation.

Chapter 5

Optically induced potential in a fluid of light

In chapter 2, the nonlinear Schrödinger equation describing the dynamics of a photon fluid in propagating geometry has been derived. In its most general form, this equation involves an effective potential that can either trap (*ie* guide) or deflect the light depending on its sign. Such a potential in photon fluids is created by a local modification of the refractive index. Inducing, in a controlled manner, local changes in the refractive index might then open up new possibilities in studying paraxial photon fluids. We can for instance think about trapping transversely the light in potentials of any shape. The photon fluid will then behave like a trapped 2-dimensional Bose-Einstein condensate, which can be interesting to investigate optical analog of many-body phenomena arising in those systems. We can also think about studying to what extent the interaction between photons affects the localization of light in random potentials [100]. Generating a defect on the paraxial photon fluid flow (by means of a localized negative refractive index modulation) is also a way of probing superfluidity in our systems, by measuring either the cancellation of the drag force on this defect [29, 101], or the amount of light it scatters at the normal/superfluid transition. This latter point is what motivates us in finding a way of controlling the refractive index felt by a fluid of light. In this chapter, I report an all-optical method to achieve this end, which requires to address at the same time the D_1 and the D_2 lines of rubidium. I thus first extend the theoretical description of chapter 1 to the case of a 4-level N-type system. I therefore strongly encourage you to read chapter 1 before, as most of the notations and concepts I use here have already been introduced in the latter. In a second part, I discuss how we generate local defects in the experiments, using quasi Bessel beams; some results of this second section have been published in: "Attenuation-free non-diffracting Bessel beams", Optics Express, Vol. 27, Issue 21, pp. 30067-30080 (2019) [102].

5.1 Modified dielectric response in a N-type atomic system

As we have seen in chapter 1, alkaline vapors are versatile platforms to study nonlinear optics phenomena since the sign and amplitude of the third-order dielectric susceptibility $\chi^{(3)}$ are easily tunable changing the laser frequency. So far however, we have only slightly exploited the resources offered by the rubidium fine and hyperfine structures. On figure 5.1, the sketch of the 3-level system introduced in chapter 1 has been replicated. In this model, a single coupling field addresses one of the rubidium D -lines.

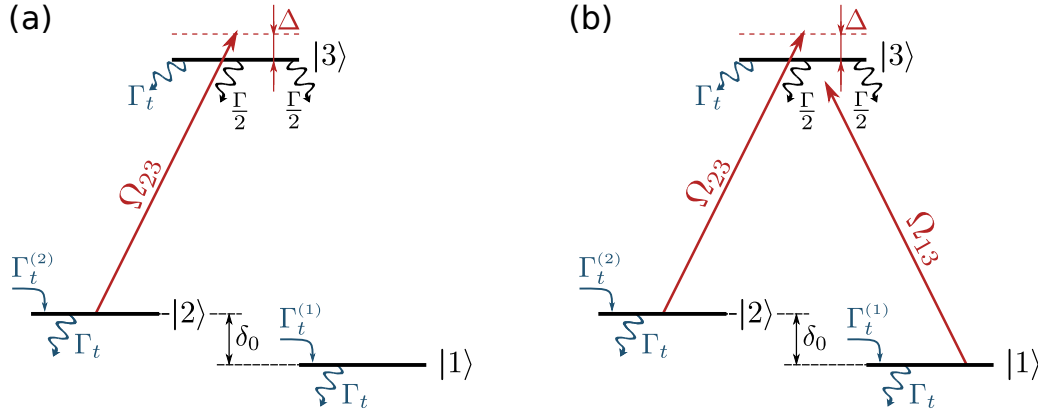


Figure 5.1: Sketch of the 3-level system described in chapter 1. The levels $|1\rangle$ and $|2\rangle$ stand for the two hyperfine ground states of the D -lines while $|3\rangle$ stands either for the fine level $5^2P_{1/2}$ (D_1 line) or for $5^2P_{3/2}$ (D_2 line). A single laser field (red arrows) couples the ground states to the excited state. It is detuned from the $|2\rangle \rightarrow |3\rangle$ transition by Δ . On figure (a), we assume it only addresses the $|2\rangle \rightarrow |3\rangle$. Reversely, this single laser field couples both ground states to the excited states on figure (b).

If we send a second laser field on the $|1\rangle \rightarrow |3\rangle$ transition for instance, we can then locally control the atomic coherence between states $|1\rangle$ and $|2\rangle$ and therefore the strength of the nonlinear susceptibility induced by the first beam on the $|2\rangle \rightarrow |3\rangle$ transition. This kind of "lambda" (Λ) configuration provides the basic framework for studying phenomena such as Electromagnetically Induced Transparency (EIT) [39]. In the past years, highly enhanced self-Kerr and cross-Kerr nonlinearity [103] have been experimentally measured by taking advantage of the atomic resources in three-level EIT systems. However, in all the schemes that involve two laser fields driving simultaneously the same D -line, interaction between those fields is likely to occur through four-wave-mixing or stimulated Raman processes. The strength of this interaction strongly depends on the beams wave-vectors, that defines the phase-matching condition of the wave-mixing processes. This might thus be a constraint which we do not want to concern ourselves about. In order to locally tune the linear and nonlinear dielectric susceptibilities induced by one of the two lasers inside the vapor cell, we can also think about addressing simultaneously both D -lines. In that case, wave-mixing is not likely to occur anymore because the beams frequencies are very different from one another (see figure 1.1). Such a configuration has been depicted on figure 5.2. Levels $|1\rangle$ and $|2\rangle$ still stand for the lower and upper hyperfine states of $5^2S_{1/2}$.

- On figure 5.2(a), $|3\rangle$ and $|4\rangle$ are the fine states $5^2P_{1/2}$ (D_1 line) and $5^2P_{3/2}$ (D_2 line). In this 4-level model, we assume that the hyperfine structure of each of these states can be neglected, which amounts to saying that the lasers detunings Δ_d and Δ_f are large compared to the typical hyperfine splitting in $5^2P_{1/2}$ ($\delta_{D_1} \simeq 213$ MHz for ^{85}Rb) and in $5^2P_{3/2}$ ($\delta_{D_2} \simeq 361$ MHz for ^{85}Rb) respectively. The meaning of the indices "d" and "f" will be explained latter in this section.
- The splitting δ_{D_1} between the two upper states of the D_1 line is actually significant. As you may have seen, it is almost twice the value of δ_{D_2} . In figure 5.2(b), we thus fully describe the D_1 line, $|3\rangle$ and $|4\rangle$ standing in that case for the upper and lower hyperfine states of $5^2P_{1/2}$ and $\delta_{34} = \delta_{D_1}$. I still neglect the hyperfine structure of $5^2P_{3/2}$ (which is represented by the fifth level in this 5-level system).

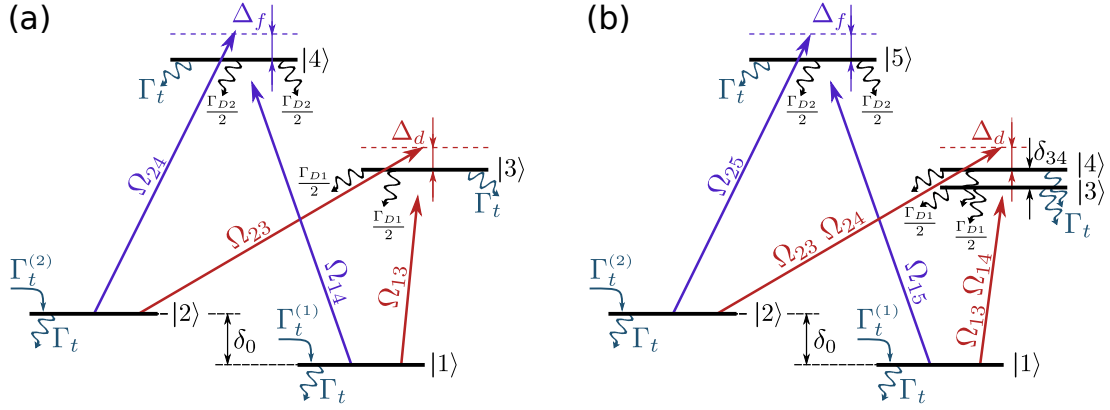


Figure 5.2: Four (a) and five-level system (b) in a double N-type configuration.

As we will see later on, driving strongly the D_1 line with the "red" laser ($\lambda_d \simeq 796$ nm) induces a modulation of the ground state populations, which in turn affects the dielectric susceptibility induced by the "blue" laser ($\lambda_f \simeq 780$ nm), as χ depends on the population difference between ground and excited states. In other words, the red laser locally tunes the refractive index seen by the blue one, according to its intensity distribution in the transverse plane. This refractive index modulation δn behaves as a repulsive ($\delta n < 0$) or an attractive ($\delta n > 0$) potential for the blue laser, depending on its sign. The areas where $\delta n < 0$ act thus as light-induced wave-guides for the blue laser. "Light guiding light" effects have been widely studied in a great variety of physical systems [18, 104, 105] including hot rubidium vapors. Truscott *et al.* [105] have demonstrated for instance the guiding of a probe beam, detuned to the red side of the D_2 line, by a powerful Laguerre-Gaussian beam addressing the D_1 line. Reversely, areas where $\delta n < 0$ act as impenetrable obstacles on which the blue light scatters. In this section, I will mainly focus on this second case and provide a theoretical description of the refractive index change felt by the blue laser when the red one strongly drives the D_1 line. The analytical calculations below are done using the 4-level model of figure 5.2 (a) only. I will sometimes compare the results we obtain with those provided by numerical simulations of the 5-level system sketched on figure 5.2(b).

5.1.1 Transit and influx rates

In the 4-level system sketched on figure 5.2(a), the excited states $|3\rangle$ and $|4\rangle$ are likely to decay radiatively toward the ground states at the rates $\Gamma_1 \simeq 2\pi \times 5.75$ MHz and $\Gamma_2 \simeq 2\pi \times 6.07$ MHz respectively. As already mentioned in chapter 1, atoms enter and leave the beams at the transit rate Γ_t ; every state can thus decay toward the atomic reservoir at the same rate Γ_t . We assume that atoms enter the interacting area either in the ground state $|1\rangle$ or in $|2\rangle$.

Let us consider the situation depicted on figure 5.3. Two laser fields copropagate inside the rubidium vapor along the same optical axis. The small red disk on figure 5.3(b) stands for the transverse cross-section of the red laser in figure 5.2. Inside this region, both beams overlap and the atoms internal state is driven by the 4-level model sketched on figure 5.3(a). Outside this disk, only the blue beam in figure 5.2 remains and the atoms internal state is driven by the 3-level model of figure 5.1(b). Henceforward, this second beam will be referred to as the fluid ("f") or probe beam, as it will be used in experiments to create a photon fluid and probe hydrodynamical features like superfluidity. The small beam lying inside the probe will be referred to as the defect ("d") or pump beam, since it locally changes the refractive index experienced by the probe and acts, therefore, as a obstacle into the photon fluid flow. In our experiment, the probe width is much larger than the pump one: typically, $\omega_{0,d} = 40 \mu\text{m}$ and $\omega_{0,f} = 500 \mu\text{m}$. All the atoms reaching the defect have thus approximately travelled a distance $\Delta\omega = \omega_{0,f} - \omega_{0,d}$ across the probe. The average time of flight is $t_f \simeq \Delta\omega/u \simeq 1.6 \mu\text{s}$ at 400 K. Atoms interact then with the probe beam during $1.6 \mu\text{s}$ only, which is, generally speaking of course, short compare to preparation time τ_0 .

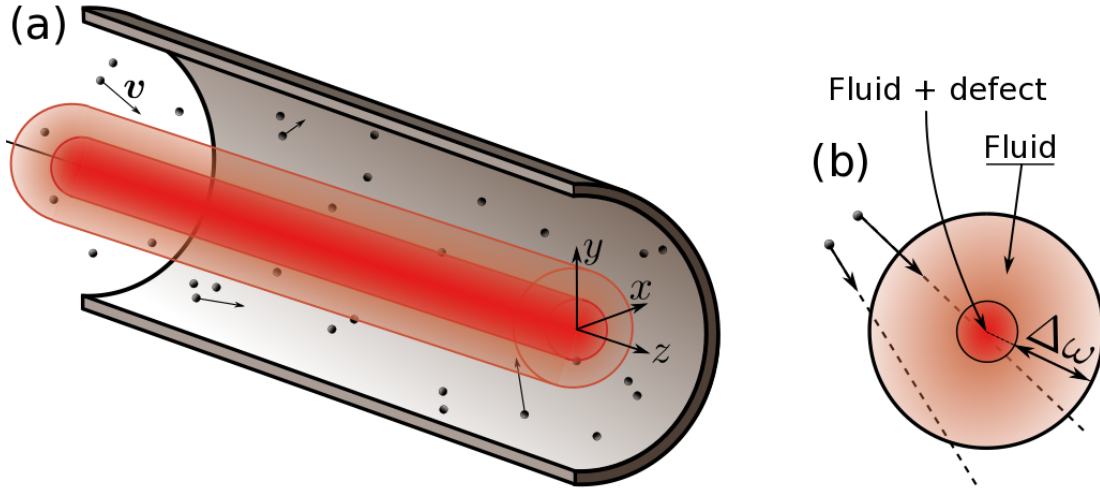


Figure 5.3: Beams configuration in the 4-level N-type system of figure 5.2. Pump (red) and probe (orange) are copropagating along the z axis. In experiments, we typically set the beam widths $\omega_{0,d}$ and $\omega_{0,f}$ to $40 \mu\text{m}$ and $500 \mu\text{m}$ respectively.

This parameter τ_0 measures the time an atom needs in order to be prepared in the steady-state by the laser field. It depends on a large set of parameters, including the temperature T , the probe detuning $\Delta_f = \omega_f - \omega_{24}$ and the Rabi frequencies Ω_{14} and Ω_{24} . The fraction β of atoms prepared in the steady-state for such a set of parameters can be evaluated following the approach developed in [41]. The probability $\mathcal{P}(t)$ to reach the equilibrium after a time t is given by: $\mathcal{P}(t) = 1 - e^{-t/\tau_0}$. The preparation time τ_0 is found in practice by computing the real parts of the eigenvalues of the Bloch matrix M in equation (1.58); τ_0 is finally defined as the inverse of the smallest of these real parts. In other words, τ_0 evaluates the duration of the transient regime associated to the slowest eigenstate to reach equilibrium. A way of roughly describing the situation would therefore be to consider that a fraction $\beta = \mathcal{P}(t_f)$ of atoms is effectively prepared in the steady-state while the remaining ones enter the defect area in their initial state, without interacting at all with the probe field. Moreover, if we assume that the atoms are – before entering the probe – in a mixture of states $|1\rangle$ and $|2\rangle$ described by the Boltzmann statistics, the influx rates $\Gamma_{t,d}^{(1)}$ and $\Gamma_{t,d}^{(2)}$ of the 4-level N-type model on figure 5.2(a) are given by the following formula:

$$\Gamma_{t,d}^{(1)} = \left[(1 - \beta) G_1 + \beta \left(\rho_{11}^{\text{in}} + \frac{\rho_{44}^{\text{in}}}{2} \right) \right] \Gamma_{t,d}, \quad (5.1)$$

$$\Gamma_{t,d}^{(2)} = \left[(1 - \beta) G_2 + \beta \left(\rho_{22}^{\text{in}} + \frac{\rho_{44}^{\text{in}}}{2} \right) \right] \Gamma_{t,d}. \quad (5.2)$$

In equations (5.1) and (5.2), ρ_{ii}^{in} stands for the proportion of atoms **prepared** by the probe laser in state $|i\rangle$ before they reach the defect area. The degeneracy weight G_i is still defined by: $G_i = g_i/(g_1 + g_2)$ (g_i being the degeneracy factor of state $|i\rangle$). The transit rate $\Gamma_{t,d}$ is equal to $2u/\sqrt{\pi}\omega_{0,f}$ as usual. The fraction $\beta = \mathcal{P}(t_f)$ has been plotted as function of the probe power and detuning on figure 5.4 for $T = 400$ K. At this temperature and for $\omega_{0,d} = 40$ μm , the transit rate $\Gamma_{t,d}$ is about 6.4 MHz (ie $\Gamma_{t,d}/\Gamma_{D_1} \simeq 18\%$).

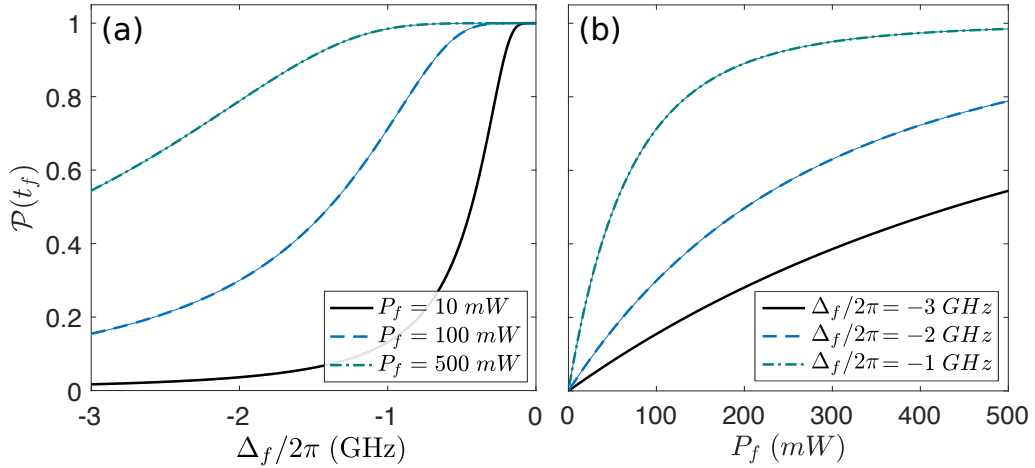


Figure 5.4: Fraction $\beta = \mathcal{P}(t_f)$ of atoms prepared in the steady-state when they reach the defect beam as function of Δ_f (a) and P_f (b). At fixed fluid power, $\mathcal{P}(t_f)$ increases by getting closer to resonance. Similarly, it increases at fixed detuning with the fluid power. Parameters: $w_{0,f} = 500$ μm , $w_{0,d} = 40$ μm and $T = 400$ K.

- At high power and small detuning (*ie* when $\Omega_{14}, \Omega_{24} \gg \Delta_f$), the probe field quickly drives the atomic internal state to the steady-state. Atoms are therefore almost all prepared by the probe in that case and $\beta \simeq 1$, as can be seen on figures 5.4(a) and (b).
- Reversely, if $\Omega_{14}, \Omega_{24} \ll \Delta_f$, there are only few atoms prepared by the probe beam. The other ones reach thus preferentially the defect in state $|2\rangle$, since $G_1 < G_2$.

5.1.2 Optical-Bloch equations and steady-state solution

Within the interaction picture and under the dipole and rotating wave approximations, one can derive the Bloch equations associated to the 4-level system sketched on 5.2 (a), using the semiclassical approach detailed in the first chapter. At the end of the day:

$$\left\{ \begin{array}{l} \frac{d\rho_{11}}{dt} = -\Gamma_{t,d} \rho_{11} + \frac{\Gamma_{D1}}{2} \rho_{33} + \frac{\Gamma_{D2}}{2} \rho_{44} + \frac{i}{2} (\Omega_d^* \rho_{31} - \Omega_d \rho_{13}) + \frac{i}{2} (\Omega_f^* \rho_{41} - \Omega_f \rho_{14}) + \Gamma_{t,d}^{(1)} \\ \frac{d\rho_{22}}{dt} = -\Gamma_{t,d} \rho_{22} + \frac{\Gamma_{D1}}{2} \rho_{33} + \frac{\Gamma_{D2}}{2} \rho_{44} + \frac{i}{2} (\Omega_d^* \rho_{32} - \Omega_d \rho_{23}) + \frac{i}{2} (\Omega_f^* \rho_{42} - \Omega_f \rho_{24}) + \Gamma_{t,d}^{(2)} \\ \frac{d\rho_{33}}{dt} = -(\Gamma_{t,d} + \Gamma_{D1}) \rho_{33} - \frac{i}{2} (\Omega_d^* \rho_{31} - \Omega_d \rho_{13}) - \frac{i}{2} (\Omega_d^* \rho_{32} - \Omega_d \rho_{23}) \\ \frac{d\rho_{44}}{dt} = -(\Gamma_{t,d} + \Gamma_{D2}) \rho_{44} - \frac{i}{2} (\Omega_f^* \rho_{41} - \Omega_f \rho_{14}) - \frac{i}{2} (\Omega_f^* \rho_{42} - \Omega_f \rho_{24}) \\ \frac{d\rho_{21}}{dt} = -\tilde{\gamma}_{21} \rho_{21} + \frac{i}{2} \Omega_d^* \rho_{31} - \frac{i}{2} \Omega_d \rho_{23} + \frac{i}{2} \Omega_f^* \rho_{41} - \frac{i}{2} \Omega_f \rho_{24} \\ \frac{d\rho_{31}}{dt} = -\tilde{\gamma}_{31} \rho_{31} + \frac{i}{2} \Omega_d \rho_{21} - \frac{i}{2} \Omega_f \rho_{34} + \frac{i}{2} \Omega_d (\rho_{11} - \rho_{33}) \\ \frac{d\rho_{32}}{dt} = -\tilde{\gamma}_{32} \rho_{32} + \frac{i}{2} \Omega_d \rho_{12} - \frac{i}{2} \Omega_f \rho_{34} + \frac{i}{2} \Omega_d (\rho_{22} - \rho_{33}) \\ \frac{d\rho_{41}}{dt} = -\tilde{\gamma}_{41} \rho_{41} + \frac{i}{2} \Omega_f \rho_{21} - \frac{i}{2} \Omega_d \rho_{43} + \frac{i}{2} \Omega_f (\rho_{11} - \rho_{44}) \\ \frac{d\rho_{42}}{dt} = -\tilde{\gamma}_{42} \rho_{42} + \frac{i}{2} \Omega_f \rho_{12} - \frac{i}{2} \Omega_d \rho_{43} + \frac{i}{2} \Omega_f (\rho_{22} - \rho_{44}) \\ \frac{d\rho_{43}}{dt} = -\tilde{\gamma}_{43} \rho_{43} + \frac{i}{2} \Omega_f \rho_{13} + \frac{i}{2} \Omega_f \rho_{23} - \frac{i}{2} \Omega_d^* \rho_{41} - \frac{i}{2} \Omega_d^* \rho_{42} \end{array} \right. \quad (5.3)$$

Equations (5.3), together with the closure relation: $\text{Tr}(\hat{\rho}) = 1$, constitute a close set of Bloch equations. As the dipole moment μ_{13} and μ_{23} are equal – see for instance (1.6) – $\Omega_{13} = \Omega_{23} = \Omega_d$. Similarly, $\Omega_{14} = \Omega_{24} = \Omega_f$. The Rabi frequencies Ω_d and Ω_f are defined by $\Omega_d = E_d \mu_d / \hbar$ and $\Omega_f = E_f \mu_f / \hbar$, where $E_d = \frac{1}{2} (\mathcal{E}_d e^{ik_d z} + cc)$ and $E_f = \frac{1}{2} (\mathcal{E}_f e^{ik_f z} + cc)$, $\mathcal{E}_{d,f}$, $k_{d,f}$ and $\omega_{d,f}$ being respectively the complex envelopes, the wave vectors and the frequencies of the defect and probe beams. We also define the quantities $\tilde{\gamma}_{21} = \gamma_{21} + i\delta_0$, $\tilde{\gamma}_{31} = \gamma_{31} - i(\Delta_d - \delta_0)$, $\tilde{\gamma}_{32} = \gamma_{32} - i\Delta_d$, $\tilde{\gamma}_{41} = \gamma_{41} - i(\Delta_f - \delta_0)$, $\tilde{\gamma}_{43} = \gamma_{43} - i\Delta_f$ and $\tilde{\gamma}_{42} = \gamma_{42} - i(\Delta_f - \Delta_d)$ for the sake of clarity. The coherence decay rates are given by: $\gamma_{ij} = \frac{1}{2}(\Gamma_i + \Gamma_j) + \gamma_{\text{col}}$, where Γ_i is the decay rate of state $|i\rangle$ (for instance, $\Gamma_3 = \Gamma_{t,d} + \Gamma_{D1}$) and γ_{col} the collision-induced decoherence rate. Finally, $\Delta_d = \omega_d - \omega_{23}$ and $\Delta_f = \omega_f - \omega_{24}$ are the defect and probe detunings with respect to the $|2\rangle \rightarrow |3\rangle$ and $|2\rangle \rightarrow |4\rangle$ transitions.

The 4-level system reaches the steady-state after a given time of evolution. At that point, the first order time derivatives are zero in (5.3). We should not expect to get a compact expression for the solution of the resulting matrix equation in that case. One of the options left to us consist in solving the steady-state Bloch equations iteratively, assuming that the driving of the D_1 line by the defect is much more efficient than the driving of the D_2 line by the probe, or in other words, that $\Omega_f \ll \Omega_d$. This kind of perturbative approach has been used in [106] to find the steady-state solution of a N-type model in an EIT configuration:

two intense laser fields (namely, the coupling and switching fields) address respectively the $|2\rangle \rightarrow |3\rangle$ and $|2\rangle \rightarrow |4\rangle$ transitions, while a less powerful one probes the $|1\rangle \rightarrow |3\rangle$ transition. In our case, the assumption $\Omega_f \ll \Omega_d$ is not necessarily fulfilled, as the probe laser (that is, the fluid) is far detuned from resonance, which allows to increase its intensity (and thus Ω_f) while remaining below the saturation threshold $I_s(\Delta_f)$. However, the linear variation $\delta n^{(1)}$ of the refractive index felt by the probe beam between inside and outside the defect area does not depend on the probe strength, by definition. Therefore, the first order expansion in Ω_f of the stationary Bloch equations provides an exact expression for $\delta n^{(1)}$ whether or not the condition $\Omega_f \ll \Omega_d$ is fulfilled. Following this comment, I thus derive in the next section the expression of $\delta n^{(1)}$ and study how it varies as function of Δ_d , Δ_f and Ω_d . In parallel, I present the results obtained with the dressed-state formalism, which is not only aesthetic but provides a physical understanding about how the optical defect is generated.

5.1.3 Linear variation of the refractive index at the defect position

i Perturbative approach

Let M stands for the steady-state Bloch matrix. The steady-state matrix equation can then be decomposed as follows: $M \boldsymbol{\rho} = (M_0 + M_f) \boldsymbol{\rho} = 0$, where M_0 and M_f are respectively the Ω_f -independent and -dependent parts of M . Since we assume $\Omega_f \ll \Omega_d$, the density matrix elements can be obtained iteratively as $\rho_{ij} = \rho_{ij}^{(1)} + \rho_{ij}^{(2)} + \rho_{ij}^{(3)} + \dots$ and the n th step of the expansion is given by:

$$M_0 \boldsymbol{\rho}^{(n)} = -M_f \boldsymbol{\rho}^{(n-1)} \quad (5.4)$$

The zeroth order equation reads: $M_0 \boldsymbol{\rho}^{(0)} = 0$. It basically describes the steady-state of the 4-level system sketched on figure 5.2(a) when the probe (blue arrows) has been switched off. In that case, the 4-level system reduces to a 3-level one and the zeroth-order equation above is the same as (1.58) when $\Omega_{13} = \Omega_{23} = \Omega_d$. Using the results of chapter 1, one can thus compute the zeroth order density matrix elements. The last three equations in (5.3) can then be solved together in the steady-state. The resulting matrix equation reads:

$$\begin{pmatrix} -\tilde{\gamma}_{41} & 0 & -\frac{i}{2} \Omega_d \\ 0 & -\tilde{\gamma}_{42} & -\frac{i}{2} \Omega_d \\ -\frac{i}{2} \Omega_d^* & -\frac{i}{2} \Omega_d^* & -\tilde{\gamma}_{43} \end{pmatrix} \begin{pmatrix} \rho_{41}^{(1)} \\ \rho_{42}^{(1)} \\ \rho_{43}^{(1)} \end{pmatrix} = -\frac{i\Omega_f}{2} \begin{pmatrix} \rho_{11}^{(0)} + \rho_{21}^{(0)} \\ \rho_{22}^{(0)} + \rho_{12}^{(0)} \\ \rho_{13}^{(0)} + \rho_{23}^{(0)} \end{pmatrix}, \quad (5.5)$$

and can be inverted in order to obtain $\rho_{41}^{(1)}$, $\rho_{42}^{(1)}$ and $\rho_{43}^{(1)}$ as follows:

$$\rho_{41}^{(1)} = \Omega_f \frac{\tilde{\gamma}_{42} \Omega_d (\rho_{13}^{(0)} + \rho_{23}^{(0)}) + i \left[(|\Omega_d|^2 + \tilde{\gamma}_{42} \tilde{\gamma}_{43}) (\rho_{11}^{(0)} + \rho_{21}^{(0)}) - |\Omega_d|^2 (\rho_{22}^{(0)} + \rho_{12}^{(0)}) \right]}{\tilde{\gamma}_{41} |\Omega_d|^2 + \tilde{\gamma}_{42} |\Omega_d|^2 + 4 \tilde{\gamma}_{41} \tilde{\gamma}_{42} \tilde{\gamma}_{43}}, \quad (5.6)$$

$$\rho_{42}^{(1)} = \Omega_f \frac{\tilde{\gamma}_{41} \Omega_d (\rho_{13}^{(0)} + \rho_{23}^{(0)}) + i \left[(|\Omega_d|^2 + \tilde{\gamma}_{41} \tilde{\gamma}_{43}) (\rho_{22}^{(0)} + \rho_{12}^{(0)}) - |\Omega_d|^2 (\rho_{11}^{(0)} + \rho_{21}^{(0)}) \right]}{\tilde{\gamma}_{41} |\Omega_d|^2 + \tilde{\gamma}_{42} |\Omega_d|^2 + 4 \tilde{\gamma}_{41} \tilde{\gamma}_{42} \tilde{\gamma}_{43}}, \quad (5.7)$$

$$\rho_{43}^{(1)} = \Omega_f \frac{\tilde{\gamma}_{41} \Omega_d^* (\rho_{22}^{(0)} + \rho_{12}^{(0)}) + \tilde{\gamma}_{42} \Omega_d^* (\rho_{11}^{(0)} + \rho_{21}^{(0)}) + i \tilde{\gamma}_{41} \tilde{\gamma}_{41} (\rho_{13}^{(0)} + \rho_{23}^{(0)})}{\tilde{\gamma}_{41} |\Omega_d|^2 + \tilde{\gamma}_{42} |\Omega_d|^2 + 4 \tilde{\gamma}_{41} \tilde{\gamma}_{42} \tilde{\gamma}_{43}}. \quad (5.8)$$

Inside the defect area, the linear response of the vapor to the probe field is characterized by the linear dielectric susceptibility $\chi_{f,\text{in}}^{(1)} = \frac{2N}{\epsilon_0 \mathcal{E}_f} (\mu_{14} \rho_{41}^{(1)} + \mu_{24} \rho_{42}^{(1)})$. The linear variation of the refractive index felt by the probe between inside and outside the defect is thus given by:

$$\delta n^{(1)} = n_{\text{in}}^{(1)} - n_{\text{out}}^{(1)} \simeq \frac{1}{2} \text{Re} [\chi_{f,\text{in}}^{(1)} - \chi_{f,\text{out}}^{(1)}] \quad (5.9)$$

where $n_{\text{in}}^{(1)}$ and $n_{\text{out}}^{(1)}$ are the linear refractive indices seen by the probe inside and outside the defect area respectively. The real part of the susceptibility $\chi_{f,\text{in}}^{(1)}$ is plotted on figure 5.5(a) as function of Δ_d and Δ_f , and the linear index modulation $\delta n^{(1)}$ on 5.5(c) as function of Δ_d , at a fixed probe detuning $\Delta_f = -2\pi \times 2$ GHz and for different defect powers. The simulations have been performed for $w_{0,d} = 50 \mu\text{m}$, $w_{0,f} = 0.5$ mm and $T = 415$ K. Doppler broadening has been taken into account.

As you can see, the spectrum of $\chi_{f,\text{in}}^{(1)}$ is relatively complex. Let's analyse it step by step. When the defect beam is highly red-detuned it does not drive the $|2\rangle \rightarrow |3\rangle$ transition very efficiently and even less the $|1\rangle \rightarrow |3\rangle$ transition. In that case, cutting the 2D map along some vertical line will make the resulting profile look like the plot on figure 1.10(a). Nevertheless, on figure 1.10(a), the centers of the $|1\rangle \rightarrow |4\rangle$ and the $|2\rangle \rightarrow |4\rangle$ transition lines lie exactly at the transition frequencies ω_{14} and ω_{24} . On figure 5.5(a), even when the defect beam is highly red-detuned, the lines centers are slightly blue-shifted from the transition frequencies (black dotted lines). This light-shift can be seen as the AC analog of the Stark-effect [107], that shifts the spectral line of atoms and molecules when submitted to constant electric field. It increases as $\Omega_d^2/4|\Delta_d|$ at large detunings. Here, $\Omega_d \simeq 2\pi \times 4.3$ GHz, which explains why at tens of gigahertz detunings, the light-shift is still clearly visible. When $\Delta_d = -2\pi \times 10$ GHz for instance, it is about $2\pi \times 470$ MHz. The defect beam is intense enough to off-resonantly drive the rubidium D_1 line.

This is also reflected in the amplitude of the spectral lines. On figure 1.10(a), the amplitude of $\text{Re}[\chi]$ close to $\Delta_f = 0$ is larger than close to $\Delta_f = \delta_0$ (where δ_0 is the hyperfine splitting between ground states), because atoms are more likely to get inside the beam in state $|2\rangle$, which is more degenerated. As the Rabi frequency of the probe is small ($\Omega_f \simeq 2\pi \times 4.3$ MHz), atoms will predominantly reach the defect area in state $|2\rangle$. But as soon as they get inside, they will be pumped by the defect beam, from state $|2\rangle$ to state $|1\rangle$ for instance when it is moderately red-detuned. This is why the amplitude of the real part of $\chi_{f,\text{in}}^{(1)}$ is higher close to $\Delta_f = \delta_0$ than to $\Delta_f = 0$ in that case.

So far, we have only discussed what happens when the defect beam is far from resonance. When it drives $|1\rangle \rightarrow |3\rangle$ (resp. the $|2\rangle \rightarrow |3\rangle$) resonantly, the $|1\rangle \rightarrow |4\rangle$ (resp. $|2\rangle \rightarrow |4\rangle$) transition line splits into two. This effect is known as the Autler-Town splitting [40] and is qualitatively understood as follows. By driving resonantly the $|1\rangle \rightarrow |3\rangle$ (resp. $|2\rangle \rightarrow |3\rangle$) transition line, the defect quickly modulates the ground state population $\rho_{11}^{(0)}$ (resp. $\rho_{22}^{(0)}$), which oscillates at the Rabi frequency Ω_d . The linear absorption of the probe beam on the $|1\rangle \rightarrow |4\rangle$ (resp. $|2\rangle \rightarrow |4\rangle$) transition is thus also modulated at Ω_d , creating sidebands on the probe absorption spectrum, the Autler-Town lines, visible on the absorption profile of figure 5.5(b) where the fluid frequency is scanned for $\Delta_d = 0$. The same features can be observed on figure 5.5(a), as real and imaginary parts of the susceptibility are related to each other through the Kramers-Kronig relations. In the following paragraph, I will show how to precisely describe the Autler-Town splitting as well as the level anti-crossing visible on figure 5.5(a) using the dressed-state formalism.

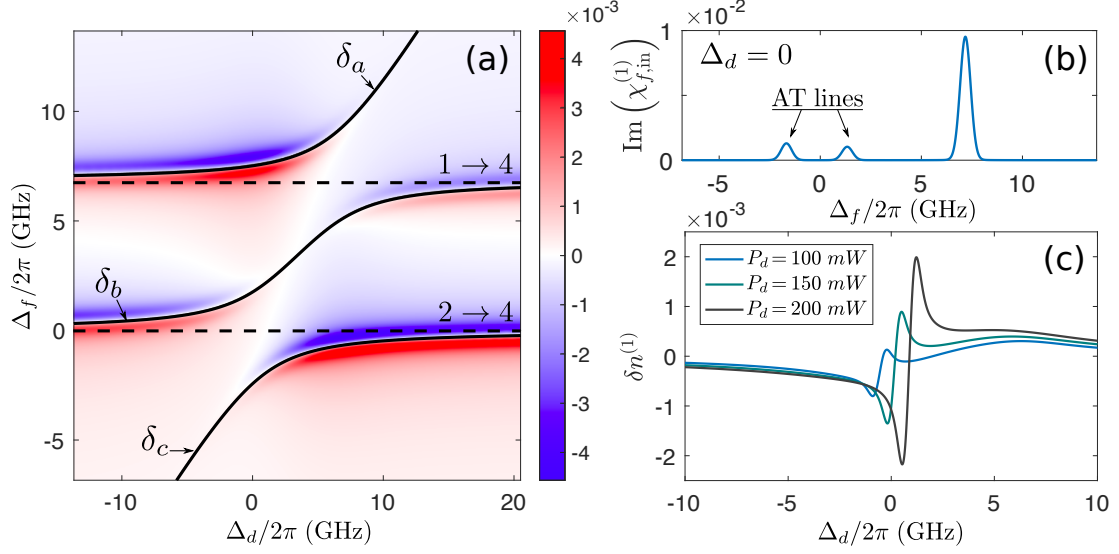


Figure 5.5: (a) Real part of $\chi_{f,\text{in}}^{(1)}$. The $|1\rangle \rightarrow |4\rangle$ and $|2\rangle \rightarrow |4\rangle$ spectral lines split into two when the defect beam is at resonance with $|1\rangle \rightarrow |3\rangle$ ($\Delta_d = \delta_0$) and $|2\rangle \rightarrow |3\rangle$ ($\Delta_d = 0$) respectively (Autler-Town effect). The energy shifts $\hbar\delta_a$, $\hbar\delta_b$ and $\hbar\delta_c$ of the dressed states $|a, n\rangle$, $|b, n\rangle$ and $|c, n\rangle$ have been plotted (black lines) as function of the defect detuning. (b) Imaginary part of $\chi_{f,\text{in}}^{(1)}$ as function of Δ_f (for $\Delta_d = 0$). The Autler-Town (AT) sidebands of the $|2\rangle \rightarrow |4\rangle$ transition are clearly visible on the left. The absorption peak on the right starts being blue-shifted from $\Delta_f = \delta_0$ ($\simeq 6.8$ GHz here, since we deal with rubidium 87). (c) Linear index modulation for different defect powers P_d . Parameters: $w_{0,d} = 50$ μm , $w_{0,f} = 500$ μm and $T = 415$ K. In (a-c), $\mathcal{P}_f = 10$ μW . In (a-b), $\mathcal{P}_d = 200$ mW.

ii Dressed-state formalism

The analytical expressions of the first-order density matrix elements allow us to calculate the weak probe field response for arbitrary values of the parameters and provides a detailed description of how this response is modified by the defect field. Nevertheless, the algebraic complexity of equations (5.6), (5.7) and (5.8) prevents us from getting a simple physical insight into the behaviour of $\chi_{f,\text{in}}^{(1)}$. An alternative approach is the so-called dressed-state formalism, which is particularly convenient for describing the photon-atom interaction in the strong coupling limit. Since detailed descriptions of the dressed-state theory can be found elsewhere [108–110], I will limit myself to applying it to the current situation.

The coupling between the D_1 line and the defect beam can be modeled by a 3-level system, interacting with a quasi-resonant laser field, whose Hamiltonian is: $\hat{H} = \hat{H}_F + \hat{H}_A + \hat{H}_I$. \hat{H}_F , \hat{H}_A and \hat{H}_I are the atomic, the field and the interaction parts of \hat{H} respectively [111]:

$$\begin{cases} \hat{H}_F = & \hbar\omega_d \hat{a}_d^\dagger \hat{a}_d \\ \hat{H}_A = & \hbar\omega_{21} |2\rangle \langle 2| + \hbar\omega_{31} |3\rangle \langle 3| \\ \hat{H}_I = & \frac{\hbar\Omega_d^*}{2} \hat{a}_d |3\rangle \langle 1| + \frac{\hbar\Omega_d}{2} \hat{a}_d^\dagger |1\rangle \langle 3| + \frac{\hbar\Omega_d^*}{2} \hat{a}_d |3\rangle \langle 2| + \frac{\hbar\Omega_d}{2} \hat{a}_d^\dagger |2\rangle \langle 3|, \end{cases} \quad (5.10)$$

where \hat{a}_d and \hat{a}_d^\dagger are the annihilation and creation operators of a photon in the defect beam.

We set the ground state energy to 0. Let's $|i, n\rangle$ be the eigenstate of the uncoupled atom plus field Hamiltonian, where i labels the atomic state while n stands for the number of photons in the defect field. Under the quasi-resonance condition, the levels $|1, n\rangle$, $|2, n\rangle$ and $|3, n-1\rangle$ become a quasi-degenerate triplet ξ_n ; the energy levels of the uncoupled atom plus field system split thus into such triplets, consecutively separated by the photon energy $\hbar\omega_d$. The interaction Hamiltonian introduces couplings between states lying in the same triplet. In the basis $\{|1, n\rangle, |2, n\rangle, |3, n-1\rangle\}$, \hat{H} is given by:

$$\hat{H}_n = \hat{H} - n\hbar\omega \mathbb{1} = \begin{pmatrix} 0 & 0 & \frac{\hbar\Omega_d}{2} \\ 0 & \hbar\delta_0 & \frac{\hbar\Omega_d}{2} \\ \frac{\hbar\Omega_d^*}{2} & \frac{\hbar\Omega_d^*}{2} & \hbar(\delta_0 - \Delta_d) \end{pmatrix}, \quad (5.11)$$

where $\mathbb{1}$ stands for the 3×3 identity matrix. The three dressed states of ξ_n — $|a, n\rangle$, $|b, n\rangle$ and $|c, n\rangle$ — and their energies — $\hbar\delta_a$, $\hbar\delta_b$ and $\hbar\delta_c$ — are obtained by diagonalizing the Hamiltonian \hat{H}_n in equation (5.11). As long as $\Omega_d \neq 0$, the matrix on the right-hand side of (5.11) has rank 3, whatever the value of Δ_d . The dressed states are thus always given by a linear superposition of all the unperturbed states $|1, n\rangle$, $|2, n\rangle$ and $|3, n-1\rangle$ in the triplet. The fourth level in the dressed-state representation is simply given by $|4, n\rangle$ as it is not coupled to the defect field. When the probe frequency is tuned over the whole D_2 line, transitions from $|1, n\rangle$ or $|2, n\rangle$ to $|4, n\rangle$ occur. Moreover, the eigenstates of \hat{H}_n contain all $|1, n\rangle$ and $|2, n\rangle$. In the dressed-state picture, there are therefore three allowed transitions between the excited state $|4, n\rangle$ and the dressed states of the n th multiplicity. That is why three peaks are visible on the absorption spectrum of figure 5.5(b). The shifts $\hbar\delta_i = \hbar\delta_0 - E_i$ of the dressed-state energies from the unperturbed energy of state $|2\rangle$, $\hbar\delta_0$, have been plotted as function of Δ_d (in h units) on figure 5.5(a) (black lines). The dressed-state formalism correctly predicts the splitting and the level anti-crossing observed in figure 5.5(a).

5.1.4 Total variation of the refractive index at the defect position

The definition of the refractive index modulation seen by the probe beam at the defect position can be extended to take nonlinear contributions into account. The total variation of refractive index between inside and outside the defect beam cross-section is given by:

$$\delta n = n_{\text{in}} - n_{\text{out}} \simeq \frac{1}{2} \text{Re} [\chi_{f,\text{in}} - \chi_{f,\text{out}}]. \quad (5.12)$$

The susceptibilities $\chi_{f,\text{in}}$ and $\chi_{f,\text{out}}$ are obtained by solving numerically the steady-state matrix equations for the 4- and the 3-level models respectively. The resulting refractive index modulation δn is plotted as function of Δ_d and Δ_f on figures 5.6(a) and (b), with (b) and without (a) Doppler broadening. These results are compared — on figure 5.6(c) and (d) — to the index change we get by solving the 5-level N-type model of figure 5.2(b) (describing more accurately the D_1 line), with (d) and without (c) Doppler-broadening. As you can see, the latter smooths out the discrepancy between the 4- and 5-level results, indicating that the 4-level model is sufficient to describe the physics at play. As for the linear index modulation, the sign and the strength of δn can be tuned changing the defect and the fluid frequencies. A positive (resp. negative) δn will locally act as an attractive (resp. repulsive) potential for the photon fluid. However, in order to ensure the robustness of the fluid of light against modulational instabilities, the probe should be red-detuned from the $|2\rangle \rightarrow |4\rangle$ transition

(n_2 is negative in that case). We are therefore only interested in the region where $\Delta_f < 0$ on the 2D maps 5.6(c) and (d), magnified on figures 5.6(e) and (f).

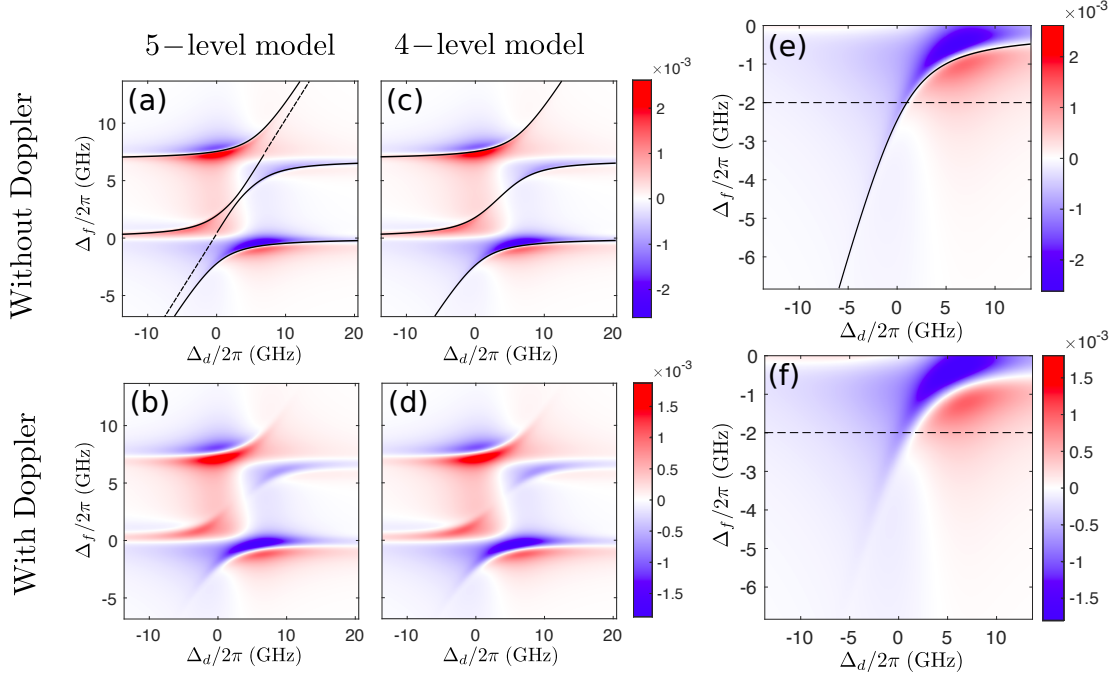


Figure 5.6: Total refractive index variation at the defect position. (a)-(b): Results of the calculations for the 4-level system of figure 5.2(a). The black lines represent the energy shift (in h units) of the the three dressed states composing the triplet ξ_n (see paragraph 5.1.3 ii). (c)-(d) Results of the calculations for the 4-level system of figure 5.2(b). The dresses-state approach introduced in the previous paragraph is extended to describe the full hyperfine structure of the D_1 line. The black lines represent the energy shift (in h units) of the four dressed states composing the quadruplet ξ_n in that case. The central ones are separated by $\delta_{34} \simeq 815$ MHz (for rubidium 87), when $\Delta_d = \delta_0/2$. On figures (e) and (f), we zoom in the region where $\Delta_f < 0$ (since in our experiments, Δ_f must be negative to ensure that $n_2 < 0$). At a given probe detuning (for instance $\Delta_f = -2$ GHz, black dotted line), tuning the defect frequency enables us to generate either attractive (*ie* guiding) or repulsive potentials into the photon fluid. Parameters: $w_{0,d} = 50 \mu\text{m}$, $w_{0,f} = 500 \mu\text{m}$, $\mathcal{P}_d = 200 \text{ mW}$, $\mathcal{P}_f = 50 \text{ mW}$ and $T = 415 \text{ K}$. Calculations performed for rubidium 87.

The inside susceptibility $\chi_{f,\text{in}}$ can also be computed by using the dressed-state formalism introduced in the preceding section. This approach enables, for instance, to isolate in $\chi_{f,\text{in}}$ the contribution of each dressed-state transition $|i, n\rangle \rightarrow |4, n\rangle$, which can help us getting a deeper insight into the spectra of figure 5.6. In the next two paragraphs, I will therefore digress a little bit and extend the dressed-state approach of subsection 5.1.3.

i 4-level system in the dressed-state picture

As in subsection 5.1.3, let's describe the coupling between the D_1 line and the defect field using the dressed-state formalism. Let's then $|a, n\rangle$, $|b, n\rangle$ and $|c, n\rangle$ stand for the three dressed states in the triplet ξ_n . As already mentioned previously, these states can always be expressed as a linear superposition of all the unperturbed states in the multiplicity ξ_n : $|i, n\rangle = \alpha_i |1, n\rangle + \beta_i |2, n\rangle + \gamma_i |3, n-1\rangle$ (i lies in $\{a, b, c\}$), with $|\alpha_i|^2 + |\beta_i|^2 + |\gamma_i|^2 = 1$ (normalization). The coefficients α_i , β_i and γ_i are obtained by diagonalizing \hat{H}_n in eq. (5.11). Using the normalization of $|1, n\rangle$ and the closure relation $\sum_i |i, n\rangle \langle i, n| = \mathbb{1}$, it is straightforward to show that $\sum_i |\alpha_i|^2 = 1$. Similarly, $\sum_i |\beta_i|^2 = \sum_i |\gamma_i|^2 = 1$. The decay rate from the state $|4, n\rangle$ to the dressed state $|i, n\rangle$ is given by $\Gamma_i = \frac{1}{2} (|\alpha_i|^2 + |\beta_i|^2) \Gamma_2$ and $\sum_i \Gamma_i = \Gamma_2$. The ground states $|1, n\rangle$ and $|2, n\rangle$ both appear in the expansion of the dressed states on the unperturbed basis of ξ_n . These two states are constantly filled by fresh atoms entering the defect area. Every dressed state in the triplet is therefore associated to a filling rate $\Gamma_t^{(i)}$ defined by: $\Gamma_t^{(i)} = \frac{1}{2} |\alpha_i|^2 \Gamma_{t,d}^{(1)} + \frac{1}{2} |\beta_i|^2 \Gamma_{t,d}^{(2)}$, and here again $\sum_i \Gamma_t^{(i)} = \Gamma_{t,d}$.

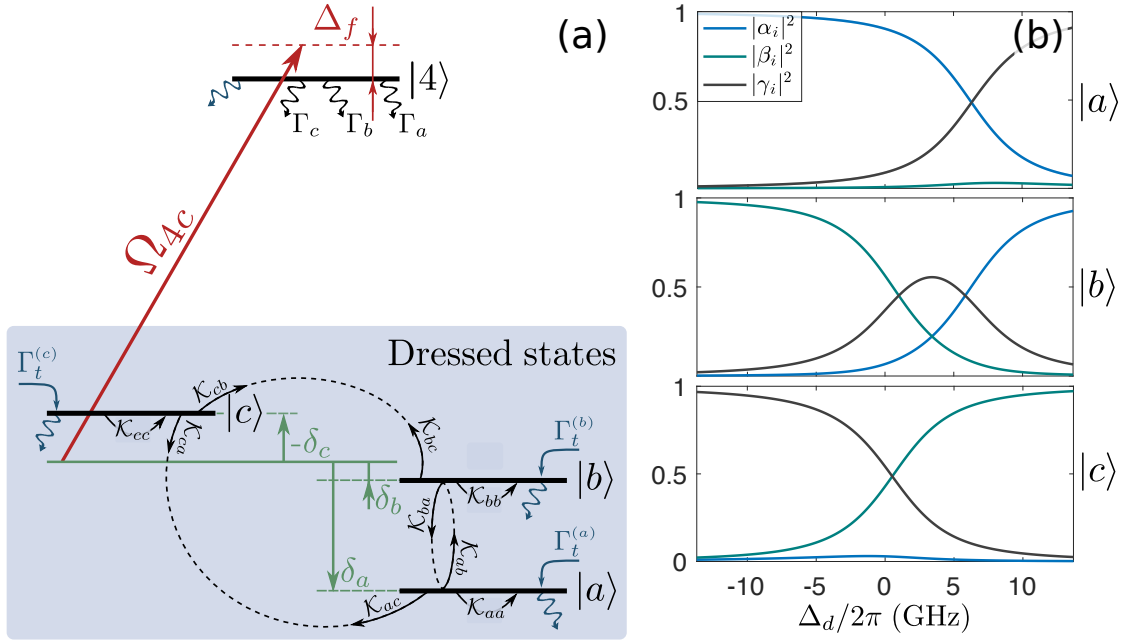


Figure 5.7: (a) Dressed-state model. The decay rates $\mathcal{K}_{i,j}$ couple the dressed states $|a\rangle$, $|b\rangle$ and $|c\rangle$ together. The blue arrows stand, as usual, for the transit filling and decay rates. The energy of the dressed state $|i\rangle$ is shifted with respect to the unperturbed energy of $|2\rangle$ (green horizontal line) by $\hbar\delta_i$. I assume the probe beam couples each dressed state to the unperturbed excited state $|4\rangle$ independently (the total optical response is then the sum of the responses of all the $|i\rangle \rightarrow |4\rangle$ transition lines). The dipole moment μ_{4i} (and thus Ω_{i4}) depends on which transition is addressed by the probe field. (b) Variation of the amplitudes $|\alpha_i|^2$, $|\beta_i|^2$ and $|\gamma_i|^2$ for $|a\rangle$ (top), $|b\rangle$ (middle) and $|c\rangle$ (bottom).

For the sake of correctness, we must also take the decay rate of dressed states into account. The unperturbed excited state $|3, n-1\rangle$ ends up decaying toward level $|1, n\rangle$ or level $|2, n\rangle$ and releases at that time one photon in the defect field. Since $|i, n\rangle$ contains $|1, n\rangle$, $|2, n\rangle$ and $|3, n-1\rangle$ (whatever i), this decay process happens not only in between dressed states but also within the states themselves. We therefore introduce $\mathcal{K}_{ij} = \frac{1}{2}|\gamma_i|^2 (|\alpha_j|^2 + |\beta_j|^2) \Gamma_1$ (i and j lie inside $\{a, b, c\}$), which is the decay rate from $|i, n\rangle$ to $|j, n\rangle$; $|\gamma_i|^2$ and $|\alpha_i|^2 + |\beta_i|^2$ are respectively the probability for $|i, n\rangle$ of being in the excited state $|3, n-1\rangle$ or in one of the ground states $|1, n\rangle$ or $|2, n\rangle$. The total decay rate \mathcal{K}_i of $|i, n\rangle$ is thus finally given by: $\mathcal{K}_i = \sum_j \mathcal{K}_{i,j} = |\gamma_i|^2 \Gamma_1$ and, once again, $\sum_i \mathcal{K}_i = \Gamma_1$.

For the sake of clarity, all the notations introduced before have been gathered on figure 5.7. In the dressed-state picture, $|a, n\rangle$, $|b, n\rangle$ and $|c, n\rangle$ can be regarded as ground states for the excited level $|4, n\rangle$. As already mentioned, the energies of the dressed states are shifted from the unperturbed energy of level $|2, n\rangle$ (sketched by the green line on figure 5.7(a)) by $\hbar\delta_a$, $\hbar\delta_b$ and $\hbar\delta_c$ respectively. Figure 5.7(b) shows the variations of $|\alpha_i|^2$, $|\beta_i|^2$ and $|\gamma_i|^2$ with Δ_d (at $\Omega_d = 2\pi \times 4.3$ GHz) for $|a\rangle$ (top), $|b\rangle$ (middle) and $|c\rangle$ (bottom).

REMARK. The decay rate between two states is proportional to the square of the dipole matrix element between these states. Being an odd operator, the dipole moment $\hat{\mathbf{d}}$ cannot change the number of photons in the defect field and must therefore couple ξ_n to adjacent multiplicities $\xi_{n\pm 1}$ [108]. Consequently, the dressed state $|i, n\rangle$ in ξ_n cannot decay toward the other states in this multiplicity (as I have supposed above) but toward those in ξ_{n-1} . For a complete and rigorous treatment of spontaneous emission in a dressed-atom system, the reader may refer to [108, 110]. However, our description still provides very good results, that are in excellent agreement with those obtained by directly solving equation (5.3) in the steady-state, as we will see later on.

ii Optical Bloch equations in the dressed-state picture

Let's now derive the Bloch equations associated to the 4-level dressed-state system sketched on figure 5.7(a). The fluid detuning is still defined by: $\Delta_f = \omega_f - \omega_{24}$, where ω_{24} is the frequency of the unperturbed $|2\rangle \rightarrow |4\rangle$ transition. The laser detuning should then be set to $-\delta_i$ in order to drive resonantly the transition from $|i, n\rangle$ to $|4, n\rangle$. The dipole moment associated to this transition is obtained by evaluating the dipole matrix element between $|i, n\rangle$ and $|4, n\rangle$: $\mu_{i4} = |\langle i, n | \hat{\mathbf{d}} | 4, n \rangle| = |\alpha_i + \beta_i| \mu_f$. The Rabi frequency depends thus on the transition addressed by the probe field. For the sake of simplicity, I will supposed from now on that the transitions are probed one by one by the probe beam as depicted in figure 5.7(a). The total optical response is thus obtained by summing the response of each individual transition. When the probe addresses the $|c, n\rangle \rightarrow |4, n\rangle$ transition for instance, the Optical Bloch equations read:

$$\begin{cases} \frac{d\rho_{aa}}{dt} = -(\Gamma_{t,d} + \mathcal{K}_{ab} + \mathcal{K}_{ac}) \rho_{aa} + \mathcal{K}_{ba} \rho_{bb} + \mathcal{K}_{ca} \rho_{cc} + \Gamma_a \rho_{44} + \Gamma_t^{(a)} \\ \frac{d\rho_{bb}}{dt} = \mathcal{K}_{ab} \rho_{aa} - (\Gamma_{t,d} + \mathcal{K}_{ba} + \mathcal{K}_{bc}) \rho_{bb} + \mathcal{K}_{cb} \rho_{cc} + \Gamma_b \rho_{44} + \Gamma_t^{(b)} \\ \frac{d\rho_{cc}}{dt} = \mathcal{K}_{ac} \rho_{aa} + \mathcal{K}_{bc} \rho_{bb} - (\Gamma_{t,d} + \mathcal{K}_{ca} + \mathcal{K}_{cb}) \rho_{cc} + \Gamma_c \rho_{44} + \Gamma_t^{(c)} + \frac{i}{2} (\Omega_{c4}^* \rho_{4c} - \Omega_{c4} \rho_{c4}) \\ \frac{d\rho_{44}}{dt} = -(\Gamma_{t,d} + \Gamma_{D2}) \rho_{44} - \frac{i}{2} (\Omega_{c4}^* \rho_{4c} - \Omega_{c4} \rho_{c4}) \\ \frac{d\rho_{4c}}{dt} = \frac{i}{2} \Omega_{c4} (\rho_{cc} - \rho_{44}) - \tilde{\gamma}_{4c} \rho_{4c} \end{cases} \quad (5.13)$$

where $\tilde{\gamma}_{4c} = (\Gamma_2 + \mathcal{K}_c)/2 + \Gamma_{t,d} - i(\Delta_f - \delta_c)$. Since the fluid couples only $|c, n\rangle$ and $|4, n\rangle$, the dielectric susceptibility $\chi_{c4} = \frac{2N}{\epsilon_0 \mathcal{E}_f} \mu_{c4} \rho_{4c}$ is similar to the susceptibility of an atomic two-level system. We also know, by looking at the real part of $\tilde{\gamma}_{4c}$, that the decoherence rate of the $|c, n\rangle \rightarrow |4, n\rangle$ transition (that is, the linewidth) is given by $(\Gamma_2 + \mathcal{K}_c)/2 + \Gamma_{t,d}$. The coherence ρ_{4c} is obtained by solving the steady-state matrix equation below, derived from the Bloch equations above by setting the time derivatives to zero:

$$\begin{pmatrix} \mathcal{T}_{aa} - (\Gamma_{t,d} + \mathcal{K}_a) & \mathcal{T}_{ba} & \mathcal{T}_{ca} & 0 & 0 \\ \mathcal{T}_{ab} & \mathcal{T}_{bb} - (\Gamma_{t,d} + \mathcal{K}_b) & \mathcal{T}_{cb} & 0 & 0 \\ \mathcal{T}_{ac} & \mathcal{T}_{bc} & \mathcal{T}_{cc} - (\Gamma_{t,d} + \mathcal{K}_c) & \frac{i\Omega_{c4}^*}{2} & -\frac{i\Omega_{c4}}{2} \\ \frac{i\Omega_{c4}}{2} & \frac{i\Omega_{c4}^*}{2} & i\Omega_{c4} & -\tilde{\gamma}_{4c} & 0 \\ \frac{i\Omega_{c4}^*}{2} & \frac{i\Omega_{c4}}{2} & i\Omega_{c4}^* & 0 & -\tilde{\gamma}_{4c}^* \end{pmatrix} \begin{pmatrix} \rho_{aa} \\ \rho_{bb} \\ \rho_{cc} \\ \rho_{4c} \\ \rho_{c4} \end{pmatrix} = - \begin{pmatrix} \Gamma_t^{(a)} + \Gamma_a \\ \Gamma_t^{(b)} + \Gamma_b \\ \Gamma_t^{(c)} + \Gamma_c \\ -\frac{i\Omega_{c4}}{2} \\ \frac{i\Omega_{c4}^*}{2} \end{pmatrix} \quad (5.14)$$

where $\mathcal{T}_{ij} = \mathcal{K}_{ij} - \Gamma_j$ (for i and j in $\{a, b, c\}$). Moreover, if we suppose that $\Gamma_1 = \Gamma_2 = \Gamma$ (which is a reasonable assumption as $\Gamma_1/\Gamma_2 \simeq 0.95$), the matrix \mathcal{T} becomes symmetric since: $\mathcal{T}_{ij} \simeq -\frac{1}{2} (|\alpha_i|^2 + |\beta_i|^2) (|\alpha_j|^2 + |\beta_j|^2) \Gamma$. In that case, χ_{c4} reads as follows:

$$\chi_{c4} = \frac{2N}{\epsilon_0 \mathcal{E}_f} \mu_{c4} \rho_{4c} \simeq \frac{\alpha_{4c}(0)}{\omega_{4c}/c} \frac{i - 2 \left(\frac{\Delta_f - \delta_c}{\bar{\gamma}_c + \bar{\gamma}_4} \right)}{1 + 4 \left(\frac{\Delta_f - \delta_c}{\bar{\gamma}_c + \bar{\gamma}_4} \right)^2 + \left(\frac{\mathcal{E}_f}{\mathcal{E}_s} \right)^2}, \quad (5.15)$$

where $\alpha_{4c}(0)$ is the linear line-center absorption coefficient and \mathcal{E}_s the line-center saturation field strength, which is defined by:

$$\mathcal{E}_s = \frac{\hbar}{\mu_{c4}} \sqrt{\bar{\gamma}_c + \bar{\gamma}_4} \left[\frac{\bar{\gamma}_a \bar{\gamma}_b \bar{\gamma}_c - (\mathcal{T}_{aa} \bar{\gamma}_b \bar{\gamma}_c + \mathcal{T}_{bb} \bar{\gamma}_a \bar{\gamma}_c + \mathcal{T}_{cc} \bar{\gamma}_a \bar{\gamma}_b)}{2 \bar{\gamma}_a \bar{\gamma}_b + (\mathcal{T}_{bc} - 2 \mathcal{T}_{bb}) \bar{\gamma}_a + (\mathcal{T}_{ac} - 2 \mathcal{T}_{aa}) \bar{\gamma}_b} \right]^{1/2}. \quad (5.16)$$

In equations (5.15) and (5.16), the total decay rates $\bar{\gamma}_a$, $\bar{\gamma}_b$, $\bar{\gamma}_c$ and $\bar{\gamma}_4$ of the dressed-states $|a, n\rangle$, $|b, n\rangle$, $|c, n\rangle$ and $|4, n\rangle$ have been introduced. For i lying in $\{a, b, c\}$, $\bar{\gamma}_i = K_i + \Gamma_{t,d}$ whereas $\bar{\gamma}_4 = \Gamma + \Gamma_{t,d}$. The off-resonance saturation intensity can finally be expressed as: $\mathcal{I}_s(\Delta_f) = \mathcal{I}_s(0) [1 + 4 (\Delta_f - \delta_c)^2 / (\bar{\gamma}_c + \bar{\gamma}_4)^2]$ where $\mathcal{I}_s(0) = \frac{1}{2} \epsilon_0 c |\mathcal{E}_s|^2$. The dressed-state formalism provides therefore a value for the linewidth as well as for the saturation intensity of the $|c, n\rangle \rightarrow |4, n\rangle$ transition. At fixed defect power P_d and detuning Δ_d , equation (5.15) predicts then how the $|c, n\rangle \rightarrow |4, n\rangle$ transition line saturates and broadens increasing the fluid power, which is far from being obvious looking at the steady-state solution of 5.3. One can similarly derive equations for χ_{a4} and χ_{b4} . The total susceptibility $\chi_{f,\text{in}}$ inside the defect cross-section is finally given by: $\chi_{f,\text{in}} = \sum_i \chi_{i4}$. The imaginary part of $\chi_{f,\text{in}}$ has been plotted on figure 5.8 as function of Δ_f , by using the dressed state approach (blue curve) and by directly solving the steady-state matrix equation derived from 5.3 (dashed line). The defect detuning was set to zero and we use for the computation the same parameters as in figure 5.6. The agreement between both descriptions is excellent.

5.1.5 Saturation of δn

In photon fluid experiments, we constantly need to change the fluid power P_f in order to tune the nonlinear change of refractive index $\Delta n = n_2 \mathcal{I}_0$ and access different flow regimes (superfluid, supercritical, etc). In the present situation, acting on the fluid power does not only modify the fluid properties but also the defect strength in two different ways:

- A change in the fluid power will first impact the preparation rates by either increasing or decreasing the number of atoms prepared in the steady-state.
- Increasing the fluid power can also make the refractive index modulation δn quickly saturate and results consequently in a reduction of the defect strength.

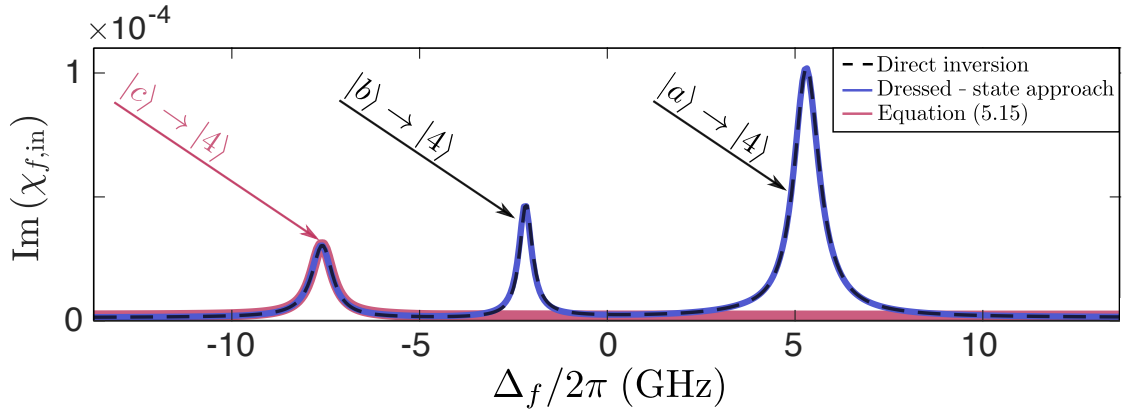


Figure 5.8: Comparison between the dressed-state approach and the numerical inversion of the steady-state matrix equation derived from 5.3. Parameters are the same as for 5.6.

Both these effects contribute to modify the defect amplitude when the fluid power changes, which is not desirable in photon fluid experiments where the aim is rather to study how a fluid of light flows in a fixed potential landscape $\delta n(r_\perp)$ as function of Δn in particular. Therefore, the question is: can we change the fluid power while keeping the defect depth (or height, depending on the sign of δn) almost constant? In order to answer this question, we have plotted on figure 5.9(a)-(e) the evolution of δn as function of Δ_d and \mathcal{P}_f , for different values of \mathcal{P}_d . In all these plots, the probe detuning is fixed to $\Delta_f = -2\pi \times 3$ GHz which is closed to the experimental value. The temperature is 415 K and the widths of the beams are, as usual, $\omega_{0,d} = 50 \mu\text{m}$ and $\omega_{0,f} = 500 \mu\text{m}$. Let's first focus on 5.9(b). This figure is obtained for a relatively low defect power, since $\mathcal{P}_d = 10$ mW (that is, $\Omega_d \simeq 2\pi \times 1$ GHz) in that case. The probe power \mathcal{P}_f varies in eight steps from 25 (blue) to 200 mW (purple). There are two notable features in this plot. First, a dip, at $\Delta_d = 0$ and second, a peak, located at $\Delta_d = \delta_0$ (black dashed line). When $\Delta_d \simeq 0$, atoms are pumped from state $|2\rangle$ to state $|1\rangle$ by the defect beam. The probe beam, red-detuned from the $|2\rangle \rightarrow |4\rangle$ transition, interacts therefore with a lower density of atoms in state $|2\rangle$ inside than outside the defect cross-section, hence the negative δn . Reversely, when $\Delta_d \simeq \delta_0$, atoms are pumped from state $|1\rangle$ to state $|2\rangle$, which induces a positive δn this time. Setting the defect detuning to zero will thus locally generate a repulsive potential in the photon fluid ($\delta n < 0$) while setting it at δ_0 will create an attractive (guiding) potential. As you can notice, δn does not

vary much with the fluid power. The potential height (or depth) will then remains almost constant increasing P_f , which is precisely what we desire. Figure 5.9(c)-(e) shows the same as 5.9(b) for higher defect powers (respectively 50, 100 and 200 mW). On 5.9(c) and (d), the dip and the peak of 5.9(b) are broader but still visible. A new feature, indicated by the black arrow, that was barely discernible on 5.9(b), starts developing as P_d increases, and move from left to right. This local variation of δn arises when Δ_d satisfies $\delta_c(\Delta_d, P_d) = \Delta_f$. When this condition is fulfilled, the defect beam brings the $|c, n\rangle \rightarrow |4, n\rangle$ transition at resonance with the probe field, by shifting the energy of the dressed state $|c, n\rangle$ in such a way that the probe detuning Δ_f is compensated (see figure 5.7(a)). When P_d increases, the Autler-Town splitting between the two dressed states $|b, n\rangle$ and $|c, n\rangle$ becomes larger.

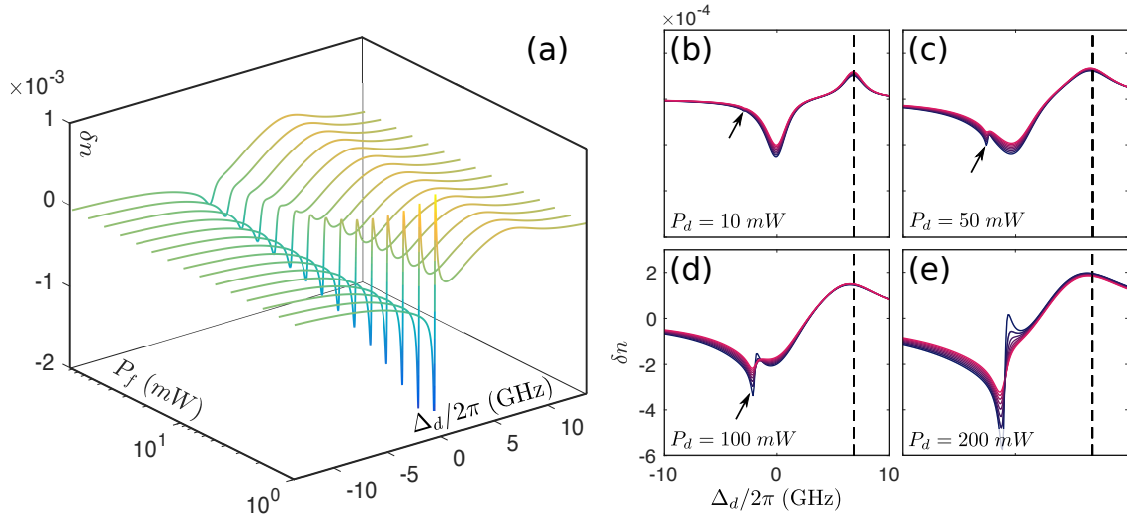


Figure 5.9: (a) shows the evolution of δn as function of the defect detuning Δ_d when the fluid power increases gradually. The saturation by the probe of the $|c, n\rangle \rightarrow |4, n\rangle$ transition makes δn strongly depend on P_f , close to $\Delta_d \simeq -2\pi \times 1$ GHz. (b)-(e) show the same as in (a): δn has been plotted as function of Δ_d for different fluid powers, ranging from 25 (blue) to 200 mW (magenta). The black arrow indicates the contribution of the $|c, n\rangle \rightarrow |4, n\rangle$ transition line, when it is resonantly driven by the probe field. Parameters: $w_{0,d} = 50 \mu\text{m}$, $w_{0,f} = 500 \mu\text{m}$ and $T = 415$ K. Results obtained for a ^{87}Rb vapor.

In other words, the energy shift $\delta_c(\Delta_d, P_d)$, increases with P_d . Therefore, the point at which the horizontal line defined by $\Delta_f = -2\pi \times 3$ GHz crosses δ_c on figure 5.5(a) shifts to the right, explaining why the detuning at which $\delta_c(\Delta_d, P_d) = \Delta_f$ is blue-shifted when P_d increases. Moreover, the contribution of the $|c, n\rangle \rightarrow |4, n\rangle$ transition line to the inside susceptibility $\chi_{f,\text{in}}$ seems to get larger and larger when the defect power steps up. When $P_d = 200$ mW (e), we might be tempted to set the defect detuning where the dip is the deepest. Nevertheless, at this detuning ($\Delta_d \simeq -2\pi \times 1$ GHz), the index modulation δn varies pretty fast with the probe power: from $P_f = 25$ mW (blue) to $P_f = 200$ mW (magenta), δn decreases by half, because of the saturation of the $|c, n\rangle \rightarrow |4, n\rangle$ transition. Figure 5.9(a) shows this effect more in detail, for the same parameters as in 5.9(e). Let's summarize all that has been said. If we look for generating a repulsive potential in the photon fluid, we can either:

- (1) drive resonantly the $|2\rangle \rightarrow |3\rangle$ transition with the defect field while keeping its power sufficiently low in order to neglect the contribution of the $|c, n\rangle \rightarrow |4, n\rangle$ transition, as in figures 5.9(b) and (c). In that case, the physical mechanism underlying the variation of refractive index at the defect position is optical pumping from $|2\rangle$ to $|1\rangle$. This configuration has the benefit of reducing the variations of δn with the fluid power. However, as the $|2\rangle \rightarrow |3\rangle$ transition is not totally saturated in that case, absorption of the defect beam along propagation is expected.
- (2) completely saturate the D_1 line and use the large contribution of the $|c, n\rangle \rightarrow |4, n\rangle$ transition when it is resonantly driven by the probe field, that is, when Δ_d satisfies the condition $\delta_c(\Delta_d, P_d) = \Delta_f$, as in figure 5.9(e). In that case, variation in the fluid power is not suitable as it will also change the height of the potential. Nevertheless, low absorption and self-effects (focusing, defocusing) on the defect field are expected since the D_1 line is highly saturated this time.

5.1.6 Other routes ?

As mentioned in the introduction of this section, several other routes have been investigated to generate local changes of refractive index in rubidium vapors. We should first mention the work of Truscott *et al.* [105], in which the guiding of a probe beam in a donuts-shaped all-optical wave-guide is demonstrated. Truscott and co-workers used the optical pumping between the D -lines ground states of rubidium to generate their wave-guide, just as we do. Their scheme has been analysed in the works of Kapoor *et al.* [112] and Andersen *et al.* [113], where the optical Bloch equations of the 5-level system on figure 5.2 are solved numerically. In this section, we improve their theoretical description using the dressed-state formalism.

More recently, all-optical wave-guiding has been reported in warm atomic vapors by driving a Raman transition off-resonantly [114]. This technique can be used to enhance the efficiency of nonlinear processes at very low light intensities [115]. Other schemes taking advantage of the coherences between the atomic levels can be used to induce refractive index changes. Image guiding as for instance be reported using electromagnetically induced transparency (EIT) in a lambda and double lambda systems [116]. Following the work of Sheng *et al.* [106], Silva and co-workers have investigated the possibility of observing superfluid flows of light in a four-level N-type atomic system [117]. Three lasers are involved in this scheme, referred to as the probe, the control and the switching fields in [117]. The probe and the control drive the $|1\rangle \rightarrow |3\rangle$ and $|2\rangle \rightarrow |3\rangle$ transitions respectively (EIT configuration) while the switching field addresses the $|2\rangle \rightarrow |4\rangle$ transition. The level schematic is the same as on figure 5.2(a). The fluid of light is formed by the probe beam here. The possibilities offered by this system are manifold, as it simultaneously allows to control the strength of the nonlinear interaction experienced by the probe and to imprint refractive index changes using the switching field. This configuration represents thus a versatile alternative to optical pumping schemes.

5.2 Optical defect shaping with a Spatial Light Modulator

In the previous section, we have seen how to induce a potential on the photon fluid forming the probe beam (tuned to the D_2 line), by driving the D_1 line with an intense and spatially localized defect field. Up to now, we have put aside the problem of propagation inside the rubidium cell. We only studied the refractive index modulation created over the transverse plane at a given position z on the optical axis. At this position, the defect cross-section as well as the powers of the beams are fixed. Reality is more complex, as we should ideally maintain the potential height (or depth) all along the propagation inside the cell, in order for this potential to be "stationary" with respect to the effective time $\tau = zn_0/c$. We must therefore face issues such as the defect beam absorption – that will make the local index modulation δn vary along z – or its collimation over the whole propagation inside the rubidium cell. The question is thus: what are the experimental requirements to fulfill, regarding the probe and the defect beams, in order for the potential to be "stationary"? I will answer this question from a theoretical point of view first, before explaining in a second step how these requirements are implemented in our experiments.

5.2.1 Experimental requirements

Our primary goal is to locally generate a potential in the photon fluid (that is, an obstacle) in order to study how the fluid will flow around. In the ideal case, this obstacle should remain unchanged over the propagation, as mentioned above. This basically suggests two things. First, the defect beam creating the obstacle has to be collimated. In other words, the defect cross-section should only slightly changes with the propagation distance. Second, the defect power has to remain (almost) constant along z , that is, the absorption of the defect beam should be negligible or somehow compensated over the propagation. Moreover, as we saw in the previous section, increasing the fluid power may also reduce the obstacle amplitude. For the sake of simplicity, I will suppose that the fluid frequency is sufficiently red-detuned from the $|2\rangle \rightarrow |4\rangle$ transition, so that the fluid transmission through the cell is above 70%. For example, let's consider a 1 mm diameter beam propagating inside a 2.5 cm cell, filled with a pure vapor of rubidium 87. In that case, the beam transmission at 415 K ranges from 83% ($\mathcal{P}_f = 1 \mu\text{W}$) to 89% ($\mathcal{P}_f = 0.5 \text{ W}$), when the laser frequency is 3 GHz red-detuned from the $|2\rangle \rightarrow |4\rangle$ transition. In such situations, we can neglect the dependence of δn on \mathcal{P}_f . Let's therefore focus on the crux of the issue: the defect beam collimation and absorption.

i Defect beam collimation

The first thing that comes to mind is to focus a Gaussian beam inside the cell to generate the obstacle. The Rayleigh length $z_r = \pi\omega_{0,d}^2/\lambda_d$ defines, in that case, the typical distance over which the defect beam is collimated. More precisely, it is the distance from the waist at which the beam radius increases by a factor $\sqrt{2}$ (in intensity). If we want to collimate the defect over 2.5 cm (which is the length of the cell we use in experiments), the minimum width $\omega_{0,\text{lim}}$ we can reach is about $\sqrt{\lambda L/\pi} \simeq 80 \mu\text{m}$. Using the value of the nonlinear index of refraction n_2 reported in 2.3.2 iii ($n_2 \simeq 2.1 \times 10^{-10} \text{ m}^2/\text{W}$), a 2 mm diameter probe beam of 200 mW induces an on-axis nonlinear change of refractive index Δn of nearly 2.6×10^{-5} . The healing length $\xi \sim 1/k\sqrt{\Delta n}$ is then about $25 \mu\text{m}$, which is less than a third of $\omega_{0,\text{lim}}$.

As we shall see in chapter 6, probing the superfluidity requires a defect that is comparable in size to ξ . Focusing a Gaussian beam inside the cell to generate the obstacle is therefore not suitable for our application. Instead, one can think about using non-diffracting beams such as Airy (parabolic) [118] or zero-order Bessel beams. The latter have been introduced by Durnin *et al.* [119] and result from the interference of an infinite number of plane waves whose relative wave-vectors constitute the generating lines of the so-called Bessel cone. The radial intensity distribution of zero-order Bessel beams is described by the zero-order Bessel function of the first kind: a high intensity central peak is surrounded by an infinite number of concentric rings of decreasing intensity. Although perfect Bessel beams are only mathematical objects (as they will carry an infinite energy otherwise), spatially limited (or quasi-) Bessel beams can be realized experimentally. Those beams have found various applications – in optical trapping [120,121], laser machining [122], nonlinear optics [123,124] and imaging [125,126] for instance – as their central cores stay collimated on a distance that is orders of magnitude longer than the Rayleigh length z_r . The diffraction-free feature of zeroth-order Bessel beams make them attractive for our application. They have already been used in [29] to produce non-diffracting obstacle in superfluid light.

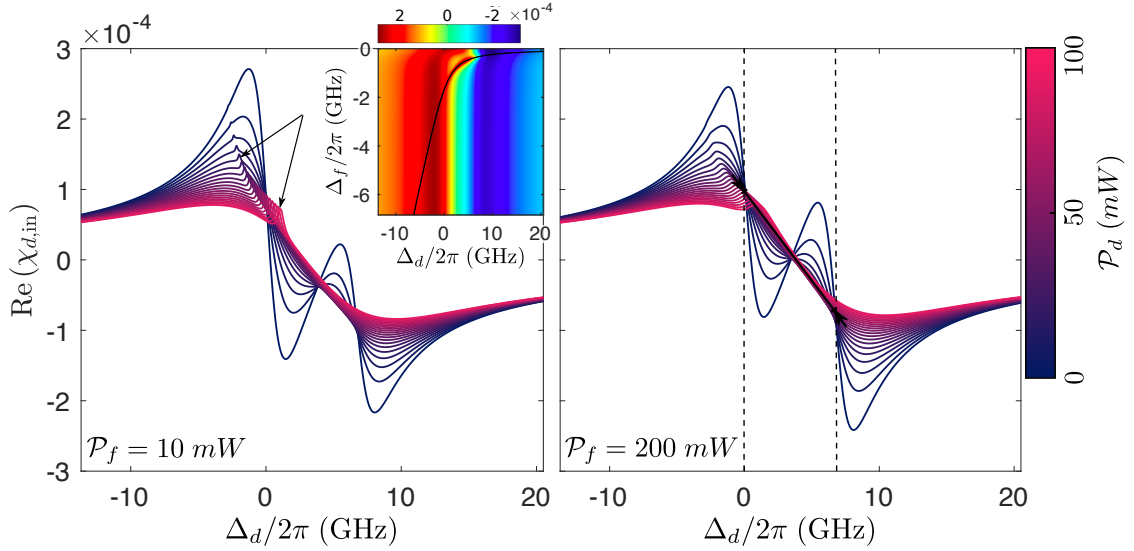


Figure 5.10: Real part of $\chi_{d,\text{in}}$ as function of Δ_d for different defect powers, which varies in twenty steps from 5 (blue) to 100 mW (magenta). Left: $\mathcal{P}_f = 10$ mW. When the probe is at resonance with the $|c, n\rangle \rightarrow |4, n\rangle$ transition (that is, when Δ_d satisfies $\delta_c(\Delta_d, \mathcal{P}_d) = \Delta_f$), it slightly affects the inside susceptibility $\chi_{d,\text{in}}$, creating peaks in the spectra of $\text{Re}[\chi_{d,\text{in}}]$ (black arrows). These peaks move from left to right when \mathcal{P}_d increases. The inset shows the variation of $\text{Re}[\chi_{d,\text{in}}]$ with Δ_d and Δ_f . Right: $\mathcal{P}_f = 200$ mW. The peaks are still visible but broader (because of the power broadening of the $|c, n\rangle \rightarrow |4, n\rangle$ transition line). There are points on both graphs at which $\text{Re}[\chi_{d,\text{in}}]$ does not depend much on the defect power \mathcal{P}_d ; they are located at $\Delta_d = 0$, $\Delta_d = \delta_0/2$ and $\Delta_d = \delta_0$. At these detunings, self-effects on the defect beam are expected to be small. The parameters are: $w_{0,d} = 25 \mu\text{m}$, $w_{0,f} = 500 \mu\text{m}$, $T = 415$ K and $\Delta_f = -2\pi \times 3$ GHz. Results obtained for a ^{87}Rb vapor.

However, Bessel beams — such as Gaussian ones — are sensitive to self-effects. For instance, a radial broadening (resp. compression) of the Bessel beam central peak is expected along its propagation in self-defocusing (resp. self-focusing) mediums [127]. This is problematic as it means that the width $\omega_{0,d}$ of the defect beam will change along z . In order to know the defect detunings at which self-effects are the weakest, the real part of the susceptibility $\chi_{d,in}$ has been plotted on figure 5.10 as function of Δ_d for different defect and probe powers. This quantity characterizes the optical response of the rubidium vapor to the defect field. It also defines the refractive index felt by the defect: $n_d = 1 + \frac{1}{2}\text{Re}[\chi_{d,in}]$. When the latter does not depend much on the defect intensity, self-effects are expected to be small. Indeed, self-focusing or -defocusing arise when the refractive index depends on the beam intensity. Figure 5.10 shows the spectra of $\text{Re}[\chi_{d,in}]$ at various defect powers, ranging from $\mathcal{P}_d = 5$ mW (blue) to $\mathcal{P}_d = 100$ mW (magenta), for $\mathcal{P}_f = 10$ mW (left) as well as $\mathcal{P}_f = 200$ mW (right). The simulation has been performed for $\omega_{0,d} = 25$ μm (comparable to ξ), $\omega_{0,f} = 500$ μm and $T = 415$ K, as usual. At low defect power, the $|1\rangle \rightarrow |3\rangle$ and $|2\rangle \rightarrow |3\rangle$ transition lines are both discernible (as in figure 1.10), but not anymore at high power, where the D_1 line is completely saturated. As you may have noticed, there are values of Δ_d for which $\text{Re}[\chi_{d,in}]$ does not evolve much with the defect power. They are located at $\Delta_d = 0$, $\Delta_d \simeq \delta_0/2$ and $\Delta_d = \delta_0$ respectively. The fact that $\text{Re}[\chi_{d,in}]$ (and, by extension, n_d) does not depend on \mathcal{P}_d at $\Delta_d = 0$ is particularly interesting, since the best obstacle — at low defect power — is precisely obtained at this detuning (see figure 5.9(b) for example). Apart from the specific values of Δ_d mentioned above, it seems hard to make n_d not dependent on \mathcal{P}_d . One can think about over-saturating the D_1 line with the defect, that is, making the on-axis Bessel beam intensity order of magnitude bigger than the saturation intensity. That way, the Bessel core will roughly speaking see an uniform refractive index at positions for which the light intensity is higher than the saturation intensity. This is of course a very simplified picture. As far as I know, there is no reference in the literature studying the impact of saturation on the propagation of Bessel beams. In practice, we do saturate the vapor and it does not seem to really affect the beam shape (in the cell output plane at least). Moreover, we have noticed that the best collimation is obtained when the defect is several hundreds of megahertz blue-detuned from the $|2\rangle \rightarrow |4\rangle$ transition. In that case, the variation in the width of the Bessel central peak is less than 10% between the input and the output plane of the cell.

ii Defect beam absorption

Another issue to face is the absorption of the defect light inside the vapor cell. Since the defect is tuned almost resonantly to the D_1 line, strong absorption is expected, at least at small defect powers. This is indeed what we can see on figure 5.11, where the transmission $t = \exp(-\alpha_d L)$ has been plotted as function of Δ_d , for defect powers ranging from 5 mW (blue) to 100 mW (magenta). On the left, $\mathcal{P}_f = 10$ mW while on the right, $\mathcal{P}_f = 200$ mW. The vapor cell is 2.5 cm long here. The other parameters are the same as for figure 5.10. The absorption coefficient α_d is defined by: $\alpha_d = k_d \text{Im}[\chi_{d,in}]$, where k_d is the wave-vector of the defect field. As you can see, absorption is not negligible for $\Delta_d = 0$ and $\Delta_d = \delta_0$ at low defect powers (and can be even stronger decreasing \mathcal{P}_d below 5 mW). If we choose not to fully saturate the D_1 line, in order to only take benefit of optical pumping between ground states to generate the obstacle (as for example in 5.9(b) and (c)), we should then somehow compensated the defect absorption over propagation. A method — based on the

on-axis shaping of the Bessel beam intensity profile — is presented to this end in the next subsection. Reversely, if we choose to work in the saturating regime, that is, a high defect powers, absorption is not anymore an issue, since transmission rapidly grows above 90%. I would like to conclude this paragraph explaining the origin of the small amplitude peaks you may have noticed on the transmission spectra (on the slope of the left transmission dip). This small "transparency window" is opened by the probe field when it resonantly drives the $|c, n\rangle \rightarrow |4, n\rangle$ transition (that is, when Δ_d fulfills $\delta_c(\Delta_d, \mathcal{P}_d) = \Delta_f$). That is why the peaks position moves to the right when \mathcal{P}_d steps up (see 5.1.5). The width of the peaks increases with the fluid power (because of the power broadening of the $|c, n\rangle \rightarrow |4, n\rangle$ transition line). The same features are also visible on the spectra of figure 5.10 (black arrows).

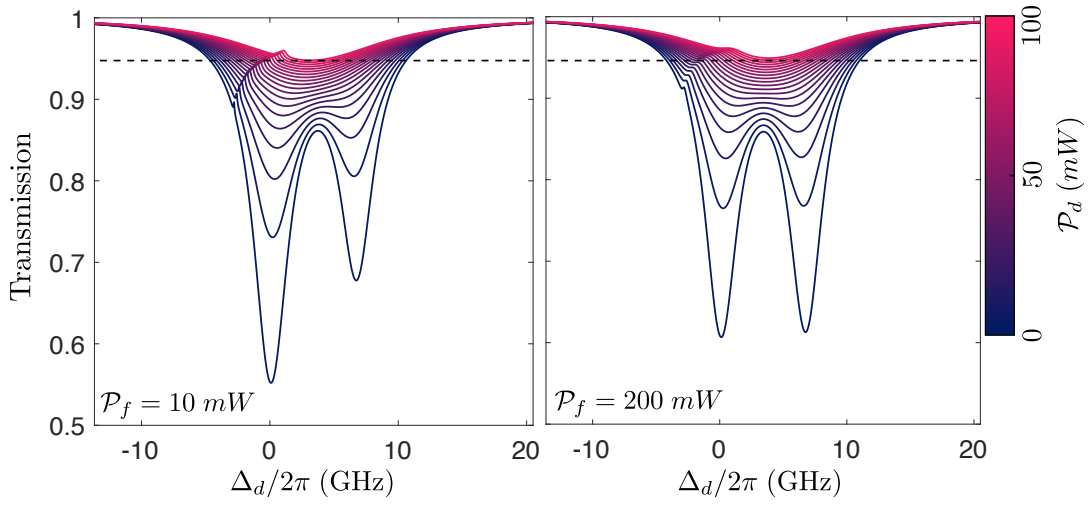


Figure 5.11: Transmission of the defect beam through a 2.5 cm long cell as function of Δ_d , for different defect powers. \mathcal{P}_d increases in twenty steps from 5 (blue) to 100 mW (magenta). Left: $\mathcal{P}_f = 10$ mW. Right: $\mathcal{P}_f = 200$ mW. The same peaks as in figure 5.10 are visible on both graphs. By driving resonantly the $|c, n\rangle \rightarrow |4, n\rangle$ transition when $\delta_c(\Delta_d, \mathcal{P}_d) = \Delta_f$, the probe opens a small transparency windows for the defect field. At high defect power, the saturation of the D_1 line leads to transmissions above 90%. In that case, we can safely neglect the absorption of the defect beam. However, at low defect power, absorption is not negligible anymore and should somehow be compensated (see next subsection for details). The parameters used here are the same as for figure 5.10.

5.2.2 Absorption-compensated Bessel Beam

As we have seen in the previous subsection, absorption of low power defect beams prevents the obstacle amplitude from being constant along the propagation inside the vapor cell. We therefore started asking ourselves if it was somehow possible to compensate absorption — at least along the optical axis — by shaping the Bessel beam on-axis intensity profile. This questioning goes well beyond the framework of obstacle generation in photon fluids, since absorption (or diffusion) is the main limitation in a wide range of optical applications.

In bio imaging for instance, light-sheet microscopy – which allows selective illumination of tissues and fast 3D imaging of live organisms at the cellular scale [128] – is until now limited by the field of view, that is, the penetration depth of the illuminating beam inside the sample. Tissues are highly diffusive optical mediums. Imaging through is therefore a challenging task. Selective plane illumination microscopy could thus also benefit from the development of attenuation-resistant Bessel beams, that would have a significantly better penetration depth. In the literature, the generation of such beams with exponential intensity axicons [129] and with computer generated holograms [130] has been reported. In both cases, the Bessel beam on-axis intensity is tailored so as to exponentially increase over the optical axis and exactly counterbalance the exponential decay $\exp(-\alpha z)$ of the Beer-Lambert law. The coefficient α is the linear attenuation coefficient, describing either diffusion or absorption losses inside the optical medium. In [130], the attenuation-resistant light field (referred to as "frozen waves") results from the superposition of equal frequency Bessel beams, generated by modulating only the amplitude of an incident plane-wave, using a Spatial Light Modulator (or SLM). In this subsection, I present a more versatile method, based on both the phase and amplitude shaping of an incident Gaussian beam [131,132]. It allows compensating attenuation up to $\alpha = 200 \text{ m}^{-1}$ – whatever the loss mechanism – by using real space shaping with a reflective phase-only SLM. However, it is worth noting that this technique works for compensating **linear attenuation** only. We therefore assume α does not depend on the beam intensity. In the following paragraphs, I will first present the theoretical background on which the method is based, before showing the results we obtained using absorbing (rubidium vapor) and diffusive (aqueous milk suspension) optical mediums. The content of this subsection has been published in "Attenuation-free non-diffracting Bessel beams", Optics Express, Vol. 27, Issue 21, pp. 30067-30080 (2019) [102].

i Shaping Bessel beams on-axis intensity

At a given position z_0 on the optical axis (from now on, $z_0 = 0$), the electric field envelope $\mathcal{E}(x, y, z_0 = 0)$ of the laser beam is related to its spatial spectrum $\mathcal{S}(k_x, k_y, z_0 = 0)$ through:

$$\mathcal{E}(x, y, 0) = \int_{-\infty}^{\infty} \int_{-\infty}^{\infty} \mathcal{S}(k_x, k_y, 0) \exp[-i(k_x x + k_y y)] dk_x dk_y. \quad (5.17)$$

For a radially symmetric laser beam, equation 5.17 can be rewritten as follows [132]:

$$\mathcal{E}(r, 0) = \frac{1}{2\pi} \int_0^{\infty} \mathcal{S}(k_{\perp}, 0) J_0(r k_{\perp}) k_{\perp} dk_{\perp}, \quad (5.18)$$

where J_0 is the zero-order Bessel function of the first kind, r the transverse radial coordinate and $k_{\perp} = \sqrt{k_x^2 + k_y^2}$ the transverse wave-vector. The spatial spectrum $\mathcal{S}(k_{\perp}, 0)$ is the Hankel transform of the electric field envelope $\mathcal{E}(r, 0)$. As mentioned in [133], equation 5.18 shows that a radially symmetric field can be regarded as a superposition of zero-order Bessel fields. Each of these Bessel components propagates without diffracting [119] as $J_0(r k_{\perp}) \exp[i k_z z]$, where $k_z = \sqrt{k_0^2 - k_{\perp}^2}$ is the longitudinal wave-vector of a given Bessel mode. Consequently, the on-axis electric field at position z , $\mathcal{E}(r = 0, z)$, can be obtained from (5.18) as:

$$\mathcal{E}(r = 0, z) = \frac{1}{\pi} \int_0^{\infty} \mathcal{S}(\sqrt{k_0^2 - k_z^2}, z = 0) \exp[i k_z z] k_z dk_z. \quad (5.19)$$

In Fourier space, the spatial spectrum of an ideal zero-order Bessel beam is a ring of radius $k_{\perp} = k_0 \sin(\theta)$. Therefore, the light rays that describe the beam propagation are distributed over a cone of angle θ . This angle sets the spot size, that is, the full width at half-maximum (FWHM) of the central peak in the transverse intensity profile. It is equal to $2.27/k_0 \sin(\theta)$ for an ideal zero-order Bessel beam. Each of the modes coming in the spectral decomposition equation (5.18) propagates in free-space with a slightly different longitudinal wave-vector $k_z = k_0 \cos(\theta)$, as can be seen in (5.19). They thus merge with different cone angles and at distinct positions along the optical axis. The on-axis electric field results then from the interference arising between these individual modes. If one wants to design a Bessel beam with a given on-axis intensity profile $\mathcal{I}(z) = |\mathcal{E}(r = 0, z)|^2$ along the optical axis, the spatial spectrum \mathcal{S} must be engineered according to the following formula :

$$\mathcal{S}(k_{\perp}, z_0 = 0) = \frac{1}{k_z} \int_0^{\infty} \sqrt{\mathcal{I}(z)} \exp[i(k_{z0} - k_z)z] dz. \quad (5.20)$$

The spectrum \mathcal{S} is centered around the longitudinal wave-vector of the target Bessel beam $k_{z0} = k_0 \cos(\theta_0)$. This formula gives a physical insight about the engineering process that will be used to compensate attenuation along the z -axis. The initial electric field $\mathcal{E}(r, z_0 = 0)$ that will produce a Bessel beam with a cone angle θ_0 and an on-axis intensity profile $I(z)$ can be evaluated using equations (5.18) and (5.20). In the following paragraph, we briefly describe how to generate the target beam, by shaping in real-space the phase and amplitude of a Gaussian beam with a Spatial Light Modulator (SLM). Fourier space shaping may also be considered [133]. Nevertheless, in that case, only the incident light distributed over the thin ring forming the intensity distribution of the Bessel beam in Fourier space is used. A large part of the light in the incident Gaussian beam will thus be filtered out by the SLM. Much higher efficiency can then be obtained using real space shaping technique.

(a) Phase and amplitude shaping with a phase-only SLM

We define $z_0 = 0$ to be the position of the SLM chip on the optical axis. By discretizing the electric field according to the SLM matrix ($N_x \times N_y$), the target electric field $\mathcal{E}(i, j, z = 0^+)$ (right after the SLM) can be decomposed in amplitude $\mathcal{A}(i, j)$ and phase $\Phi(i, j)$, where $0 \leq i \leq N_x$ and $0 \leq j \leq N_y$ are the pixel coordinates. As suggested by Davis *et al.* [134], locally reducing the phase wrapping contrast allows for a modulation of the light scattered in the first diffraction order, with a single hologram. We apply this method using a phase-only SLM. The expression of the SLM phase mask Ψ can always be written as follows:

$$\Psi(i, j) = \mathcal{M}(i, j) \bmod [\mathcal{F}(i, j) + \Phi_g(i, j), 2\pi]. \quad (5.21)$$

The function \mathcal{F} contains the phase information of the target electric field and Φ_g stands for the grating phase ramp, used to separate the different diffraction orders in Fourier space. The total phase, $\mathcal{F} + \Phi_g$, is wrapped by the modulo operation. The diffraction efficiency is locally tuned by the modulation function \mathcal{M} ($0 \leq \mathcal{M}(i, j) \leq 1$). The complex amplitude of the field diffracted in the first order can be expressed as follows [131, 132]:

$$\mathcal{E}_1(i, j, z = 0^+) = \mathcal{A}_{\text{in}}(i, j) \text{sinc}[\pi \mathcal{M}(i, j) - \pi] \exp[i(\mathcal{F}(i, j) + \pi \mathcal{M}(i, j))], \quad (5.22)$$

where \mathcal{A}_{in} is the amplitude of the incident laser beam on the SLM. By identifying \mathcal{E}_1 with the target electric field, one can obtain the functions \mathcal{F} and \mathcal{M} solving the system:

$$\mathcal{M}(i, j) = 1 + \frac{1}{\pi} \text{sinc}^{-1} \left(\frac{\mathcal{A}(i, j)}{\mathcal{A}_{\text{in}}(i, j)} \right), \quad (5.23)$$

$$\mathcal{F}(i, j) = \Phi(i, j) - \pi \mathcal{M}(i, j). \quad (5.24)$$

The inverse sinc function (sinc^{-1}) is defined on $[-\pi, 0]$ here. Computing this function at each points of the hologram is usually demanding ($N_x \times N_y$ operations). However, if both the incident and the first order diffracted beams are radially symmetric, we only need to determine the radial profile of the modulation function. For beams centered on the SLM chip, equation (5.23) can be simplified such that:

$$m(i) = 1 + \frac{1}{\pi} \text{sinc}^{-1} \left(\frac{\mathcal{A}(i, N_y/2)}{\mathcal{A}_{\text{in}}(i, N_y/2)} \right), \quad (5.25)$$

where i is an integer running from 0 to $N_x/2$ (we assume $N_x \geq N_y$ here). The modulation matrix \mathcal{M} can be fully reconstructed from m using a circular interpolation, which requires computing the inverse sinc function for $N_x/2$ points only instead of $N_x \times N_y$. In practice, we start by cleaning-up the incident laser beam, that is, by filtering out in Fourier space its high transverse wave-vector components thanks to a small pinhole aperture. The incident Gaussian beam is radially symmetric in the SLM plane afterwards ($\omega_{x,y} \simeq 3.3 \pm 0.1$ mm).

(b) Target on-axis intensity profile

In principle, arbitrary on-axis intensity profiles can be generated using the method above. In this paragraph, I introduce the target profile $\mathcal{I}(z)$ we use to maintain the central peak intensity constant along the propagation in a uniform and linear lossy medium. Let L and α stand respectively for the propagation length and the linear attenuation coefficient of the optical medium. According to the Beer-Lambert's law, the transmittance t of the medium decays exponentially with the propagation distance: $t = \exp(-\alpha z)$. Therefore, the on-axis intensity should exponentially increase along the z -axis, such that $\mathcal{I}(z) \sim \exp(\alpha z)$, in order to compensate for losses. We ramp the on-axis intensity up (from 0 to $\mathcal{I}(z_1) = \mathcal{I}_0$), until the entrance plane position z_1 , before making it exponentially increase over the distance L . We then bring it back to zero smoothly. The full on-axis target profile we designed can finally be described by the following equation:

$$\mathcal{I}(z) = \begin{cases} \mathcal{I}_0 \left[\frac{\sin(C_1 z / z_1)}{\sin(C_1)} \right]^2 & \text{if } 0 \leq z \leq z_1 \\ \mathcal{I}_0 \exp[\alpha(z - z_1)] & \text{if } z_1 \leq z \leq z_2 \\ \mathcal{I}_{\text{max}} \sin^2 \left[C_2 + \left(\frac{\pi}{2} - C_2 \right) \frac{z - z_2}{z_3 - z_2} \right] & \text{if } z_2 \leq z \leq z_3 \\ \mathcal{I}_{\text{max}} \sin^2 \left[\frac{\pi}{2} \left(1 - \frac{z - z_3}{z_4 - z_3} \right) \right] & \text{if } z_3 \leq z \leq z_4. \end{cases} \quad (5.26)$$

For all the measurements we performed, we set $z_1 G^2 = 1.5$ cm, $z_2 G^2 = z_1 G^2 + L$ and $z_4 G^2 = 3 z_1 G^2 + L$, where $G = 0.5$ stands for the telescope demagnification factor which optically conjugates the SLM chip and the plane $z = 0$. The constants C_1 and C_2 as well as z_3 are chosen in order to make the profile continuous and differentiable (see [102] for details).

In what follows, the target profile has been normalized to 1 dividing $\mathcal{I}(z)$ by the maximum intensity $\mathcal{I}_{\max} = \mathcal{I}_0 [1 + \exp(\alpha L)]$. The spatial spectrum associated to $\mathcal{I}(z)$ has been derived analytically in [102] using equation (5.20). As all the parts composing the target profile can be expressed either by an exponential rising function or a sine square function, computing the spatial spectra associated to the generic functions $\mathcal{I}_{\exp}^{i \rightarrow j}(z) = \mathcal{I} \exp[\alpha(z - z_i)]$ as well as $\mathcal{I}_{\sin}^{i \rightarrow j}(z) = \mathcal{I} \sin^2\left(a \frac{z - z_i}{z_j - z_i} + b\right)$ is enough. The derivation of the related spectra $\mathcal{S}_{\sin}^{i \rightarrow j}$ and $\mathcal{S}_{\exp}^{i \rightarrow j}$ is a bit laborious but straightforward; we only give the final result here:

$$\mathcal{S}_{\sin}^{i \rightarrow j} = \sqrt{\mathcal{I}} \frac{l}{k_z} \left[a \frac{\cos(a) - \cos(a+b)}{a^2 - (\delta k l)^2} - i \delta k \frac{\sin(a) e^{i \delta k z_i} - \sin(a+b) e^{i \delta k z_j}}{a^2 - (\delta k l)^2} \right], \quad (5.27)$$

$$\mathcal{S}_{\exp}^{i \rightarrow j} = -\sqrt{\mathcal{I}} \frac{2}{k_z} \frac{e^{i \delta k z_i} - \exp(\alpha l/2) e^{i \delta k z_j}}{\alpha + 2i \delta k}, \quad (5.28)$$

with $l = z_j - z_i$ and $\delta k = k_{z0} - k_z$. We obtain the spectrum adding the spectral contributions coming from the different parts of the profile: $\mathcal{S} = \mathcal{S}_{\sin}^{0 \rightarrow 1} + \mathcal{S}_{\exp}^{1 \rightarrow 2} + \mathcal{S}_{\sin}^{2 \rightarrow 3} + \mathcal{S}_{\sin}^{3 \rightarrow 4}$. The target electric field is finally derived by computing the inverse Hankel transform of \mathcal{S} with (5.18).

(c) Compensating for the refractive index stretching

When the linear refractive index n_0 of the medium is not equal to one – as it has implicitly been assumed in the preceding paragraphs – the target Bessel beam will undergo refraction at the medium entrance and output planes. From the Snell's refraction law, one finds that: $\sin(\theta_i) = n_0 \sin(\theta_r)$, where θ_i and θ_r stand respectively for the incident and refractive cone angles of a given Bessel mode. By introducing the transverse spatial wave-vector, that is, $k_{\perp} = n_0 k_0 \sin(\theta)$, we easily show that $k_{\perp}^{(i)} = k_{\perp}^{(r)}$. Therefore, according to equation (5.18), the transverse shape of the target Bessel beam is not modified by successive refractions [135]. Nevertheless, the cone angle does change, as soon as the Bessel beam enters the medium.

If $n_0 > 1$, the inner cone angle θ_r is smaller than the external one and the Bessel beam will cover a distance longer than in air. This stretching of the beam inside the medium will necessarily reduce the compensation coefficient by a factor n_0 . So as to counteract this effect, we constrict the exponentially rising part of the target on-axis intensity profile beforehand by a factor n_0 (as suggested in [130]). In other words, we replace L by L/n_0 and α by αn_0 in the second line of equation (5.26). By doing so, the stretching of the beam will compensate exactly the exponential attenuation in the medium, as sketched on figure 5.12. Indeed, using equation (5.20) and the change of variable $z \rightarrow \tilde{z} = n_0(z - z_1)$, one can derive the spectrum $\mathcal{S}_{\exp}^{1 \rightarrow 2}$ associated to the exponential rising part of the on-axis profile (between z_1 and z_2):

$$\begin{aligned} \mathcal{S}_{\exp}^{1 \rightarrow 2} &= \sqrt{\mathcal{I}_0} \frac{e^{i(k_{z0} - k_z) z_1}}{n_0 k_z} \int_0^L \exp(\alpha \tilde{z}/2) e^{i(k_{z0} - k_z) \tilde{z}/n_0} d\tilde{z} \\ &= -\frac{i}{n_0 k_z} \frac{\sqrt{\mathcal{I}_0} e^{i(k_{z0} - k_z) z_1}}{(k_z - k_{z0})/n_0 + i \frac{\alpha}{2}} \left(1 - e^{-i[(k_z - k_{z0})/n_0 + i \frac{\alpha}{2}]L} \right). \end{aligned} \quad (5.29)$$

The on-axis electric field $\mathcal{E}(r=0, z)$ is related to the spectrum \mathcal{S} by the Fourier transform of equation (5.19). Using (5.29) and (5.19) and the change of variable $\bar{k}_z = (k_z - k_{z0})/n_0$, we can derive the on-axis electric field $\mathcal{E}_{\exp}^{1 \rightarrow 2}(r=0, z)$ associated to $\mathcal{S}_{\exp}^{1 \rightarrow 2}$:

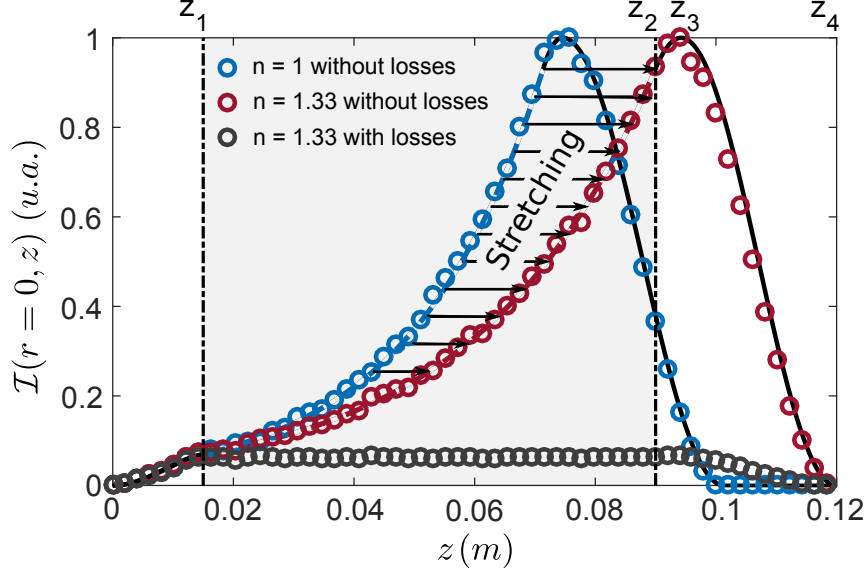


Figure 5.12: Numerical simulation of the longitudinal refractive index stretching of the on-axis target profile. When the medium refractive index n_0 is not equal to one, the calculated profile must be stretched by n_0 to compensate for refraction. Blue, red and grey circles are obtained by solving numerically the evolution of the Bessel beam in air (blue), in a lossless (red) as well as in a lossy material (grey) of refractive index $n_0 = 1.33$. The simulation data obtained for $n_0 \neq 1$ can be deduced from the data obtained for $n_0 = 1$ by stretching the z -axis by a factor n_0 between z_1 and z_2 . We adjust the exponentially growing section of the target on-axis profile (blue dotted line) such that the stretched Bessel beam ends up compensating for the good attenuation coefficient α . When losses are taken into account, the on-axis intensity remains constant all along the propagation inside the medium.

$$\mathcal{E}_{\text{exp}}^{1 \rightarrow 2}(r=0, \delta z) = \sqrt{\mathcal{I}_0} e^{i k_{z0}(z_1 + \delta z/n_0)} \times \left[\frac{-i}{\pi} \int_0^\infty \frac{1 - e^{-i[\bar{k}_z + i\alpha/2]L}}{\bar{k}_z + i\alpha/2} e^{i\bar{k}_z \delta z} d\bar{k}_z \right]. \quad (5.30)$$

As z lies in the interval $[z_1, z_2]$ and $z_2 = z_1 + L/n_0$, $\delta z = n_0(z - z_1)$ varies from 0 to L . The phase $\Phi_l = k_{z0}(z_1 + \delta z/n_0)$ is the phase accumulated by the Bessel beam along its propagation from z_1 to z_2 . Since the medium is supposed to be linear, this contribution is the only one we expect. The term inside the brackets in equation (5.30) should then be real. Let's divide the integral in two parts, I_1 and I_2 , as follows:

$$I_1(\delta z) = \frac{-i}{\pi} \int_0^\infty \frac{\bar{k}_z - i\alpha/2}{\bar{k}_z^2 + (\alpha/2)^2} e^{i\bar{k}_z \delta z} d\bar{k}_z \quad (5.31)$$

$$I_2(\delta z) = \frac{i}{\pi} \exp(\alpha L/2) \int_0^\infty \frac{\bar{k}_z - i\alpha/2}{\bar{k}_z^2 + (\alpha/2)^2} e^{-i\bar{k}_z(L-\delta z)} d\bar{k}_z. \quad (5.32)$$

From equations (5.31) and (5.32), we can derive the real parts of I_1 and I_2 : $\text{Re}(I_1) = 0$ and $\text{Re}(I_2) = \exp(\alpha\delta z/2)$. The on-axis electric field $\mathcal{E}_{\text{exp}}^{1 \rightarrow 2}(r=0, \delta z)$ is finally given by:

$$\begin{aligned}\mathcal{E}_{1,2}(r=0, \delta z) &= \sqrt{\mathcal{I}_0} e^{i k_{z0}(z_1 + \delta z/n_0)} \times [\text{Re}(I_1) + \text{Re}(I_2)] \\ &= -\sqrt{\mathcal{I}_0} e^{i k_{z0}(z_1 + \delta z/n_0)} \exp(\alpha\delta z/2).\end{aligned}\quad (5.33)$$

and exponentially increases, as required, over the propagation distance δz in the medium. By replacing L with L/n_0 and α with αn_0 in the expression of the target on-axis intensity profile equation (5.26), we therefore manage to counterbalance the refractive stretching of the Bessel beam and compensate for the good attenuation coefficient α .

ii Experimental setup

The experimental setup I built to generate attenuation-resistant Bessel beams has been depicted on figure 5.13. The continuous-wave laser beam produced by a TA Pro laser system is sent onto the optical table through a high power fiber. A polarized beam splitter (PBS), preceded by a half wave-plate ($\lambda/2$), splits the outgoing beam in two parts. The low power reflection is focused onto a photo-diode (PD) in order to monitor the stability of the fiber output power. The transmitted part is magnified four times using a telescope formed by two converging lenses of 50 and 200 mm focal lengths respectively. A small pinhole aperture is positioned in the focal plane of the 50 mm focal lens in order to filter out the high transverse wave-vector components of the Gaussian beam. After the telescope, the beam has a diameter of 6.6 mm and is perfectly radially symmetric. It reflects on the SLM chip, which is strictly perpendicular to the optical axis. The SLM used for the experiment is a liquid crystal on silicon phase-only modulator (LCOS), with an effective area of 1272×1024 pixels and a pitch of $12.5 \mu\text{m}$. Because of the grating imprinted on the SLM, the first order diffracted beam propagates at a small angle from the incidence axis. A succession of two telescopes – formed respectively by the lenses L_1 and L_2 on one side ($f_1 = 750 \text{ mm}$ and $f_2 = 150 \text{ mm}$) and by L_3 and L_4 on the other ($f_1 = 100 \text{ mm}$ and $f_2 = 250 \text{ mm}$) – conjugates the SLM chip and the $z = 0$ plane with a demagnification factor $G = 0.5$. In between the telescopes, a delay line as been set up in order to roughly position the starting of the exponential rising section in the entrance plane of the cell. Another translation stage, on which the mirrors M_1 and M_2 are mounted, allows the fine tuning of this positioning. The output plane of the medium is imaged by a 4-f arrangement onto a microscope objective which is set up on a computer controlled translation stage. By moving the objective along the optical axis, one can monitor the Bessel beam evolution along z . The last lens on the beam path images the plane we look at on the CMOS camera, positioned in the focal plane. The magnification factor G' of the whole imaging system is 13.6 ± 0.1 . An example of the Bessel beam transverse intensity distribution, captured close to the maximum of the target on axis profile ($z = z_3$), is shown on the inset (a) of figure 5.13. The hologram displayed on the SLM in order to obtain this image is shown on the inset (b) (for zero grating). Let's finally mention that the choice of the lenses L_1 , L_2 , L_3 and L_4 (and thus, of the demagnification factor G) is conditioned by the length of the lossy medium we deal with. For biological applications, G should at least be divided by 10, as pointed out in the following paragraph.

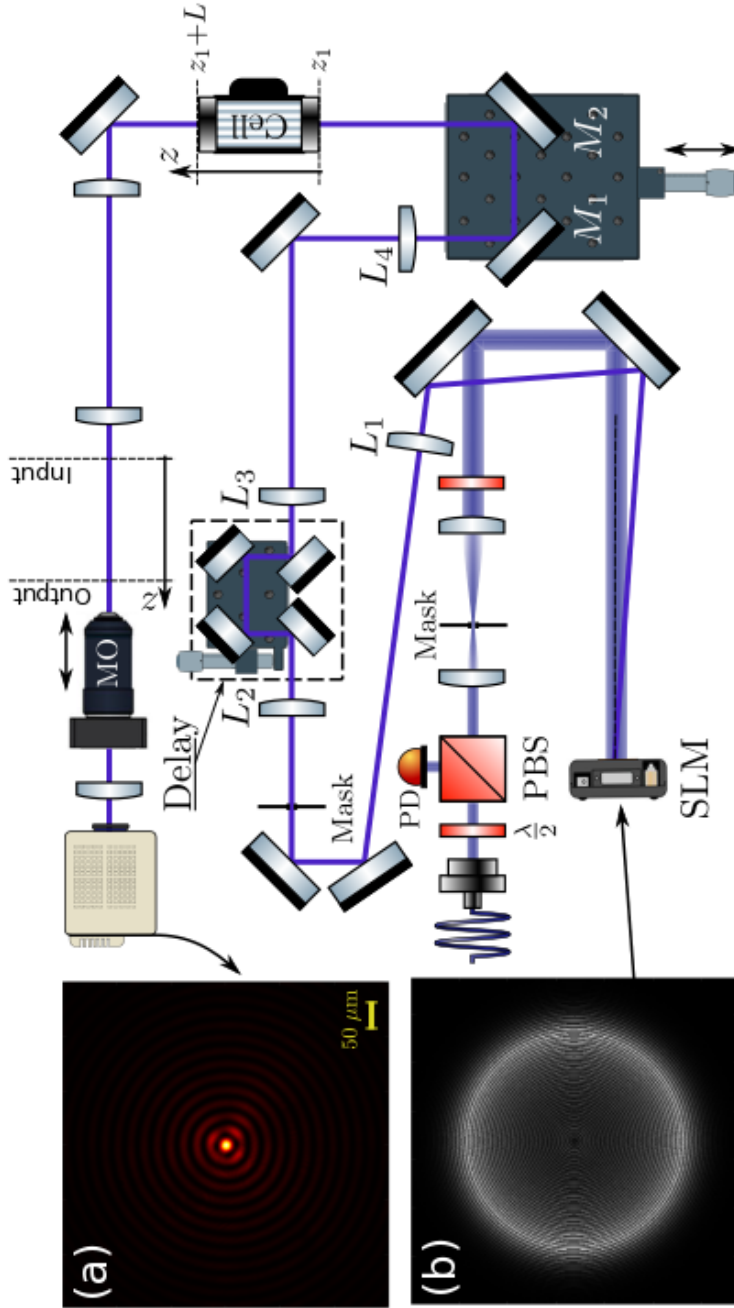


Figure 5.13: Experimental setup. The beam is magnified before reaching the SLM at normal incidence. An example of hologram displayed on the SLM is shown on inset (b) (without grating for clarity). The contrast of the phase wrapping is spatially modulated so as to shape the Bessel beam on-axis intensity. The first diffraction order is selected by filtering out the others in the focal plane of L_1 . The telescopes $\{L_1, L_2\}$ and $\{L_3, L_4\}$ conjugates the SLM chip with the cell entrance plane. The delay line and the translation stage (over which the mirrors M_1 and M_2 are fixed) allows to set precisely z_1 (starting of the exponentially rising section of the target profile) in the cell entrance plane. The output plane is imaged onto a microscope objective by a 4-f system. Moving the objective along the optical axis enables us to measure the on-axis profile. The transverse profile at z_3 of the generated Bessel beam is shown on inset (a).

iii Experimental results

The first step toward the on-axis compensation of attenuation is to check that the transverse and longitudinal intensity profiles of the experimentally measured Bessel beam (in air) fit the target ones, obtained by simulations. We design the target beam in order to compensate 96% attenuation over a lossy, 7.5 cm long medium. The 2D maps shown on figure 5.14(a) and the profiles of figures 5.14(b) and (c) are obtained by scanning slowly ($v = 2 \text{ mm.s}^{-1}$) the microscope objective along the z -axis. Both the transverse (blue circles on figure (b)) and the longitudinal profiles (blue line on figure (c)) of the measured Bessel beam are in excellent agreement with the target profiles (black dashed line). The latter are obtained by numerically solving the evolution of the transverse electric field from $z = 0$ to L with the second order split-step method. We take as initial condition a field with the SLM imprinted phase Ψ and the radially symmetric Gaussian envelope of the SLM input beam. In order to accurately determine the central peak intensity along z – as presented in figure 5.14(c) – we fit with a Gaussian profile the region delimited by the two white dashed lines on both sides of the central peak (figure 5.14(a)), as illustrated on figure 5.14(b) (red solid line). The width of the central peak, along the propagation, is found to be constant (at $\pm 5\%$), as shown on the inset of figure 5.14(b). This measurement demonstrates that we are able to control the longitudinal intensity profile without altering the non-diffracting behavior of the Bessel beam. More importantly, we observe, as required, an exponential increase of the on-axis intensity along z . Nevertheless, small intensity oscillations can be observed at the beginning of the measured on-axis profile on figure 5.14(c). They are basically due to high longitudinal frequency truncation [132], as k_z is upper bounded by the laser wave-vector k_0 . The oscillation amplitude can be reduced further by increasing the Bessel cone angle θ_0 .

The lossy medium is then positioned on the beam path. Fitting the on-axis intensity profile with the function (5.26) provides the position z_2 where the medium output plane should set. We then translates this position using the translation stage sketched on figure 5.13 until z_2 matches the medium output plane position on the optical axis. This plane is imaged on the camera using the imaging system described on figure 5.13. The 0.5 mm depth of field of the imaging system and the standard deviation on the fit parameters translate into a $\pm 1 \text{ mm}$ uncertainty on the medium output plane position. Three different media (contained in three different glass cells) have been used so as to determine if attenuation-resistant Bessel beams are capable of compensating attenuation along the optical axis. Two cells are filled with isotopically pure rubidium vapors (the first (7.5 cm long), with ^{87}Rb only, and the second (2.5 cm long), with ^{85}Rb only). The third one (2.5 cm long) contains a diffusive aqueous suspension of milk. Rubidium cells are heated up to 140°C . At this temperature, the atomic density is large ($n_a \simeq 2 \text{ to } 5 \times 10^{13} \text{ atoms/cm}^3$). By tuning the laser frequency ν_0 over the rubidium D_2 for instance, we can change the transmission over several orders of magnitude, without affecting significantly the refractive index of the vapor, which remains close one (with $\pm 1\%$ fluctuations). The transmission of the water-milk mixture can be tuned changing the milk concentration. Remaining under highly diluted condition, the medium refractive index stays close to the water one $n_w \simeq 1.33$. As explained above, we should balance in this case the change of refracting index stretching the Bessel beam along the optical axis, replacing beforehand in the target profile L and α with L/n and αn respectively.

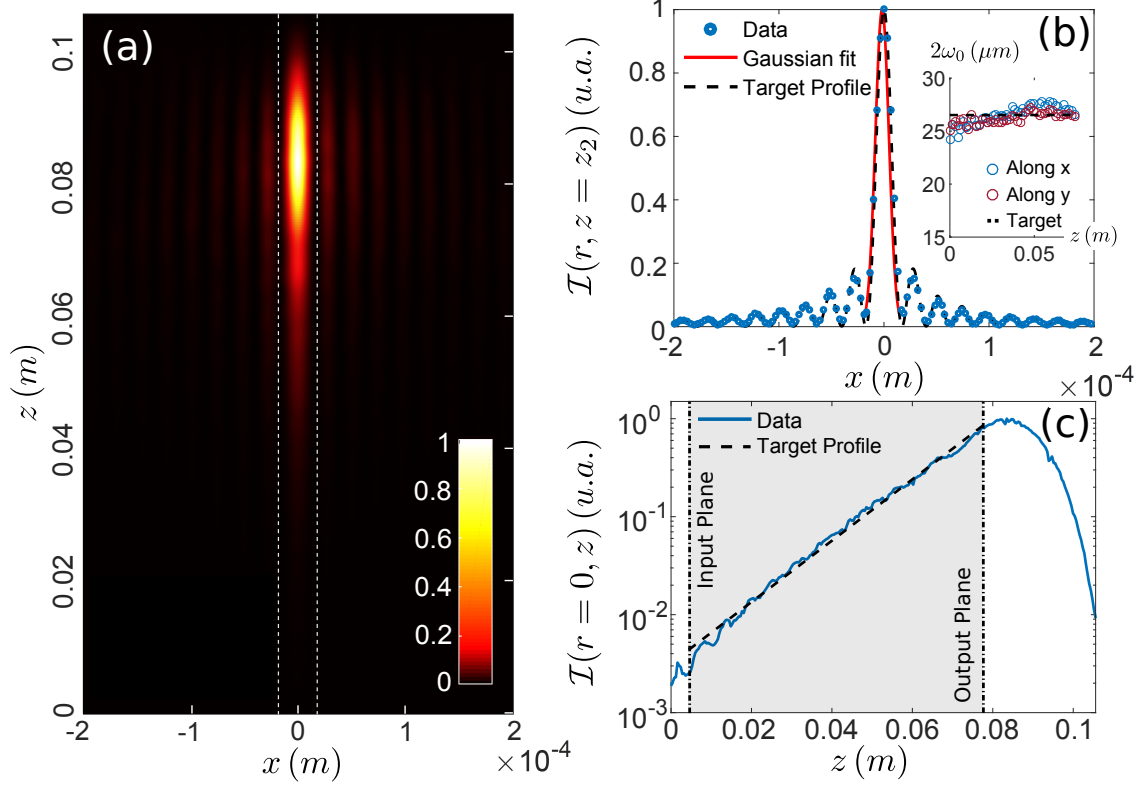


Figure 5.14: Experimental characterization of the reconstructed Bessel beam. The Bessel cone angle θ_0 was set to $(1/G) \times 8.5$ mrad, where $G = 0.5$ is the overall demagnification factor of the telescopes $\{L_1, L_2\}$ and $\{L_3, L_4\}$. The 2D map on figure (a) is obtained by scanning slowly ($v = 2$ mm.s $^{-1}$) the microscope objective along the z axis and capturing a frame every second. The white dotted lines on both sides of the central peak define the region where the Gaussian fit is performed. The transverse and longitudinal intensity profiles of the reconstructed Bessel beam have been plotted respectively on the figures (b) and (c), in the absence of lossy material. (b): Blue dots are experimental data obtained by cutting at $z = 8.5$ cm the 2D map (a). The dashed line is the target profile calculated numerically and the red solid line a Gaussian fit of the central peak, performed to extract its width. Inset: Dots are the fitted peak diameter $2\omega_0$ as function of z (blue along x and red along y). The black dashed line is the calculated target peak diameter. Data shows a change of less than 5% over the length of the medium ($L = 7.5$ cm), confirming the non-diffractive nature of the attenuation-resistant Bessel beam in the transverse plane. (c): The blue line is a cut of the 2D map (a) along the z -axis. It matches perfectly with the calculated on-axis intensity profile (black dashed line) in the region where it increases exponentially (shaded area).

We design the target profile in order to compensate attenuation over 7.5 cm long materials, whatever the length of the cell we use. The overall Bessel beam power is reduced to keep the input peak intensity \mathcal{I}_0 lower than the rubidium on-resonance saturation intensity \mathcal{I}_s ($\mathcal{I}_s \simeq 2.5 \text{ mW/cm}^2$ for linearly polarized light). We finally measure the peak intensity in the entrance plane (without cell) and in the output plane (with cell) in order to evaluate the on-axis transmission through the lossy medium. To do so, we perform the fit on five different images of the central Bessel spot with a 2D-Gaussian function. The measured transmission is shown on figure 5.15. The blue stars and the orange circles represent the experimental data obtained with the 2.5 cm and the 7.5 cm long vapor cells respectively. The grey diamonds are the data we get using the water-milk mixture. The 4% reflectivity of the cell windows has been taken into account. The black dashed line represents a perfect on-axis compensation (that is, an on-axis transmission of one). Most of the experimental points lie slightly under it. This small discrepancy comes from the input plane intensity measurements rather than from the output plane ones. Indeed, the on-axis intensity is oscillating in the medium input plane (as you can see for instance on figure 5.14(c)). Moreover, the relative position of the cell output plane with respect to z_2 (and thus of the input plane with respect to z_1) is known with a precision of $\pm 1 \text{ mm}$. This two factors together induce an uncertainty on the input intensity measurements that is reported on figure 5.15 (errorbars). The two red lines represent the transmission of a non-saturating collimated beam (computed using the Beer-Lambert law) through a 2.5 cm and a 7.5 cm long lossy material respectively.

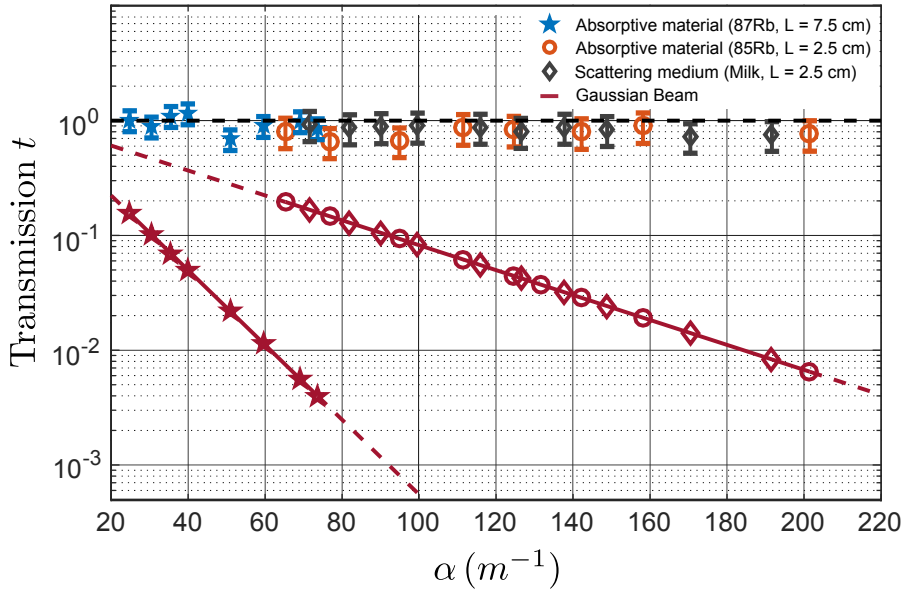


Figure 5.15: Measure of the on-axis transmission t of the Bessel beam as a function of the attenuation coefficient α . Data obtained with the rubidium vapors have been plotted in blue stars (^{87}Rb) and orange circles (^{85}Rb). Data obtained with the water-milk mixture have been plotted in grey diamonds. The two red lines show the transmission expected from the Beer-Lambert law through a 2.5 cm and a 7.5 cm long lossy material

iv Applications and limitations

In previous experiments, compensations of 10% and 30% attenuation have been achieved, using attenuation-resistant frozen waves and exicon (that is, exponential intensity axicon) respectively. In comparison, the method we developed allows compensation of attenuation coefficients up to 200 m^{-1} (which is equivalent to a transmission of 5×10^{-3} through a 2.5 cm long lossy material). This is a crucial advantage for light-sheet microscopy for instance, since the diffusive coefficients of biological tissues commonly observed with this technique range typically from 50 to 200 cm^{-1} [136, 137]. Indeed, using the same target profile as for the last orange circle on figure 5.15 (for which $\alpha \simeq 200 \text{ m}^{-1}$) and reducing the overall demagnification factor G by a factor 10 will constrict the length of the generated Bessel beam by a factor 100 (as it scales with G^2). Therefore, the latter will compensate for an attenuation coefficient 100 times bigger than the target one (that is, for $\alpha = 200 \text{ cm}^{-1}$), over a distance which is now $L/100 = 250 \mu\text{m}$. For such values of the attenuation coefficient, the penetration depth of our attenuation-resistant Bessel beam is therefore expected to be more than $100 \mu\text{m}$ longer than the best value reported in the literature so far [137], which would constitute an improvement of almost 170% of the current field of view inside highly diffusive samples.

Nevertheless, the non-diffracting feature of Bessel beams comes at the cost of the presence of high-energy side lobes, that are known to degrade the imaging contrast of fluorescence light sheet microscopy by inducing photo-bleaching [138]. For ideal zero-order Bessel beams, the intensity of the first ring surrounding the central spot is about 17% of the peak intensity. This can also be an issue in photon fluid experiments. If we use a Bessel beam as a defect, whether or not it compensates for attenuation, the rings around the central peak will also generate a change of refractive index. This creates, at the end of the day, a complex potential landscape for the photon fluid, that is not acting anymore as a spatially localized obstacle. We should thus think about a way to cancel the Bessel beam side lobes while preserving, at least, its non-diffracting feature. Following the work of G. Di Dominico *et al.* in [139], I will present in the next subsection a method based on the generation of "droplet beams", which are formed by making interfere two Bessel beams with specific cone angles θ_1 and θ_2 . For some values of the ratio θ_2/θ_1 , the intensity of the side lobes is significantly reduced. Obviously, droplet beams do not allow to compensate attenuation along the optical axis. Keeping the amplitude of the obstacle constant requires therefore to saturate the rubidium vapor with the droplet beam all along the optical axis.

5.2.3 Droplet beam

i Optimizing the side lobe cancellation

As mentioned previously, diffraction-free droplet beams are generated in practice by making interfere a set of plane-waves whose wave-vectors lie on two different co-axial cones of angles θ_1 and θ_2 respectively. For some specific values of the ratio θ_2/θ_1 , droplet beams exhibit significantly lower side lobes than simple zero-order Bessel beams, as a result of the selective destructive interference between the two Bessel fields forming a droplet. In order to find theoretically the ratio θ_2/θ_1 providing the minimum amount of power distributed over the droplet side-lobes, we can start by considering the generic expression describing the in-air electric field $\mathcal{E}(r, z, \theta)$ of a zero-order quasi Bessel beam of cone angle θ [119]:

$$\mathcal{E}(r, z, \theta) = \mathcal{E}_0 \frac{\omega_0(0)}{\omega_0(z)} J_0 \left(\frac{rk_r(\theta)}{1 + iz/z_r} \right) \exp \left\{ i \left[\left(k - \frac{1}{2} \frac{k_r^2(\theta)}{k} \right) z - \Phi_g(z) \right] \right\} \cdots \times \exp \left\{ \left[\frac{i}{2} \frac{k}{R(z)} - \frac{1}{\omega_0^2(z)} \right] \left[r^2 + \frac{k_r^2(\theta)}{k^2} z^2 \right] \right\}. \quad (5.34)$$

In formula (5.34), J_0 is the zero-order Bessel function of the first kind, r the radial coordinate and $k_r(\theta) = k \sin(\theta)$ the Bessel beam transverse wave-vector. We have also introduced the width $\omega_0(z) = \omega_0(0) \sqrt{1 + (z/z_r)^2}$ of the Gaussian envelope along the z -axis ($z = 0$ being the position of the waist and $z_r = \pi \omega_0^2(0)/\lambda$ the Rayleigh length), the radius of curvature of the beam wavefront: $R(z) = z [1 + (z_r/z)^2]$ as well as the Gouy phase shift: $\Phi_g = \text{atan}(z/z_r)$. The electric field of the droplet beam is then given by: $\mathcal{E}_d(r, z) = \mathcal{E}_1(r, z, \theta_1) + \mathcal{E}_2(r, z, \theta_2)$ and the total power distributed over its side-lobes, at $z = 0$, by:

$$\mathcal{P}_{d,sl} = 2\pi \int_{r_{\min}}^{\infty} |\mathcal{E}_1(r, 0, \theta_1) + \mathcal{E}_2(r, 0, \theta_2)|^2 r dr, \quad (5.35)$$

where r_{\min} is the radial distance associated to the first minimum in the intensity pattern. In [139], the authors compare the amount of power $\mathcal{P}_{d,sl}$ in the side-lobes of a droplet beam with the power $\mathcal{P}_{b,sl}$ in the side-lobes of a Bessel Gauss beam, having the same on-axis intensity. They compute, for different values of θ_2/θ_1 , the ratio $\mathcal{P}_{d,sl}/\mathcal{P}_{b,sl}$ at the waist position $z = 0$. In our case, we are more interested in the ratio between the droplet peak intensity \mathcal{I}_0 and the intensity \mathcal{I}_1 of the first side lobe, as we look for the value of θ_2/θ_1 for which it cancels. This ratio is plotted as function of θ_2/θ_1 on figure 5.16(a) (black line), for $z = 0$, where the droplet on-axis intensity is maximal.

As you can see, it exhibits a minimum close to $\theta_2/\theta_1 = 0.4$. One might then be tempted to choose this value for θ_2/θ_1 in experiments. However, the ratio between \mathcal{I}_0 and the intensity \mathcal{I}_{\max} of the brightest droplet side-lobe (blue line) exhibits, at $\theta_2/\theta_1 = 0.4$, a local maximum. We thus compromise, setting θ_2/θ_1 close to 0.5 (black arrow) in practice.

On the same graph, the axial FWHM of the Droplet beam, FWHM_d , has also been reported. It is normalized by twice the Rayleigh length $z_r(\omega_{0,d}) = \pi \omega_{0,d}^2/\lambda$, that is, by the axial FWHM of a focused Gaussian beam having a waist equal to the radial width $\omega_{0,d}$ of the droplet peak. As you can see, FWHM_d increases faster and faster with θ_2/θ_1 , until it reaches a maximum for $\theta_2/\theta_1 = 1$ (that is, when the droplet becomes a quasi Bessel beam with a cone angle θ_1). This behaviour can be intuitively understood as follows. The interference between the two co-axial Bessel fields forming the droplet beam modulates periodically its on-axis intensity. When θ_2/θ_1 decreases, the difference between the longitudinal wave-vectors of these two fields increases and makes therefore the axial extend of the droplet (*ie* FWHM_d) smaller. For $\theta_2/\theta_1 = 0.5$, $\text{FWHM}_d / (2z_r(\omega_{0,d})) \simeq 2$. Consequently, even if the axial FWHM of the droplet is smaller than for Bessel beams, it remains twice larger than the Gaussian one. This is of crucial importance. Apart from being perfectly collimated, unlike Gaussian beams, droplet beams allows to create much smaller defects, for a given cell length L , than their Gaussian homologs. In order to compare more visually the in-air propagation of a Gaussian, a droplet and a Bessel beams – having the same transverse width $\omega_{0,d}$ in the plane $z = 0$ – the theoretical intensity distributions of these three fields in the xz plane (top view) have

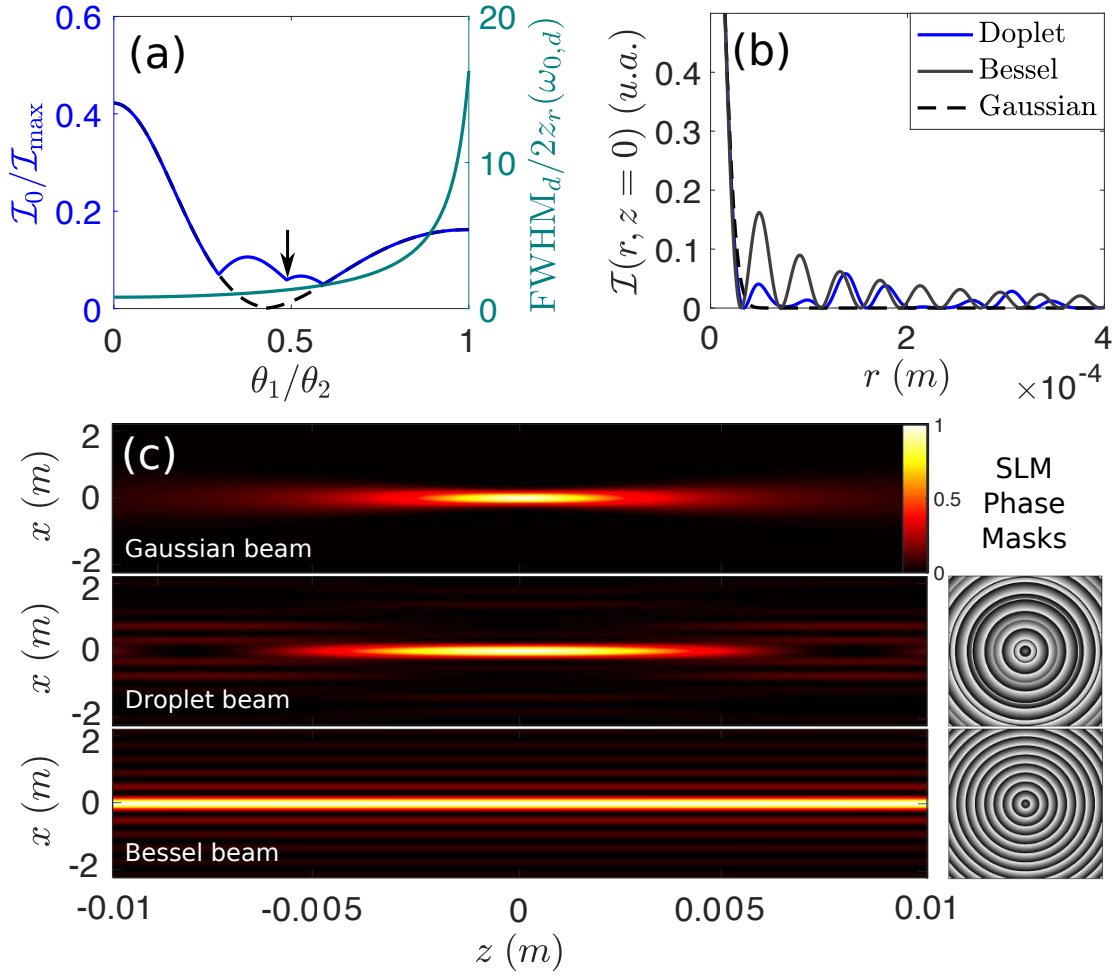


Figure 5.16: (a) Blue curve: plot of the ratio between the droplet peak intensity \mathcal{I}_0 and the intensity of the brightest side-lobe \mathcal{I}_{\max} as function of θ_2/θ_1 . Black dashed line: plot of the ratio between \mathcal{I}_0 and the intensity of the first side lobe \mathcal{I}_1 . Both curves are obtained for $z=0$. The axial FWHM of the droplet beam, FWHM_d , is plotted on the same graph (cyan curve) as function of θ_2/θ_1 . It is normalized by the axial FWHM of a Gaussian beam having a waist equal to the droplet radial width $\omega_{0,d}$, *ie*, by twice the Rayleigh length $z_r(\omega_{0,d}) = \pi\omega_{0,d}^2/\lambda$. The black arrow on figure (a) indicates the value we have chosen for the cone angles ratio in experiments ($\theta_2/\theta_1 \simeq 0.5$). Figures (b) and (c) show the transverse intensity profile and the in-air propagation (top view, xz plane) of a Gaussian, a droplet ($\theta_2/\theta_1 = 0.5$) and a Bessel-Gauss beam. They all have the same transverse width in the $z = 0$ plane ($\simeq 25 \mu\text{m}$). The intensities of the droplet first and second side-lobes have been reduced by 72% and 85% respectively with respect to the Bessel ones. On the right of figure (c), the phase masks displayed on the SLM in order to generate the droplet and the Bessel beams are shown. Parameters: for the droplet and Bessel beams, the width of the Gaussian envelope in (5.34) is $G \times 3.3 \text{ mm}$ and $G \times \theta_1 = 0.008 \text{ rad}$, where $G = 2/3$ is the overall demagnification factor of the telescopes conjugating the SLM chip and the cell input plane. Figure inspired from [139].

been plotted on figure 5.16(c). The quasi Bessel beam exhibits an invariant transverse profile along the propagation axis. Nevertheless, half of the energy it carries is distributed over its side lobes [139]. In contrast, the Droplet maintains an extended (but limited) depth of focus – which is twice longer than for the Gaussian beam – but provides a significantly enhanced energy confinement across the central peak. This is confirmed by figure 5.16(b), on which the radial profiles (at $z = 0$) of the three beams of figure 5.16(b) have been plotted. The amount of light in the first and second side-lobes is respectively 72% and 85% lower for the droplet than for the Bessel beam. Moreover, the intensity \mathcal{I}_{\max} of the brightest droplet ring is less than 6% of the peak intensity \mathcal{I}_0 , and, within a circle of $120 \mu\text{m}$ radius around the central peak, the intensity does not exceed 4% of \mathcal{I}_0 . All this suggests that droplets beams are good candidates to generate localized and collimated defects in photon fluid experiments.

ii Experimental results

The experimental setup we use to generate droplet beams is the same as the one sketched on figure 5.13. Only the focal lengths of the various lenses in 5.13 change. The overall demagnification factor of the telescopes conjugating the SLM chip and the cell entrance plane is now $G = 2/3$, while the magnification factor of the imaging system is 10.8 ± 0.2 . The width of the input Gaussian beam diffracting on the SLM grating is still about 3.3 mm. In contrast with what is done in [139], the droplet is obtained by shaping the phase of this Gaussian beam in real space directly. An example of grating displayed on the SLM to this end is shown on the right of figure 5.16(c). It is simply obtained by wrapping the phase of: $\exp[i\mathbf{k}_r(\theta_1) \cdot \mathbf{r}] + \exp[i\mathbf{k}_r(\theta_2) \cdot \mathbf{r}]$ ($\mathbf{k}_r(\theta) \cdot \mathbf{r}$ being the phase shift provided by an axicon to create a quasi Bessel beam with a cone angle θ). By moving the microscope objective along the z -axis (see figure 5.13), we can image the plane in which the droplet peak intensity is the highest (that is, the plane $z = 0$). Figure 5.17 shows the radial intensity distribution we measure in that case for different cone angles θ_1 . The data (purple circles) are obtained by radially averaging the 2D map on the top right corner of each graph. The radial profiles on figures 5.17(a) and (b) are obtained for $G \times \theta_1 = 8.0 \text{ mrad}$ and $G \times \theta_1 = 5.0 \text{ mrad}$. In both cases, the ratio θ_2/θ_1 is equal to 0.52. The target (theoretical) profiles have been plotted on both graphs in black solid. As you can see, the agreement between the expected and the measured radial intensity distributions is excellent. The side-lobes are correctly cancelled as required. The radial width, $\omega_{0,d}$, of the droplet peak when $G \times \theta_1 = 8.0 \text{ mrad}$ is $25 \mu\text{m}$ and $38 \mu\text{m}$ for $G \times \theta_1 = 5.0 \text{ mrad}$. In this last case, the longitudinal extent of the droplet beam is around 22 mm (against 8.4 mm when $G \times \theta_1 = 8.0 \text{ mrad}$, see figure 5.16(c)). This fits well with the length of the vapor cell we use in experiments, which is 2.5 cm long. Therefore, we choose the droplet beam obtained for $G \times \theta_1 = 5.0 \text{ mrad}$ to generate the obstacle in our photon fluids. It results indeed from the best balance we found between a small droplet radial width, a good side-lobes cancellation and a long droplet axial extent. This last point is actually what seriously restricts the choice of the parameters θ_1 and θ_2/θ_1 . Increasing the axial FWHM of the droplet by decreasing θ_1 comes at the cost of an increase in the beam radial width. Similarly, increasing it by raising up the ratio θ_2/θ_1 comes at the cost of an increase in the first droplet side-lobe intensity \mathcal{I}_1 , which is not suitable to produce a localized obstacle.

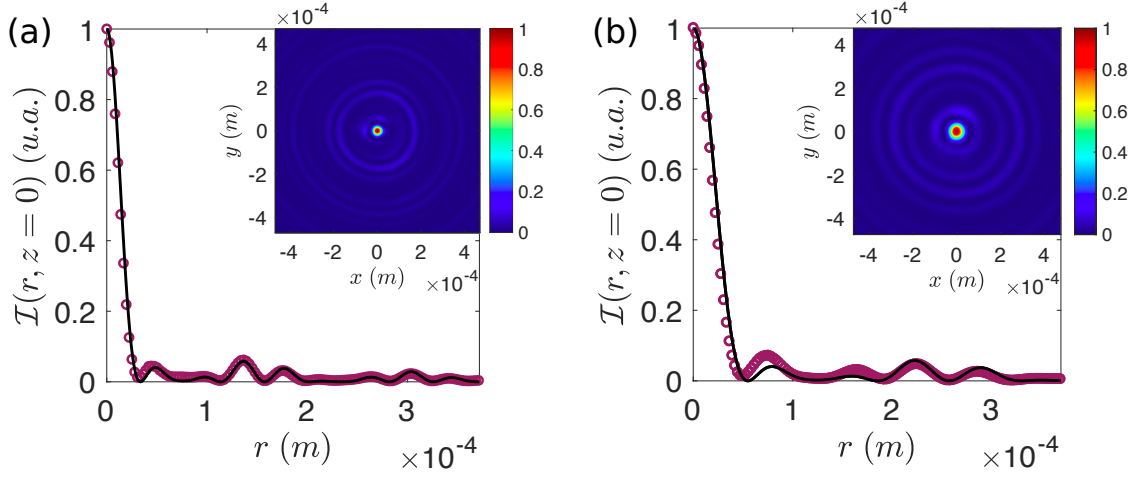


Figure 5.17: Comparison between the droplet target and measured radial intensity profiles. (a): $G \times \theta_1 = 8.0$ mrad and (b): $G \times \theta_1 = 5.0$ mrad. In both cases, we have set $\theta_2/\theta_1 = 0.52$. For $G \times \theta_1 = 8.0$ mrad, the radial width of the Droplet peak is $25 \mu\text{m}$. It is $38 \mu\text{m}$ when $G \times \theta_1 = 5.0$ mrad. The data (purple circles) are obtained by radially averaging the 2D intensity distributions plotted on the top right corner of each graph. These two images have been captured by translating the microscope objective of figure 5.13 along the optical axis until the droplet peak intensity was maximized. The overall magnification factor of the imaging system is equal to 10.8 ± 0.2 .

Chapter 6

Outlook - Probing superfluidity

In chapter 4, the measurement of the dispersion relation of density waves travelling onto paraxial photon fluids in warm rubidium vapor has been reported. I have shown that this dispersion relation exhibits a linear trend at low excitation wave-vectors. In other words, density waves travelling onto the photon fluid with those wave-vectors behave as collective phonons in the transverse plane, whose velocity is given by the speed of sound $c_s = \sqrt{n_2 \mathcal{I}_0}$. According to the Landau criterion for superfluidity, presented in subsection 2.3.3, c_s defines a critical speed v_c below which the photon fluid cannot theoretically dissipate energy by emitting sound-like excitations. In other words, a fluid of light moving toward an obstacle much smaller than the healing length ξ at a velocity lower than c_s should flow around it without scattering. In chapter 5, we saw how to generate such an obstacle in the photon fluid by locally changing the refractive index it experiences using non-diffracting droplet beams. Therefore, all the ingredients are there to observe in our system frictionless flows of light around an all-optical obstacle. In this section, I first give a short historical overview about superfluidity. I then briefly review the various theoretical methods proposed to probe it in paraxial photon fluids and comment recent results obtained by Michel *et al.* in [29]. I finally present some preliminary results I obtained using our platform.

6.1 Introduction and historical perspective

Superfluidity, that is, the ability of a fluid to move without any friction, is without any doubt one of the most striking phenomenon observed in many-body physics. It was first observed in 1934 in liquid helium-4 [140] and has given rise since then to a huge amount of theoretical and experimental studies, as with liquid helium-3 [141] or ultra-cold atomic vapors [142]. In those systems, superfluidity (as Bose-Einstein condensation) manifests itself when the bosons forming the quantum fluid are cooled down below some critical temperature at which it undergoes a transition from normal to superfluid. At very low temperatures, the De Broglie wavelengths of atoms is of the order of the inter-atomic spacing. This delocalization allows to describe the fluid with a single macroscopic wave-function, which plays the role of an order parameter in the Ginzburg-Landau theory of phase transitions [62]. The dynamics of the weakly interacting bosons can then be described – in the mean field approximation – by the Gross-Pitaevskii equation (named after E. P. Gross and L. P. Pitaevskii) which drives the space-time evolution of the order parameter. As we saw in chapter 2, this equation is analogous to the nonlinear Schrödinger equation. Photon fluids share consequently strong similarities with atomic Bose Einstein condensates or superfluid helium. The possibility to observe superfluid motion of light was initially suggested by Y. Pommeau and S. Rica [143] and further investigated by Chiao *et al.* [9] in Kerr mediums embedded in optical cavities. Experimental observations of superfluid flows of light were reported few years later in exciton-polariton condensates [14, 15]. Recently, the first clear evidence of superfluidity in cavityless systems has been reported by Michel *et al.* in [29]. A brief review of their work is presented in subsection 6.2.2.

As mentioned earlier, the most common way of probing superfluidity in photon fluids is to introduce a spatially localized defect into the flow and look at the perturbations it generates. In exciton-polariton experiments, defects of different sizes and shapes appear naturally in the growth process of microcavity samples. In paraxial fluids of light, the obstacle has to be created by changing locally the refractive index of the nonlinear material either by using an other light source [29], or by directly installing a piece of dielectric inside the medium [28]. Depending on the relative value between the flow velocity and the speed of sound, various nonlinear hydrodynamical phenomena can be observed. At low velocity, the flow remains practically unaffected by the obstacle [15], which is the hallmark signature of superfluidity. When the flow speed matches the critical velocity, quantized vortices start being nucleated, as reported in excitons-polariton [16, 144] and in cavityless systems [28]. These vortices are topological phase singularities characterized by a quantized circulation. They appear right after the breakdown of superfluidity. At high velocity, the Cherenkov emission of Bogoliubov waves as well as the generation of dark solitons have been observed [17, 145]. Nevertheless, in most of the experimental studies cited above, quantitative measurements probing the fluid/superfluid threshold are missing. It would be interesting, for instance, to measure the effects of the defect diameter and height on the critical speed. This requires however to develop a robust technique to measure the flow velocity v at which the transition from normal to superfluid occurs. In the following section, I thus briefly review the methods used so far to characterise this threshold.

6.2 Flow of light around an all-optical defect

As mentioned before, probing superfluidity in paraxial photon fluids requires to generate a local variation of refractive index – acting as an obstacle – all along the Kerr medium and to study how the fluid flows around. The purpose of this section is to provide a short overview of the various flow regimes we can observe in that case by tuning the parameters, namely, the flow velocity, the fluid density and the defect width and height. A complete description of the variety of phenomena observed past an obstacle in photon fluids can be found in [19,56]. Throughout all this chapter, the **probe** names the beam forming the **photon fluid**.

6.2.1 Theory and simulations

Throughout this subsection, I consider that the fluid of light is formed by a wide and intense Gaussian probe propagating (in the transverse plane) toward a spatially localized obstacle, located at $\mathbf{r}_\perp = \mathbf{0}$. This obstacle is generated by a Gaussian-shaped modulation δn of the refractive index of the form:

$$\delta n = \delta n(0) \exp[-(r_\perp/\omega_{0,d})^2]. \quad (6.1)$$

I suppose that the on-axis change of refractive index does not depend on the propagation distance z inside the medium. This condition is fulfilled experimentally if the droplet beam forming the defect saturates the rubidium vapor across the entire cell. The z -evolution of the probe field envelope \mathcal{E}_0 can be described using the nonlinear Schrödinger equation (2.9). From the hydrodynamical perspective, it is as if the probe beam was flowing toward the defect at a velocity $\mathbf{v} = \mathbf{k}_\perp/k_0$ (where $\mathbf{k}_\perp = k_0 \sin \theta_i \mathbf{e}_x$ is the probe transverse wave-vector). In order to illustrate the various flow regimes of the photon fluid in this configuration, I solve the NLSE using a second-order split step method. The intensity distribution of the probe beam at the medium output plane is shown on figure 6.1, for different sets of parameters. The series of images (a1)-(a4) are obtained at high probe power, while the series (b1)-(b4) show the results of the simulation at low probe power, that is, in the quasi-linear regime. On all these figures, the background fluid flows rightward. Its density has been subtracted. The probe creates a nonlinear refractive index change of 2.0×10^{-5} that yields a healing length of about $30 \mu\text{m}$ and a speed of sound c_s of 4.5 mrad . The obstacle is located at $\mathbf{r}_\perp = \mathbf{0}$ (white circle). Its width $\omega_{0,d}$ is equal to the healing length ξ and $\delta n(0) = 25 \times \Delta n$.

Let's first focus on the series (b1)-(b4). On figure (b1), the photon fluid is at rest ($v = 0$). The concentric rings visible on this image are spherical waves emitted from the defect in the medium entrance plane. We could observe the formation of a similar pattern by throwing a stone in standing water. As you can notice, spherical waves are not anymore centered on the defect location on figures (b2), (b3) and (b4). The flow velocity is non-zero on these images and steps up from left to right. Spherical waves are therefore dragged rightward with the flow in that case. At non-zero fluid velocities, we also observe the formation of well contrasted fringes upstream from the obstacle. This is due to interferences between the incoming fluid and the light back-scattered by the defect.

On figure (a1), the photon fluid is at rest but its density is much higher than on figure (b1). Spherical waves are also emitted in that case. However, they travel in the transverse plane at a speed greater than or equal to the sound velocity c_s . This explains why a region of uniform intensity surrounds the defect on figure (a1). This is also clearly visible on the inset profile,

showing a cut of the intensity distribution along the x -axis. On figure (a1), the flow velocity is sub-critical ($v < v_c$). In that case, the fluid flows around the obstacle without any friction. In other words, the incident light is not scattered by the obstacle in that case. The absence of interference fringes upstream from the defect as compared to the linear case (see figure (b2)) is a hallmark signature of superfluid flow of light.

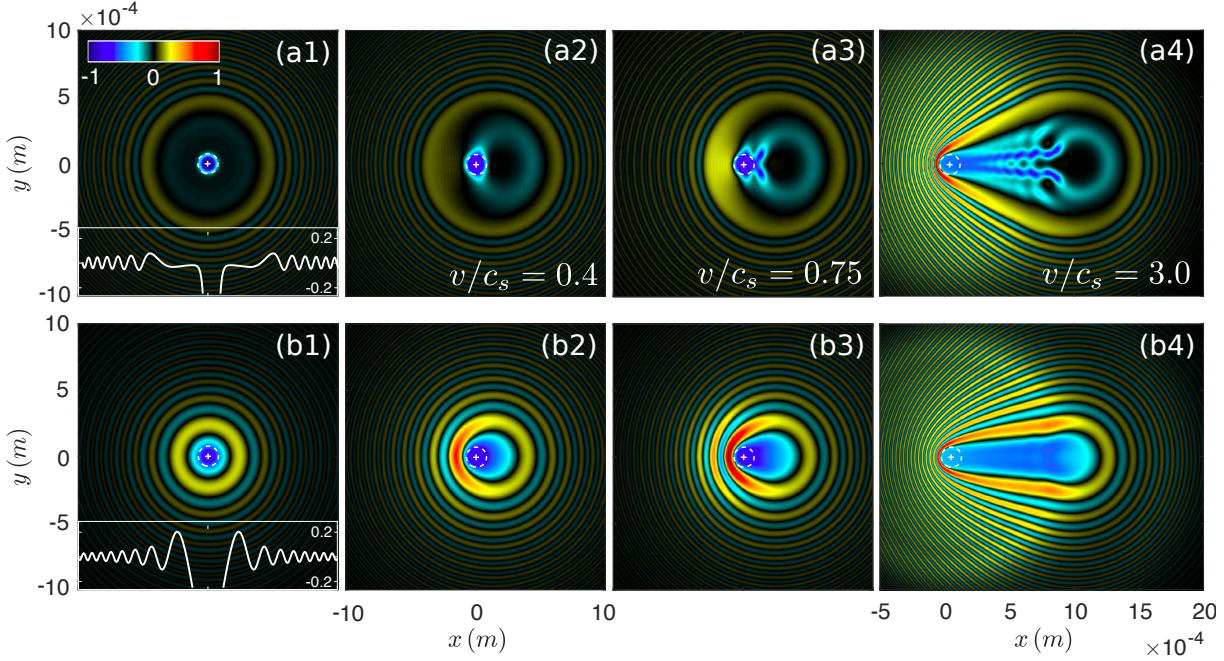


Figure 6.1: Near-field scattering patterns at high (a) and low (b) background densities for $v/c_s = 0$ (1), $v/c_s = 0.4$ (2), $v/c_s = 0.75$ (3) and $v/c_s = 3.0$ (4). The images (a2)-(a4) show some of the most significant examples of the intensity distribution in the exit plane. On all the images (except (a1) and (b1) where the fluid is at rest), the flow goes rightward. (a2): Superfluid regime. The photon fluid moves toward the obstacle (white dotted circle) at a speed lower than the critical velocity and flows around without any friction. This results in a cancellation of the interference fringes upstream from the obstacle. Those fringes are, reversely, well contrasted in the linear regime (figure (b2)). (a2): Breakdown of superfluidity. A pair of quantized vortices is visible downstream from the obstacle. The amount of light back-scattered by the defect remains much lower than in the linear case (see figure (b2)). (a3): Highly turbulent regime. The flow is super-critical (*ie* $v > v_c$). A Cherenkov cone of aperture $\sin(\theta) = c_s/v$ forms downstream from the obstacle in that case. On the contrary, in the linear regime (figure (b3)), the fringes resulting from the interference of the incident and scattered light exhibit a standard parabolic shape. Inside the Cherenkov cone, pairs of oblique solitons are emitted downstream from the obstacle and end up breaking in quantized vortex/anti-vortex pairs. Parameters: The width of the background beam is 2.0 mm and its on-axis intensity is $\mathcal{I}_f = 2.0 \times 10^5$ W/m². The nonlinear refractive index n_2 is equal to 1.0×10^{-10} m²/W, and thus, $\Delta n = 2.0 \times 10^{-5}$. Consequently, $\xi \simeq 30$ μ m and $c_s \simeq 4.5$ mrad. Finally, we set $\omega_{0,d} = \xi$ and $\delta n(0) = 25 \times \Delta n$. The nonlinear medium is 7.5 cm long.

On figure (a3), the speed of the flow matches the critical speed. A pair of quantized vortices (blue spots) is nucleated downstream and starts being dragged by the flow. The image (a3) is therefore obtained right before the breakdown of superfluidity. As you may have noticed, the flow velocity at which this occurs is not equal to but slightly lower than c_s ($v/c_s = 0.75$). This effect has been reported in [146]: in the vicinity of an extended defect (*ie*, when $\xi \lesssim \omega_{0,d}$) the local flow velocity becomes super-critical close to the obstacle, even in the case where the flow is sub-critical (*ie* $v < c_s$) far away from it. This is due to the local bending of the streamlines around the extended defect, which locally modifies the flow velocity of the fluid. We consequently expect the critical speed to depend on the fluid velocity as well as on the defect width. This dependence is illustrated on figure 6.2, where the phase diagram obtained by scanning v and $\omega_{0,d}$ has been sketched. The critical speed $v_c(v, \omega_{0,d})$, represented by the thick black line, separates the superfluid phase (I) to the regime where quantized vortices are generated (II). By increasing continuously the defect size at fixed flow velocity (red line, $v/c_s = 0.75$), we can thus probe the transition from phase (I) to phase (II).

Figure (a4) illustrates the strongly turbulent regime observed at high flow speeds. Two trains of oblique solitons are formed past the obstacle. They end up breaking in pairs of quantized vortices with opposite vorticities. We can also notice the cone-shaped structure of the fringes arising from the interference of the incoming and scattered light downstream from the defect. This effect can be interpreted as a result of Cherenkov radiations of Bogoliubov excitations by the obstacle [56] (hence the name of "Cherenkov cone"). The cone angle is related to the sound velocity by the formula: $\sin(\theta) = c_s/v$. On figure (b4), the intensity distribution in the exit plane obtained at low background density is plotted for the same flow velocity as on (a4). In that case, the interference fringes exhibit a standard parabolic shape.

6.2.2 Probing the superfluid phase transition

The ways of tracking superfluidity in photon fluids are manifold. In this subsection, I review some of the experimental methods developed so far for this purpose.

- The detection of quantized vortices in the wake of an obstacle is commonly considered as a hallmark signature of superfluidity. This is the method I use to numerically probe the transition from phase (I) to phase (II) in figure 6.2. The observation of such vortices has been reported in exciton-polariton systems [16, 144] and more recently in paraxial photon fluids [28]. The dimension of vortices is of the order of the healing length [28], which is typically few tens of microns in our experiment. Therefore, using standard spatial phase interferometry is enough to locate vortices in our system, which makes photon fluids a promising toolbox for studying vortex nucleation in superfluid light.
- As we saw in the previous section, the elastic scattering on the defect at low background densities is no longer expected to occur at high densities (when $v < v_c$), because the light becomes superfluid. Therefore, at the superfluid transition, the amount of light scattered by the defect should sharply drop. This can either be measured in real space (see subsection 6.2.3) or in Fourier space, by measuring the power distributed over the so-called Rayleigh ring. Amo *et al.* have experimentally demonstrated the collapse of this scattering ring at the normal/superfluid threshold in [15]. In the subsection 6.3.2, examples of Rayleigh rings generated by the scattering of the photon fluid on our all-optical defect are shown (see for instance figure 6.7(a)).

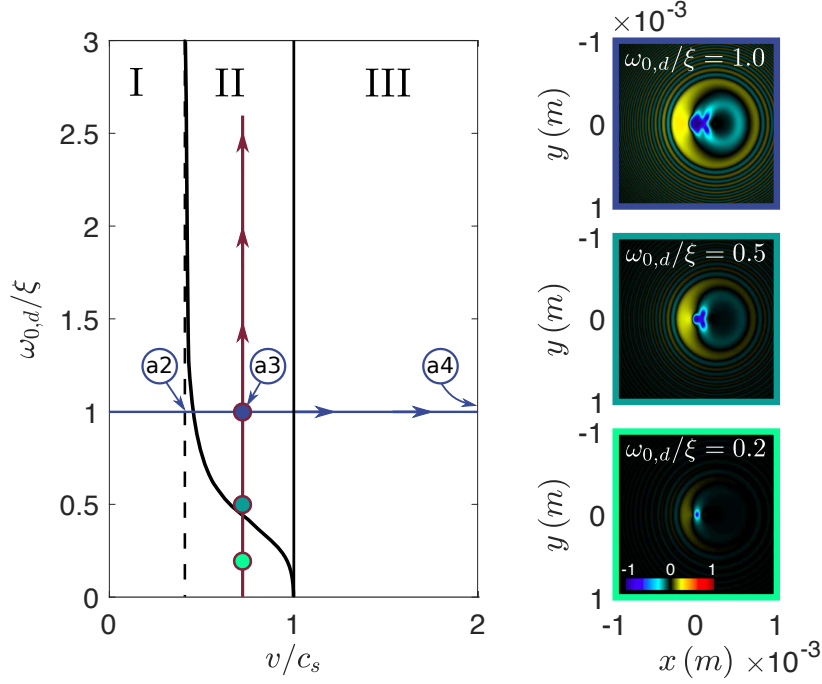


Figure 6.2: Phase diagram obtained by scanning the flow speed v and the defect width $\omega_{0,d}$. This diagram splits into three different regions: I, II and III. The first one (I) corresponds to the superfluid phase alone, the second one (II) to the regime where quantized vortices are nucleated onto the superfluid and the third one (III) to the supersonic and turbulent regime. By scanning the defect width a fixed background density and flow velocity, we can probe the transition from phase I to II (red line). Indeed, when $\omega_{0,d}/\xi = 0.2$ (green-framed image), the fluid flows around the defect without neither scattering nor emitting vortices, which is not the case at larger defect width (cyan- and blue-framed images). Reversely, we can fixed the defect size and scan the flow velocity (blue solid line). In that case, both the transitions I/II and II/III are probed. This is what has been done on figures 6.1(a1)-(a4) for instance. The simulation parameters are the same as for figures 6.1.

- In quantum fluids, the normal/superfluid transition is usually observed through the drop of the drag force exerted by the quantum fluid on a movable obstacle [147–150]. Following theoretical works studying the cancellation of the drag force in superfluid exciton-polariton condensates [151–154], Larré *et al.* have recently proposed a concrete way of measuring it in propagating photon fluids [101]. As mentioned in their paper, the propagating geometry offers the possibility of using movable and/or deformable obstacles by directly immersing a piece of dielectric (a rod) in the nonlinear material. The local variation of the fluid density around the dielectric generates a force on the obstacle which, by moving backward, induces a spatial variation of the liquid pressure. The joint action of both these effects results in a total force per unit area acting on the defect that is proportional to the upstream/downstream variation of the fluid density. Larré *et al.* predicts that this force linearly increases with the background density in the normal regime before suddenly dropping to zero when reaching the superfluid one.

However, installing a piece of dielectric inside a nonlinear medium is a challenging task in practice. In subsection 6.3.3, I briefly present a way of doing it in rubidium vapors. An alternative is to generate the defect optically – as we do using droplet beams – and try to measure the optical analog of the drag force cancellation by measuring either the upstream/downstream variation in the intensity, $\mathcal{I}_+ - \mathcal{I}_-$, or directly the defect displacement in the output plane of the medium. This is what Michel *et al.* have done experimentally; they report in [29] the first clear evidence of superfluid flow of light in the paraxial geometry. The following subsection is a review of their work.

6.2.3 Comments on the results of Michel *et al.*

As mentioned previously, Michel *et al.* report in [29] two distinct experimental evidences of the normal/superfluid transition occurring in their propagating fluid of light. They use a 1 cm long photo-refractive crystal (SBN:61) as Kerr medium in their experiment. The defect is generated by saturating the crystal with an intense Bessel beam whose central core radius is about $6\mu\text{m}$. The on-axis refractive index depletion $\delta n(0)$ it creates is equal to -2.2×10^{-4} . The photon fluid is formed by a Gaussian probe whose width is $270\mu\text{m}$. The fluid intensity, \mathcal{I}_f , can be tuned from 0 to 350 mW/cm^2 and the flow velocity, v , from 0 to $\pm 1.3 \times 10^{-2}\text{ mrad}$.

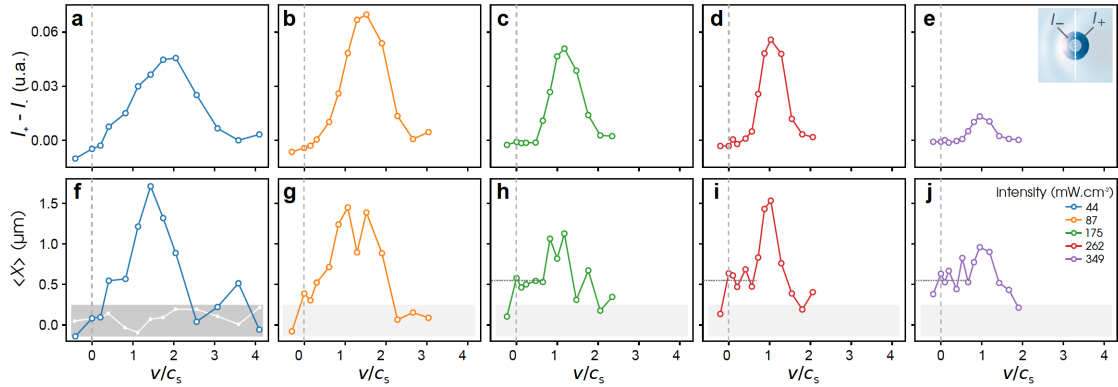


Figure 6.3: Results obtained by Michel *et al.* in [29]. Figures (a-e): Local intensity difference $\mathcal{I}_+ - \mathcal{I}_-$ measured at the exit plane of the photo-refractive crystal they use in experiments as function of v/c_s , for different values of the fluid intensity \mathcal{I}_f . The basic measurement idea is illustrated on the inset of figure (e). The original image is cropped around the obstacle and the intensity is averaged over two regions of space, downstream (\mathcal{I}_-) and upstream (\mathcal{I}_+) from the defect. At low background densities (figures (a) and (b)), $\mathcal{I}_+ - \mathcal{I}_-$ starts increasing from $v/c_s = 0$ while at high densities (figures (c) to (e)), a plateau forms at low flow speeds, which ends when v matches the critical speed v_c . This is a clear signature of superfluidity. Michel *et al.* go further by probing the transverse displacement $\langle X \rangle$ of the obstacle induced by the local variations in the intensity of the background fluid for the same input conditions as for figures (a) to (g). The results are shown on figures (f) to (j). While the defect starts being dragged with the flow from $v/c_s = 0$ on (f) and (g), its position remains unchanged at low flow velocities on (h) and (i). This constitutes a hallmark signature of the cancellation of the drag force exerted by the fluid on the obstacle at the normal/superfluid transition.

When the fluid power is maximum, Δn is about 1×10^{-4} which yields $\xi \simeq 6.2 \mu\text{m}$. Therefore, the defect is always smaller than or equal to ξ in the experiment carried out by Michel *et al.*

Figure 6.3, taken from [29], shows the results they obtained using the configuration above. On figures (a-e), the intensity variation $\mathcal{I}_+ - \mathcal{I}_-$ at the crystal exit plane is plotted as function of v/c_s for various probe intensities. At low background densities (see figures (a) and (b)), $\mathcal{I}_+ - \mathcal{I}_-$ increases from $v/c_s = 0$. In other words, as soon as the flow velocity is non-zero, the obstacle starts being dragged by the fluid. On the contrary, at high background densities, (see figures (c), (d) and (e)), a plateau at $\mathcal{I}_+ - \mathcal{I}_- = 0$ clearly forms at low flow velocities, which indicates that the drag force exerted by the fluid on the obstacle vanishes in that case. This demonstrates that light is superfluid deep in the subsonic regime. As mentioned in [29], the curves obtained at different intensities do not fall on a single universal curve, although the flow velocity is normalized on each graph by the related speed of sound. This is expected, as changing the probe intensity affects both the healing length and the relative strength of the obstacle with respect to the nonlinear change of refractive index, *ie* the ratio $\delta_n(0)/\Delta n$. This index matching effect may explain why the maximal amount of scattered light on figure (e) is much lower than on figures (a)-(d). When $\mathcal{P}_f = 349 \text{ mW}$, Δn is of the order of 1.0×10^{-4} which yields $\delta_n(0)/\Delta n \simeq 2$. The defect then only induces a perturbative potential. This is why it is barely visible at high fluid power on the image 2(c) of [29]. Nevertheless, index matching can not explain the plateau observed on figures (a)-(e) that really constitute a clear signature of superfluidity.

In order to go further, Michel *et al.* have measured the position $\langle X \rangle$ of the obstacle at the crystal exit plane, as function of v/c_s still, for the same probe intensities as on figures (a-e). The method used to that end is described in details in the supplementary materials of [29]. I thus only comment the experimental results obtained with this second technique, that are shown on figures (f-j). As you may have noticed, the position of the defect at the exit plane starts drifting from $v/c_s = 0$ at low background densities, on figures (g) and (h). Reversely, it remains constant at low flow velocities on figures (h) and (i), where the density is higher. Nevertheless, the defect displacement does not cancel exactly in that case, even deep in the subsonic regime. This surprising effect is not explained in text. However, the results are still in good agreement with those in figures (a-e). For example, the critical speeds in (c) and (d) correspond fairly well to the ones measured in (h) and (i). It would have been interesting to see if the motion of the defect in real space leads additionally to a drift of the ring-shaped far-field intensity distribution of the Bessel beam forming the obstacle. If it is the case, this could have provided a easier way of probing the normal/superfluid transition.

6.3 Preliminary results

In this section, I present the preliminary results we obtained recently using droplet beams to generate an all-optical defect into our photon fluid. I first describe the experimental setup before showing images of the scattering patterns we observe both in real and in Fourier space. In this latter case, we measure the amount of light scattered into the Rayleigh ring at various flow velocities and show that it quickly drops with the fluid intensity passing some threshold. However, the reasons underlying this phenomenon are still not clear. It could arise from superfluidity as well as from the reduction of the obstacle strength at high fluid intensities because of saturation. The results shown in this section should thus be viewed with caution.

6.3.1 Experimental setup and settings

The experimental setup is sketched on figure 6.4. The way the defect beam (blue) is created is described in subsection 5.2.3. I will therefore not comment the blue path here. For details, please refer to figure 5.13. The probe (red) is a continuous-wave laser beam produced by the Ti-Sapphire laser source of subsection 2.1.2. It is sent onto the optical table through a single-mode polarization-maintaining fiber. The power of the outgoing beam can be tuned turning the half wave-plate facing the fiber output. The probe beam is magnified four times, reflects onto the mirror M_3 (hold in a piezo-actuated mirror mount) and gets inside the Mach-Zehnder interferometer afterwards. The latter is, as usual, protected against air flows by a box made of Plexiglas (which greatly enhances the interferometer stability). A small part of the probe beam is transmitted by the PBS while the remaining high power part is reflected toward the cell. The transmitted beam (referred to as the reference from now on) provides the reference we need to retrieve the phase of the probe beam at the medium output plane. It reflects onto a mirror mounted on a piezo-actuated translation stage (PEM). Scanning the high tension applied across the piezo allows to modulate the length of the reference arm and thus to scan over 2π the relative phase between probe and reference. The probe and the defect beams enter together inside the 2.5 cm cell, filled with a pure vapor of rubidium 85. In this configuration, they are co-propagating. The photon fluid generated by the probe flows toward the defect at a velocity $\mathbf{v} = \mathbf{k}_\perp/k_0$, where $\mathbf{k}_\perp = k_0 \sin(\theta_i)\mathbf{e}_x$ stands for the probe transverse wave-vector. In this experiment, the z -axis is defined by the propagation direction of the defect beam. The piezo-actuated mount of M_3 allows to finely tune the angle θ_i between probe and defect. The cell exit plane is imaged onto the CMOS camera using the imaging system described in subsection 5.2.3. The overall magnification factor is $G = 10.8 \pm 0.2$. A dichroic bandpass filter (DF) – whose center wavelength is 780 nm – filters out the defect beam, which addresses the rubidium D_1 line ($\lambda_d \simeq 795$ nm). In this way, only the scattering pattern created by the obstacle onto the photon fluid is captured.

At the time at which preliminary data were acquired, a clear understanding of the mechanism underlying the generation of the refractive index modulation in the photon fluid was missing. We thus chose the laser detunings in order to fulfill certain basic conditions. We first want the defect to be collimated inside the cell. We then look for a detuning Δ_d at which the variation of the droplet width between the input and output planes does not exceed 10%. We also want the height of the repulsive potential δn to be as large as possible of course. In experiments, the vapor temperature is about 140°C and the probe is 2.0 GHz red-detuned from the $F = 3 \rightarrow F'$ transition of the ^{85}Rb D_2 line. In that case, we empirically find that the best was to blue-detune the defect beam from the $F_g = 3 \rightarrow F_e = 3$ transition of the ^{85}Rb D_1 line by 400-500 MHz. I would like to mention here that an isotopically pure vapor of rubidium 87 is more suitable to perform this experiment. Indeed, the vapor we used contains a small but non-zero fraction of ^{87}Rb atoms, which are almost at resonance with the probe beam when it is 2.0 GHz red detuned from the $F = 3 \rightarrow F'$ transition of the ^{85}Rb D_2 line. This is clearly visible on figure 2.3(b) for instance. Even if the fraction of ^{87}Rb atoms is small, the transmission of the laser beam is greatly reduced when it gets closer to the $F = 2 \rightarrow F'$ transition of the ^{87}Rb D_2 line. In addition to increasing the absorption of the probe beam, ^{87}Rb atoms also affect the refractive index it feels. Using a vapor of rubidium 87 would solve this issue, as red-detuning the probe from the $F = 2 \rightarrow F'$ transition of the ^{87}Rb D_2 line will not bring it at resonance with any transition of ^{85}Rb .

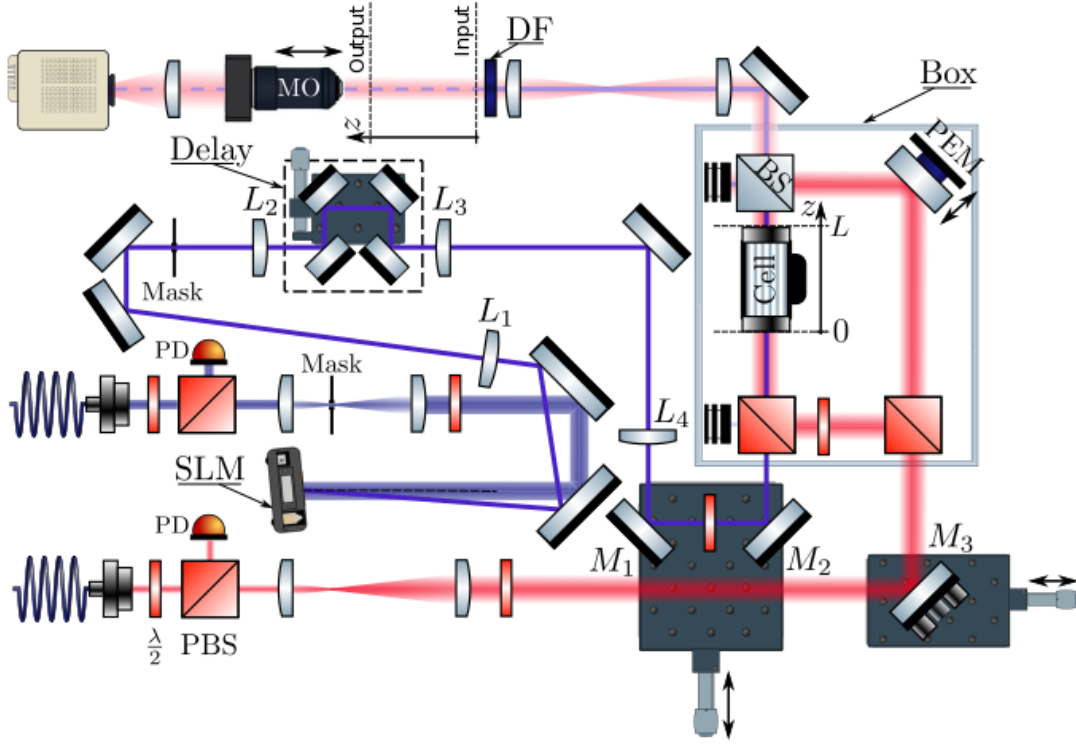


Figure 6.4: Experimental setup. The paths of the defect and the probe beams are sketched in blue and red respectively. The way the defect beam is generated by shaping, in real space, the phase of a wide Gaussian beam with a phase-only SLM is described in subsection 5.2.3. The resulting droplet beam has an axial extent of almost 2.5 cm and a width $\omega_{0,d}$ of $40 \mu\text{m}$. Its propagation direction in the cell defines the optical axis. The probe beam is magnified before entering the Mach-Zehnder interferometer. At that point, it splits into a low power (reference) and a high power parts. The low power beam provides the reference we need to retrieve the phase of the photon fluid at the medium output plane (using the scanning phase interferometry introduced in paragraph 2.3.3 i). The high power one enters with the defect inside the cell. The angle θ_i between these beams – that is, the speed at which the fluid flows toward the obstacle – can be finely tuned using the piezo-actuated mount of the mirror M_3 . The diffraction patterns observed on figure 6.5 are obtained by imaging the cell exit plane with the imaging system described in subsection 5.2.3. By removing the objective from the beam path, we are able to image the k-space and observe the diffraction rings shown on figures 6.6 and 6.7(a). The rings of the droplet beam are barely visible on those images as it is filtered out by the bandpass dichroic filter (DF).

6.3.2 Real-space scattering pattern

All the results I present in this subsection have been obtained by generating obstacles with the droplet beam whose transverse profile is shown on figure 5.17(b). The resulting repulsive potential is Gaussian and its width a bit larger than $40 \mu\text{m}$. The maximum on-axis intensity reachable in experiments using this droplet beam is about $1.3 \times 10^7 \text{ W/m}^2$. Only 10% of the beam overall power is distributed over the droplet central core. This explains why we cannot easily reach higher on-axis intensity experimentally. However, this is enough to saturate the rubidium vapor across the entire cell. The probe beam is much larger than the droplet core ($\omega_{0,f} \simeq 0.9 \text{ mm}$) in order for the fluid density to be nearly uniform in the vicinity of the defect. Images of the near-field diffraction patterns observed, at low fluid density (linear regime), by imaging the cell exit plane onto the camera are shown on figure 6.5.

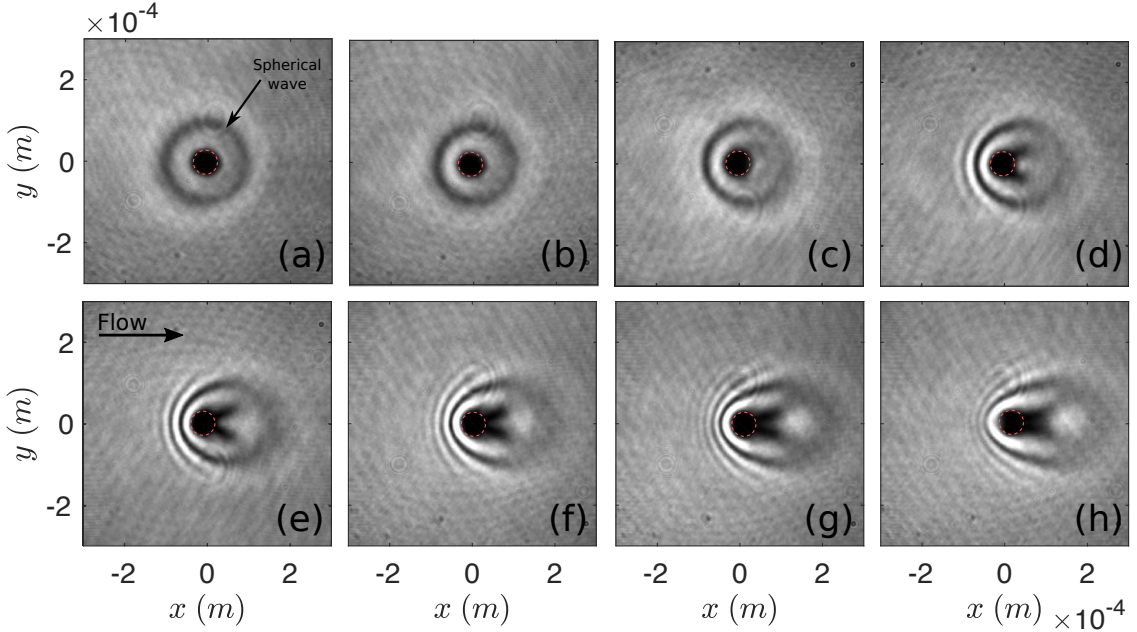


Figure 6.5: Near-field scattering patterns at low background density ρ_0 . The droplet beam generates a negative Gaussian index modulation ($\delta n < 0$), whose width $\omega_{0,d}$ is about $40 \mu\text{m}$. The resulting potential is repulsive explaining why a dark spot is visible at the position where the defect lies (red dotted circle). (a): The photon fluid is at rest ($v = 0$). A spherical wave is created as soon as probe and defect enter the cell and propagate away from the defect. (b)-(h): The photon fluid is flowing rightward. The flow velocity steps up from one image to the next. On figure (d), interference fringes upstream from the obstacle start appearing. Light is scattered backward by the repulsive defect and interferes with the incoming fluid. On (g) and (h), the contrast of the fringes before the obstacle decreases. The kinetic energy of the photon fluid is large compared to the height of the potential and light just go through without being back-scattered [155]. We can finally notice that the spherical wave visible on figure (a) is dragged with the flow and drifts rightward.

Figure 6.5(a) shows the image obtained when the photon fluid is at rest (no transverse flow). The obstacle is located at $\mathbf{r}_\perp = \mathbf{0}$ (red dotted circle). As the potential is repulsive ($\delta n < 0$), the fluid is pushed away from the defect, thereby creating the dark central spot on the image. A spherical wave is emitted in the cell input plane and travels radially onto the photon fluid. On figure (a), the benefit of using droplet beams to generate the obstacle is clearly visible. While standard quasi Bessel-Gauss beams induce a concentric succession of ring-shaped refractive index modulations in the fluid (as can be seen on figure 2(a) of [29] for example), droplet beams only create one main index depletion, since the power distributed over the external rings is drastically reduced, because of interferences. From figure (b) to figure (h), the flow velocity of the photon fluid progressively steps up and interference fringes start thus developing upstream from the obstacle. As in simulations of figure 6.1, the spherical wave is dragged rightward by the photon fluid. We can also notice that the contrast of the fringes in figures (g) and (e) is lower than at smaller flow velocities. At such high speeds, the kinetic energy of the fluid is certainly larger than the potential barrier formed by the obstacle and photons start thus tunneling through. This tunneling effect, theoretically described in [155], have been studied experimentally by Wan *et al.* [26] in 1D photon fluids.

6.3.3 Far-field diffraction pattern

We also investigate the far-field diffraction pattern formed by the scattering of the fluid on the obstacle. Images of the Rayleigh rings observed in k -space at different probe powers and flow velocities are shown on figure 6.6. On the upper series of images (a), $v = 18$ mrad, while on the lower one, $v = 23$ mrad. The origin of the k_x - and k_y -axes lies at the center of the droplet rings (see figure 6.7(a)). The full images have been cropped in order to show only the back scattering part of the Rayleigh ring. Its radius is equal to the transverse wave-vector of the probe beam $\mathbf{k}_\perp = k_0 \sin(\theta_i) \mathbf{e}_x$, explaining why it is larger on the series (a) than on (b).

As you may have seen, the amount of light distributed over the half ring first increases with the probe power \mathcal{P}_f , reaches a maximum and then decreases when further stepping up \mathcal{P}_f . We also notice a decrease in the radius of the scattering ring from figures (a1) to (a6) that is observed in simulations too. Indeed, when c_s rises toward the flow velocity, simulations show that the Rayleigh ring is deformed and develops a corner at \mathbf{k}_\perp . This corner consequently squeezes the ring in the k_y direction (see [56] for details).

We can finally mentioned the fact that the amount of light back-scattered by the defect is lower at large flow velocities (b) than at small ones (a). This is certainly due to the previously mentioned tunnelling effect. We can go further by quantitatively measuring the power \mathcal{P}_s distributed over the half scattering ring as function of the fluid power \mathcal{P}_f . The results are presented on figure 6.7(b), for different flow velocities. Figure 6.7(a) shows the Rayleigh ring observed in k -space when $v = 23$ mrad and $\mathcal{P}_f = 1$ mW. The fluid saturates the image on the left. The droplet rings, centered at $\mathbf{k}_\perp = \mathbf{0}$, are also visible. We can check that the ratio between the radius of the droplet outer and inner rings is 0.52 as expected. The white frame enclosing the right-hand part of the scattering ring delineates the area where the intensity is integrated. The points on figure 6.7(b) arise from this integration at various probe powers. The resulting curves are in agreement with the qualitative observations made on figure 6.6. Indeed, whatever the flow velocity, the power of the back-scattered light increases with \mathcal{P}_f , reaches a maximum value at some critical fluid power $\mathcal{P}_{f,\text{crit}}$ before quickly dropping to zero. It is tempting to attribute this collapse of back- scattering to superfluidity. Nevertheless,

crucial information are missing, such as the value of the sound velocity c_s , which prevents us from concluding with certainty. Moreover, we did not capture the near-field images related to the data points on figure 6.7(b). We are thus unable to tell if the obstacle is still visible in the cell output plane when \mathcal{P}_s is decreasing.

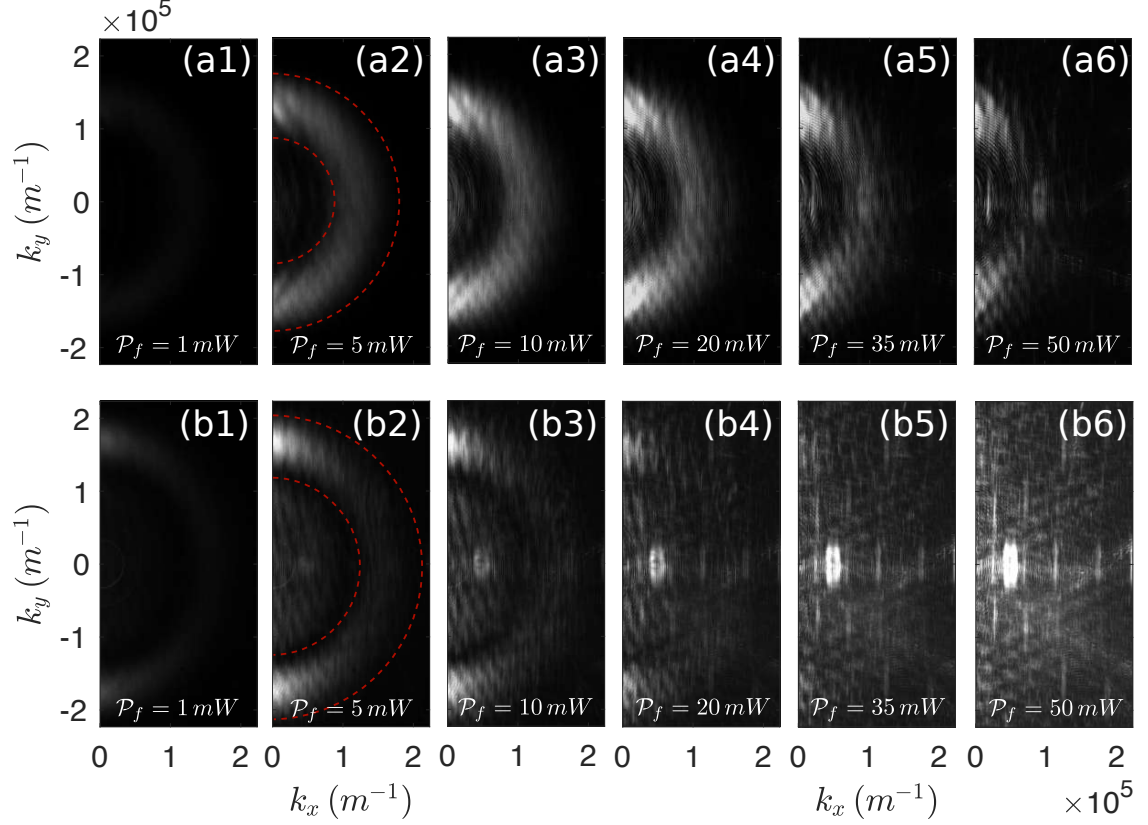


Figure 6.6: Diffraction patterns observed in far-field (k -space) at different fluid powers \mathcal{P}_f , for $v = 18$ mrad (a) and $v = 23$ mrad (b). The k_x/k_y -axes origin-point lies at the center of the droplet rings. The probe is located at $k_x = -k_0 v$ and is thus not visible on the images. The exposure is the same for the upper (a) and lower series (b). The scattering of the fluid on the defect is responsible for the apparition of a ring-shaped structure in far field whose radius is defined by the norm of the probe transverse wave-vector. On series (a) and (b), the power distributed over the scattering ring increases first with \mathcal{P}_f , reaches a threshold and then decreases. A more quantitative analysis can be found on figure 6.7(b). On series (a), the radius of the ring seems to decrease with \mathcal{P}_f . A similar behaviour is reported in [56].

Otherwise, it would mean that the strength of the obstacle $\delta n(0)$ becomes comparable to the nonlinear change of refractive index $\Delta n(\mathbf{r}_\perp)$ surrounding the defect at high probe powers. In that case, the decrease in the back-scattering would be due to the matching between the refractive indices inside and outside the obstacle cross-section. This should not be confused with superfluidity, which causes the suppression of back-scattering even when $\delta n(0) \gg \Delta n$, as mentioned previously when discussing the results of Michel *et al.* [29]. On figure 6.1(b) for instance, superfluidity is observed despite the fact that $\delta n(0)/\Delta n = 25$.

It is also worth mentioning that if the drop of \mathcal{P}_s is due to superfluidity, the flow velocity v should then match the critical speed v_c when $\mathcal{P}_f = \mathcal{P}_{f,\text{crit}}$. As we deal with extended defect, we expect v_c to be lower than c_s . Therefore, the sound velocity should, at least, be equal to the flow velocity. This requires $\Delta n > v^2 \sim 4 \times 10^{-4}$. Even if the probe is close to resonance, reaching such high values of Δn is unrealistic regarding the available power ($\mathcal{P}_f < 1$ W).

Moreover, we can observe that the critical power $\mathcal{P}_{f,\text{crit}}$ at which \mathcal{P}_s starts dropping slightly decreases when stepping up the flow velocity. This is not expected if we attribute the collapse of back-scattering to superfluidity. Scanning the probe power as in figure 6.7(b) affects both the sound velocity and the healing length. In the phase diagram of figure 6.2, such a scan of the fluid density – at fixed defect size $\omega_{0,d}$ and flow velocity v – is like following leftward the curve of equation $y(x) = k\omega_{0,d}v/x$ (where k is the probe wave-vector). For the values of the flow velocity considered here, $k\omega_{0,d}v$ ranges from 5.8 to 7.4. We thus expect the curves $x \rightarrow y_1(x)$, $x \rightarrow y_2(x)$ and $x \rightarrow y_3(x)$ (related to $v_1 = 18$ mrad, $v_2 = 20$ mrad and $v_3 = 23$ mrad) to cross the thick black curve of the phase diagram almost at the same abscissa x . Therefore, $\frac{v_1}{c_{s,1}} \simeq \frac{v_2}{c_{s,2}} \simeq \frac{v_3}{c_{s,3}}$. Since $v_1 < v_2 < v_3$, the preceding equation requires that $c_{s,1} > c_{s,2} > c_{s,3}$. As the sound velocity scales with the square root of the fluid density, we should consequently observe that $\mathcal{P}_{f,\text{crit}}$ increases with the flow velocity. This is not what we measured however. For all the reasons mentioned above, superfluidity is certainly not the cause of the collapse of back-scattering on figure 6.7(b), which is more likely to arise from index matching effect.

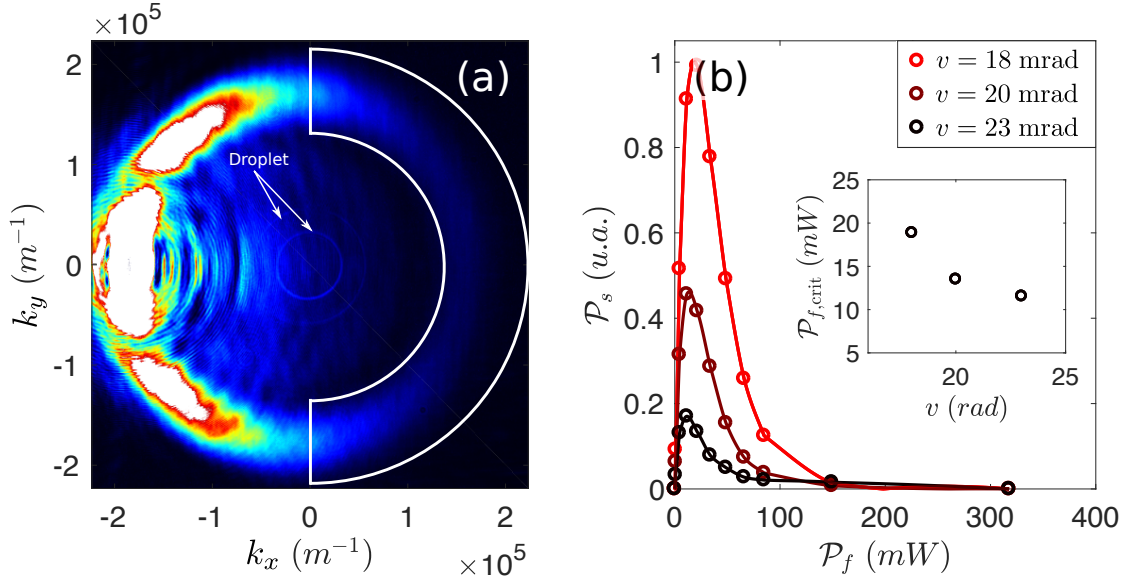


Figure 6.7: (a): Scattering ring observed in far-field for $v = 23$ mrad and for $\mathcal{P}_f = 1.0$ mW. The two rings forming the intensity distribution of the droplet beam in k -space are visible. By integrating the intensity within the white frame, we can measure the amount of light back-scattered by the obstacle as function of the fluid power \mathcal{P}_f . The results are shown on figure (b) for different flow velocities v . When \mathcal{P}_f increases, the power \mathcal{P}_s distributed over the right half of the diffraction ring first increases, reaches a maximum and then decreases. The critical fluid power $\mathcal{P}_{f,\text{crit}}$ – at which \mathcal{P}_s starts dropping – slightly decreases when the flow velocity steps up. This behaviour is not expected if we suppose that the drop in the back-scattering power is due to superfluidity.

6.4 Future works

Rigorously probing the superfluidity of light in rubidium vapors by studying the scattering of the photon fluid on an all-optical defect requires to complete quite a few preliminary steps. We should first of all characterize the change of refractive index δn induced by the droplet beam in the fluid of light (for different sets of parameters) and compare the results with the theory developed in the preceding chapter. For this purpose, we can for instance set to zero the probe transverse wave-vector and measure the phase accumulated by the photon fluid in the vicinity of the obstacle (using the scanning phase interferometry of subsection 2.3.3 i). One of the most crucial point consists in precisely characterizing the effects of the probe on the defect strength. Once this is done, we can start studying the scattering of the fluid of light on the obstacle. The first step is to investigate in details the physics of the transient regime, that is, the emission of spherical waves in the cell input plane. We can for example measure the velocity at which those waves propagate in the transverse plane. This could provide a convenient way of accessing the speed of sound *in situ*.

The last but not least challenge is to probe superfluidity itself by measuring simultaneously the scattering patterns in real and in k -space. To that end, the best is to scan the probe transverse wave-vector while keeping its power constant. By measuring the phase of the photon fluid at the cell output plane, we can also think about observing and studying the spontaneous nucleation of quantized vortices in the wake of the defect. This would complete the study of superfluidity in our system.

As mentioned in subsection 6.2.2, we also currently investigate the possibility of probing optomechanically the normal/superfluid transition in hot rubidium vapors. Following the theoretical proposal by Larré *et al.* [101], we plan to install a nanofiber in a vacuum chamber filled with a pure vapor of rubidium. A sketch of the experimental setup has been depicted on figure 6.8(a) (top view). The laser beam enters the Kerr medium from the left and propagates at a small angle with respect to the z -axis. The nanofiber is mechanically clamped to the entrance window. We assume it is aligned along the z -axis when the laser is off. Because of the radiation pressure, the nanofiber should bend when switching the laser on. We expect this bending to increase with the laser intensity until reaching the normal/superfluid threshold. At that point, Larré *et al.* predict a fast drop in the fiber deflection ζ , which returns to its initial position. In practice, the fiber is hold on both ends. Indeed, it seems difficult if not impossible to cut a nanofiber keeping it straight as it spontaneously tends to wind onto itself. Numerical simulations predicting the deflection ζ at the center of the nanofiber (in vacuum) has been performed by Maxime Joos in [156] using the Mie scattering theory. In its work, Maxime Joos considers a laser beam having a normal incidence onto a 10 mm long nanofiber. With the available laser resources, we can expect in that case a displacement ranging from 0.1 to 1 μm , depending on the laser polarization and on the diameter of the nanofiber used in experiments. In fine, however, we would like to make the laser propagates at a small angle with respect to the nanofiber. We expect the displacement ζ to be much lower in that case. We are thus currently looking for a way of increasing the momentum transferred by the laser to the fiber. A possibility would be to deposit some metallic reflective coating on its surface. In any event, we must also be able to accurately measure the nanometric deflection of the nanofiber at its center. This is done using an optical ruler whose principle is explained below.

A gold nanoparticle is dropped onto the fiber and positioned inside a standing-wave created by reflecting a green laser on a mirror, as shown on figures 6.8 (b) and (c). The nanoparticle scatters part of the light coming from the standing-wave into the nanofiber. As the amount of scattered light depends on the nanoparticle position in the standing-wave, we can retrieve the deflection of the fiber by simply measuring its output power using a photo-diode (PD). This method, developed by Maxime Joos [156] and further improved by Chengjie Ding, allows to measure the position of the nanoparticle with an accuracy of ± 20 nm (figure (d)).

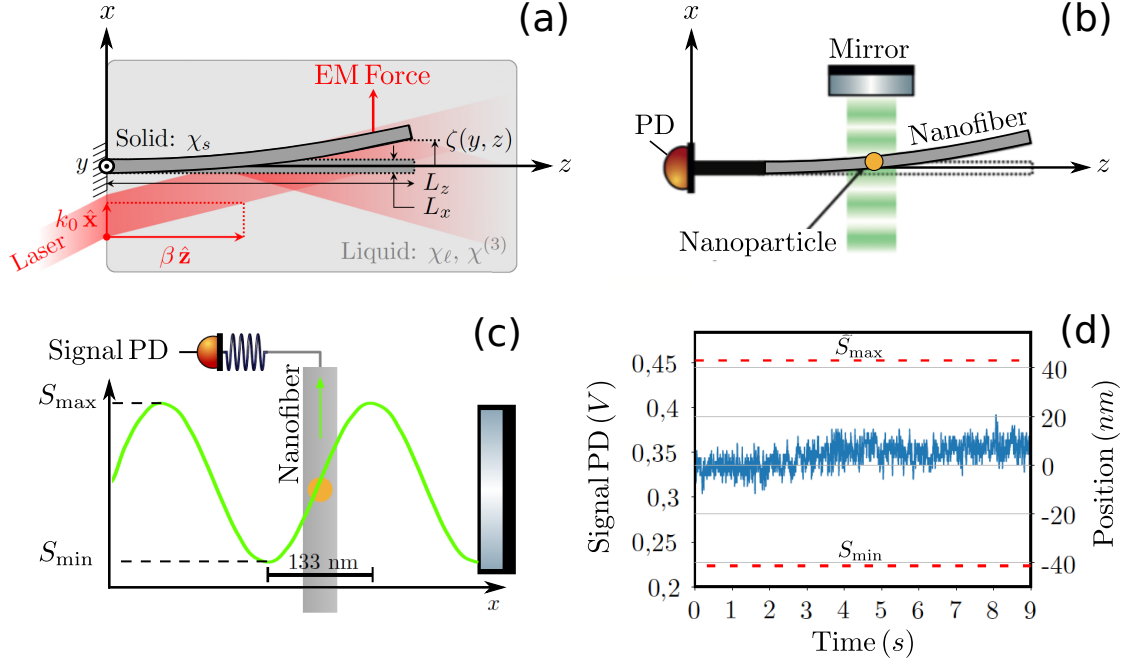


Figure 6.8: Optomechanical signature of superfluidity. (a): Sketch of the experimental setup proposed by Larré *et al.* in [101]. The left end of the obstacle is clamped to the cell entrance window and its right end is free to move. Initially, the obstacle is aligned along the z -axis. When the laser is switched on, the obstacle bends under the radiation pressure. The position $\zeta(x, L_z)$ of the right tip increases with the fluid intensity \mathcal{I}_f before dropping to zero when passing through the normal/superfluid transition. (b) and (c): Displacement measurement. A gold nanoparticle is dropped onto a nanofiber (obstacle). A standing-wave is created by reflecting a laser beam on a mirror. The nanoparticle diffuses more or less light into the fiber depending on its position inside this standing-wave. By collecting the scattered light with a photo-diode (PD), we can measure $\zeta(x, L_z)$ with an accuracy of ± 20 nm (see figure (d)).

Summary and future works

General conclusion

The primary purpose of this thesis was to study some of the hydrodynamic properties of a propagating photon fluid in hot rubidium vapors. While photons are not interacting particles in vacuum, they are inside the rubidium vapor, when the laser is tuned close to an atomic resonance. This interaction between photons, mediated by the atomic ensemble, makes the laser beam behave as a fluid flowing in the plane perpendicular to the optical axis when it propagates through the vapor. The dynamics of this fluid of light is driven by the nonlinear Schrödinger equation, which shares strong similarities with the Gross–Pitaevskii equation. The latter describes the space-time evolution of atomic Bose-Einstein condensates in the mean-field approximation. Those systems exhibit in particular the ability of flowing without experiencing any friction, that is, without dissipating energy. Our desire to observe such superfluid flow of light in our system has driven the entire work presented in this manuscript.

The strength of the photon-photon interaction in Kerr mediums is characterized by the material nonlinear refractive index n_2 . This quantity thus plays a crucial role in experiments. In rubidium vapors, repulsive interactions between photons are obtained by red-detuning some laser beam from one of the D -lines. In chapter 1, we first describe the optical response of the rubidium vapor under this near-resonance laser excitation with a two-level model. This simplistic description is improved afterwards by taking into account optical pumping between the D -line ground states as well as the finite transit time of atoms across the beam. Using this extended model, we derive a general expression for the dielectric susceptibility. In order to further refine our theoretical description, Doppler broadening and nonlocality, arising from the ballistic transport of excited atoms in hot vapors, have also been included.

Chapter 2 begins with the derivation of the nonlinear Schrödinger equation. The connection with the Gross Pitaevskii equation is established and discussed in details. We then focus on describing the dynamics of small amplitude density waves travelling onto the photon fluid. Using the Bogoliubov transform, we show that those waves obey the so-called Bogoliubov dispersion relation, which exhibits two different regimes. It first starts by linearly increasing at low excitation wave-vectors, where density waves behave as collective phonons travelling all at the same speed (the sound velocity), before developing a quadratic trend, characteristic of a particle-like dispersion. According to the Landau criterion for superfluidity, showing the existence of the sound velocity would guarantee the observation of superfluid flows of light in our system. I consequently dedicate an important part of my time to measuring the dispersion relation of density fluctuations. The results are shown in chapter 4.

In chapter 3, the tools and the methods used to generate the photon fluid on one hand and characterise it on the other are introduced. We start by presenting the rubidium cell and its heating system before describing the laser sources. An important part of this chapter is dedicated to presenting two techniques we used to access the nonlinear refractive index n_2 . Both are based on measuring the self-phase accumulated by a wide Gaussian beam during its propagation inside the vapor cell. The first one consists in counting the number of rings appearing in the far-field intensity distribution of the beam. The correct counting procedure, taking into account the Gouy phase shift, is described in both the 1D and 2D cases. To do so, we have extended the approach followed by Nicolas Pavloff in an unpublished work of 2018.

The second method consists in measuring the spatial variations of the nonlinear phase shift accumulated by the beam using the scanning phase interferometry. We show additionally, using numerical simulations, that both techniques are accurate as long as the thin medium approximation is fulfilled. This is the case as long as the characteristic propagation length over which self-defocusing starts affecting the beam shape is longer than the cell.

In chapter 4, the dispersion relation of small amplitude density fluctuations travelling onto the fluid of light is measured. Following the work of Vocke *et al.* [52], we first try to measure the difference in the phase velocity between two plane waves propagating on top of low and high density background fluids. At the medium output plan, this results in a shift between the crests of these two waves, that depends on their wavelength. We show that the theoretical description of Vocke *et al.* is incomplete as they do not account for the propagation of the conjugate beam in the cell, which is spontaneously generated (because of four-wave mixing) in the input plane. Following the work of Larré *et al.* [71], we derive an exact formula to calculate the shift using the Bogoliubov formalism. This formula depends on the dispersion relation of density waves but the latter can only be retrieved from the shift at the expense of a complex numerical inversion. We thus claim that this method is not suitable to measure the dispersion relation of density waves. We still however demonstrate that the shift is not saturating at large modulation wavelength – both experimentally and numerically – which contradicts the results of Vocke *et al.* In order to access the dispersion, we propose a new experimental scheme based on measuring the group velocity of a small Gaussian wave-packet travelling onto the photon fluid. Beside the fact that this technique overcomes all the main limitations of the shift measurement, it also provides a much deeper understanding about the physics at play. By probing the sound-like regime of the dispersion, the wave-packet splits into a pair of counter-propagating Bogoliubov wave-trains in the cell entrance plane, which both travel at the speed of sound. Reversely, when probing the particle-like regime, the wave-packet behaves as a free particle moving at a velocity that increases linearly with its wave-vector. This nonlinear refraction law is theoretically described using the Bogoliubov formalism and illustrated by performing numerical simulations. The experimental results are in excellent agreement with theory at low background density, when transport-induced nonlocality is taken into account. The dispersion relation retrieved using the group velocity measurement exhibits a linear increase at low excitation wave-vectors which is characterised by the sound velocity. The way the later depends on the fluid density is investigated and exactly matches theory without any fitting parameter. At the end of chapter 4, we also report the observation of quasi-particle interferences occurring between the counter-propagating Bogoliubov wave-packets at the cell exit plane.

Demonstrating the existence of a sonic regime in the dispersion relation is a key requirement for the observation of superfluidity. In order to go one step further, the way the fluid flows around a localized obstacle should be investigated. In chapter 5, the method used to generate such an obstacle in our system is described. In photon fluids, any local change of refractive index acts as a defect into the flow. In rubidium vapors, localized refractive index changes can be induced by red-detuning the fluid from one of the D -line while strongly driving the other with an intense defect field. This situation is first theoretically investigated using a open 4-level N-type atomic model. The optical Bloch equations are derived and solved using first a perturbative approach and then the dressed-state formalism. This second method helps us getting a deeper insight into the process underlying the generation of the obstacle

into the fluid of light. We show that the strength and the sign of the potential induced by the defect field can be tuned by changing its power and/or its frequency. We also alert the reader to the fact that varying the power of the fluid surrounding the defect also affects its strength. The second section of chapter 5 is dedicated to presenting the methods used in experiments to produce the defect beam. The later should ideally fulfill certain requirements such as being collimated and keeping the same strength across the full cell. Its diameter should also be comparable to the healing length – which is typically of the order of few tens of microns. We chose to use Bessel beams whose diffraction-free features enable to generate collimated defects of appropriate size all along the cell. Moreover, we show that designing the on-axis intensity profile of Bessel beam enables to compensate linear absorption during propagation. This technique, that is based on the real space shaping of a Gaussian beam with a phase-only spatial light modulator, finds a wide variety of applications, in bio-imaging in particular, where the huge absorption and diffusion coefficients of living tissues make the illumination of such samples challenging. Nevertheless, generating obstacles with attenuation-resistant Bessel beams (or standard quasi-Bessel beams) is not the most suitable option as the rings surrounding the Bessel central core are intense enough to also change the refractive index. In experiments, we prefer instead using droplet beams, which results from the interference between two co-propagating co-axial Bessel beams having different cone angles. They offer the benefit of being perfectly collimated while reducing the power distributed over the rings compared to standard quasi-Bessel beams.

In chapter 6, we finally present some preliminary results obtained by bringing all the previous ingredients together. Images of the near-field and far-field scattering patterns generated by making the fluid flow toward the defect are shown. So far, we did not observe clear signature of superfluidity, but effects such as the collapse of the Rayleigh ring in k -space should be further investigated and may provide the experimental evidence we look for.

Future works

Propagating photon fluids in nonlinear mediums are a versatile and highly tunable platform to study the rich physics of quantum fluids. However, those systems are intrinsically limited by the length of the nonlinear medium, that fixes, once and for all, the "time" over which they are evolving. Beside the fact that long mediums are often required to make this time of evolution as large as possible, probing the dynamics of the photon fluid is really challenging, as we can only image in practice the medium exit plane. One possible way of overcoming this issue is to measure the full electric field (intensity plus phase) at the output plane of a short cell, by using a shearing interferometric camera [157] for example. We can then tailor the input field to make it match the output one, shaping its intensity and/or phase using a digital micro-mirror device and a SLM. This re-injection strategy [158] would provide a way of extending the evolution "time" (by performing many loops) while resolving the "temporal" dynamics of the photon fluid (using a short cell for instance). However, the role played by the air/medium interfaces in this time-loop needs to be further investigated.

The control over the photon fluid temporal evolution can be further improved by adding confinement in the transverse direction. This can be done by modifying the refractive index experienced by the fluid as shown in chapter 5. By using ring-shaped confining beam, we can for instance create a light-induced wave-guide inside the vapor cell and trap the photon fluid in the resulting harmonic potential. In these circumstances, the system is scale-invariant and a new type of 2D breathers, recently discovered in [61], may be observed. Optically-induced potentials are also promising tools to study the interplay between localization features and superfluidity. Illuminating the rubidium cell with an amorphous speckle light [159] is a way of creating "stationary" disordered potential landscapes into the photon fluid, that are necessary to investigate the competition between localization and superfluid transport [100]. Using the "light guiding light" strategy also provides a way of implementing evaporative cooling of photon fluids [160], which is a key requirement for accelerating and thus observing Bose-Einstein condensation of light.

An important frontier in fluid of light research is to go beyond mean field and observe purely quantum phenomena. Because light propagating in atomic vapors is a well controlled system which has already proved to be an excellent source of quantum correlated beams [41, 161], we believe that it could be the first platform to lay the groundwork for studying quantum effects in propagating photon fluids. One step in this direction would be to observe the optical analogue of the dynamical Casimir effect [58]. This can be achieved using the same experimental configuration as in section 4.2, but without stimulating the emission of the Bogoliubov modes this time. In that case, because of the sudden jump of the photon-photon interaction in the cell entrance plane, pairs of quantum-correlated Bogoliubov excitations are spontaneously emitted in that plane, seeded by vacuum. The main challenge is now to find a technique to measure the correlations between these excitations, using certainly some sophisticated homodyne detection scheme.

Bibliography

- [1] P. A. Franken, A. E. Hill, C. W. Peters, and G. Weinreich. Generation of optical harmonics. *Phys. Rev. Lett.*, 7:118–119, Aug 1961.
- [2] T. H. Maiman. Stimulated optical radiation in ruby. *Nature*, 187(4736):493–494, 1960.
- [3] Maneesh Jain, Hui Xia, G. Y. Yin, A. J. Merriam, and S. E. Harris. Efficient nonlinear frequency conversion with maximal atomic coherence. *Phys. Rev. Lett.*, 77:4326–4329, Nov 1996.
- [4] M. Fleischhauer and M. D. Lukin. Dark-state polaritons in electromagnetically induced transparency. *Phys. Rev. Lett.*, 84:5094–5097, May 2000.
- [5] M. D. Lukin and A. Imamoglu. Nonlinear optics and quantum entanglement of ultraslow single photons. *Phys. Rev. Lett.*, 84:1419–1422, Feb 2000.
- [6] M. Brambilla, L. A. Lugiato, V. Penna, F. Prati, C. Tamm, and C. O. Weiss. Transverse laser patterns. ii. variational principle for pattern selection, spatial multistability, and laser hydrodynamics. *Phys. Rev. A*, 43:5114–5120, May 1991.
- [7] K. Staliunas. Laser ginzburg-landau equation and laser hydrodynamics. *Phys. Rev. A*, 48:1573–1581, Aug 1993.
- [8] M. Vaupel, K. Staliunas, and C. O. Weiss. Hydrodynamic phenomena in laser physics: Modes with flow and vortices behind an obstacle in an optical channel. *Phys. Rev. A*, 54:880–892, Jul 1996.
- [9] Raymond Y. Chiao and Jack Boyce. Bogoliubov dispersion relation and the possibility of superfluidity for weakly interacting photons in a two-dimensional photon fluid. *Phys. Rev. A*, 60:4114–4121, Nov 1999.
- [10] Jack Boyce and Raymond Y. Chiao. Transverse oscillation arising from spatial soliton formation in nonlinear optical cavities. *Phys. Rev. A*, 59:3953–3958, May 1999.
- [11] J. Kasprzak, M. Richard, S. Kundermann, A. Baas, P. Jeambrun, J. M. J. Keeling, F. M. Marchetti, M. H. Szymańska, R. André, J. L. Staehli, V. Savona, P. B. Littlewood, B. Deveaud, and Le Si Dang. Bose–einstein condensation of exciton polaritons. *Nature*, 443(7110):409–414, 2006.

- [12] J. J. Baumberg, P. G. Savvidis, R. M. Stevenson, A. I. Tartakovskii, M. S. Skolnick, D. M. Whittaker, and J. S. Roberts. Parametric oscillation in a vertical microcavity: A polariton condensate or micro-optical parametric oscillation. *Phys. Rev. B*, 62:R16247–R16250, Dec 2000.
- [13] R. Balili, V. Hartwell, D. Snoke, L. Pfeiffer, and K. West. Bose-einstein condensation of microcavity polaritons in a trap. *Science*, 316(5827):1007–1010, 2007.
- [14] A. Amo, D. Sanvitto, F. P. Laussy, D. Ballarini, E. del Valle, M. D. Martin, A. Lemaître, J. Bloch, D. N. Krizhanovskii, M. S. Skolnick, C. Tejedor, and L. Viña. Collective fluid dynamics of a polariton condensate in a semiconductor microcavity. *Nature*, 457(7227):291–295, 2009.
- [15] Alberto Amo, Jérôme Lefrère, Simon Pigeon, Claire Adrados, Cristiano Ciuti, Iacopo Carusotto, Romuald Houdré, Elisabeth Giacobino, and Alberto Bramati. Superfluidity of polaritons in semiconductor microcavities. *Nature Physics*, 5(11):805–810, 2009.
- [16] D. Sanvitto, S. Pigeon, A. Amo, D. Ballarini, M. De Giorgi, I. Carusotto, R. Hivet, F. Pisanello, V. G. Sala, P. S. S. Guimaraes, R. Houdré, E. Giacobino, C. Ciuti, A. Bramati, and G. Gigli. All-optical control of the quantum flow of a polariton condensate. *Nature Photonics*, 5(10):610–614, 2011.
- [17] A. Amo, S. Pigeon, D. Sanvitto, V. G. Sala, R. Hivet, I. Carusotto, F. Pisanello, G. Leménager, R. Houdré, E. Giacobino, C. Ciuti, and A. Bramati. Polariton superfluids reveal quantum hydrodynamic solitons. *Science*, 332(6034):1167–1170, 2011.
- [18] G. A. Swartzlander and C. T. Law. Optical vortex solitons observed in kerr nonlinear media. *Phys. Rev. Lett.*, 69:2503–2506, Oct 1992.
- [19] Iacopo Carusotto and Cristiano Ciuti. Quantum fluids of light. *Rev. Mod. Phys.*, 85:299–366, Feb 2013.
- [20] Christophe Josserand and Sergio Rica. Coalescence and droplets in the subcritical nonlinear schrödinger equation. *Phys. Rev. Lett.*, 78:1215–1218, Feb 1997.
- [21] W. J. Firth and D. V. Skryabin. Optical solitons carrying orbital angular momentum. *Phys. Rev. Lett.*, 79:2450–2453, Sep 1997.
- [22] Humberto Michinel, María J. Paz-Alonso, and Víctor M. Pérez-García. Turning light into a liquid via atomic coherence. *Phys. Rev. Lett.*, 96:023903, Jan 2006.
- [23] María J Paz-Alonso and Humberto Michinel. Superfluidlike motion of vortices in light condensates. *Physical review letters*, 94(9):093901, 2005.
- [24] Shu Jia, Wenjie Wan, and Jason W Fleischer. Dispersive shock waves in nonlinear arrays. *Physical review letters*, 99(22):223901, 2007.
- [25] Wenjie Wan, Shu Jia, and Jason W Fleischer. Dispersive superfluid-like shock waves in nonlinear optics. *Nature Physics*, 3(1):46, 2007.

- [26] Wenjie Wan, Stefan Muenzel, and Jason W Fleischer. Wave tunneling and hysteresis in nonlinear junctions. *Physical review letters*, 104(7):073903, 2010.
- [27] Wenjie Wan, Assaf Avidan, and Jason W Fleischer. Nonlinear wave scattering by small barrier potentials. In *Frontiers in Optics*, page FThD4. Optical Society of America, 2008.
- [28] David Vocke, Kali Wilson, Francesco Marino, Iacopo Carusotto, Ewan M Wright, Thomas Roger, Brian P Anderson, Patrik Öhberg, and Daniele Faccio. Role of geometry in the superfluid flow of nonlocal photon fluids. *Physical Review A*, 94(1):013849, 2016.
- [29] Claire Michel, Omar Boughdad, Mathias Albert, Pierre-Élie Larré, and Matthieu Bellec. Superfluid motion and drag-force cancellation in a fluid of light. *Nature communications*, 9(1):2108, 2018.
- [30] Daniel A Steck. Rubidium 85 d line data, 2001.
- [31] Daniel A Steck. Rubidium 87 d line data, 2001.
- [32] Paul Siddons, Charles S Adams, Chang Ge, and Ifan G Hughes. Absolute absorption on rubidium d lines: comparison between theory and experiment. *Journal of Physics B: Atomic, Molecular and Optical Physics*, 41(15):155004, 2008.
- [33] Alan Robert Edmonds. *Angular momentum in quantum mechanics*, volume 4. Princeton university press, 1996.
- [34] Jon Sagle, RK Namiotka, and John Huennekens. Measurement and modelling of intensity dependent absorption and transit relaxation on the cesium line. *Journal of Physics B: Atomic, Molecular and Optical Physics*, 29(12):2629, 1996.
- [35] F Arecchi and R Bonifacio. Theory of optical maser amplifiers. *IEEE Journal of Quantum Electronics*, 1(4):169–178, 1965.
- [36] Carlos Alexandre Brasil, Felipe Fernandes Fanchini, and Reginaldo de Jesus Napolitano. A simple derivation of the lindblad equation. *Revista Brasileira de Ensino de Física*, 35(1):01–09, 2013.
- [37] Leonard Mandel and Emil Wolf. *Optical coherence and quantum optics*. Cambridge university press, 1995.
- [38] GS Agarwal. Rotating-wave approximation and spontaneous emission. *Physical Review A*, 4(5):1778, 1971.
- [39] K.-J. Boller, A. Imamoglu, and S. E. Harris. Observation of electromagnetically induced transparency. *Phys. Rev. Lett.*, 66:2593–2596, May 1991.
- [40] S. H. Autler and C. H. Townes. Stark effect in rapidly varying fields. *Phys. Rev.*, 100:703–722, Oct 1955.
- [41] Quentin Glorieux. *Etude theorique et experimentale des correlations quantiques obtenues par melange a quatre ondes dans une vapeur atomique*. PhD thesis, 2010.

- [42] Joyee Ghosh, R Ghosh, F Goldfarb, J-L Le Gouët, and F Bretenaker. Analysis of electromagnetically induced transparency and slow light in a hot vapor of atoms undergoing collisions. *Physical Review A*, 80(2):023817, 2009.
- [43] Mason Klein, M Hohensee, DF Phillips, and RL Walsworth. Electromagnetically induced transparency in paraffin-coated vapor cells. *Physical Review A*, 83(1):013826, 2011.
- [44] Yanhong Xiao, Irina Novikova, David F. Phillips, and Ronald L. Walsworth. Diffusion-induced ramsey narrowing. *Phys. Rev. Lett.*, 96:043601, Feb 2006.
- [45] M Bruvelis, J Ulmanis, NN Bezuglov, K Miculis, C Andreeva, B Mahrov, D Tretyakov, and A Ekers. Analytical model of transit time broadening for two-photon excitation in a three-level ladder and its experimental validation. *Physical Review A*, 86(1):012501, 2012.
- [46] J. E. Thomas and W. W. Quivers. Transit-time effects in optically pumped coupled three-level systems. *Phys. Rev. A*, 22:2115–2121, Nov 1980.
- [47] Geol Moon and Heung-Ryoul Noh. A comparison of the dependence of saturated absorption signals on pump beam diameter and intensity. *JOSA B*, 25(12):2101–2106, 2008.
- [48] T. Wang, C. Greiner, J. R. Bochinski, and T. W. Mossberg. Experimental study of photon-echo size in optically thick media. *Phys. Rev. A*, 60:R757–R760, Aug 1999.
- [49] Donald H Close. Strong-field saturation effects in laser media. *Physical Review*, 153(2):360, 1967.
- [50] Stephan Skupin, Mark Saffman, and Wieslaw Krolikowski. Nonlocal stabilization of nonlinear beams in a self-focusing atomic vapor. *Physical review letters*, 98(26):263902, 2007.
- [51] EL Lewis. Collisional relaxation of atomic excited states, line broadening and interatomic interactions. *Physics Reports*, 58(1):1–71, 1980.
- [52] David Vocke, Thomas Roger, Francesco Marino, Ewan M Wright, Iacopo Carusotto, Matteo Clerici, and Daniele Faccio. Experimental characterization of nonlocal photon fluids. *Optica*, 2(5):484–490, 2015.
- [53] Dieter Suter and Tilo Blasberg. Stabilization of transverse solitary waves by a nonlocal response of the nonlinear medium. *Phys. Rev. A*, 48:4583–4587, Dec 1993.
- [54] S. Skupin, O. Bang, D. Edmundson, and W. Krolikowski. Stability of two-dimensional spatial solitons in nonlocal nonlinear media. *Phys. Rev. E*, 73:066603, Jun 2006.
- [55] Robert W Boyd. *Nonlinear optics*. Elsevier, 2003.
- [56] Iacopo Carusotto. Superfluid light in bulk nonlinear media. *Proceedings of the Royal Society A: Mathematical, Physical and Engineering Sciences*, 470(2169):20140320, 2014.

- [57] Lev Pitaevskii and Sandro Stringari. *Bose-Einstein condensation and superfluidity*, volume 164. Oxford University Press, 2016.
- [58] Pierre-Élie Larré and Iacopo Carusotto. Propagation of a quantum fluid of light in a cavityless nonlinear optical medium: General theory and response to quantum quenches. *Phys. Rev. A*, 92:043802, Oct 2015.
- [59] Henry C Yuen and Bruce M Lake. Instabilities of waves on deep water. *Annual Review of Fluid Mechanics*, 12(1):303–334, 1980.
- [60] Govind P Agrawal. Nonlinear fiber optics. In *Nonlinear Science at the Dawn of the 21st Century*, pages 195–211. Springer, 2000.
- [61] Raphaël Saint-Jalm, Patricia CM Castilho, Édouard Le Cerf, Brice Bakkali-Hassani, J-L Ville, Sylvain Nascimbene, Jérôme Beugnon, and Jean Dalibard. Dynamical symmetry and breathers in a two-dimensional bose gas. *Physical Review X*, 9(2):021035, 2019.
- [62] Franco Dalfovo, Stefano Giorgini, Lev P Pitaevskii, and Sandro Stringari. Theory of bose-einstein condensation in trapped gases. *Reviews of Modern Physics*, 71(3):463, 1999.
- [63] Erwin Madelung. Eine anschauliche deutung der gleichung von schrödinger. *Naturwissenschaften*, 14(45):1004–1004, 1926.
- [64] E. G. Turitsyna, S. V. Smirnov, S. Sugavanam, N. Tarasov, X. Shu, S. A. Babin, E. V. Podivilov, D. V. Churkin, G. Falkovich, and S. K. Turitsyn. The laminar–turbulent transition in a fibre laser. *Nature Photonics*, 7(10):783–786, 2013.
- [65] Julien Fatome, Christophe Finot, Guy Millot, Andrea Armaroli, and Stefano Trillo. Observation of optical undular bores in multiple four-wave mixing. *Physical Review X*, 4(2):021022, 2014.
- [66] Shu Jia, Mikko Haataja, and Jason W Fleischer. Rayleigh–taylor instability in nonlinear schrödinger flow. *New Journal of Physics*, 14(7):075009, 2012.
- [67] John William Strutt Baron Rayleigh. *The theory of sound*, volume 2. Macmillan, 1896.
- [68] Dmitry Sergeevich Petrov et al. *Bose-Einstein condensation in low-dimensional trapped gases*. PhD thesis, Universiteit van Amsterdam [Host], 2003.
- [69] Neda Ghofraniha, Claudio Conti, Giancarlo Ruocco, and Stefano Trillo. Shocks in nonlocal media. *Physical review letters*, 99(4):043903, 2007.
- [70] Andreas Schmitt. Introduction to superfluidity. *Lect. Notes Phys*, 888(1), 2015.
- [71] Pierre-Elie Larre, Stefano Biasi, Fernando Ramiro-Manzano, Lorenzo Pavesi, and Iacopo Carusotto. Pump-and-probe optical transmission phase shift as a quantitative probe of the bogoliubov dispersion relation in a nonlinear channel waveguide. *The European Physical Journal D*, 71(6):146, 2017.

- [72] NN Bogoljubov, Vladimir Veniaminovic Tolmachov, and DV Širkov. A new method in the theory of superconductivity. *Fortschritte der physik*, 6(11-12):605–682, 1958.
- [73] David Emanuel Frank Vocke et al. *Analogue gravity in nonlocal fluids of light*. PhD thesis, Heriot-Watt University, 2017.
- [74] CJ Hawthorn, KP Weber, and RE Scholten. Littrow configuration tunable external cavity diode laser with fixed direction output beam. *Review of scientific instruments*, 72(12):4477–4479, 2001.
- [75] Sebastian D Saliba, Mark Junker, Lincoln D Turner, and Robert E Scholten. Mode stability of external cavity diode lasers. *Applied optics*, 48(35):6692–6700, 2009.
- [76] PW Smith and R Hänsch. Cross-relaxation effects in the saturation of the 6328-Å neon-laser line. *Physical Review Letters*, 26(13):740, 1971.
- [77] Aleksandr Nikolaevich Nesmeyanov. Vapor pressure of the chemical elements. 1963.
- [78] Neven Šantić, Adrien Fusaro, Sabeur Salem, Josselin Garnier, Antonio Picozzi, and Robin Kaiser. Nonequilibrium precondensation of classical waves in two dimensions propagating through atomic vapors. *Phys. Rev. Lett.*, 120:055301, Feb 2018.
- [79] Omar Boughdad, Aurélien Eloy, Fabrice Mortessagne, Matthieu Bellec, and Claire Michel. Anisotropic nonlinear refractive index measurement of a photorefractive crystal via spatial self-phase modulation. *Optics express*, 27(21):30360–30370, 2019.
- [80] Mansoor Sheik-Bahae, Ali A Said, and Eric W Van Stryland. High-sensitivity, single-beam n^2 measurements. *Optics letters*, 14(17):955–957, 1989.
- [81] Jiangwei Wang, Mansour Sheik-Bahae, AA Said, David J Hagan, and Eric W Van Stryland. Time-resolved z-scan measurements of optical nonlinearities. *JOSA B*, 11(6):1009–1017, 1994.
- [82] E Carcolé, J Campos, and S Bosch. Diffraction theory of fresnel lenses encoded in low-resolution devices. *Applied optics*, 33(2):162–174, 1994.
- [83] WR Callen, BG Huth, and RH Pantell. optical patterns of thermally self-defocused light. *Applied Physics Letters*, 11(3):103–105, 1967.
- [84] SD Durbin, SM Arakelian, and YR Shen. Laser-induced diffraction rings from a nematic-liquid-crystal film. *Optics letters*, 6(9):411–413, 1981.
- [85] Luogen Deng, Kunna He, Tiezhong Zhou, and Chengde Li. Formation and evolution of far-field diffraction patterns of divergent and convergent gaussian beams passing through self-focusing and self-defocusing media. *Journal of Optics A: Pure and Applied Optics*, 7(8):409, 2005.
- [86] Cesar M Nascimento, Márcio ARC Alencar, Sabino Chávez-Cerda, Monique GA da Silva, Mario R Meneghetti, and Jandir M Hickmann. Experimental demonstration of novel effects on the far-field diffraction patterns of a gaussian beam in a kerr medium. *Journal of Optics A: Pure and Applied Optics*, 8(11):947, 2006.

- [87] Q. Fontaine, T. Bienaimé, S. Pigeon, E. Giacobino, A. Bramati, and Q. Glorieux. Observation of the bogoliubov dispersion in a fluid of light. *Phys. Rev. Lett.*, 121:183604, Oct 2018.
- [88] N. Pavloff. Optical hydrodynamics for nonlinear light propagation. http://lptms.u-psud.fr/nicolas_pavloff/talks, 2018.
- [89] JP McClure and R Wong. Multidimensional stationary phase approximation: boundary stationary point. In *The Selected Works of Roderick SC Wong*, pages 359–371. World Scientific, 2016.
- [90] Simin Feng and Herbert G Winful. Physical origin of the gouy phase shift. *Optics letters*, 26(8):485–487, 2001.
- [91] Alexander Minovich, Dragomir N Neshev, Alexander Dreischuh, Wieslaw Krolikowski, and Yuri S Kivshar. Experimental reconstruction of nonlocal response of thermal nonlinear optical media. *Optics letters*, 32(12):1599–1601, 2007.
- [92] K Creath. Phase-shifting holographic interferometry. In *Holographic Interferometry*, pages 109–150. Springer, 1994.
- [93] DS Jin, JR Ensher, MR Matthews, CE Wieman, and Eric A Cornell. Collective excitations of a bose-einstein condensate in a dilute gas. *Physical review letters*, 77(3):420, 1996.
- [94] M-O Mewes, MR Andrews, NJ Van Druten, DM Kurn, DS Durfee, CG Townsend, and W Ketterle. Collective excitations of a bose-einstein condensate in a magnetic trap. *Physical review letters*, 77(6):988, 1996.
- [95] R Onofrio, C Raman, JM Vogels, JR Abo-Shaeer, AP Chikkatur, and W Ketterle. Observation of superfluid flow in a bose-einstein condensed gas. *Physical review letters*, 85(11):2228, 2000.
- [96] J Steinhauer, R Ozeri, N Katz, and N Davidson. Excitation spectrum of a bose-einstein condensate. *Physical review letters*, 88(12):120407, 2002.
- [97] Quentin Fontaine, Pierre-Elie Larré, Giovanni Lerario, Tom Bienaimé, Simon Pigeon, Daniele Faccio, Iacopo Carusotto, Elisabeth Giacobino, Alberto Bramati, and Quentin Glorieux. Interferences between bogoliubov excitations and their impact on the evidence of superfluidity in a paraxial fluid of light. 2020.
- [98] Tiago D. Ferreira, Nuno A. Silva, and A. Guerreiro. Superfluidity of light in nematic liquid crystals. *Phys. Rev. A*, 98:023825, Aug 2018.
- [99] BB Baizakov, AM Kamchatnov, and M Salerno. Matter sound waves in two-component bose-einstein condensates. *Journal of Physics B: Atomic, Molecular and Optical Physics*, 41(21):215302, 2008.
- [100] Mordechai Segev, Yaron Silberberg, and Demetrios N Christodoulides. Anderson localization of light. *Nature Photonics*, 7(3):197, 2013.

- [101] Pierre-Élie Larré and Iacopo Carusotto. Optomechanical signature of a frictionless flow of superfluid light. *Physical Review A*, 91(5):053809, 2015.
- [102] Quentin Fontaine, Huiqin Hu, Simon Pigeon, Tom Bienaimé, E Wu, Elisabeth Giacobino, Alberto Bramati, and Quentin Glorieux. Attenuation-free non-diffracting besell beams. *Optics express*, 27(21):30067–30080, 2019.
- [103] Hoonsoo Kang and Yifu Zhu. Observation of large kerr nonlinearity at low light intensities. *Phys. Rev. Lett.*, 91:093601, Aug 2003.
- [104] Matthew Morin, Galen Duree, Gregory Salamo, and Mordechai Segev. Waveguides formed by quasi-steady-state photorefractive spatial solitons. *Optics letters*, 20(20):2066–2068, 1995.
- [105] A. G. Truscott, M. E. J. Friese, N. R. Heckenberg, and H. Rubinsztein-Dunlop. Optically written waveguide in an atomic vapor. *Phys. Rev. Lett.*, 82:1438–1441, Feb 1999.
- [106] Jiteng Sheng, Xihua Yang, Haibin Wu, and Min Xiao. Modified self-kerr-nonlinearity in a four-level n-type atomic system. *Physical Review A*, 84(5):053820, 2011.
- [107] J. Stark. Beobachtungen über den effekt des elektrischen feldes auf spektrallinien. i. quereffekt. *Annalen der Physik*, 348(7):965–982, 1914.
- [108] Claude Cohen-Tannoudji and Serge Reynaud. Dressed-atom description of resonance fluorescence and absorption spectra of a multi-level atom in an intense laser beam. *Journal of Physics B: Atomic and Molecular Physics*, 10(3):345, 1977.
- [109] Claude Cohen-Tannoudji and Serge Reynaud. Modification of resonance raman scattering in very intense laser fields. *Journal of Physics B: Atomic and Molecular Physics*, 10(3):365, 1977.
- [110] Claude Cohen-Tannoudji and Serge Reynaud. Simultaneous saturation of two atomic transitions sharing a common level. *Journal of Physics B: Atomic and Molecular Physics*, 10(12):2311, 1977.
- [111] Changjiang Wei, Dieter Suter, Andrew SM Windsor, and Neil B Manson. ac stark effect in a doubly driven three-level atom. *Physical Review A*, 58(3):2310, 1998.
- [112] Rakesh Kapoor and GS Agarwal. Theory of electromagnetically induced waveguides. *Physical Review A*, 61(5):053818, 2000.
- [113] JA Andersen, MEJ Friese, AG Truscott, Z Ficek, PD Drummond, NR Heckenberg, and H Rubinsztein-Dunlop. Light guiding light: Nonlinear refraction in rubidium vapor. *Physical Review A*, 63(2):023820, 2001.
- [114] Praveen K Vudyasetu, David J Starling, and John C Howell. All optical waveguiding in a coherent atomic rubidium vapor. *Physical review letters*, 102(12):123602, 2009.

- [115] MD Lukin and A Imamoglu. Nonlinear optics and quantum entanglement of ultra-slow single photons. *Physical Review Letters*, 84(7):1419, 2000.
- [116] O Firstenberg, M Shuker, N Davidson, and A Ron. Elimination of the diffraction of arbitrary images imprinted on slow light. *Physical review letters*, 102(4):043601, 2009.
- [117] Nuno A Silva, JT Mendonça, and Ariel Guerreiro. Persistent currents of superfluidic light in a four-level coherent atomic medium. *JOSA B*, 34(10):2220–2226, 2017.
- [118] Miguel A Bandres, Julio C Gutiérrez-Vega, and Sabino Chávez-Cerda. Parabolic nondiffracting optical wave fields. *Optics letters*, 29(1):44–46, 2004.
- [119] JJJM Durnin, JJ Miceli Jr, and JH Eberly. Diffraction-free beams. *Physical review letters*, 58(15):1499, 1987.
- [120] Tomáš Čižmár, Veneranda Garcés-Chávez, Kishan Dholakia, and Pavel Zemánek. Optical conveyor belt for delivery of submicron objects. *Applied Physics Letters*, 86(17):174101, 2005.
- [121] V Garcés-Chávez, David McGloin, H Melville, Wilson Sibbett, and Kishan Dholakia. Simultaneous micromanipulation in multiple planes using a self-reconstructing light beam. *Nature*, 419(6903):145, 2002.
- [122] François Courvoisier, Jie Zhang, MK Bhuyan, Maxime Jacquot, and John Michael Dudley. Applications of femtosecond bessel beams to laser ablation. *Applied Physics A*, 112(1):29–34, 2013.
- [123] Miguel A Porras, Alberto Parola, Daniele Faccio, Audrius Dubietis, and Paolo Di Trapani. Nonlinear unbalanced bessel beams: stationary conical waves supported by nonlinear losses. *Physical review letters*, 93(15):153902, 2004.
- [124] P Polesana, Michel Franco, Arnaud Couairon, D Faccio, and P Di Trapani. Filamentation in kerr media from pulsed bessel beams. *Physical Review A*, 77(4):043814, 2008.
- [125] Pascal Dufour, Michel Piché, Yves De Koninck, and Nathalie McCarthy. Two-photon excitation fluorescence microscopy with a high depth of field using an axicon. *Applied optics*, 45(36):9246–9252, 2006.
- [126] Ming Zhao, Han Zhang, Yu Li, Amit Ashok, Rongguang Liang, Weibin Zhou, and Leilei Peng. Cellular imaging of deep organ using two-photon bessel light-sheet nonlinear structured illumination microscopy. *Biomedical optics express*, 5(5):1296–1308, 2014.
- [127] Pontus Johansson, Dan Anderson, Mietek Lisak, and Mattias Marklund. Nonlinear bessel beams. *Optics Communications*, 222(1):107 – 115, 2003.
- [128] Jan Huiskens, Jim Swoger, Filippo Del Bene, Joachim Wittbrodt, and Ernst HK Stelzer. Optical sectioning deep inside live embryos by selective plane illumination microscopy. *Science*, 305(5686):1007–1009, 2004.

- [129] Ilya Golub, Theodore Mirtchev, Jonathan Nuttall, and Dagan Shaw. The taming of absorption: generating a constant intensity beam in a lossy medium. *Optics letters*, 37(13):2556–2558, 2012.
- [130] Michel Zamboni-Rached. Diffraction-attenuation resistant beams in absorbing media. *Optics Express*, 14(5):1804–1809, 2006.
- [131] Eliot Bolduc, Nicolas Bent, Enrico Santamato, Ebrahim Karimi, and Robert W Boyd. Exact solution to simultaneous intensity and phase encryption with a single phase-only hologram. *Optics letters*, 38(18):3546–3549, 2013.
- [132] Ismail Ouadghiri-Idrissi, Remo Giust, Luc Froehly, Maxime Jacquot, Luca Furfaro, John M Dudley, and Francois Courvoisier. Arbitrary shaping of on-axis amplitude of femtosecond bessel beams with a single phase-only spatial light modulator. *Optics express*, 24(11):11495–11504, 2016.
- [133] Tomáš Čižmár and Kishan Dholakia. Tunable bessel light modes: engineering the axial propagation. *Optics express*, 17(18):15558–15570, 2009.
- [134] Jeffrey A Davis, Don M Cottrell, Juan Campos, María J Yzuel, and Ignacio Moreno. Encoding amplitude information onto phase-only filters. *Applied optics*, 38(23):5004–5013, 1999.
- [135] D Mugnai and P Spalla. Electromagnetic propagation of bessel-like localized waves in the presence of absorbing media. *Optics Communications*, 282(24):4668–4671, 2009.
- [136] Maureen Johns, Cole A Giller, Dwight C German, and Hanli Liu. Determination of reduced scattering coefficient of biological tissue from a needle-like probe. *Optics express*, 13(13):4828–4842, 2005.
- [137] Jonathan Nylk, Kaley McCluskey, Miguel A Preciado, Michael Mazilu, Zhengyi Yang, Frank J Gunn-Moore, Sanya Aggarwal, Javier A Tello, David EK Ferrier, and Kishan Dholakia. Light-sheet microscopy with attenuation-compensated propagation-invariant beams. *Science advances*, 4(4):eaar4817, 2018.
- [138] Liang Gao. Optimization of the excitation light sheet in selective plane illumination microscopy. *Biomedical optics express*, 6(3):881–890, 2015.
- [139] Cancellation of bessel beam side lobes for high-contrast light sheet microscopy. *Scientific Reports*, 8(1):17178, 2018.
- [140] Pyotr Kapitza. Viscosity of liquid helium below the λ -point. *Nature*, 141(3558):74, 1938.
- [141] D. D. Osheroff, R. C. Richardson, and D. M. Lee. Evidence for a new phase of solid he^3 . *Phys. Rev. Lett.*, 28:885–888, Apr 1972.
- [142] Immanuel Bloch, Jean Dalibard, and Sylvain Nascimbene. Quantum simulations with ultracold quantum gases. *Nature Physics*, 8(4):267, 2012.

- [143] Y. Pomeau and S. Rica. Diffraction non linéaire. *C. R. Acad. Sci. Paris*, (397):1287, 1993.
- [144] Gaël Nardin, Gabriele Grosso, Yoan Léger, Barbara Pietka, François Morier-Genoud, and Benoît Deveaud-Plédran. Hydrodynamic nucleation of quantized vortex pairs in a polariton quantum fluid. *Nature Physics*, 7(8):635, 2011.
- [145] G. Grosso, G. Nardin, F. Morier-Genoud, Y. Léger, and B. Deveaud-Plédran. Soliton instabilities and vortex street formation in a polariton quantum fluid. *Phys. Rev. Lett.*, 107:245301, Dec 2011.
- [146] Th Frisch, Yves Pomeau, and Sergio Rica. Transition to dissipation in a model of superflow. *Physical review letters*, 69(11):1644, 1992.
- [147] G. W. Rayfield. Roton emission from negative ions in helium ii. *Phys. Rev. Lett.*, 16:934–936, May 1966.
- [148] C. A. M. Castelijns, K. F. Coates, A. M. Guénault, S. G. Mussett, and G. R. Pickett. Landau critical velocity for a macroscopic object moving in superfluid ^3He : Evidence for gap suppression at a moving surface. *Phys. Rev. Lett.*, 56:69–72, Jan 1986.
- [149] C. Raman, M. Köhl, R. Onofrio, D. S. Durfee, C. E. Kuklewicz, Z. Hadzibabic, and W. Ketterle. Evidence for a critical velocity in a bose-einstein condensed gas. *Phys. Rev. Lett.*, 83:2502–2505, Sep 1999.
- [150] D. E. Miller, J. K. Chin, C. A. Stan, Y. Liu, W. Setiawan, C. Sanner, and W. Ketterle. Critical velocity for superfluid flow across the bec-bcs crossover. *Phys. Rev. Lett.*, 99:070402, Aug 2007.
- [151] Michiel Wouters and Iacopo Carusotto. Superfluidity and critical velocities in nonequilibrium bose-einstein condensates. *Phys. Rev. Lett.*, 105:020602, Jul 2010.
- [152] AC Berceanu, E Cancellieri, and FM Marchetti. Drag in a resonantly driven polariton fluid. *Journal of Physics: Condensed Matter*, 24(23):235802, 2012.
- [153] P.-É. Larré, N. Pavloff, and A. M. Kamchatnov. Wave pattern induced by a localized obstacle in the flow of a one-dimensional polariton condensate. *Phys. Rev. B*, 86:165304, Oct 2012.
- [154] P.-É. Larré, N. Pavloff, and A. M. Kamchatnov. Polarization hydrodynamics in a one-dimensional polariton condensate. *Phys. Rev. B*, 88:224503, Dec 2013.
- [155] M Albert, T Paul, N Pavloff, and P Leboeuf. Dipole oscillations of a bose-einstein condensate in the presence of defects and disorder. *Physical review letters*, 100(25):250405, 2008.
- [156] Maxime Joos. Dispositifs hybrides: nanoparticules couplées à une nanofibre optique. 2018.

- [157] YY Hung and CY Liang. Image-shearing camera for direct measurement of surface strains. *Applied Optics*, 18(7):1046–1051, 1979.
- [158] Sebabrata Mukherjee, Harikumar K Chandrasekharan, Patrik Öhberg, Nathan Goldman, and Robert R Thomson. State-recycling and time-resolved imaging in topological photonic lattices. *Nature communications*, 9(1):4209, 2018.
- [159] D Di Battista, D Ancora, M Leonetti, and G Zacharakis. Tailoring non-diffractive beams from amorphous light speckles. *Applied Physics Letters*, 109(12):121110, 2016.
- [160] A Chiocchetta, P-É Larré, and I Carusotto. Thermalization and bose-einstein condensation of quantum light in bulk nonlinear media. *EPL (Europhysics Letters)*, 115(2):24002, 2016.
- [161] Quentin Glorieux. Quantum optics in dense atomic media: From optical memories to fluids of light. *arXiv preprint arXiv:1812.08602*, 2018.